Karlsruhe Institute of Technology

Systematic Studies of the Micro-Bunching Instability with an Additional Corrugated Structure Impedance at KARA

Zur Erlangung des akademischen Grades eines
DOKTORS DER NATURWISSENSCHAFTEN (Dr. rer. nat.)

von der KIT-Fakultät für Physik des
Karlsruher Instituts für Technologie (KIT)
genehmigte

DISSERTATION
von

M.Sc. Sebastian Maier
aus Ettlingen

Tag der mündlichen Prüfung: 03.05.2024
Erstgutachterin: Prof. Dr. Anke-Susanne Müller
Zweitgutachter: Prof. Dr. Ulrich Husemann

Abstract

The micro-bunching instability is a roadblock on the way to high brilliance and high peak power synchrotron light sources and electron storage rings. To study, understand, and control the creation of substructures in the longitudinal phase-space and bunch profile, an additional and exchangeable impedance will be installed in the Karlsruhe Institute of Technology (KIT) storage ring Karlsruhe Research Accelerator (KARA).

This thesis studies a pair of plates with periodic rectangular corrugations as impedance sources. The investigations cover the impact of the different corrugation parameters on the impedance, the impact of the additional impedance on the longitudinal beam dynamics, and the study of the influence of the machine and beam settings on the most effective impedance. The latter gives an insight into the underlying mechanisms of the micro-bunching instability. Furthermore, different manufacturing methods and the production of prototypes are presented.

Kurzfassung

Die Mikrobündelungs-Instabilität (engl. micro-bunching instability) ist eine Barriere auf dem Weg zu Synchrotron-Lichtquellen und Elektronen-Speicherringen mit höherer Brillanz und Spitzenleistung. Um die Entstehung der Substrukturen im longitudinalen Phasenraum und Bunch-Profil zu untersuchen, zu verstehen und zu kontrollieren wird eine zusätzliche und austauschbare Impedanz in den KIT-Speicherring KARA eingebaut.

In dieser Arbeit wird ein Plattenpaar mit periodischen und rechteckigen Vertiefungen als zusätzliche Impedanzquelle untersucht. Die Untersuchungen behandeln den Einfluss der unterschiedlichen Parameter der Vertiefungen auf deren Impedanz, den Einfluss der zusätzlichen Impedanz auf die longitudinale Strahldynamik und die Ermittlung des Einflusses der Maschinen- und Strahlparameter auf die effektivste Impedanz. Letzteres ermöglicht Einblicke in die Mechanismen, die der Mikrobündelungs-Instabilität zugrunde liegen. Darüber hinaus werden verschiedene Fertigungsverfahren und die Produktion erster Prototypen präsentiert.

Contents

1. Introduction

This thesis presents a simulation study of the beam dynamics in the bursting regime of the micro-bunching instability under the influence of an additional corrugated structure impedance for the Karlsruhe Research Accelerator (KARA) storage ring. In the bending sections of circular accelerators, synchrotron radiation is emitted. Electron storage rings and synchrotron light sources are particle accelerators which are optimized in terms of the production of the synchrotron radiation. This radiation ranges from the microwave to the X-ray frequency range and is an important tool for research in a wide range of scientific fields. An important area is the THz frequency range, since there is a lack of other sources this frequency range. It has been proven that for certain imaging techniques THz radiation is benefical in comparison with X-ray, because no ionization side effects occur. Intense pulses of THz radiation find a wide range of scientific applications [1], of which the *in situ* monitoring of chemical reactions with THz rotational spectroscopy [2] can be mentioned as an example.

In order to meet the increasing demands of such experiments, synchrotron light sources need to provide increasingly higher brilliance. Apart from a reduction of the transverse emittance of the particle beam, the higher brilliance can be achieved by increasing the photon flux. The photon flux can be increased by compressing the electron bunches to achive longitudinal coherence of the photon pulses. Thereby, the short electron bunches causes the emission of coherent synchrotron radiation (CSR). Unlike incoherent synchrotron radiation, the power of CSR does not scale linearly with the number of photons but quadratically. As a result, the flux of emitted photons can be amplified by several orders of magnitude. However, only if the wavelength of the photons is greater than the emitting structure, the radiation will be emitted coherently. To extend these high-power CSR into the THz frequency range, the longitudinal size of the electron bunches must be reduced to the single-digit picosecond timescale.

To reach these short bunches at the KARA storage ring, dedicated magnet optics with reduced momentum compaction factor, referred to as low-α_c, is used [3; 4]. In the regime of very short bunches with typical bunch length of 2 ps to 10 ps, the emitting structures interact with their self-emitted CSR, which can result in non-linear phenomena and complex dynamics like the so-called micro-bunching instability [5; 6; 7]. This interaction can be described accurately by the wakefields and impedance in the storage ring. The micro-bunching instability leads to deformations of the longitudinal bunch profile by the periodic creation and disappearance of sub-bunches over time. The temporal evolution of the longitudinal substructures causes quasi-periodic outbursts of intense THz radiation [4; 8; 9]. These outbursts are an obstacle to high brilliance, peak power, and a temporal stable photon flux, which are required for the different applications. On the other hand, the substructures are a source of THz radiation, opening a new frequency range of intense CSR. To make use of this THz radiation and to overcome the limitations of photon flux stability and brilliance, outbursts have to be properly controlled.

At the MLS[1], X. Deng *et al.* [10] generate high-power CSR by controlling the instability due to the creation of a Steady-state micro-bunching (SSMB). In contrast, C. Evain *et al.* [11] use a feedback control at a constant bunch current to sustain the micro-bunching instability at the Synchrotron SOLEIL[2]. In this way, the substructures do not evolve over time by giving additional perturbation on the bunch profile, so the intense CSR is stable over time. At the KARA storage ring, a fast feedback control, based on reinforcement learning, is under comissioning to enhance and stabilize the emitted CSR for the whole current decay [12; 13]. All these methods to create or stabilize the substructures are based on a periodic energy redistribution by either a laser pulse (SSMB) or a manipulation of the acceleration voltage.

However, in this thesis the energy redistribution is realized by an additional impedance source. The impedance of the storage ring describes the interaction of the electron beam with its environment and the resulting wake potentials cause a position-dependent energy redistribution and thereby affect the longitudinal bunch profile and beam dynamics including the micro-bunching instability. Therefore, the manipulation of the impedance by a dedicated geometric impedance and the resulting changes in the beam dynamics give insights in the underlying mechanisms. For the controlled manipulation of the impedance by a dedicated structure, a corrugated plate has been chosen and installed in several linear accelerators for various purposes. Such a corrugated structure creates an impedance only in a well-defined frequency range, which is specified by the dimensions of the corrugations. At LINAC[3]-based free-electron laser (FEL) facilities, like the SwissFEL [14] and PAL-XFEL [15], corrugated structures are installed and tested as energy dechirper. K. L. Bane *et al.* [16; 17] have tested a cylindrical corrugated pipe at a linear accelerator at Brookhaven's Accelerator Test Facility (ATF). This structure is used to produce local and intense Smith-Purcell radiation [18] in the THz frequency range. However, to the best of our knowledge, in a storage ring where the beam is frequently manipulated at every turn, such a structure has not yet been installed. Still S. A. Antipov *et al.* [19] from DESY[4] have simulated that a corrugated structure can reduce the bunch length for a beam current regime, at which the micro-bunching instability does not occur. However, this study neglected the dominant beam-coupling impedance at the KARA storage ring, on top of which the corrugated structure impedance is only a perturbation. Furthermore, the study is done for only a single corrugation dimension setting.

For the KARA storage ring it is planned to install such an additional impedance source to study, understand, and control the micro-bunching instability. This requires detailed and systematic simulation studies to define the optimal structure geometry, to affect the beam dynamics most effectively. Based on this, the structure need to be designed and manufactured. The corrugation dimensions on the scale of 100 µm, combined with the necessary structure length of 20 cm, place high demands on the impedance simulations and the possible manufacturing methods.

This thesis presents the impact of the impedance of an additional corrugated structure on the longitudinal beam dynamics, especially in the beam current regime of the micro-bunching instability at the KARA storage ring, while taking the relevant beam-coupling impedance into account. The structure to be installed will consist of a pair of horizontal parallel plates with periodic rectangular corrugations (see Figure 1.1). After setting the relevant theoretical framework (Chapter 2), the KARA facility, the operation mode providing the short bunches, and the planned location of the impedance manipulation chamber are presented (Chapter 3). Next, the used and (further) developed methods to

---

[1] Metrology Light Source, Berlin, Germany

[2] Optimized Light Source of Intermediate Energy to LURE (fr. Source optimisée de lumière d'énergie intermédiaire du LURE), Saint-Aubin, France

[3] Linear accelerator

[4] German Electron Synchrotron (dt. Deutsches Elektronen-Synchrotron), Hamburg, Germany

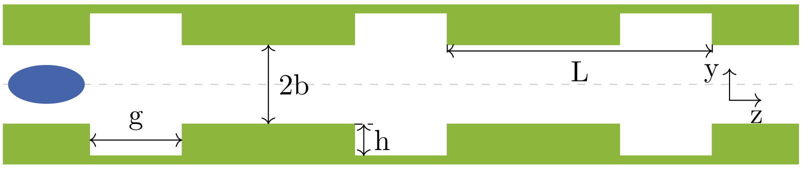

Figure 1.1. Corrugated plates The corrugated pipe in cross-section with the relevant geometric parameters are shown. The electron bunch is indicated in blue and travels along the dashed line through the structure.

analyze the simulation data are explained (Chapter 5).

The studies discussed in this thesis are split into three parts. First, the influence of the different corrugation dimensions on its impedance is investigated in Chapter 6. These systematic scans can be used to determine the corrugation design that will provide a specific, well-defined impedance. Following in Chapter 7, results of longitudinal beam dynamics simulations in dependence on the additional corrugated plate impedances are shown. Thereby, the impact of the impedance on the emitted CSR and the properties of the micro-bunching instability are presented. The study of the influence of the machine settings on the most effective impedance to affect micro-bunching instability reveals one of the underlying mechanisms that drive the instability. Finally, different manufacturing methods, their advantages, disadvantages, and the acceptable tolerances are discussed in Chapter 8.

2. Theoretical Framework

This chapter outlines the theoretical framework which is necessary for this thesis. The first part explains the basics of particle acceleration, especially in a synchrotron as a storage ring. Subsequently, the theory behind beam dynamics, incoherent synchrotron radiation (ISR) and coherent synchrotron radiation (CSR) are explained. Afterward, the concept of impedances and wake fields is introduced, and different impedances, such as the CSR impedance and the impedance of a corrugated structure, are presented. The following Section explains the Vlasov-Fokker-Planck equation, which allows the calculation of the longitudinal beam dynamics under the influence of the machine impedance. The interaction of the particle beam with the self-emitted CSR - calculated by the CSR impedance - results in the so-called micro-bunching instability, which is also introduced in this Section. In the last Section radio frequency (RF), networks and the scattering matrix are explained as key parameters to describe such a network and can be used to characterize the corrugated plates before the installation in the Karlsruhe Research Accelerator (KARA) storage ring.

2.1. Overview of Accelerator Physics

This Section summarizes the working principles of particle accelerators, mainly circular accelerators. A more in-depth treatment of this topic can be found in textbooks such as [20] and [21].

2.1.1. Acceleration of Charged Particles

Particles which travel through an electromagnetic field with the charge q and the velocity $\vec{v}$ witness a Lorentz force

$$\vec{F} = q \cdot \left(\vec{E}_{\mathrm{el}} + \vec{v} \times \vec{B}\right) \tag{2.1}$$

with the electric field $\vec{E}_{\mathrm{el}}$ and the magnetic flux density $\vec{B}$. This force results in both longitudinal and transverse acceleration, such as an energy gain due to the particle motion inside the electromagnetic field from $\vec{r}_1$ to $\vec{r}_2$

$$\Delta E = \int_{\vec{r}_1}^{\vec{r}_2} \vec{F} \cdot \mathrm{d}\vec{r} = q \cdot \int_{\vec{r}_1}^{\vec{r}_2} \left(\vec{E}_{\mathrm{el}} + \vec{v} \times \vec{B}\right) \cdot \mathrm{d}\vec{r} \quad . \tag{2.2}$$

Since $\mathrm{d}\vec{r} = \vec{v} \cdot \mathrm{d}t$ is parallel to the velocity $\vec{v}$, the term $\left(\vec{v} \times \vec{B}\right) \cdot \mathrm{d}\vec{r}$ is equal to zero. Consequently, the magnetic field does not contribute to the energy gain, and Equation (2.2) simplifies to

$$\Delta E = q \cdot \int_{\vec{r}_1}^{\vec{r}_2} \vec{E}_{\mathrm{el}} \cdot \mathrm{d}\vec{r} = q \cdot U \quad , \tag{2.3}$$

where U is the voltage or electric potential difference between the points $\vec{r}_1$ and $\vec{r}_2$.
In contrast to acceleration, a deflection of charged particles can be achieved with both electric and magnetic fields. Equation (2.1) points out that in the ultra-relativistic case

($v \approx c$), the force induced by the magnetic field is higher than for the electric field by a factor of c. Consequently, an electric field of $300\,\frac{\mathrm{MV}}{\mathrm{m}}$ is required to create the same force as a 1 T magnetic field. Because such an E-field is not practical, primarily magnetic fields are used for the deflection and guidance of the charged particles. The perpendicular part of the Lorentz force, generated by a constant magnetic field, acts as a centripetal force

$$\frac{m_0 \cdot v^2}{\rho} = q \cdot v \cdot \left|\vec{B}\right| \tag{2.4}$$

with the mass of the electron m_0 and the bending radius ρ. Hence, the bending radius increases linearly with the momentum $p = m \cdot v$ of the particle:

$$\rho = \frac{p}{q \cdot \left|\vec{B}\right|} \quad . \tag{2.5}$$

In the ultra-relativistic case, the relationship between energy and momentum converges to $E = \sqrt{(m_0 \cdot c^2)^2 + (p \cdot c)^2} \approx p \cdot c$, so that:

$$\rho \approx \frac{E}{c \cdot q \cdot \left|\vec{B}\right|} \quad . \tag{2.6}$$

2.1.2. Synchrotron as a Storage Ring

The theoretical concept of the synchrotron was developed by E. M. McMilian and published in 1945[22], after which the first synchrotron was built up at the University of California in the second half of the 1940s. In contrast to other circular accelerators, such as cyclotrons [23] or microtrons [24], the bending radius of the particles is kept constant as the the particle momentum increases. Consequently, following from Equation (2.6), the magnetic field must increase simultaneously with the momentum of the particle to keep them in the desired orbit. This allows to build up larger accelerators, which can have particle energies in the GeV range for electrons or even TeV range for protons. Since in a synchrotron, in addition to the dipole magnets, other elements such as diagnostics, insertion devices, and acceleration elements are required, the magnets are grouped in bending sections with straight in-between sections for the other elements. Therefore, the synchrotrons are built up as a polygon instead of a perfect circle.

Historically, and for low energies, electrostatic fields were used for particle acceleration. The fed-in energy was thereby limited by the breakdown voltage and resulting spark-overs, so nowadays, alternating electromagnetic fields are in use instead. Due to frequent passing, in principle, only one RF acceleration section is needed in a circular accelerator, which provides a sinusoidal voltage

$$U(t) = U_{\mathrm{acc}} \cdot \sin\left(2\pi \cdot f_{\mathrm{RF}} \cdot t\right) \quad , \tag{2.7}$$

with the acceleration voltage amplitude U_{acc} and the RF-frequency f_{RF}.

For the usage of synchrotrons as a storage ring, the energy losses over a whole turn must be compensated by the regained energy in the acceleration section. Since the right amount of energy is only provided at a certain phase, the particle beam is not continuous but split into packages - the so-called bunches, which must arrive in the RF section at the synchronous phase Ψ_{s}. This results in a strict relation between the revolution frequency $f_{\mathrm{rev}} = \frac{C}{v}$ (with the circumference C) and the RF frequency

$$f_{\mathrm{RF}} = h \cdot f_{\mathrm{rev}} \quad , \tag{2.8}$$

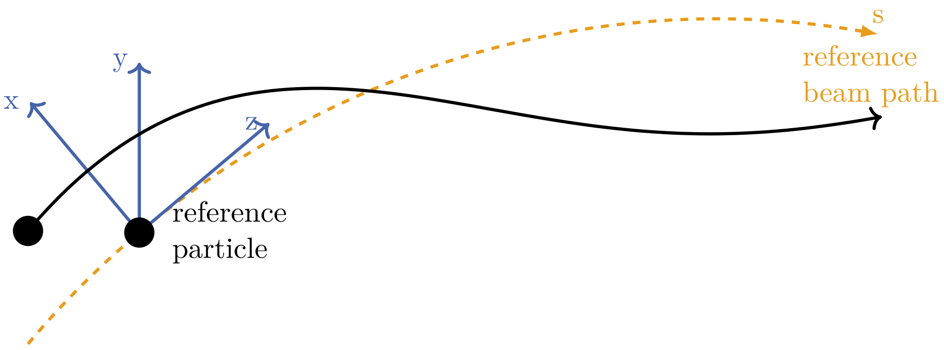

Figure 2.1. Particle position relative to reference particle. The relative deviation from the synchronous particle is given in the Frenet-Serret coordinate system, where z at a given point in time is given as the deviation tangential to the reference orbit. The coordinates x and y describe the transverse offset.

where h is an integer called the harmonic number, which also defines the theoretical maximal number of bunches that can be stored in the synchrotron.
The current of a single bunch or the whole beam is connected to the number of particles and the revolution frequency via the elementary charge e

$$I = \frac{q}{T} = q \cdot f_{\text{rev}} = -e \cdot N \cdot f_{\text{rev}} \tag{2.9}$$

with the number of particles N and the charge q.
Synchrotrons can also be operated as storage rings and store the particles over several hours. During storage, particles are lost, e.g. due to scattering with residual gas atoms or with particles in a single bunch. Usually, synchrotrons are used as the last part of the pre-accelerator chain of the storage ring. If the synchrotron provides particles with the end energy (full-energy injector), the storage ring can operate in the top-up mode, where particles are frequently injected into the storage ring so that the number of particles and the beam current can be kept almost constant. In other particle accelerator facilities, the last synchrotron is used as a storage ring after the synchronous ramping of the magnets and the particle's energy, which is why this type is called a ramping machine. At KARA, the particles can only be injected into the storage ring before the ramping, so the beam current decreases over time.
The position of any particle at a given time t is given relative to a hypothetical particle on the reference orbit (referred to as synchronous particle), which is described with the ideal trajectory $\vec{s}(t)$ and the ideal momentum p_{s}. The relative deviation from the synchronous particle is given in the orthogonal comoving Frenet-Serret coordinate system[21], where z at a given point in time is given as the deviation tangential to the reference orbit (see Figure 2.1). The coordinates x and y describe the transverse offset.

2.2. Beam Dynamics

In the previous section, only particles with the reference momentum p_{s} and therefore - according to Equation (2.6) - a constant bending radius, which travel on the orbit of the synchronous particle are discussed. Due to momentum spread and divergence, additional higher-order magnet elements are necessary for the guidance to keep the particles in a stable and closed orbit. The first part of this section focuses on the impact of especially quadrupoles on transverse beam dynamics. In contrast, in the second part, the longitudinal movement of the bunch relative to the synchronous particle is discussed.

2.2.1. Transverse Beam Dynamics

Transverse divergence cannot only be controlled but even suppressed through additional magnetic fields. Since the dimensions of the transverse deviation from the synchronous orbit are small against the bending radius ρ, the vertical magnetic field - leading to horizontal deflection - can be described by a Taylor expansion of Equation (2.4) around the orbit of the synchronous particle (x=0) [20] by:

$$\begin{aligned}\frac{q}{p}B_\mathrm{y} &= \frac{1}{0!}\frac{q}{p}B_\mathrm{y}(0) &&+\frac{1}{1!}\frac{q}{p}\frac{\mathrm{d}B_\mathrm{y}(x)}{\mathrm{d}x}x &&+\frac{1}{2!}\frac{q}{p}\frac{\mathrm{d}^2B_\mathrm{y}(x)}{\mathrm{d}x^2}x^2 &&+\dots\\ &= \underbrace{\frac{1}{0!}\frac{1}{\rho}}_{\text{Dipole}} &&+\underbrace{\frac{1}{1!}k\cdot x}_{\text{Quadrupole}} &&+\underbrace{\frac{1}{2!}m\cdot x^2}_{\text{Sextupole}} &&+\dots.\end{aligned} \tag{2.10}$$

The field of a dipole magnet with opposite poles above and below the particle path is independent of the horizontal position. Therefore, it can be used for the deflection in the horizontal plane to keep the particles on a circular orbit with the bending radius ρ. That is why the dipole magnets are also called bending magnets. Since the horizontal momentum is changed the most in the bending magents, they are the primary regimes in which synchrotron radiation is emitted. This is explained in detail in Section 2.3.
The second term describes the field of a magnetic quadrupole, which scales linearly with the horizontal deviation from the center of the magnet, with the quadrupole strength parameter $k = \frac{q}{p}\frac{\mathrm{d}B_\mathrm{y}(x)}{\mathrm{d}x}$. The resulting Lorentz force in the horizontal plane points towards the center of the magnet, making these magnets employed as focal lenses to collimate the divergent beam. In contrast to optical lenses, the quadrupole field only focuses on one, but defocuses the beam in the other transverse plane. Therefore, a set of at least two quadrupoles with a relative rotation by 90 ° and a correct distance is necessary for an overall net focusing.
The first two orders are enough for guidance and holding the particles in a closed orbit. For simulations and calculations of particle tracks, often only these orders are used as a simplification because the two transverse planes are not coupled in the second-order description. Since only field components up to the linear position dependency are considered, this is called "*linear optics*".
However, most synchrotrons and storage rings use at least sextupole magnets with their strength $m = \frac{1}{2}\frac{q}{p}\frac{\mathrm{d}^2B_\mathrm{y}(x)}{\mathrm{d}x^2}$ to compensate chromaticity effects caused by the focussing of particles with different energies in the quadrupoles. The chromaticity characterizes the energy-depending focusing and thus behaves analogously to the color aberration in optics. Using even higher-order magnets is possible and done in some accelerators to correct the field errors in the sextupole magnets.
Under the assumption of only linear optics, no momentum deviation $\frac{\Delta p}{p_\mathrm{s}} = 0$, and no coupling between the horizontal and vertical plane, the transverse motion around the synchronous particle can be described by Hill's differential equation [25] by:

$$u''(s) + K(s)\cdot u(s) = 0 \quad , \tag{2.11}$$

in which $u(s)$ is a transverse deviation in x or y. For the two different planes, the function $K(s)$ is given as $K_\mathrm{x}(s) = -k(s) + \frac{1}{\rho(s)^2}$ and $K_\mathrm{y}(s) = k(s)$, whereby the different sign in the term $k(s)$ is a result of the different focusing in the horizontal and vertical plane. In the vertical plane, there is no bending due to the dipole magnets, so the bending radius is infinite, and the term $\frac{1}{\rho^2}$ vanishes. The function $K(s)$ is periodic with the accelerator orbit length L_0 so that $K(s + L_0) = K(s)$ is fulfilled. The homogeneous Hill's differential

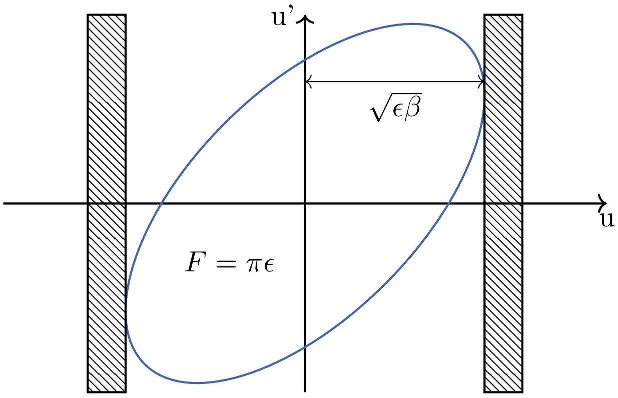

Figure 2.2. Transverse phase space ellipse. The particle trajectory encloses an ellipse in the transverse phase space (u, u'). Based on Liouville's theorem, the area of the ellipse is constant under conservative forces. The maximal transverse deviation of stable particles is given by $\sqrt{\epsilon\beta}$. This also defines the minimal aperture of the beam pipe (hatched areas) - based on [20]

equation can be solved with the approach [26; 20]

$$u(s) = \sqrt{\epsilon \cdot \beta(s)} \cdot \cos\left(\Psi(s) + \Psi_{\mathrm{s}}\right) \tag{2.12}$$

with the single particle emittance ϵ, the betatron-function β(s), and the synchronous phase Ψ_{s}. This oscillation around the synchronous particle in both transverse planes is referred to as betatron oscillation. The emittance is a measure of the ellipse area, which is enclosed by the particle's trajectory in the transverse phase space, which is spanned by the transverse position and momentum (u, u') of the particle and shown in Figure 2.2. The theorem of Liouville [27] states that the area of the ellipse is constant under the influence of conservative forces and is given by $F = \pi\epsilon$. However, the shape and orientation of the ellipse change in dependence on the position on the synchronous orbit. Due to radiation losses and energy regain, the Liouville theorem is invalid for the longitudinal phase space (and the transverse phase space), which will be discussed in the next section.
Equation (2.12) shows directly that at each point of the beam pipe, the stable particles with the largest transverse deviation have to fulfill $\cos\left(\Psi(s) + \Psi_{\mathrm{s}}\right) = \pm 1$ and consequently the envelope that contains all particles is given by:

$$u_{\mathrm{env.}}(s) = \pm\sqrt{\epsilon\beta(s)} \quad . \tag{2.13}$$

In the previous discussion, the momentum of the synchronous particle p_{s} was assumed for all particles. Following Equation (2.6), slight momentum deviations Δp result in varying bending radii and, therefore, different paths. In the vertical plane, this dispersion is insignificant because the dipoles mainly cause a horizontal deflection. Indeed, Equation (2.11) must be extended for the horizontal plane to an inhomogeneous differential equation:

$$x''(s) + \left(\frac{1}{\rho(s)^2} - k(s)\right) \cdot x(s) = \frac{1}{\rho(s)} \cdot \frac{\Delta p}{p_{\mathrm{s}}}. \tag{2.14}$$

The particular solution can be found with the dispersion $D(s) = \frac{x_{\mathrm{p}}(s)}{\frac{\Delta p}{p_{\mathrm{s}}}}$ as $x_{\mathrm{p}} = D(s) \cdot \frac{\Delta p}{p_{\mathrm{s}}}$. The dispersion orbit D(s) describes the path for a particle with the relative momentum deviation $\frac{\Delta p}{p_{\mathrm{s}}} = 1$, so that the vertical dispersion is negligible. Therefore, the solution of the inhomogeneous Hill's equation is given by:

$$u(s) = \sqrt{\epsilon \cdot \beta_\mathrm{u}(s)} \cdot \cos\left(\Psi(s) + \Psi_\mathrm{s}\right) + D_\mathrm{u}(s) \cdot \frac{\Delta p}{p_\mathrm{s}} \quad . \tag{2.15}$$

Consequently, the root mean square (RMS) transverse beam size σ_u can be determined from the envelope of the betatron oscillation, corrected with an additional dispersion term [21]:

$$\sigma_\mathrm{u}(s) = \sqrt{\epsilon \cdot \beta_\mathrm{u} + \left(D_\mathrm{u}(s)\frac{\sigma_\mathrm{p}}{p_\mathrm{s}}\right)^2} \tag{2.16}$$

with the RMS momentum spread σ_p.

2.2.2. Longitudinal Beam Dynamics

Analogous to the particle motion in the other planes, the longitudinal beam dynamics directly depends on the particle momentum and its deviation from the synchronous momentum p_s. The theoretical particle traveling with p_s on the synchronous orbit arrives at the synchronous phase $\sin\Psi_\mathrm{s} = \frac{W_0}{e \cdot U_\mathrm{acc}}$ of the RF voltage in the cavity. At this phase, the energy radiated per revolution W_0 is regained. This synchrotron radiation loss will be discussed in detail in Section 2.3. In longitudinal beam dynamics, changing the bending radius due to a momentum offset leads to different path lengths and consequently to a different arrival time and phase in the RF cavity. In the ultrarelativistic case, electrons with lower momenta take a shorter path and arrive earlier in the cavity[5]. Vice versa, high momentum particles arrive later at the RF section. Suppose the accelerator sets the synchronous phase on the falling positive flank of the RF voltage, the earlier electrons with lower momentum arrive at a phase with a higher accelerating field and regain a larger amount of energy, whereas the later electrons (p>p_s) gain less energy (illustrated in Figure 2.3). For all electrons, this results in focus towards the synchronous momentum, which is why this effect is called phase focusing. Performing on the rising positive flank leads to a defocusing of the momentum, resulting in losing the beam.

From this, an equation of motion can be derived (based on [20]), which describes the so-referred synchrotron oscillation. The energy change of a single particle per revolution can be determined by

$$\delta E = eU_\mathrm{acc} \sin\left(\Psi_\mathrm{s} + \Delta\Psi\right) - W \quad . \tag{2.17}$$

For a small momentum deviation ($\Delta p \ll p_\mathrm{s}$), the energy loss depends linearly on the particle energy deviation $W = W_0 + \frac{\mathrm{d}W}{\mathrm{d}E}\Delta E$. Accordingly, the difference in the energy gain of an off-momentum particle compared to the synchronous particle can be described by

$$\Delta E = eU_\mathrm{acc}\left[\sin\left(\Psi_\mathrm{s} + \Delta\Psi\right) - \sin\Psi_\mathrm{s}\right] - \frac{\mathrm{d}W}{\mathrm{d}E}\Delta E \quad , \tag{2.18}$$

which can be simplified and summarized by a Taylor expansion of the sinusoidal term for a small $\Delta\Psi$ to

$$\Delta E = eU_\mathrm{acc} \cdot \Delta\Psi \cos\Psi_\mathrm{s} - \frac{\mathrm{d}W}{\mathrm{d}E}\Delta E \quad . \tag{2.19}$$

Since the period of the synchrotron oscillation T_s goes over multiple turns ($T_\mathrm{rev} \ll T_\mathrm{s}$), the time derivative of ΔE can be obtained by dividing Equation (2.19) by T_rev. From this, the second derivative can be obtained as

$$\Delta\ddot{E} = \frac{eU_\mathrm{acc}}{T_\mathrm{rev}}\Delta\dot{\Psi} \cdot \cos\Psi_\mathrm{s} - \frac{\mathrm{d}W}{\mathrm{d}E}\frac{1}{T_\mathrm{rev}}\Delta\dot{E} \quad . \tag{2.20}$$

---

[5] This is the case for a positive momentum-compaction factor α_c. In the case of negative α_c, the correlation between momentum deviation and arrival time is inverted.

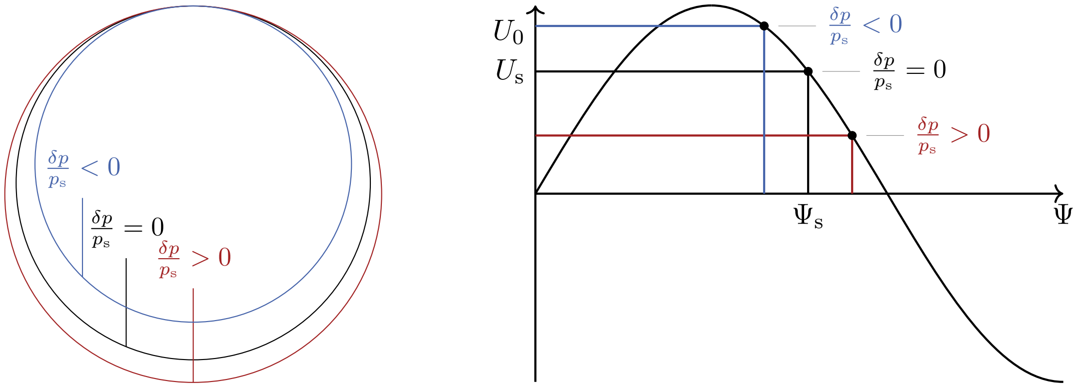

(a) **(b)**

Figure 2.3. Principle of phase-focussing. (a) Particles with a higher momentum (red) than the synchronous particle (black) travel on a longer path and vice versa. (b) By accelerating on the falling positive flank, these delayed particles experience a smaller voltage and gain less energy than the synchronous particle. Consequently, the particles are focused towards the synchronous particle. This Figure is based on [26].

The relation between the relative deviation of the particle's orbit length or revolution time is given by the momentum compaction factor α_c and the slippage factor η_c, respectively

$$\frac{\Delta L}{L_0} = \alpha_c \frac{\Delta p}{p_s} \quad , \quad \frac{\Delta T}{T_{\mathrm{rev}}} = \eta_c \frac{\Delta p}{p_s} \quad .. \tag{2.21}$$

The momentum compaction factor is defined as the integral of the dispersion D over a whole turn [21]

$$\alpha_c = \frac{1}{L_0} \oint \frac{D(s)}{\rho(s)} \mathrm{d}s \quad , \tag{2.22}$$

so that only the dispersion inside the bending magnets is relevant, where ρ is finite. The zero-th-order slippage factor $\eta_c = \alpha_c - \frac{1}{\gamma^2}$ converges to α_c for ultra-relativistic particles ($v \approx c$).

Deduced from Equations (2.8) and (2.21), a shift in the phase can be determined by:

$$\Delta\Psi = h \cdot \omega_{\mathrm{rev}} \Delta T = 2\pi \cdot h \frac{\eta_c}{\beta^2} \frac{\Delta E}{E} \quad . \tag{2.23}$$

Substituting the derivative of this term into Equation (2.20) results in

$$\Delta\ddot{E} = \frac{eU_{\mathrm{acc}}}{T_{\mathrm{rev}}} \frac{2\pi}{T_{\mathrm{rev}}} \frac{\eta_c}{\beta^2} \cos\Psi_s \frac{\Delta E}{E} - \frac{\mathrm{d}W}{\mathrm{d}E} \frac{1}{T_{\mathrm{rev}}} \Delta\dot{E} \quad , \tag{2.24}$$

which is the motion of a harmonic damped oscillator $\Delta\ddot{E} + 2\alpha_z \Delta\dot{E} + \omega_s^2 \Delta E = 0$ with the damping constant

$$\alpha_z = \frac{1}{\tau_D} = \frac{1}{2T_{\mathrm{rev}}} \frac{\mathrm{d}W}{\mathrm{d}E} \tag{2.25}$$

and the synchrotron frequency

$$\omega_s = \omega_{\mathrm{rev}} \sqrt{-\frac{eU_{\mathrm{acc}} \cdot h}{2\pi \cdot E} \frac{\eta_c}{\beta^2} \cos\Psi_s}. \tag{2.26}$$

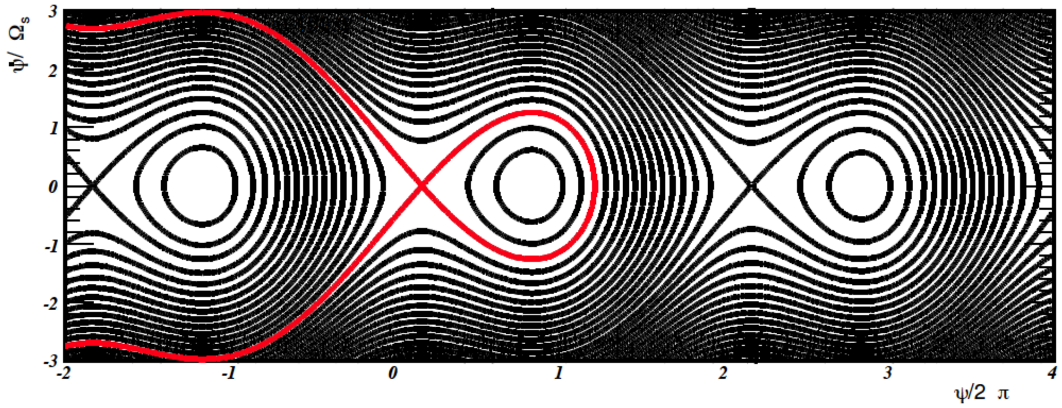

Figure 2.4. Separatrix. The red line indicates the separatrix, which separates the stable and unstable trajectories in the longitudinal phase space. Only particles inside the separatrix can be stored in the accelerator [26].

The RMS natural bunch length σ_0 is defined as the length of the particle bunch at a low bunch charge so that the energy radiation and gain are in equilibrium [28; 21]:

$$\sigma_0 = \frac{c\,|\alpha_\mathrm{c}|}{2\pi \cdot f_\mathrm{s}} \cdot \frac{\sigma_\mathrm{p}}{p_\mathrm{s}} \propto \frac{\alpha_\mathrm{c}^{\frac{1}{2}} \cdot E^{\frac{1}{2}}}{U_\mathrm{acc}^{\frac{1}{2}}} \tag{2.27}$$

with the adjustable machine parameters momentum compaction factor α_c, particle energy E, and RF voltage amplitude U_acc. In Figure 2.4, the longitudinal phase space and possible trajectories in it are illustrated. The red line marks the most extreme stable and closed trajectory called separatrix, whereby the area inside is the RF bucket. The maximal stable momentum deviation is described by the height of the bucket and is referred to as its RF acceptance (MA).

2.3. Synchrotron Radiation

If the momentum of charged particles changes, they lose energy due to the radiation of electromagnetic waves based on the fundamental rules of electrodynamics, which is explained in detail by J. D. Jackson [29]. The emission power in the ultra-relativistic case (E»m_0c) can be described by the Lorentz-invariant version of the equation by J. Larmor [30], which characterizes the radiation due to a momentum change in the non-relativistic case ($E \approx m_0c^2$). Since the radiation for longitudinal momentum change (acceleration) is negligible, only the transverse momentum change (deflection) is taken into account [26] for the determination of the total radiated power. This kind of radiation has been detected for the first time at a 70 MeV electron synchrotron of General Electric in 1946 [31], which is why it is referred to as synchrotron radiation. A.-M. Liénard has already described the equation for the radiation power in the relativistic case for transverse momentum change at the end of the 19th-century [32]:

$$P_\mathrm{s} = \frac{e^2 \cdot c}{6\pi \cdot \epsilon_0} \frac{1}{(m_0 \cdot c^2)^4} \frac{E^4}{\rho^2} \quad , \tag{2.28}$$

which shows that the radiation power is insignificant for the non-relativistic case. The scaling with $1/m_0^4$ means that only electrons emit a significant radiation power in the KARA energy range (E_KARA=0.5 GeV - 2.5 GeV).

As discussed in Section 2.1.2, the lost energy of each turn has to be regained in the cavities and, therefore, determines the synchronous phase. Assuming that the energy loss is small compared to the particle energy E, the energy loss per revolution can be calculated by integrating the power loss over one turn. Since the power loss is only finite in the bending sections with a finite bending radius, the power loss is given by [26]:

$$W_0 = \oint P_{\mathrm{s}} \mathrm{d}t = P_{\mathrm{s}} \cdot t_{\mathrm{b}} = \frac{e^2}{3 \cdot \epsilon_0 \cdot (m_0 \cdot c^2)^4} \frac{E^4}{\rho} = \frac{C_\gamma}{\rho} E^4 \tag{2.29}$$

with Sand's constant $C_\gamma = \frac{4\pi}{3} \frac{r_{\mathrm{c}}}{(m_0 c^2)^3} = 8.8575 \times 10^{-5} \frac{\mathrm{m}}{\mathrm{GeV}^3}$ and the time in the bending magnets $t_{\mathrm{b}} = \frac{2\pi\rho}{c}$.
In the rest frame of the particle, the radiation has an angular distribution characteristic of a Hertzian dipole. However, in an enormously boosted laboratory frame, the radiation is emitted in a small cone tangential to the particle's orbit with the opening angle $\tan\Theta \approx \frac{1}{\gamma}$ with relativistic properties $\gamma = \frac{1}{\sqrt{1-\beta^2}}$ and $\beta = \frac{v}{c}$. For the KARA storage ring at an energy of 1.3 GeV, the angle can be determined via the approximation for small angles $\tan\Theta \approx \Theta = 0.4\,\mathrm{mrad} = 0.02\,°$.
A sharp bundling of the radiation is an appealing property to meet the requirements regarding brilliance, high flux, short pulses, and a broad power spectrum. Therefore, the time structure and the resulting power spectrum are of great interest. For example, a single electron emits a very short electromagnetic pulse of the length Δt towards a fixed observer in every turn. This results in the typical frequency of the power spectrum [20]:

$$\omega_{\mathrm{typ.}} = \frac{2\pi}{\Delta t} = \frac{3\pi \cdot c \cdot \gamma^3}{2 \cdot \rho} \quad . \tag{2.30}$$

Since the pulse length at the KARA storage ring is typically in the range of attoseconds ($\sim 1 \times 10^{-18}\,\mathrm{s}$), the spectrum extends over a large frequency range. The emitted radiation power per unit frequency is determined by [20]:

$$\frac{\mathrm{d}P}{\mathrm{d}\omega} = \frac{P_{\mathrm{s}}}{\omega_{\mathrm{c}}} \frac{9\sqrt{3}}{8\pi} \frac{\omega}{\omega_{\mathrm{c}}} \int_{\omega/\omega_{\mathrm{c}}}^{\infty} K_{5/3}(\xi)\, \mathrm{d}\xi \tag{2.31}$$

with the integrated modified Bessel function $K_{5/3}$ and the critical frequency ω_{c}

$$\omega_{\mathrm{c}} = \frac{\omega_{\mathrm{typ.}}}{\pi} = \frac{3 \cdot c \cdot \gamma^3}{2 \cdot \rho} \tag{2.32}$$

and is shown in Figure 2.5a for a single particle. The critical frequency is the frequency that splits the spectrum into two parts of identical integrated radiation power. The so-called incoherent synchrotron radiation (ISR) spectrum of a whole bunch with $N_{\mathrm{e}} \approx 10^9$ particles can be calculated from the single particle power spectrum:

$$\frac{\mathrm{d}P_{\mathrm{ISR}}}{\mathrm{d}\omega} = N_{\mathrm{e}} \frac{\mathrm{d}P}{\mathrm{d}\omega} \quad . \tag{2.33}$$

2.3.1. Coherent Synchrotron Radiation

Under special conditions, the bunches can also emit coherent synchrotron radiation (CSR) in addition to the ISR. If the coherence criterium is fulfilled, that the bunch length is in the order or even smaller than the photon wavelength ($\sigma_0 \leq \lambda$), a significant power amplification can be reached since the photons are emitted nearly in phase. For a very short bunch with the length $\sigma_0/c = 5\,\mathrm{ps}$ the coherence criteria is fullfilled for frequencies up to $f = \frac{c}{\sigma_0} = \frac{\omega}{2\pi} = 2 \times 10^{11}\,\frac{1}{\mathrm{s}} = 200\,\mathrm{GHz}$. Therefore, the spatial particle distribution

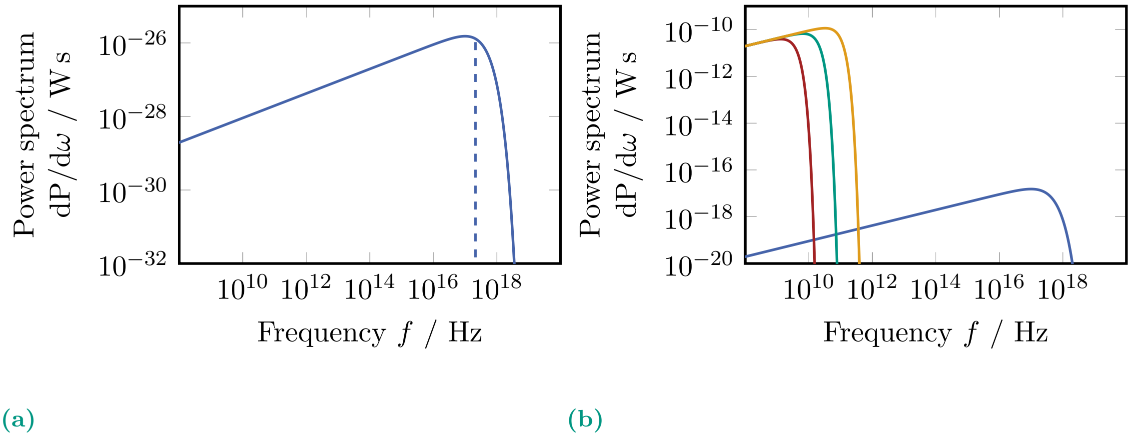

(a) **(b)**

Figure 2.5. **Coherent and incoherent synchrotron radiation spectrum.** (a) If a charged particle moves on a circular orbit, each momentum change causes power radiation with a spectrum over a broad frequency range. The critical frequency (dashed line) splits its spectrum into two parts of identical integrated emission power. (b) The incoherent synchrotron radiation (ISR) (blue) of a bunch scales linear with the number of particles $N_\mathrm{e} = 1 \times 10^9$. For wavelengths that fulfill the coherence criterium, the CSR exceeds the ISR by N_e. The frequency range of the CSR is defined by the bunch length (red: $\sigma_0/c = 50\,\mathrm{ps}$, green: $\sigma_0/c = 10\,\mathrm{ps}$, and orange: $\sigma_0/c = 2\,\mathrm{ps}$).

influences the CSR power spectrum [21]

$$\frac{\mathrm{d}P_\mathrm{CSR}}{\mathrm{d}\omega} = N_\mathrm{e}\left(N_\mathrm{e}-1\right)\mathcal{F}\left(\omega\right)\frac{\mathrm{d}P}{\mathrm{d}\omega} \tag{2.34}$$

via the form-factor $\mathcal{F}(\omega)$, which is defined as the absolute square of the Fourier transform of the particle distribution $\varrho(\vec{r})$ in the bunch, so that in case of a Gaussian bunch charge distribution, the form-factor is also a Gaussian distribution [33]

$$\mathcal{F}\left(\omega\right) = \left|\int \varrho(\vec{r})\mathrm{e}^{i\vec{k}\cdot\vec{r}}\mathrm{d}\vec{r}\right|^2 = \mathrm{e}^{-\left(\frac{\sigma_0\omega}{c}\right)^2} \quad . \tag{2.35}$$

The total power spectrum of a bunch is given as the sum of the ISR and CSR radiation:

$$\frac{\mathrm{d}P_\mathrm{tot.}}{\mathrm{d}\omega} = \frac{\mathrm{d}P_\mathrm{CSR}}{\mathrm{d}\omega} + \frac{\mathrm{d}P_\mathrm{ISR}}{\mathrm{d}\omega} = N_\mathrm{e}\left[1+\left(N_\mathrm{e}-1\right)\mathcal{F}\left(\omega\right)\right]\frac{\mathrm{d}P}{\mathrm{d}\omega} \quad . \tag{2.36}$$

Since - in contrast to the ISR - the CSR scales quadratically and not linearly with the number of emitting particles, the CSR dominates the radiation power and can lead to enhancement by several orders of magnitude, for the frequency range in which the coherence criterium is fulfilled. The CSR is negligible for higher frequencies, and only the incoherent radiation contributes to the total emitted power.

2.4. Impedances and Wake Fields

> *‘ It is like when you are upset about something and then you think about it, you become more upset. And this [is] something that you create on yourself. It is a self-induction thing. This is a bit [of] what happens. The beam creates a problem for itself- through environment’* (G. Franchetti, 2016[34])

In Section 2.2.2, the energy gain in the RF cavities has been discussed. The potential in these cavities depends nearly on the longitudinal position in the bunch and leads, in

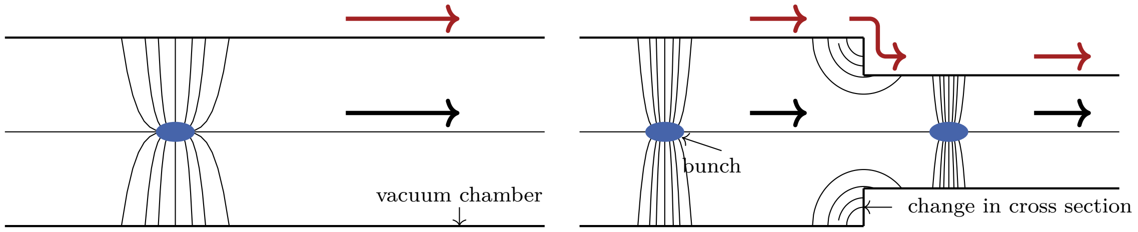

(a) **(b)**

Figure 2.6. Wakefield environment. (a) For a perfect conductive beam pipe, the mirror charges travel parallel to the beam so that no forces act back on the beam. (b) For a beam pipe with a finite resistivity or in places with a change of the cross-section, the image charges fall behind and create wakefields. These fields affect the beam dynamics of the trailing particles and bunches. (based on H. Wiedemann [21])

combination with the phase focussing to a rotation in the phase space. The early particles gain more energy and move upwards in phase space, whereas the late particles move downwards due to the smaller energy gain. However, there are other potentials in a storage ring, which are not linear and do not lead to a rotation but deformation of the particle distribution in the longitudinal phase space.

In a perfectly conducting surrounding beam pipe, the beam induces mirror charges which move parallel to the beam (Figure 2.6a) without any losses and retrospective forces on the bunch. For a resistive beam pipe or in places with a change in the cross-section of the beam pipe, the mirror charges are left behind (Figure 2.6b). In these cases, wakefields are created, which act back on the following particles. These particles mostly belong to the same bunch, so an energy redistribution results in an intra-bunch interaction. In case the field persists long enough, even an interaction with particles of the following bunches is possible.

The generated wake can be quantified by the three parameters wake-function $W(\mathrm{z})$ (caused by a single particle), wakefield $E(\mathrm{z})$ (caused by a particle bunch), and the wake-potential $V(\mathrm{z})$. All these quantities are connected by [35]

$$V(z) = \int_0^L E(z,s)\mathrm{d}s = eN_\mathrm{b}\int_{-\infty}^{\infty} W(z-z')\varrho(z')\mathrm{d}z' \tag{2.37}$$

with the particle density distribution ϱ in the bunch. To accommodate causality, the Heaviside step function [36] is used in the wake-function $W(z) \propto \Theta(z)$.

Often, the description in the frequency domain is used. Therefore, the impedance is defined as the Fourier transform of the wake function [37; 38] and is related to the wake potential by

$$Z^{\parallel}(\omega) = \int_{-\infty}^{\infty} W_\mathrm{z}(z)\mathrm{e}^{-i\omega z/v}\frac{\mathrm{d}z}{v} = \frac{\int_{-\infty}^{\infty} V_\mathrm{z}(z)\mathrm{e}^{-i\omega z/v}\frac{\mathrm{d}z}{v}}{\tilde{\varrho}(\omega)} \tag{2.38}$$

with the Fourier transform of the longitudinal bunch profile $\tilde{\varrho}(\omega)$.

Throughout this thesis, the convention for the forward Fourier transform $\tilde{f}(\omega) = \int f(x)\mathrm{e}^{-i\omega x}\mathrm{d}x$ and inverse Fourier transform $f(x) = \frac{1}{2\pi}\int \tilde{f}(\omega)\mathrm{e}^{i\omega x}\mathrm{d}\omega$ are chosen. The different signs in the exponent for the different conventions only affect the sign of the imaginary part. This defines the direction of causality, where either a negative or positive value of z stands for the particles ahead of the synchronous particle. In the convention used in this thesis, a negative value of z means a position in front of the synchronous particle. Consequently, the impedance fulfills the characteristics [39] $Z^*(f) = Z(-f)$ and $\Re\left(Z\left(0\right)\right) = 0$. Based on the relation between the bunch shape and the impedance in Equation (2.38), Y. D. Yoon *et al.* [40]

showed the method to create arbitrary bunch shapes by tailoring the wake potential, in a steady-state distribution and under the assumption of zero energy loss.
Following from Equation (2.38), the frequency dependency of the impedance and the bunch length define the range of the wake. A narrow-band impedance creates a remain for a long time and causes bunch-by-bunch and even turn-by-turn interactions. In contrast, wakefields, caused by wide-range impedances, decay quickly. These fields give rise to interactions between particles within the same bunch.
The impact on the dynamics of the particle beam is evident when looking at the energy losses due to the interaction with the surroundings via the wakefield. It can be calculated by substituting Equation (2.37) into Equation (2.3):

$$\Delta E(z) = \varrho \cdot V = e^2 N_\mathrm{b} \int_{-\infty}^{\infty} W(z-z')\varrho(z')\mathrm{d}z' \tag{2.39}$$

$$= \frac{e^2 N_\mathrm{b}}{2\pi} \int_{-\infty}^{\infty} Z^{\|}(\omega)\tilde{\varrho}(\omega)\mathrm{e}^{-i\omega z/v}\mathrm{d}\omega \tag{2.40}$$

and can be averaged over a whole turn to

$$\overline{\Delta E} = e^2 N_\mathrm{b} \int_{-\infty}^{\infty} Z^{\|}(\omega)\left|\tilde{\varrho}(\omega)\right|^2 \mathrm{d}\omega \quad . \tag{2.41}$$

It can be seen that the energy losses only depend on the impedance in the frequency range of the bunch spectrum [28], which shows an important advantage of the consideration in the frequency domain. Furthermore, it can be shown that the imaginary part of the impedance either has an inductive effect ($\Im(Z^{\|}) > 0$) and lengthens the bunch or has a capacitive effect ($\Im(Z^{\|}) <0$) and reduces the bunch length. In contrast, the real part of the impedance defines the energy loss and asymmetric deformations of the bunch.
The loss is characterized by the so-called loss factor k_l, which is defined by $\overline{\Delta E} = -k_\mathrm{l} q_\mathrm{bunch}^2$ and is related to the longitudinal impedance of the accelerator by [28]

$$k_\mathrm{l} = -\frac{1}{N_\mathrm{b}} \int_{-\infty}^{\infty} Z^{\|}(\omega)\left|\varrho(\omega)\right|^2 \mathrm{d}\omega \quad . \tag{2.42}$$

Under the assumption of Gaussian particle distribution, the loss factor can be written as [21]

$$k_\mathrm{l} = \frac{1}{\sqrt{2\pi}\sigma_0} \int_{-\infty}^{\infty} V \cdot \mathrm{e}^{\left(-\frac{s^2}{\sigma_0^2}\right)} \mathrm{d}s \quad . \tag{2.43}$$

The relation between the wake loss factor and the total deposited power loss is given by [41]

$$P_\mathrm{b} = I^2 \cdot T_0 \cdot N_\mathrm{bunch} \cdot k_\mathrm{l} \tag{2.44}$$

with the revolution time T_0 and the number of bunches N_bunch.

2.4.1. Resistive Wall

As mentioned earlier in this section, the shape of the surrounding beam pipe and its changes in cross-section can be described by its impedance. In general, the beam pipe of a storage ring is not built from a perfect conductor but from a metal with finite conductivity and, therefore, resistivity. Consequently, the particles lose energy due to the interaction of the fields with the surface of the beam pipe. This effect can be described by the so-called resistive wall impedance, which is given for a cylindric beam pipe with the radius b by K. Y. Ng [37] for the whole ring by

$$Z_\mathrm{RW}^{\|}(f) = [1 - i\mathrm{sgn}(f)] \sqrt{\frac{Z_\mathrm{vac}\mu_\mathrm{r}}{\pi c \sigma_\mathrm{c}}} \frac{C}{2b} \sqrt{|f|} \tag{2.45}$$

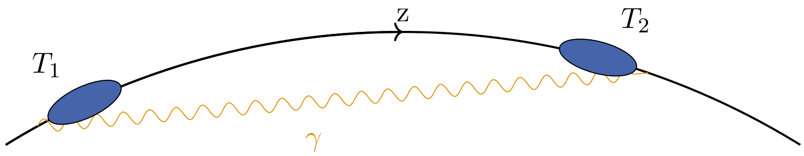

Figure 2.7. Synchrotron radiation impedance. A photon emitted by the particle at the end of the bunch can catch up with the head of the bunch since it takes a non-curved path through the bending section. Therefore, the bunch interacts with its self-emitted synchrotron radiation.

with the conductivity of the beam pipe material σ_{c}, its relative permeability μ_{r}, the circumference C of the accelerator, and the vacuum impedance Z_{vac}=$120\pi\,\Omega$.

2.4.2. Collimator

The second geometric impedance which will be described here is referred to as collimator impedance. A collimator is a device installed to reduce the aperture of the beam. The collimator impedance is composed of the impedance of discontinuous changes in the cross-section from radius b to a (with $b > a$) and back again. In the high frequency limit case $\gamma > kb \gg 1$ with wave number $k = \frac{\omega}{c}$, it is defined as [42; 37]:

$$Z^{\|}_{\mathrm{Coll.}}(f) = \frac{Z_{\mathrm{vac}}}{\pi} \ln\frac{b}{a} \quad . \tag{2.46}$$

It has to be taken into account that the imaginary part vanishes ($\Im(Z) = 0$) only for an infinitesimally short collimator, where the two steps in the beam pipe cannot be considered individually. Otherwise, the imaginary part is not negligible.
Mostly, the purpose of elements such as collimators is not to create an additional impedance. Tapers can be used to reduce the impact on the impedance by eliminating the discontinuities of the beam pipe cross-section.
K. Y. Ng and K. Bane present a long list of several geometric impedances in [43].

2.4.3. CSR Impedance

A different impedance type is based on the interaction of a particle bunch with its self-emitted CSR. As described in Section 2.3, the synchrotron radiation is emitted in a narrow cone tangentially to the bunch orbit in the bending sections. The radiation takes the non-curved path through this section and thus interacts with the radiating bunch again. In contrast to the geometric impedances, in which, due to causality, energy can only be transferred to the following particles, the CSR impedance can also transfer energy to particles further ahead in the particle bunch, which is illustrated in Figure 2.7.
Although many different models describe this self-interaction, the CSR impedance can be characterized by only considering a single bunch traveling on its circular path in the free space of a vacuum without the surrounding conductive beam pipe. This simple model by J. B. Murphy *et al.* [44] results, for an iso-magnetic ring with the length $2\pi \cdot \rho$, in the

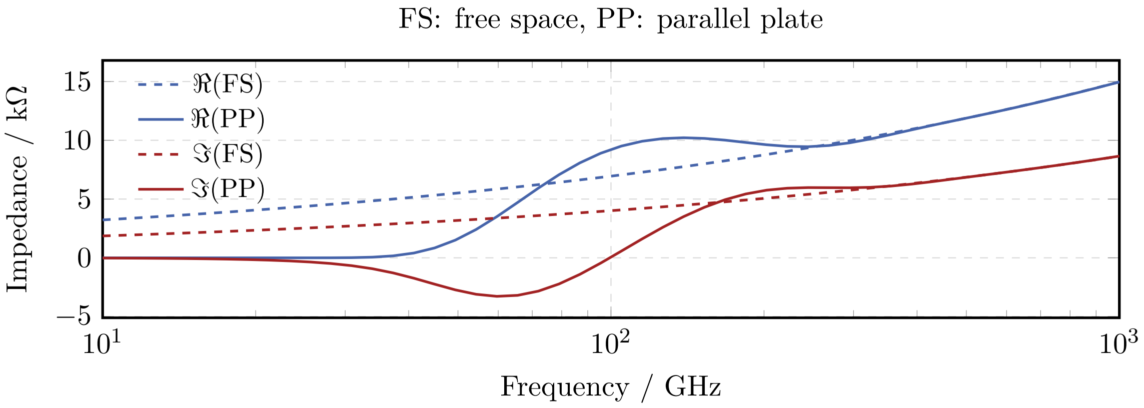

Figure 2.8. CSR impedance. The real and imaginary part of the CSR impedance is shown. The parallel plate impedance (solid line) has been calculated for the KARA beam pipe parameters. The parallel plate model converges to the free space (dashed line) approximation for high frequencies.

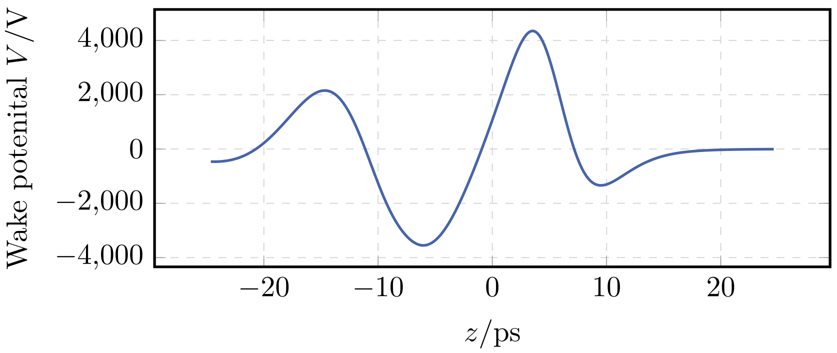

Figure 2.9. Wake potential. The longitudinal wake potential is simulated with Inovesa with a Gaussian bunch profile and the KARA parallel plate CSR impedance. In the convention used in this thesis, a negative value of z means a position in front of the synchronous particle.

impedance

$$Z^{\parallel}_{\mathrm{FS}}(f) = Z_{\mathrm{vac}} \frac{\Gamma\left(2/3\right)}{3^{1/3}} \left(\frac{\sqrt{3}}{2} + \frac{i}{2}\right) n^{1/3} \tag{2.47}$$

with $n = f/f_{\mathrm{rev}}$.
For a more accurate description, the model is extended with two infinite, perfectly conducting plates, between which the charged particles circulate on their circular path. The impedance of the parallel plate model is given by [45; 46]:

$$Z^{\parallel}_{\mathrm{PP}}(f) = Z_{\mathrm{vac}} \frac{4\pi^2 2^{1/3}}{c^2} \left(\frac{\rho}{h_{\mathrm{c}}}\right) n^{-1/3} \times \sum_p \left(\mathrm{Ai}'(u_{\mathrm{p}})\mathrm{Ci}'(u_{\mathrm{p}}) + u_{\mathrm{p}}\mathrm{Ai}(u_{\mathrm{p}})\mathrm{Ci}(u_{\mathrm{p}})\right) \quad , \tag{2.48}$$

in which the primes mark the deviation and with the Airy functions of the first kind (Ai), second kind Bi, Ci=Ai-iBi, and $u_{\mathrm{p}} = \frac{\pi^2(2p+1)^2}{2^{2/3}} \left(\frac{\rho}{h_{\mathrm{c}}}\right)^2 n^{-4/3}$. The distance between the plates corresponds to the height of the beam pipe h_{c}. In the limit $h_{\mathrm{c}} \rightarrow \infty$, this impedance converges to the free space CSR impedance. Both are shown in Figure 2.8 for KARA

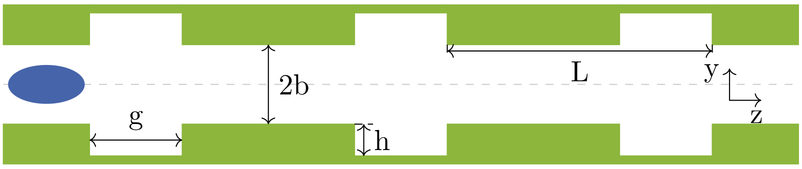

Figure 2.10. Corrugated plates. The cross-section of the corrugated plates with the relevant geometric parameters is shown. The electron bunch is indicated in blue and travels along the dashed line through the structure.

dimensions ρ=5.559 m and h_c=32 mm.
It has already been proven that the beam dynamics and threshold of the micro-bunching instability (explained in detail in Section 2.7) agree with measurements within uncertainties. The KARA impedance is described by its CSR parallel plate impedance by M. Brosi *et al.* [47]. Exemplarily, the wake potential based on the CSR interaction is shown in Figure 2.9 for a perfectly Gaussian bunch.

2.4.4. Corrugated Pipe

In a synchrotron, all the previously mentioned impedances are unavoidable due to CSR emission and changes in the beam pipe cross-section because of, e.g., diagnostics or vacuum pumps. However, the impedance can also be specifically tailored on purpose to manipulate, understand, and control the beam dynamics. This can be accomplished, e.g., by using a beam pipe with periodic and rectangular corrugations of depth h, longitudinal gap g, and periodic length L, which is shown schematically in Figure 2.10. Under the consideration of a cylindric, metallic beam pipe with the radius b and small corrugations ($L \lesssim h \ll b$), the interaction with the beam pipe behaves in the same way as for a beam pipe with a thin dielectric layer [48]. In both cases, the wakefield and the impedance can be described by a loss-free resonator and can be written as [49; 43]:

$$E^{\parallel}(z) \approx \frac{Z_{\text{vac}} c}{\pi b^2} \cos\left(k_{\text{res}} z\right) \tag{2.49}$$

$$\frac{Z^{\parallel}}{L} = \frac{Z_{\text{vac}}}{\pi b^2} \left[\pi k_{\text{res}} \delta\left(k^2 - k_{\text{res}}^2\right) + i \cdot \text{P.V.}\left(\frac{k}{k^2 - k_{\text{res}}^2}\right)\right] \tag{2.50}$$

with the resonance wave number $k_{\text{res}} = \frac{2\pi f_{\text{res}}}{c} = \sqrt{\frac{2L}{bgh}}$, Z_{vac}= $120\pi\,\Omega$, the δ-distribution, and the principal value P.V.(x) [50].
The above-described model represents wake for the asymptotic steady-state case with a large number N_{corr} of corrugations. S. A. Heifets and S. A. Kheifets [51] and R. L. Gluckstern [52] have already studied the transition from a single-cavity to a periodic structure and have found a condition for the steady-state depending on the frequencies:

$$N_{\text{corr}} > \pi \frac{2\pi f b^2}{L} \quad . \tag{2.51}$$

Furthermore, the length of the particle bunch affects the transient behavior and therefore influences the critical length $z_{\text{crit}} = N_{\text{corr,crit}} \cdot L$ above which the steady-state wake is reached. Simulations by K. L. F. Bane and A. Novokhatski [49] have shown good agreement with an equation derived from acceleration cavities [53]:

$$z_{\text{crit}} = \frac{b^2}{2 \cdot \sigma_0} \quad . \tag{2.52}$$

From the δ-distribution in Equation (2.50), it follows that the impedance of a corrugated beam pipe is only significant in an infinitesimally narrow frequency range around the

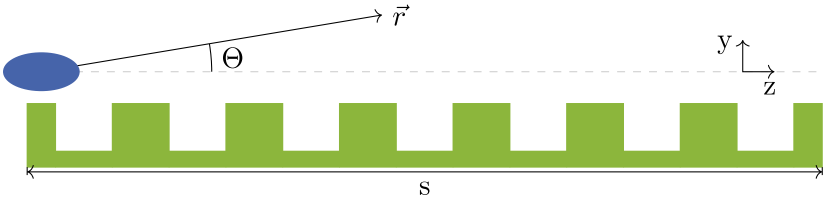

Figure 2.11. Smith-Purcell radiation. (Based on [54])

resonance frequency. Therefore, the wake should remain indefinitely, affecting the trailing bunches and turns. However, the impedance peak of an actual corrugated structure has a finite width and quality factor $Q = \frac{f_{\mathrm{res}}}{\Delta f_{\mathrm{FWHM}}}$ (discussed in detail in Chapter 6). For a suitable quality factor Q=3, the wakefield vanishes after a few single-digit pico-seconds (ps). This means that such a structure creates wake fields that can affect inner-bunch interactions and the beam dynamics of the bunches but vanishes within the KARA bunch spacing of 2 ns.

2.5. Smith-Purcell Radiation

The impedance and local wakefield of a grating, like the corrugated plate, produces diffraction radiation when the particles passes the structure at a small distance [54], which has been first discussed in 1942 by I. M. Frank [55]. Since this radiation has been firstly experimentally detected by S. J. Smith and E. M. Purcell [18] in 1953, it is called Smith-Purcell radiation (SPR). In Figure 2.11, a schematic sketch of SPR is shown. Thereby, the vector $\vec{r}$ points towards an observer under the angle Θ. For a fixed Θ, the spectrum of the SPR is narrow-banded and defined by dispersion relation of the radiation [56]

$$n\lambda = L\left(\frac{1}{\beta} - \cos\Theta\right) \quad , \tag{2.53}$$

with the relativistic β, and the periodic length L of the grating. However, the wavelength and frequency depends strongly on the emission angle, so that a moving observer detects a broad spectrum of the SPR.

The structure of this radiation pulse is defined by the impedance, and therefore the dimensions of the corrugations. The following description is based on [16] by K. L. F. Bane *et al.* , who installed such a structure in a linear accelerator at Brookhaven's Accelerator Test Facility. The wakefield of the structure causes a radiation pulse of the charactersitic frequency $f_{\mathrm{c,SPR}}$=f_{res}, that travels behind the electron beam through the structure with its group velocity $v_{\mathrm{g}} = \left(1 - \frac{2h}{b}\right) \cdot c$. Since, SPR is emitted along the whole structure of the length s, the leaving pulse has the length $l = \frac{2h}{b}s$. This emitted pulse consists of $n_\lambda = \frac{l}{c} f_{\mathrm{c,SPR}} = \frac{2h \cdot s}{b} \frac{f_{\mathrm{c,SPR}}}{c}$. The spectrum of the radiation pulse, is defined as the Fourier transform of the pulse field and is defined as [16]

$$\left|\tilde{E}(f)\right| = \frac{E_0}{\pi} \frac{f}{f^2 - f_{\mathrm{c,SPR}}^2} \begin{cases} \sin\left(n_\lambda \pi \frac{f}{f_{\mathrm{c,SPR}}}\right), & n_\lambda\text{: integer} \\ \cos\left(n_\lambda \pi \frac{f}{f_{\mathrm{c,SPR}}}\right), & n_\lambda\text{: half integer} \end{cases} \quad , \tag{2.54}$$

with the peak field E_0. Thereby, the width of the main peak only depends on $f_{\mathrm{c,SPR}}$ and the number of oscillations in the pulse. For $n_\lambda \gtrsim 3$, K. L. F. Bane *et al.* [16] found the empirical relation between n_λ and the quality factor of the spectrum of the radiation pulse:

$$Q_{\mathrm{THz}} \approx n_\lambda / 1.2 \quad . \tag{2.55}$$

With the definition of n_λ, in conjunction with $f_{\mathrm{c,SPR}} = f_{\mathrm{res}} \propto \sqrt{\frac{L}{bgh}}$, the dependency of the quality factor on the corrugation parameters can be inferred by:

$$Q_{\mathrm{THz}} \propto s\,(L/g)^{0.5}\, h^{0.5} b^{-1.5} \quad . \tag{2.56}$$

Even so the SPR is produced for the corrugated structure, that will be installed in the KARA storage ring, and therefore manipulates the beam dynamics via the impedance, it is not planned to measure the emitted SPR.

2.6. Vlasov-Fokker-Planck Equation

In Section 2.2.2, it has been shown that a harmonic oscillator can describe the longitudinal movement of the bunch around the synchronous particle. The Hamiltonian [57] for such movement is given by

$$\mathcal{H} = \frac{1}{2}\left(q^2 + p^2\right) \tag{2.57}$$

with dimensionless canonical coordinate q and momentum p, which are determined by [35]

$$q \equiv \frac{z}{\sigma_0} \quad , \quad p \equiv \frac{E - E_0}{\sigma_{\mathrm{E}}} \quad . \tag{2.58}$$

In this definition, the RMS bunch length σ_0 and energy spread σ_{E} in the low-current equilibrium state without a wakefield as well as the central energy E_0 are used.
Also, a dimensionless time parameter is defined as a fraction of the synchronous period:

$$\theta = \frac{t}{T_{\mathrm{s}}} \quad . \tag{2.59}$$

Based on the Liouville theorem, the area in phase space is constant under conservative forces. The charge density $\Psi(z, E, t)$ can then be described by a differential equation developed by A. A. Vlasov [58] and is therefore referred to as the Vlasov equation (cited from [37])

$$\frac{d\Psi}{\mathrm{d}\theta} = \frac{\partial\Psi}{\partial\theta} + \frac{\partial\mathcal{H}}{\partial p}\frac{\partial\Psi}{\partial q} - \frac{\partial\mathcal{H}}{\partial q}\frac{\partial\Psi}{\partial p} = 0 \quad . \tag{2.60}$$

Due to the emission of synchrotron radiation, the longitudinal phase-space is a non-conservative system, so the Vlasov equation has to be extended. Under the assumption of a small energy spread ($\sigma_{\mathrm{E}} \ll E$), an energy-independent radiation power $P_{\mathrm{s}}(\mathrm{E}) \approx$ *const.* can be accepted. The evolution of the charge density in the phase space is described by the Vlasov-Fokker-Planck equation (VFPE) [37]

$$\frac{d\Psi}{\mathrm{d}\theta} = \frac{\partial\Psi}{\partial\theta} + \frac{\partial\mathcal{H}}{\partial p}\frac{\partial\Psi}{\partial q} - \frac{\partial\mathcal{H}}{\partial q}\frac{\partial\Psi}{\partial p} = \beta_{\mathrm{d}}\frac{\partial}{\partial p}\left(p\Psi + \frac{\partial\Psi}{\partial p}\right) \tag{2.61}$$

with the dimensionless damping time parameter $\beta_{\mathrm{d}} = \frac{1}{f_{\mathrm{s}}\tau_{\mathrm{D}}}$. This perturbation leads to an additional term in the Hamiltonian, which describes the collective effects and can be expressed by the wake potential or the impedance [59]:

$$\mathcal{H} = \frac{1}{2}\left(q^2 + p^2\right) + \frac{e f_{\mathrm{rev}}}{\sigma_{\mathrm{E}} f_{\mathrm{s}}} \int_q^\infty V_{\mathrm{c}}(q', t)\mathrm{d}q' \tag{2.62}$$

$$= \frac{1}{2}\left(q^2 + p^2\right) + \frac{e f_{\mathrm{rev}}}{\sigma_{\mathrm{E}} f_{\mathrm{s}}} \int_q^\infty \int_{-\infty}^\infty \tilde{\varrho}(f) Z^{\|}(f) \mathrm{e}^{i2\pi f q'} \mathrm{d}f \mathrm{d}q' \quad . \tag{2.63}$$

In Equation (2.62), the perturbation term is given by the energy changes of one revolution due to the collective potential V_{c} and is adjusted by the dimensionless parameters.
From Equation (2.63), it can be seen clearly that the Hamiltonian is affected by the

impedance of the accelerator as well as by the charge distribution, which itself is influenced by the impedance. This shows that the impedance can be used to impact the longitudinal beam dynamics.
In the equilibrium state, Equation (2.61) can be solved by a Gaussian energy distribution [37]

$$\Psi(q,p) = \frac{1}{\sqrt{2\pi}\sigma_{\mathrm{E}}} \mathrm{e}^{-\frac{p^2}{2\sigma_{\mathrm{E}}^2}} \varrho(q). \tag{2.64}$$

J. Haïssinski [60] developed an equation that describes the particle density distribution and is given by [37]

$$\varrho(q) = \varrho_0 \exp\left(-\frac{q^2}{2} + Q\int_0^q \int_{q''}^{\infty} \varrho(q')W(q'-q'')\mathrm{d}q'\mathrm{d}q''\right) \tag{2.65}$$

with the starting distribution ϱ_0, which ensures the distribution being normalized, the bunch charge Q, and the wake function W. This equation describes the acting of the impedance or wakefield as long as an unambiguously and temoral constant solution can be found. This is only the case for beam currents strictly below any instability thresholds.

2.7. Micro-Bunching Instability

As mentioned previously, the interaction between the particles in a bunch with its surroundings - described by the impedance - can lead to nonlinear phenomena resulting in dynamic instabilities and bunch deformations, where the bunch shape changes continuously over time. In this thesis, the investigated instability is the micro-bunching instability, which affects the longitudinal beam dynamics. It is caused by the interaction with the self-emitted CSR, which acts back as a time-dependent wake potential (described in detail in Section 2.4.3) and thereby influences the longitudinal bunch profile. The simple parallel plate model of the CSR impedance has proven to describe this interaction in good agreement with experimental results for the KARA storage ring by M. Brosi *et al.* [47].
As pointed out in Section 2.3.1 already, CSR is only emitted for wavelengths longer than the emitting structure. Consequently, the micro-bunching can only arise if the bunch is so short that its spectrum $\tilde{\varrho}(\omega)$ has a significant overlap with the CSR impedance in the frequency domain.
An empirical working model of the micro-bunching instability (based on [61]) can describe the creation of substructures on the longitudinal charge distribution. At the start, the overlap of the bunch spectrum and the impedance generates an additional wake potential, which causes an energy loss or gain depending on the longitudinal position in the bunch. This change in the energy distribution results in combination with the synchrotron oscillation, in a longitudinal bunch profile deformation [62]. For low currents below the instability threshold, this deformation leads to an asymetric bunch profile which can be described by the Haïssinski solution [60].
The bunch deformation reinforces higher frequency components in $\tilde{\varrho}(\omega)$ and thus leads to a larger overlap with the impedance. This, in turn, causes an even higher wake potential acting back on the bunch. Since the wake potential depends on the charge distribution, the self-interaction increases directly with the number of particles and, therefore, the bunch current I_{b}. Following that, a threshold current I_{thr} is given, above which the micro-bunching instability arises. Above this threshold, the interplay between wake potential and charge distribution causes finger-like substructures of the charge distribution in the longitudinal phase space. Hence, the instability affects not only the charge but also the energy distribution. Due to the rotation of the phase space with its finger-like substructures, the projection on the time axis, which shows the longitudinal bunch profile and the related emitted CSR power, is not constant anymore but changes continiously over time. In this

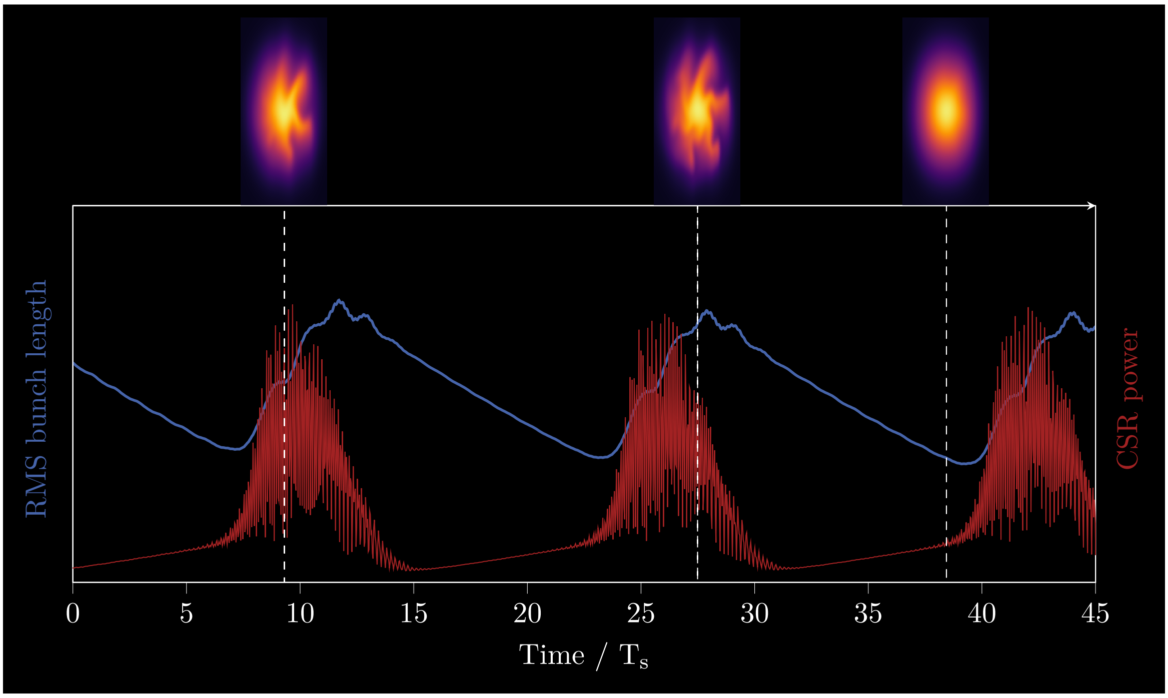

Figure 2.12. **Temporal outbursts of CSR power.** Simulated example of the temporal outburst of CSR power (red) and the corresponding periodic change of the bunch length (blue). The three longitudinal phase spaces show the creation and vanishing of the substructures. The chosen points in time of the phase spaces are from left to right: most intense CSR power, longest bunch, and shortest bunch.

regime, the self-interaction leads to a change in the bunch profile, which in turn leads to a change of the wake potential, which drives changing the bunch profile again. This closed-loop results in a continuous presence of the substructures of the charge distribution in the longitudinal phase space and consequently an enhanced emission of CSR due to these smaller emitting structures.

However, at even higher bunch currents, an additional slower effect occurs. In this regime, the stronger interaction between the CSR emission and the electron bunch leads to some self-amplification of the substructures. Over many turns, the charge in the substructures increases. The wake potential does not lead to any further enhancement at a certain point. Therefore, the fingers in the phase space are washed out, and the bunch is enlarged.

Consequently, the high-frequency components of the bunch spectrum and, thus, the wake potential are reduced. So, the radiation damping dominates the remaining, driving wake potential, and the bunch length shrinks. As soon as the bunch is short enough that the wake potential becomes dominant again and the substructures are formed, the cycle starts again. The whole cycle of creating and washing out of the substructures takes place over the range of several synchrotron periods T_s and is shown in Figure 2.12. The behavior of the cycle can be seen in the emitted CSR power and the bunch length as the characteristic sawtooth pattern, which is also called "*bursts*". Due to the pattern, this instability is also referred to as "*sawtooth instability*" in the literature (e.g., [63]).

Early studies of the micro-bunching instability have been done at the SURF II electron storage ring at the National Institute of Standards and Technology (NIST) [64]. Although the dynamics of the phase space with the micro-bunching instability is complex, it is completely reproducible, which allows systematic studies of the beam dynamics under different machine or impedance settings.

The micro-bunching instability does not cause beam losses, but the fluctuation in the longitudinal charge distribution might affect the performance and the radiation quality of a synchrotron. Thus, on the one hand, the necessary beam stability can only be reached below a certain threshold. On the other hand, the additionally provided intense coherent radiation - e.g., in the THz range - can be useful for dedicated experiments that could not be performed previously. So, the knowledge of the threshold current is crucial for both applications. The threshold current can be determined using a Vlasov-Fokker-Planck solver (VFPS) with the dominant and accurate parallel plate CSR impedance from the simulated longitudinal beam dynamics. Thereby, K. L. Bane, Y. Chai, and G. Stupakov, whose VFPS is based on an algorithm devised by R. L. Warnock and J. A. Ellison [35], have formulated a semi-empiric formula for determing the threshold current I_{thr} of the micro-bunching instability [65] under the assumption of a bunched beam. This formula describes the threshold above which the micro-bunching instability occurs as a function of the shielding parameter Π

$$\Pi = \frac{\rho^{1/2}}{\left(\frac{h_{\mathrm{c}}}{2}\right)^{3/2}}\sigma_0 \quad , \tag{2.66}$$

where ρ is the bending radius, h_{c} is the spacing between the parallel plates, and σ_0 is the natural zero-current bunch length.

For this, a linear scaling law [65] can be applied

$$S_{\mathrm{csr}} = a_{\mathrm{th}} + b_{\mathrm{th}}\Pi \tag{2.67}$$

with the empirical fit parameters $a_{\mathrm{th}} = 0.5$ and $b_{\mathrm{th}} = 0.12$.

The CSR parameter S_{csr} is defined as:

$$S_{\mathrm{csr}} = \frac{\rho^{1/3}}{\sigma_0^{4/3}} I_{\mathrm{n}} \tag{2.68}$$

with the normalized current

$$I_{\mathrm{n}} = \frac{\sigma_0}{\gamma \alpha_{\mathrm{c}} \sigma_{\mathrm{E}}^2 I_{\mathrm{A}}} I_{\mathrm{b}}. \tag{2.69}$$

In this I_{b} is the bunch current, γ is the Lorentz factor, σ_{E} is the nominal energy spread, α_{c} is the momentum compaction factor, and $I_{\mathrm{A}}=4\pi\epsilon_0 m_0 c^3/e = 17\,045\,\mathrm{A}$ is the Alfvén current. In Figure 2.13, this scaling law is shown, showing that the linear scaling fits best for $\Pi > 3$. With less shielding, the fit underestimates the simulated threshold of the instability [65]. Experiments and further simulations by P. Kuske at BESSY II and MLS [66], and M. Brosi *et al.* at KARA [47] have shown a good agreement with the equation and lead to a further validation of the model.

Not all bunch parameters can be measured directly in experiments at KARA. Therefore, it is useful to rewrite the formula for the threshold current so that it only depends on measurable machine and bunch settings [61]:

$$I_{\mathrm{thr}} = \frac{2\pi\gamma I_{\mathrm{A}} \left(c\sigma_{\mathrm{E}}^7 E^4 f_{\mathrm{s}}^7 h^4\right)^{1/3}}{\rho^{1/3}\left(f_{\mathrm{RF}}^2\sqrt{e^2U_{\mathrm{acc}}^2 - W_0^2}\right)^{4/3}} \left(a_{\mathrm{th}} + b_{\mathrm{th}} \frac{\sqrt{8}c\sigma_{\mathrm{E}} E f_{\mathrm{s}} h \rho^{1/2}}{h_{\mathrm{c}}^{3/2} f_{\mathrm{RF}}^2 \sqrt{e^2U_{\mathrm{acc}}^2 - W_0^2}}\right) \quad . \tag{2.70}$$

2.8. Propagating Electromagnetic Fields

The propagation of electric and magnetic fields depends on the boundaries conditions, for example due to the geometry of the components. In accelerators this propagation fields are mainly relevant for the acceleration to energies in the MeV range in RF cavities. However, the determination of the properties of the propagating electromagnetic waves, provide conclusions on the geometry of the component. Therefore this fields can be used

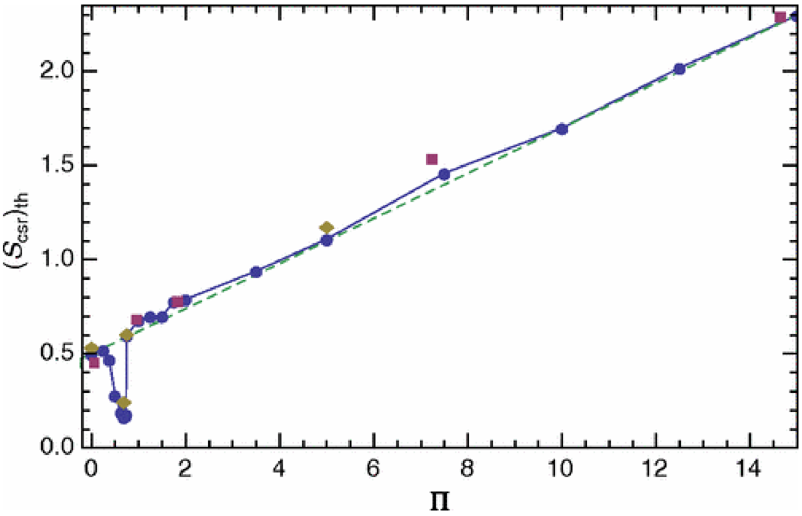

Figure 2.13. Micro-bunching instability threshold. "For the CSR wake, threshold value of S_{csr} vs shielding parameter, $\Pi = \rho^{1/2}\sigma_0/h^{3/2}$. Symbols give results of the VFP solver (blue circles), the [linearized Vlasov] LV code (red squares)), and the VFP solver with twice stronger radiation damping (olive diamonds). "([65], Figure 3)

to characterize e.g. prototypes of the corrugated plates for the impedance manipulation.

2.8.1. Electromagnetic Waves

The discussions in this section are based on A. Wolski [28] but the underlying electromagentism is well covered in general standard text books like Jackson [29].
For the determination of the wave equation for the electromagnetic fields, the differential Maxwell's equations [67]:

$$\nabla \cdot \vec{D} = \rho \quad , \tag{2.71}$$

$$\nabla \cdot \vec{B} = 0 \quad , \tag{2.72}$$

$$\nabla \times \vec{H} = \vec{J} - \frac{\partial \vec{D}}{\partial t} \quad , \tag{2.73}$$

$$\nabla \times \vec{E}_{\mathrm{el}} = -\frac{\partial \vec{B}}{\partial t} \tag{2.74}$$

are necessary. In these, the electric displacement $\vec{D} = \epsilon \vec{E}$, the magnetic intensity $\vec{H} = \frac{1}{\mu}\vec{B}$, the charge density ρ, and the electric current density $\vec{J}$ occur. In free space ρ and $\vec{J}$ are zero.
Starting from Equation (2.74), taking the curl ($\nabla\times$) on both sides of the equation, inserting the other Maxwell's equations, leads to the wave equation. The electric field needs to satisfy:

$$\nabla^2 \vec{E}_{\mathrm{el}} - \frac{1}{c^2}\frac{\partial^2 \vec{E}_{\mathrm{el}}}{\partial t^2} = 0 \tag{2.75}$$

to propagate in free space. Analog, but starting from Equation (2.73), the wave equation of the magnetic field can be found as:

$$\nabla^2 \vec{B} - \frac{1}{c^2}\frac{\partial^2 \vec{B}}{\partial t^2} = 0 \tag{2.76}$$

Following, for both electric and magnetic field plane waves can propagate in the free space without any requirements for the frequency or wave vector, which are related by the

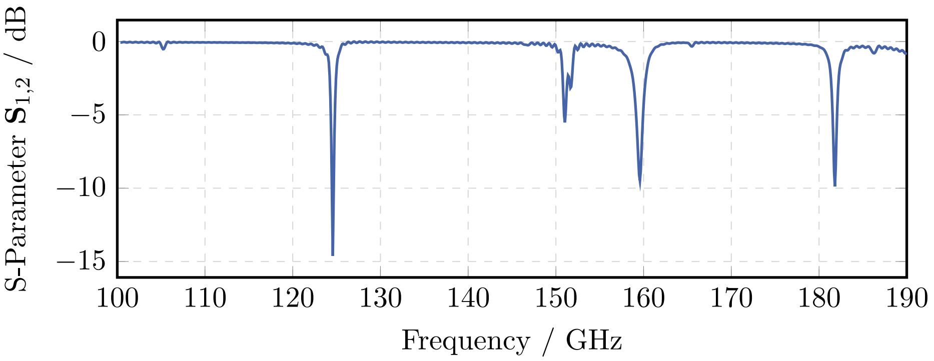

Figure 2.14. **S-parameter $\mathbf{S}_{1,2}$.** Simulated exemplary scattering matrix parameter $\mathbf{S}_{1,2}$ of a pair of corrugated plates.

dispersion relation $\frac{\omega}{|\vec{k}|} = c$. The plane electromagnetic waves are transverse waves, whose electric and magnetic fields are perpendicular to each other and the propagation direction of the wave vector $\vec{k}$.

However, these plane waves propagating in free space do not satisfy the boundary conditions within the interior of the walls of the RF cavities. In case of a perfectly conductive surface, the fields has to satisfy the boundary conditions that the tangential part of the electric field and the normal part of the magnetic field vanish at the surface.

The geometries of RF components are mostly optimized to maximize their performance and therefore cannot be described by simple geometric objects. However, the planned impedance manipulation structures for the KARA storage ring (corrugated plates) are relatively simple from the geometric point of view. Therefore, the solutions for the propagating waves in a rectangluar volume should be given. A detailed derivation is given in textbooks like A. Wolski's [28].

In each direction the tangential part of the electric field must vanish hat the walls. Therefore, only standing waves can propagate for which a integer number of periods fit between the walls. So, the boundary conditions requires:

$$k_i = \frac{m_i \pi}{a_i} \tag{2.77}$$

with the side length a_i and the integer "*mode number*" m_i. Since, the dispersion relation of the wave equation must also be fulfilled, this gives an equation for the frequencies of the wave, which can propagate in the rectangular volume:

$$\omega = \pi c \sqrt{\left(\frac{m_x}{a_x}\right)^2 + \left(\frac{m_y}{a_y}\right)^2 + \left(\frac{m_z}{a_z}\right)^2} \tag{2.78}$$

2.8.2. Eigenmodes & Scattering Matrix

As mentioned, the electromagnetic fields can be used to characterize a component or device. To fully determine the propagating electric and magnetic fields in a circuit or device, it is necessary to solve Maxwell's equation (Equations (2.71) to (2.74)). However, this might not be necessary since the solution of Maxwell's equation gives the field distribution at all points in space and time. Often, only some properties, like the current or voltage, are of interest at certain planes or positions (so-called ports). For such requirements, applying a circuit analysis to a network problem is more manageable than solving Mawell's equation. A detailed description of the network analysis can be found in textbooks like [68].

In general, it cannot be considered that the characteristic impedance is the same for all ports. This requires a more generalized wave than a pure voltage wave. For this purpose, the power wave is characterized by the amplitude $\frac{U+ZI}{2\sqrt{|\Re(Z)|}}$ The amplitude of the incident (a_i) and reflected (b_i) power waves for the i-th port of a junction are thus defined by [69]:

$$a_\mathrm{i} = \frac{U_\mathrm{i} + Z_\mathrm{i} I_\mathrm{i}}{2\sqrt{|\Re\left(Z_\mathrm{i}\right)|}} \tag{2.79}$$

$$b_\mathrm{i} = \frac{U_\mathrm{i} - Z_\mathrm{i}^* I_\mathrm{i}}{2\sqrt{|\Re\left(Z_\mathrm{i}\right)|}} \tag{2.80}$$

with the respective current I_i, voltage U_i, and impedance Z_i.

The relation between the incident and reflected wave signal at all ports of a device under test (DUT) can be described by the scattering matrix $\mathbf{S}$, so the network is completely characterized. For a n-port DUT, the scattering matrix is a $n \times n$ matrix:

$$\vec{b} = \mathbf{S} \cdot \vec{a} \tag{2.81}$$

$$\begin{pmatrix} b_1 \\ \vdots \\ b_\mathrm{n} \end{pmatrix} = \begin{pmatrix} \mathbf{S}_{1,1} & \cdots & \mathbf{S}_{1,n} \\ \vdots & \ddots & \vdots \\ \mathbf{S}_{n,1} & \cdots & \mathbf{S}_{n,n} \end{pmatrix} \begin{pmatrix} a_1 \\ \vdots \\ a_\mathrm{n} \end{pmatrix} \quad . \tag{2.82}$$

The entries of the scattering matrix, called S-parameters, can be determined by sending an incident wave in the j-th port of the DUT, while the amplitudes of the incident wave in all other ports are zero ($a_{\mathrm{i}\neq\mathrm{j}} = 0\,\mathrm{V}/\sqrt{\Omega}$). To avoid reflections, these are also terminated in matched loads. The S-parameter $S_\mathrm{i,j}$ can then be measured and calculated by [68]

$$\mathbf{S}_{i,j} = \left.\frac{b_\mathrm{i}}{a_\mathrm{j}}\right|_{a_\mathrm{k}=0\,\mathrm{V}/\sqrt{\Omega}\text{ for }k\neq j} \quad . \tag{2.83}$$

Like a waveguide or cable, a pair of parallel corrugated plates has two ports, resulting in a 2 × 2 $\mathbf{S}$-matrix. In a perfect system, all power is either transmitted or reflected. Consequently, from the energy conservation [69] follows:

$$|\mathbf{S}_{1,1}|^2 = |\mathbf{S}_{2,2}|^2 \quad \text{and} \quad |\mathbf{S}_{1,2}|^2 = |\mathbf{S}_{2,1}|^2 \quad . \tag{2.84}$$

In a lossy DUT, energy losses are caused by, e.g., skin effects of the device [70].

Since the transmission and reflection of the power are frequency-dependent, the S-parameters are generally given by $\mathbf{S}_{i,j} = \mathbf{S}_{i,j}(\omega)$. In a 2-port device, the transmission parameters $\mathbf{S}_{1,2}$ and $\mathbf{S}_{2,1}$ can be used to determine the eigenmodes of the propagating electromagnetic waves. In Figure 2.14, an example of $\mathbf{S}_{1,2}$ for a corrugated structure indicates the frequencies at which the transmission is suppressed, and the power is stored in the DUT [71]. Consequently, network analysis can be used, for example, to determine the resonance frequency and quality factor of a cavity.

3. KARA

The Karlsruhe Research Accelerator (KARA) at the Karlsruhe Institute of Technology (KIT) is described in this chapter, and its essential parameters and settings for this thesis are pointed out. The first section discusses the pre-accelerators and the main components of the KARA storage ring. Afterward, the short bunch operation mode is characterized in which the micro-bunching instability can be examined. In the last section, the specific location for the planned versatile impedance manipulation chamber is described.

3.1. Accelerator Chain & Storage Ring

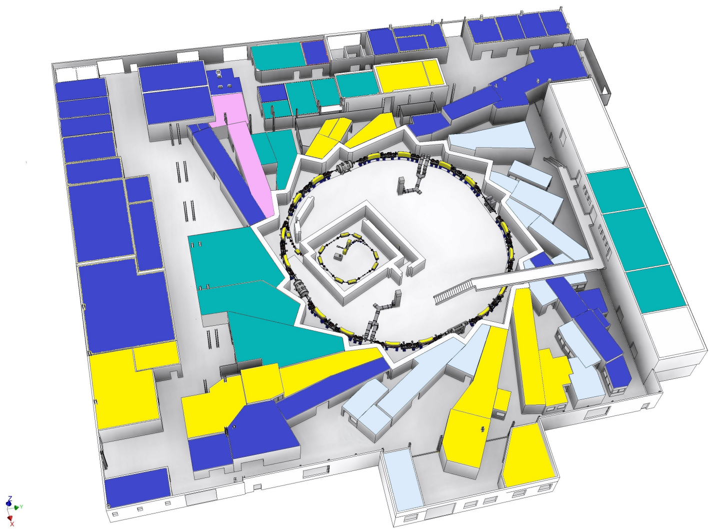

Figure 3.1. Layout of the KARA hall. The ring is built up inside the radiation safty wall. The pre-accelerators are placed inside the smaller rectangular hutch. Various beamlines (yellow, blue, and green) using different spectral parts of the synchrotron radiation are located outside of the radiation safety wall (Courtesy U. Herberger [72]).

A complex infrastructure is necessary to provide the intense radiation for the various beamlines of the KARA storage ring and synchrotron light source. Besides for example insertion devices (IDs), cooling, and vacuum technology, a chain of different pre-accelerators is needed.

At the first stage of the accelerator chain, the electrons are generated in a thermionic electron gun (E-Gun), in which they are already accelerated to the anode with a voltage of 90 kV. Afterward, the electrons are guided into a racetrack microtron with a 5.3 MeV linear accerator (Linac) between the two D-shaped dipole magnets. Since the acceleration section is run through 10 times, the electrons leave the microtron with an energy of 53 MeV [74; 75]. The final stage of the pre-accelerator chain is a booster synchrotron with a circumference of 26.4 m with a harmonic number of $h = 44$ and a simple FODO magnet lattice. A FODO

Figure 3.2. Layout of the KARA storage ring. The ring is built up of four symmetrical bending sections with four dipole magnets (yellow) each. In total, there are 40 quadrupole magnets (red) for beam focussing in both transverse planes [72].

lattice cell is composed of a focusing (F) and defocusing (D) quadrupole magnet with drift spaces (O) in between. In this booster, the energy is ramped up to the storage ring injection energy of about 500 MeV, and the electron bunch is subsequently injected into the main ring. The pre-acceleration cycle is repeated at the rate of 1 Hz until the desired current is accumulated in the storage ring. By changing the injection timing, all filling pattern from single bunch to all buckets filled can be established. Typically, up to four trains with 33 bunches each are filled in the storage ring in normal user operaton.

In principle, the energy can be ramped in the main storage ring to any value between the injection energy 500 MeV and 2.5 GeV for the user operation (UO). However, there are predefined and well-experienced settings at 0.5 GeV, 1.3 GeV, 1.6 GeV 2.3 GeV, and 2.5 GeV. The magnet lattice is built with dipole, quadrupole, and sextupole magnets with additional small correctors and kicker magnets. The magnet lattice of the storage ring has a four fold symmetry, where each sector is built from two Double-Bend-Achromat (DBA) [21]. A DBA is designed to minimize the emittance and consists of a symmetrical arrangement of two defocussing quadrupole, three focussing quadrupole, and two bending magnets. Consequently, the ring has four short and four long straight sections (see Figure 3.2), which are used for IDs, RF cavities, and diagnostics. Additionally, superconducting and permanent magnet wigglers and undulators [76; 77; 78; 79; 80] are installed in straight sections. This IDs enhance the CSR intensity and photon flux or change the spectrum of the radiation for certain beamlines. In two opposite short straight sections, there are two 500 MHz RF cavities each - powered by one klystron per section - for the acceleration and energy regain of the electrons. The most relevant machine parameters are listed in Table 3.1.

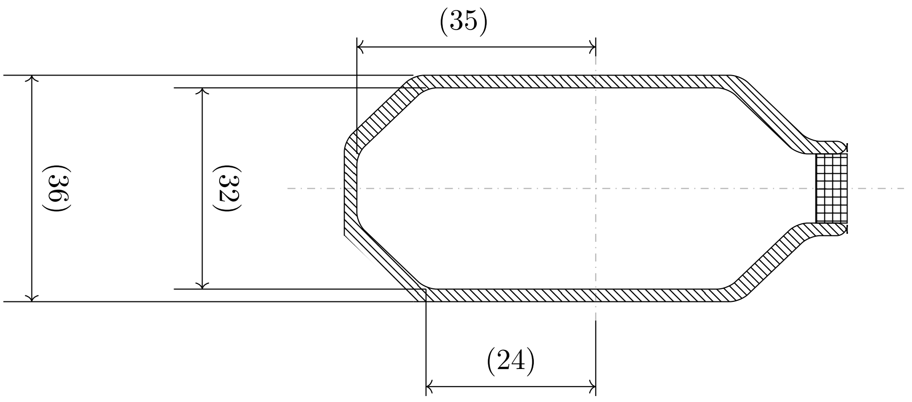

Figure 3.3. **Cross-section of the KARA beam pipe.** The water-cooled absorber (crossed, on the right) on the outside of the ring causes the asymmetry in the horizontal shape of the pipe (based on [73; 72]). The dimensions are given in millimeter (mm)

Table 3.1. **KARA machine parameters.** Machine parameters and settings that are used for the low-α_c mode are shown in red.

Parameter	**Value**
KARA circumference / m	110.4
Bending radius ρ / m	5.559
Vacuum chamber height h_c / mm	32
Electron beam energy E / GeV	1.3
RF frequency f_{RF} / MHz	499.705
Revolution frequency f_{rev} / MHz	2.7157
Harmonic number h	184
Synchrotron frequency f_s / kHz	8.87 to 15.90
Momentum compaction factor α_c	6 to 13×10^{-4}
Radiated energy/particle/revolution W_0 / keV	45.5

Parts of the synchrotron spectrum in the range from far infrared to X-rays (critical photon energy: 6 keV at UO) - according to the need of the applications - are coupled out at dedicated ports of the bendings magnets (at 0 °, 5 °, 11.25 °) and the insertion decives. The radiation is extracted to the 23 beamlines and additional diagnostic ports. At the different beamlines, the synchrotron radiation is used for a variety of purposes: imaging methods (e.g., IMAGE beamline), spectroscopy (e.g., INE[81]), or microfabrication (LIGA).

The beam pipe of the KARA storage ring has an elliptical to hexagonal shape (see in Figure 3.3) with a width of ≈75 mm and the height h_c=32 mm. The shape asymmetry is caused by the water-cooled absorber, which absorbs the stray synchrotron radiation power [73]. As mentioned in Section 2.4, the height of the chamber is a crucial parameter for the overall impedance of the accelerator. Besides the resistive wall impedance, h_c defines the cutoff frequency and wavelength $\lambda_{\text{cutoff}} \simeq \sqrt{4h_c^3\rho}$ [82] of the propagating coherent synchrotron radiation inside the beam pipe. For the KARA beam pipe, this cutoff is given by $\lambda_{\text{cutoff}} = 4.9$ mm and $f_{\text{cutoff}} \approx 61$ GHz. The suppression of lower frequencies is shown in Figure 2.8 by the difference between the parallel plate and free space CSR impedance. Compared to other light sources, such as the MAX IV 3 GeV storage ring [83], the relatively large height of the beam pipe and the short bunch length mean that not the geometric impedances but the CSR impedance is dominant at KARA. However, geometric impedances that are large enough can make a significant contribution to the overall impedance of the

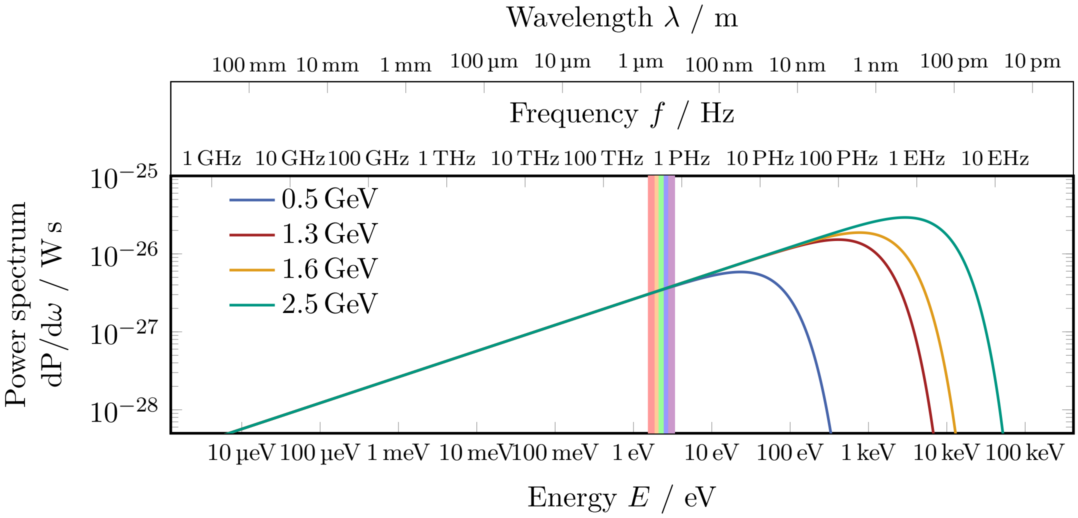

Figure 3.4. ISR spectrum. The radiated power of a single electron for different beam energies at the KARA storage ring. A higher beam energy leads to an extension of the photon spectrum to higher energies, higher frequencies, and shorter wavelengths. The colored area indicates the visible part of the electro-magnetic spectrum (adapted from J. Steinmann [73]).

KARA storage ring.

3.2. Short Bunch Operation Mode

Present-day and future storage rings and light sources have to meet the increasing demands regarding the peak power and brilliance of synchrotron radiation. Beyond that, there is a lack of sources and detectors in the THz frequency range, which, therefore, has been referred to as the "THz *gap*" [85]. Consequently, sources of intense radiation in this frequency range are needed.

As discussed in Section 2.3, the photon flux of the CSR is multiple orders of magnitude higher than for the ISR making CSR particularly interesting as a radiation source for scietific experiments. For the generation of CSR in the THz range, the bunch length must be reduced to the single-digit picosecond (ps) time scale. Following from Equation (2.27), it can be seen that the bunch length depends on two machine parameters. Its reduction can be achieved by either increasing the amplitude of the RF voltage U_{acc} whereby the slope of the acceleration voltage in the cavities at the synchronous phase is increased, or by stepwise reduction of the momentum compaction factor α_{c}. In contrast to U_{acc}, which is limited by the voltage in the cavitites, α_{c} can be varied over multiple orders of magnitude. Therefore the change in the magnet optics and consequently in α_{c} is used for the short bunch operation mode at KARA, which is also referred to as low-α_{c} mode [86; 87].

In this operation mode, the energy is fixed at 1.3 GeV and the bunch length is reduced in comparison with the normal UO with 2.5 GeV, so that the CSR is extended to the THz frequency range. In the UO, the bunch has a typical length of $\sigma = 45\,\mathrm{ps}$, whereas in the short-bunch operation mode it is reduced to the single-digit pico-second scale. Since most of the beamlines need X-ray pulses $\mathcal{O}\left(10^{18}\,\mathrm{Hz}\right)$, whose flux is much too low in the low-α_{c} mode (see Figure 3.4), this mode is usually not used for UO. To make this mode usable for UO it is crucial to overcome the micro-bunching instability and reach a state of stable substructures. Then it is possible to operate with short bunches for the intense THz radiation at higher energies for the high X-ray flux. Consequently, this low-α_{c} mode is mostly used for machine physics studies and experiments requiring ultra-short synchrotron

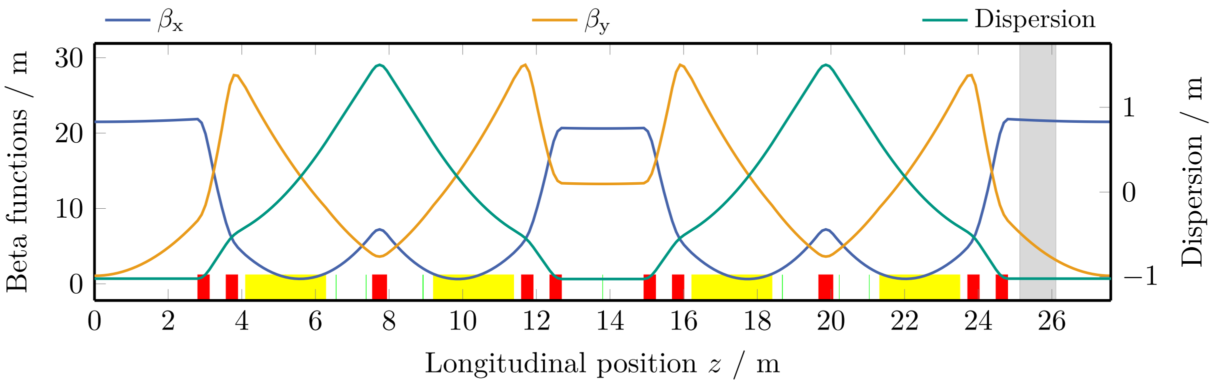

Figure 3.5. Optical functions at the 1.3 GeV **low-α_c mode.** The horizontal and vertical β, as well as the horizontal dispersion, are shown as a function of the longitudinal position in one of the four identical sectors at KARA. The position of the dipole (yellow), quadrupole (red), and sextupole (green) magnets are indicated by the boxes at the bottom (based on P. Schreiber [84]). The grey area marks the position of the planned impedance manipulation chamber in the fourth sector.

radiation pulses. This energy has been found in the past as sweet spot between the short bunch length and a resonable lifetime. This working point is well understood and is therefore used for basic experiments and theory confirmation. The resulting knowlege can be adaped for other light sources and storage rings and is important for the design of future low emittance machines [33]. Due to the shorter bunches and higher particle densities, nonlinear effects and instabilities (detailed description in Section 2.7) can occur at even lower beam currents. For all the studies of this thesis, this low-α_c mode is used. Due the shorter bunch length the current ranges of the micro-bunching instability regime can only be reached and studied at KARA in this operation mode.

To reduce the momentum compaction factor, the magnet optics and, therefore, the settings of the magnets must be changed. From Equation (2.22), it follows that the dispersion in the bending sections defines α_c. Therefore the strength of the quadrupole magnet in the middle of each DBA is adjusted so that the dispersion becomes slightly negative in some parts of the bending magnets. The dispersion and the β functions for the low-α_c mode are shown in Figure 3.5. At the KARA storage ring, different predefined quadrupole settings with corresponding and matching sextupole corrections are implemented in a range from $\alpha_c = 1 \times 10^{-2}$ for the normal operation mode down to $\alpha_c \approx 1 \times 10^{-4}$. However, it should be noted that a reduction of α_c leads to a smaller momentum acceptance [88]. The process of shortening the bunch length by reducing α_c is referred to as "*low-α_c squeeze*" [33], whereby in principle, the machine can be operated at any step of the squeezing.

The current limit of the low-α_c squeeze is defined by the stability of the quadrupole power supplies. The small fluctuations in the magnetic fields lead to beam losses due to the reduced momentum acceptance. In combination with an increased U_{acc}, the zero-current bunch length at KARA can currently be reduced down to $\sigma_0 = 1.8\,\text{ps}$ [61]. Regardless, a further reduction of the bunch length by controlling the higher order terms of the momentum compaction factor by adjusting the sextupole strength is being investigated by A. Papash *et al.* [89].

3.3. Impedance Chamber Location

A suitable place must be found in the KARA storage ring to install a corrugated structure. Due to the multiple required components of the storage ring, the available free space is very

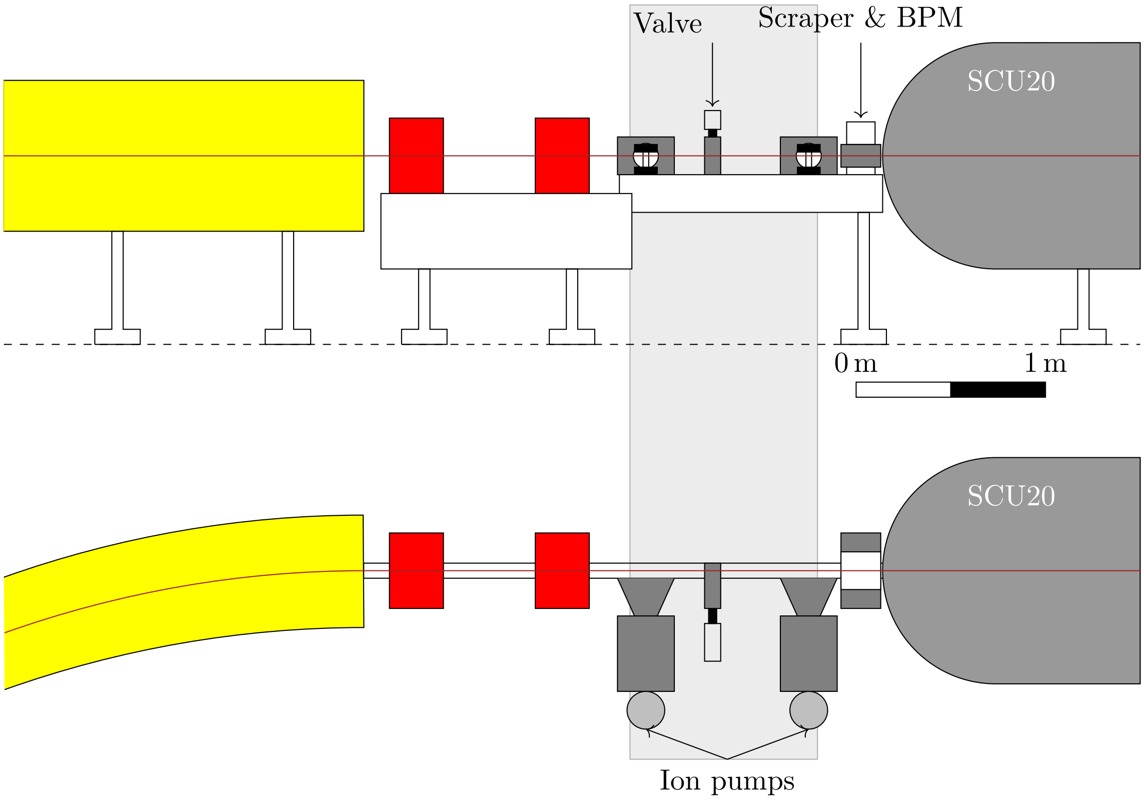

Figure 3.6. Planned chamber postion upstream SCU20. The schematics side view (top) and top view (bottom) show the planned position of the chamber (light grey) between the magnets (yellow: dipole and red: quadrupole) and the SCU20 (dark grey ellipse). The section is currently crowded with pumps, valves, a horizontal scraper, and a BPM[6](Based on [72]).

limited. It is planned to place the corrugated structure in a new versatile chamber. This chamber enables an exchange of the corrugated structures, but can in principle later also be used for other tests in the ring. Vacuum valves directly before and after the chamber and an additional vacuum pump allow a relatively easy and fast exchange of the structures or devices by only ventilating the chamber without breaking the vacuum in the rest of the machine.

The location of this chamber should be in one of the straight sections, which are mainly occupied by IDs, diagnostics, and the cavities so that the number of possible locations is minimal. There are two positions in the KARA storage ring - upstream of the CLIC[7] damping wiggler prototype [90; 76] and upstream of SCU20[8] [80] - that meet the requirements and offer about 50 cm for the versatile chamber. Both locations already have one vacuum valve in front of the ID but would need an additional one so that the chamber can be vented independently of the ID. Also, an additional bellow (≈2 cm) is needed in order to be able to put the chamber in place.

At the first option, upstream of the CLIC damping wiggler, about 51 cm of free beam pipe are available. However, it is close to the injection point and therefore inside the injection bump with three kicker magnets, which might interfere with the corrugated structure and affect the beam injection.

Upstream of the SCU20, at the second possible location, there is about 48 cm free space

---

[6] Beam Position Monitor

[7] Compact Linear Collider

[8] Superconducting Undulator with 20 mm periodic length

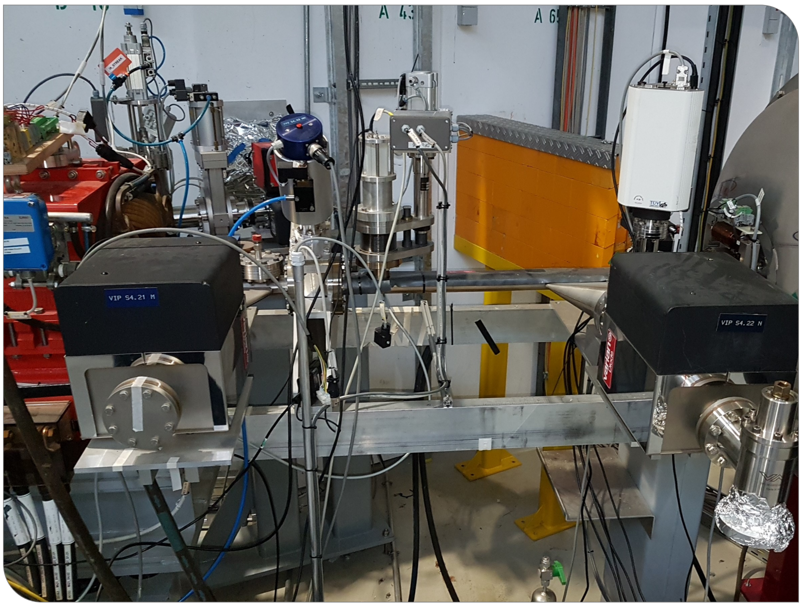

Figure 3.7. Planned chamber postion upstream of SCU20. Image of the designated chamber postion upstream of the Superconducting Undulator with 20 mm periodic length (SCU20) (Courtesy: M. J. Nasse). Between the quadrupole magnet (red) on the left side and the undulator (grey round cylinder) on the right, about 48 cm of free space is available. In this area, in addition to the impedance chamber, vacuum pumps, scrapers, and valves must also be accomodated.

available (schematic illustration in Figure 3.6 and image in Figure 3.7), which is limited in the upstream direction by the last quadrupole of the bending section. To save some space, it is possible to combine the vacuum pump port with the scraper directly upstream of the SCU20, which absorbs the synchrotron radiation (SR) to protect the undulator against radiation damage. Because the corrugated structures would not interfere with the beam injection in this position, this is the preferred option and will be used throughout this thesis. Depending on the positioning and combining of the other moveable parts (e.g., valves, pumps), the chamber will be placed between 107.93 m and 108.92 m of the KARA storage ring. The zero position at the KARA storage ring is universally defined and used throughout this thesis as the begining of sector that includes the beam injection.

Obviously, the corrugated structure has to be made of an electrically conductive metal to create the additional impedance. The embedding in the KARA storage ring and the vacuum beam pipe causes additional requirements for the material of the corrugated structure. Since multiple magnets are installed in the storage ring, a magnetic material would create further unwanted and uncontrolled magnetic fields, which affect the trajectory of the electron beam. Therefore, the material of the corrugated structure and the whole chamber has to be non-magnetic. Furthermore, the structure will be placed inside the evacuated volume, so it has to be compatible with the ultra-high vacuum (UHV) in the KARA beam pipe.

4. Simulations

For the studies throughout this thesis, two different simulation tools are used. In this chapter, the settings and relevant parameters of the simulation tools are presented. Furthermore, the simulation process and exemplary simulation results are shown. The first part of this chapter describes the settings of CST Studio Suite® 2020 (CST) for the electromagnetic simulations with the finite element method to determine the impedances and eigenmodes. Thereby, a scan of the mesh sizes in the different directions is performed to determine the necessary resolution of the mesh grid. The second part introduces the Inovesa Numerical Optimized Vlasov Equation Solver Application (Inovesa), which is used for the KARA related beam dynamics simulations by solving the VFPE (2.61) numerically.

4.1. CST Studio

To study the impedance and the eigenmodes of the corrugated structure, CST Studio Suite® 2020 (CST) [91] is used for all the simulations in this thesis. The particle wakefield solver is used for the impedance simulations and the eigenmode solver to investigate the frequency depedency of **S**-matrix elements. Even though there are individual settings and requirements for the two solvers, the investigated structure is identical, so some settings and parameters are the same for both solvers.

A 3D model of the DUT is necessary for both solvers. This DUT is built from two parallel plates, which are made up of periodically alternating teeth and gaps. Investigations of both different structure lengths s of the corrugated plates and different periodic lengths L with a fixed structure length require the flexibility of the numbers of corrugations N_corr in the model. Therefore, the corrugated plate cannot be designed as one large structure with a fixed number of corrugations. As a result, a block with ten corrugations, in which all the corrugation parameters shown in Figure 4.1 (half plate distance b, periodic length L, corrugation depth h, longitudinal gap g, and plate thickness t) as well as the plate width x_0 can be freely set for each simulation, is designed. The plate is symmetric around the $yz|_{x=0}$ plane and thus extends from $x = -\frac{x_0}{2}$ to $x = +\frac{x_0}{2}$. If not mentioned otherwise, the width x_0 has been fixed at 24 mm for all simulation throughout this thesis. This value has been chosen to avoid any boundary effects (see Section 8.1.1). The needed number of corrugations is achieved by a translation of the designed block with the repetition factor

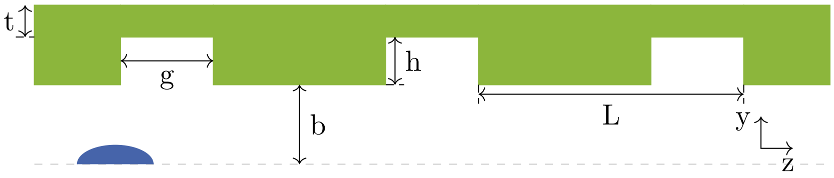

Figure 4.1. Corrugated plate. The corrugated pipe in half cross-section with the relevant geometric parameters is shown. The electron bunch is indicated in blue and travels along the dashed line through the structure.

Table 4.1. **CST material properties.** Relevant properties of the three materials which are used for the simulations.

Parameter	copper	stainless steel 1.4429	steel 1008
Type	lossy metal	lossy metal	lossy metal
Relative permeability μ_r	1	1	1
Electrical conductivity σ_el / $\frac{\mathrm{S}}{\mathrm{m}}$	5.96×10^7	1.33×10^6	7.69×10^6
Density / $\frac{\mathrm{kg}}{\mathrm{m}^3}$	8930	8000	7870
Thermal conductivity / $\frac{\mathrm{W}}{\mathrm{K\,m}}$	401	15	59.5
Specific heat / $\frac{\mathrm{J}}{\mathrm{K\,kg}}$	390	500	480
Diffusivity / $\frac{\mathrm{m}^2}{\mathrm{s}}$	1.15×10^{-4}	3.75×10^{-6}	1.58×10^{-5}
Young's modulus / $\frac{\mathrm{kN}}{\mathrm{mm}^2}$	120	200	200
Poisson's ratio	0.33	0.28	0.29

$N_\mathrm{rep} = \frac{N_\mathrm{corr}}{10} - 2$ and the translation vector $\vec{T} = (0, 0, 10 \cdot L)$ so that the correct number of blocks is created automatically for each chosen value of s and L. Based on the arbitrary chosen corrugation number ($L_\mathrm{block} = 10 \cdot L$) of the corrugated block, s and L has to be chosen in a way that N_rep is an integer value.

The repetition factor N_rep is not $\frac{N_\mathrm{corr}}{10}$ because the first and the last block are created independently of the others. The first and last block creation is caused by the special requirements of CST for the mesh at the beginning and end of the structure. The first (and last) three mesh cells must be of the same material. As will be discussed in detail soon, this fine mesh cannot be used for the whole structure, so the mesh and the blocks at the beginning and end must be defined separately. The second corrugated plate below the electron path mirrors the whole structure at the $xz|_{y=0}$-plane. Figure 4.2a shows the two plates with the particle beam in the CST wakefield solver.

The two plates are made of the same material for all the simulations. The volume between is "*filled*" with vacuum. The materials chosen for the corrugated structure have to fulfill the same requirements in the simulations as for the plates for the KARA storage ring: electrically conductive, non-magnetic (relative permeability μ_r= 1), and UHV compatible. For the studies in this thesis, three materials are used: copper, steel 1008, and stainless steel 1.4429, which is also used for the KARA beam pipe. The required properties of the first two materials are given from the CST Material Library, and the properties of the stainless steel are from the Metalcor datasheet [92]. All the relevant parameters are given in Table 4.1.

The electromagnetic skin effect must be considered to define the minimal plate thickness t. The penetration depth of the electromagnetic field is given by the skin depth [20]

$$\delta(\omega) = \sqrt{\frac{2\rho_\mathrm{el}}{\omega \cdot \mu}} \tag{4.1}$$

with the electrical resistivity $\rho_\mathrm{el} = \frac{1}{\sigma_\mathrm{el}}$ and the permeability $\mu = \mu_0 \cdot \mu_\mathrm{r}$ of the conductor. In Figure 4.3, the skin depth is shown as a function of the frequency for the three used materials. It can be seen clearly, that δ is in $\mathcal{O}(1\,\mu\mathrm{m})$ and below for the investigated frequencies in the GHz range. For the frequency $f = 100\,\mathrm{GHz}$, for example, the skin depths are δ=0.2 µm for copper and δ=1.4 µm for stainless steel. Consequently, only a shallow penetration depth and a surface interaction with the corrugation and the plate can be expected. Therefore, reducing the pipe thickness for the simulations should not impact the impedance and eigenmode parameters. However, the simulation runtime can be improved due to fewer mesh cells. Unless otherwise noted, the plate thickness is t=500 µm for all

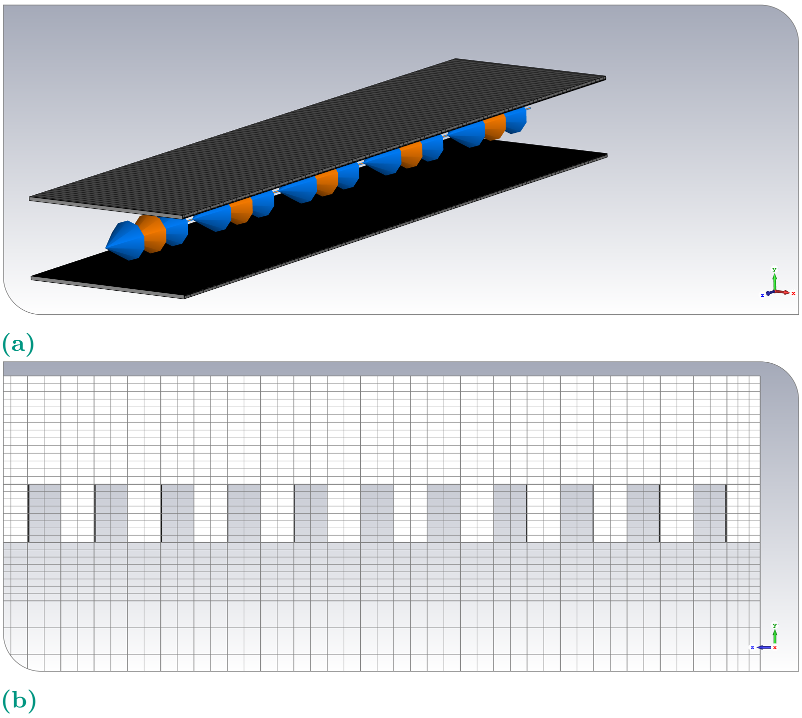

Figure 4.2. **CST 3D model.** (a) The 3D model of the structure consists of two parallel plates (grey) with periodic rectangular corrugations and a particle beam (orange and blue) in the middle. (b) A fine mesh is used inside the metallic plates (white), in the corrugations, and in the area close to the plates. In the area between the plates, a coarser grid can be used. In the longitudinal direction z, at least two cells per corrugation are required.

the simulations. The small effective skin depth of a few µm also becomes important in Chapter 8 for the manufacturing process.

For both solvers, but especially the particle wakefield solver using the finite element method (FEM), adequate size of the grid or mesh cells is crucial for precisely determining the impedance and eigenmodes. A hexahedral mesh - here by rectangular cuboids - perfectly fits the corrugations' rectangular shape. However, there are difficulties in terms of resolution, simulation accuracy, and mesh size, for example, for triangular corrugations with a side wall angle $\alpha \neq 0\,°$.

Inside the corrugations and the gaps, a fine mesh is required. With the small corrugation size ($\mathcal{O}\left(100\,\mu\mathrm{m}\right)$) and the long plates ($\mathcal{O}\left(10\,\mathrm{cm}\right)$), a extremely large number of mesh cells ($\mathcal{O}\left(10^8\right)$) and consequently a long simulation time results. Therefore, reducing the number of mesh cells is important for the systematic simulation scans of the different corrugation parameters. In the first step, the vacuum area between the two corrugated plates is split vertically into three sections. The outer sections fill the corrugation gaps and an area of the same height outside the corrugations and have the same fine mesh as the corrugations themselves. In the bulk area around the beam ($-b + h < y < +b - h$), a reduction of the mesh cells in the vertical direction is possible. Figure 4.2b shows the example of the mesh grid and the different areas with different mesh densities and sizes. In addition, two symmetry planes are used to reduce the total number of mesh cells by a factor of four to $\mathcal{O}\left(10^7\right)$. The boundary conditions used for the symmetry planes (yz- and xz-plane) are that the tangential magnetic field at the symmetry plane vanishes ($H_\mathrm{t} = 0$). The exact mesh sizes which have been used for the corrugation parameter scan have been determined by CST simulations of the wakefield and impedance for different meshes. These will be discussed at the end of the following Section 4.1.1.

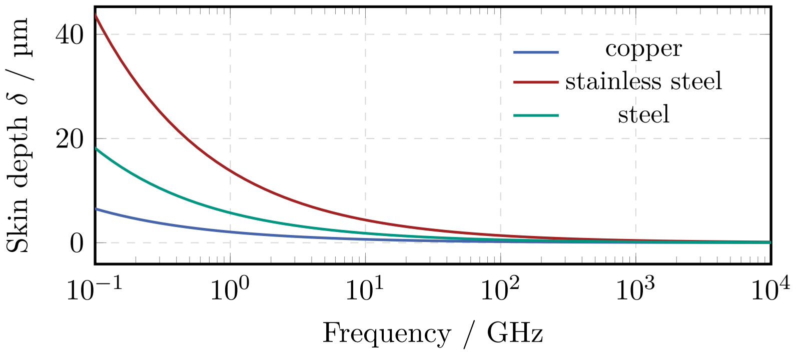

Figure 4.3. **Skin depth** δ as a function of the frequency for three different materials. In the GHz range, the skin depth is in the order of µm. The differences between the materials are caused by their electromagnetic properties, which are given in Table 4.1.

4.1.1. Impedance and wakefield

The CST particle wakefield solver is used to simulate the impedance and wakefield of the corrugated structures. Besides the general and previously discussed parameters, boundary conditions at all six sides of the structure and a particle beam, as the driving source of the wakefield determination, are required.
Since the structure with the two parallel plates is symmetrical in all three planes, the boundary conditions on the respective opposite sides are identical. On all the transversal sides (x and y), the "*electric*" ($E_\mathrm{t} = 0$) boundary condition is chosen, which operates as a perfect conductor, for which the tangential components of the electric field and the normal components of the magnetic flux vanish. Consequently, the electric field is normal to the boundaries. In the longitudinal direction, the boundaries are "*open*". With this condition, the geometry is virtually extended to infinity [93].
The particle beam is the basis for calculating the fields in each mesh cell and, therefore, for determining the wakefield. It is defined as a bunch of charged particles that travel through the structure with a constant velocity $\vec{v}$. All studies in this thesis are based on the 1.3 GeV regime at KARA. Therefore, the velocity is given by $\beta = \frac{v}{c}$ =1-7.7 $\times$ 10^{-8}. Besides the velocity, the charge q and the bunch length σ_0 characterize the Gaussian distributed line current. It should be noted that this line current has no transverse size, and thus, the typical beam size at KARA has to be taken into account in determining the necessary plate width x_0. Out of the three available wakefield integration methods, the "*indirect testbeam*" is the most accurate, but has, as a condition, that the beam pipe must not be concave. So, the cross-section of the structure at each point must be larger or equal to the cross-section of a plane plate. Since the corrugations extend the cross-section, the criteria to use the "*indirect testbeam*" method is fulfilled.
In theory, the impedance depends on the single particle wake function and is - in contrast to the wakefield E - independent of the bunch shape and length (see Equation (2.38)). However, in the CST simulations, at least the bunch length affects the simulation results of the impedance since the frequency range of the impedance calculation is defined by σ_0. The maximal frequency f_max is given as the frequency at which the charge distribution spectrum $\tilde{\varrho}$ is reduced to $k = -20\,\mathrm{dB}^9 = 0.1$. For a Gaussian bunch, the connection between the

---

[9] for amplitude, the conversion is given by: $Q = 20 \cdot \log\frac{F}{F_0}\mathrm{dB}$

bunch length and the maximal simulation frequency is given by

$$\sigma_0 \cdot f_{\max} = \frac{\sqrt{2\ln(1/k)}}{2\pi} = 341.304\,\mathrm{ps\,GHz}^{10}.$$

For the currently minimal achievable bunch length σ_0=2 ps at KARA, this maximal simulation frequency is $f_{\max} \approx 170\,\mathrm{GHz}$. However, depending on the exact simulation parameters, Inovesa requires the impedance up to $\mathcal{O}\,(\mathrm{THz})$ (see Section 4.2). To determine the impedance up to the THz range, it is necessary to reduce the bunch length even further - to non-physically short bunch lengths. For the Inovesa settings used in this thesis, the maximal demanded impedance frequency of $f_{\max} = 5.25\,\mathrm{THz}$ requires a bunch length of $\sigma_0 = 65\,\mathrm{fs}$.

Consequently, simulating the impedance Z and wakefield E in the same simulation step is impossible. Based on Equation (2.38), it is possible to simulate either Z or E and calculate the other one with the bunch profile ϱ. However, the simulation of E makes it necessary to carry out a new simulation with the same corrugation parameters for each bunch profile which is of interest. In addition, to determine the impedance, the Fourier transform of E must be divided by the bunch spectrum $\tilde{\varrho}\,(\omega)$. The contribution at the high frequencies is mostly negligible. Therefore, the divisor is very small. This would lead to unphysical divergences in the impedance for high frequencies.

The simulation of the impedance has the benefit that the quantity needed for the Inovesa simulations is given directly as a result of the CST simulations. Since the impedance is independent of the charge distribution, it is irrelevant that ϱ has to be unrealistic short. The wakefield can be calculated in the post-processing for any chosen charge distribution. Because the bunch spectrum is multiplied instead of divided by it, there are no artifacts for minimal contributions for high frequencies. In the post-processing, the wakefield is calculated by a inverse discrete Fourier transform (iDFT) from the impedance vector of the length N via

$$E^{\parallel}(t) = \frac{\Delta\omega}{\sqrt{\pi}} \sum_{k=1}^{N} Z^{\parallel}\,[k] \cdot \tilde{\varrho}\,[k]\, \mathrm{e}^{+i\cdot k\cdot\Delta\omega\cdot t} \quad . \tag{4.2}$$

Accordingly, with CST only the impedance simulations with σ_0=65 fs are performed.

As described previously, correctly estimating the needed mesh cell numbers is important for both precision simulation results and a short simulation time. Therefore, simulations have been performed to determine the minimal required mesh cell number for the different directions above which the impedance converges. In Figure 4.4a the real part of the longitudinal impedance ($\Re\left(Z^{\parallel}\right)(f)$) is shown for different numbers of vertical mesh cells inside the corrugations $N_{\mathrm{y,\,corr}} = \frac{h}{\Delta y_{\mathrm{mesh,corr}}}$. A detailed discussion of the impedance shape and the characterization with a resonator model is given in Chapters 5 and 6. For now, it is only important to see that the maximal impedance, called shunt impedance Z_0, increases to a certain value of $N_{\mathrm{y,\,corr}}$. From Figure 4.4b for $N_{\mathrm{y,\,corr}} \geq 8$, the shunt impedance does not change significantly anymore. Therefore, the mesh cell number has been fixed at $N_{\mathrm{y,\,corr}} = 8$, which leads to a mesh size of $6.25\,\mu\mathrm{m} < \Delta y_{\mathrm{mesh,corr}} < 25\,\mu\mathrm{m}$ for corrugation depths of $50\,\mu\mathrm{m} < h < 200\,\mu\mathrm{m}$. A similar scan has shown that for the vacuum bulk (from 0 to $b - h$), 60 vertical mesh cells are required to reach saturation. For a half plate distance $b = 5\,\mathrm{mm}$, this means an enlargement of the mesh cells by a factor 3 to 13 in comparison to the fine mesh inside the corrugations.

Figure 4.4b shows, as well, that two longitudinal mesh cells in all corrugation teeth and gaps are mandatory, but a further increase does not change the shunt impedance. However, the first and last tooth CST requires three cells due to special boundary demands, shown in Figure 4.2b. For a structure length of s=10 cm and a corrugation periodicity L=100 µm

---

[10] Bunch spectrum of a Gaussian bunch: $\tilde{\varrho}(\omega) = \frac{1}{\sqrt{2\pi}} \mathrm{e}^{-\frac{1}{2}\sigma_0^2\omega^2}$

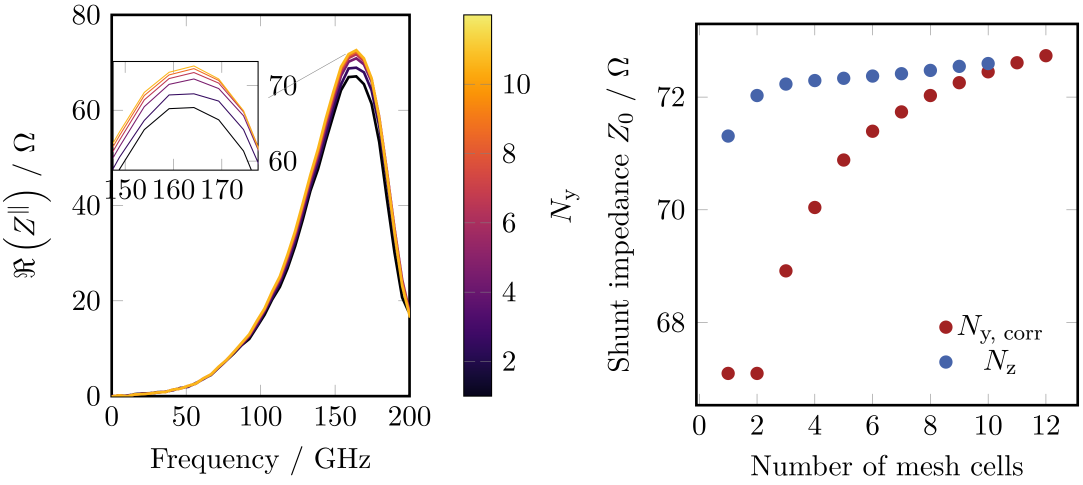

(a) **(b)**

Figure 4.4. Mesh size in CST simulations. (a) Simulated longitudinal impedance of a corrugated structure for different numbers of vertical mesh cells inside the corrugations $N_{y,corr}$ (increasing from blue over red to yellow). (b) The shunt impedance increases until a certain number of mesh cells is reached. Above the threshold, a finer mesh only affects the runtime but not the simulation result.

this results in 4000 longitudinal cells with a length of 25 µm.

4.1.2. Eigenmode

For the simulations of the frequency dependency of **S**-matrix elements (**S**-parameters) with the Eigenmode solver in the time domain, the same settings of the 3D model and the mesh grid are used as for the Wakefield solver. Instead of the particle beam, waveguide ports for all the ports of the DUT are defined. In the case of the corrugated structures, the field propagation in the longitudinal direction is of interest. Therefore, these structures can be considered and studied as a 2-port device, with a port at the longitudinal start ($z = 0$) and end ($z = s$) of the plates - oriented normal to the z-axis. In the transverse plane, both plates extend over the full plane of the structure. The orientation of the ports is defined in a way that the input signal propagates through the structure towards the other port.
To increase the frequency resolution of the **S**-parameters and to reduce the simulation runtime, the frequency range of the **S**-parameters determination is limited to $100\,\text{GHz} \lesssim f \lesssim 200\,\text{GHz}$. This is the relevant impedance frequency range and comparable to the measurable frequency range at the setup at the Institute for Pulsed Power and Microwave Technology (dt. Institut für Hochleistungsimpuls- und Mikrowellentechnik) (IHM) (see Chapter 8).
The number of modes taken for the simulation should at least contain the lowest propagating mode. A systematic scan has shown that increasing the number of modes above three does not affect the **S**-parameters of the 0th-mode any further.

4.2. Inovesa

To study the longitudinal beam dynamics, the longitudinal phase space density $\Psi(z, E, t)$ must be determined as a function of the time t. All the relevant beam dynamics parameters (e.g., bunch profile and CSR intensity) can be derived from the temporal development of the phase space. Most implementations solve the Vlasov-Fokker-Planck equation (VFPE) (Equation (2.61)) in the time domain by using the wakefields at each time step [35; 94].

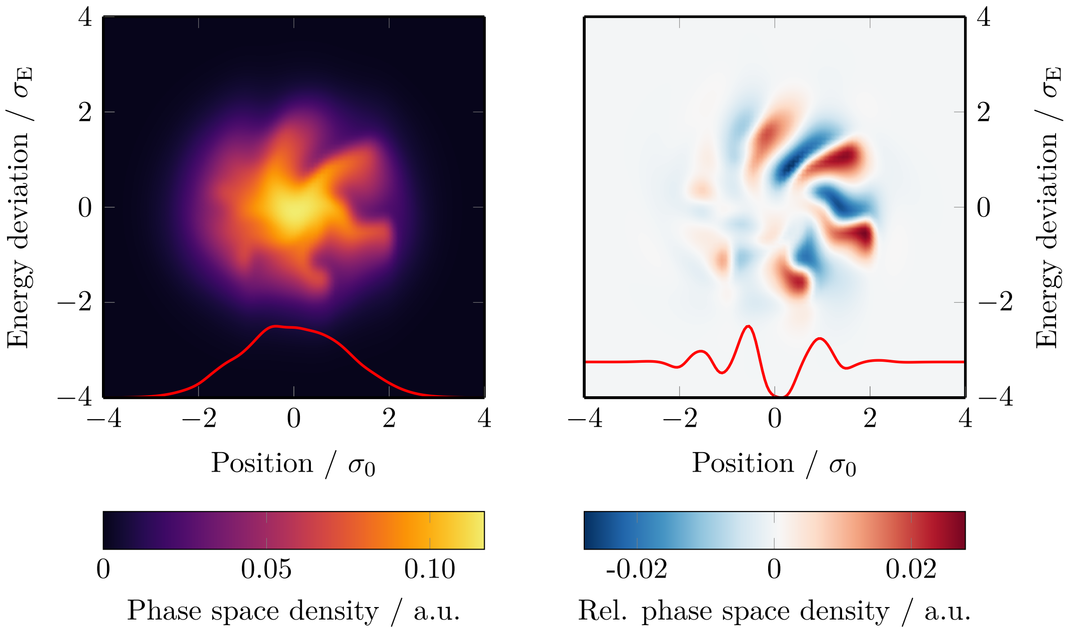

(a)

(b)

Figure 4.5. Simulated longitudinal phase space. (a) An exemplary longitudinal phase space simulated with Inovesa with only the parallel plate CSR impedance. (b) The deformation of the phase space density and the creation of the substructures can be seen more easily by subtracting the temporal-averaged phase space density. In both cases, the red line is the projection on the time axis and represents the bunch profile and the profile of the substructures, respectively.

For the simulations in this thesis, the Vlasov-Fokker-Planck solver (VFPS) Inovesa [95] is used, which has been developed by P. Schönfeldt at KIT. This implementation is massively parallelized and runs on standard desktop PCs as it solves the VFPE in the frequency domain based on the impedance of the accelerator. P. Schönfeldt *et al.* [96] have shown that Inovesa desribes the micro-bunching instabilty in good agreement with experimental results for the low-α_c operation mode at the KARA storage ring.

The simulation code used the approximation of an isomagnetic ring without straight sections and averages the wakefield homogeneously over the whole ring. Therefore, the wakefields of the corrugated structure must vanish within a single bunch revolution $T_{\text{rev}} = \frac{1}{f_{\text{rev}}} = 368\,\text{ns}$. For numerical solving of the VFPE, the phase space is discretized on a 2D matrix grid, where each entry $\Psi(z, E, t)$ represents the charge amount in the corresponding phase space volume.

The phase space density is simulated iteratively, whereby each time step $(\Psi(z, E, t) \rightarrow \Psi(z, E, t + \Delta t))$ consists of three steps. These steps are only roughly described here, but a more detailed description is given in [96; 59]. Before the first step, the bunch profile can be determined from the projection of the phase space on the position axis, and with the impedance, the wake potential of the next time step is calculated. In the first step, the rotation of the phase space is carried out. The phase space density is shifted along the position axis by an energy-dependent (y-axis) amount derived from the VFPE. Afterward, a kick, whose strength depends on the RF and wake potential of the previous step, is done. Consequently, this kick depends on the position and in the 2D grid column-dependent. Finally, the damping and diffusion is considered for all the grid cells individually by implementing the right-hand-side of Equation (2.61). The resulting phase space density is then used as a basis for the calculation of the next time step. The initial phase space distribution $\Psi(z, E, t = 0)$ can be defined by a 2D Gaussian distribution or an input file, which might be an Inovesa result file. It has been stated in [96] that the convergence to a physical state takes some simulation steps, depending on the initial phase space distribution and the simulation settings. The results of the Inovesa simulations - containing the phase space densities, derived quantities, and parameters - are saved in a HDF5 file ('.h5') [97], which can contain various data types. In Figure 4.5a, a simulated phase space is shown as an example. For better recognition of the substructure, the time-averaged - overall simulation time steps - phase space is substructured in Figure 4.5b. All the relevant beam dynamics parameters such as bunch profile, emitted CSR power, and the number of substructures can be derivered from this phase space density.

As mentioned, the impedance is an important quantity of the accelerator to properly describe the longitudinal beam dynamics in Inovesa. Per default Inovesa uses, the parallel plate CSR impedance (Equation (2.48)), which also can be deactivated or replaced by the free space CSR impedance. Additionally, any arbitrary impedance can be included via an input file (one benefit of the Inovesa simulation tool). P. Schreiber [98] has done detailed Inovesa simulation studies of the impact of geometrical impedances on the longitudinal beam dynamics. In this master's thesis he showed, inter alia, that for arbitrary impedances, the Inovesa simulation results of the bunch profile are in good agreement with the analytical solution of the Haïssinski Equation (2.65) (see e.g. Figure 4.7 in [98]). This validates the simulated longitudinal beam dynamics independent of the chosen impedance and not only for the CSR impedance.

The input file consists of an array of length $N = 1024$ for the real and imaginary part of the longitudinal impedance, with the identical frequency steps as the default CSR impedance. It has to be mentioned that the sign of the imaginary part depends on the Fourier transform convention (explained in Section 2.4), which defines the sign of causality in the time domain.

The parameters and settings for an Inovesa simulation can be loaded from a config file or individually added in the command line to start the simulation:

```
inovesa -I<BunchCurrent> -c<config>.cfg -i<InitialDistribution>.h5
-o<OutputFile>.h5 --<ParameterName><parameter> --Impedance<ImpedanceFile>.csv
```

All settable parameters that are relevant for the following simulations are described here, whereby the command line parameter name is given in bolt:

- **--AccelerationVoltage (-V):** Accelerating voltage U_{acc}
- **--BunchCurrent (-I):** Bunch current I_{b} that is in the storage ring, due to a single bunch
- **--Steps:** Simulation steps per synchrotron period
- **--SynchrotronFrequency (-f):** Synchrotron frequency f_{s}
- **--rotations:** Simulation time in terms of the synchrotron period T_{s}.
- **--alpha0:** Linear term of the momentum compaction factor α_{c}
- **--outstep:** Save results of every n-th simulation step
- **--SavePhaseSpace:** Number of full phase spaces, saved to HDF5 file. Without any further settings, the first and last simulation steps are saved by default. So, the last full phase space distribution can be used as the starting distribution for further simulations.
- **--VacuumGap:** Height of the vacuum chamber h_{c}. For positive values ($h_{\mathrm{c}} > 0$), the parallel plate CSR impedance, and for negative values ($h_{\mathrm{c}} < 0$), the free space CSR impedance is used.

The machine setting parameters f_s, α_c, and U_acc are connected via Equation (2.26), which can be rewritten as

$$f_\mathrm{s} = f_\mathrm{rev}\sqrt{\frac{h\alpha_\mathrm{c}}{2\pi E}\sqrt{e^2U_\mathrm{acc}^2 - W_0^2}} \quad . \tag{4.3}$$

Therefore, two of these three parameters must be defined, whereas the third one can be calculated.
Throughout this work, two kinds of Inovesa simulation scans are performed: current and impedance parameter scans. In the current scans, all machine and simulation parameters, as well as the impedance, are fixed. Since Inovesa does not take particle losses into account, the beam dynamics of each current has to be simulated individually to describe the current decrease over time in the real KARA storage ring. Therefore, the scan starts with a simulation at the highest current with a simulation time $T = 150\,\mathrm{T_s}$. This time is not used for further studies but as a settling time. The final state phase space density of this settling simulation is used as the start distribution of the first step for the real current scan with $T = 500\,\mathrm{T_s}$. For all the ensuing current steps, the final state density of the previous and slightly higher current simulation is used as the starting distribution. No settling time is needed for the small current steps $\Delta I \leq 10\,\mu\mathrm{A}$ since the physical state is already reached and the settings have not changed significantly. This procedure is identical to a scan with and without an additional corrugated plate impedance. For the scan of an impedance parameter, the beam current is fixed. In this scan, a simulation without an additional impedance and $T = 150\,\mathrm{T_s}$ is performed for the first settling and to provide the starting distribution for all simulations of the real impedance parameter scan with the same machine settings, except for the impedance, and the chosen beam current. Here, for each step, an individual impedance input file is loaded. Also, for this scan, the phase space density and its derived parameters are simulated for $T = 500\,\mathrm{T_s}$. Since the accelerator impedance has partially changed drastically compared to the settling simulation, the first $150\,\mathrm{T_s}$ are used as an additional settling time, so $350\,\mathrm{T_s}$ remain for the beam dynamics analysis. Inovesa is a non-interactive simulation tool. Therefore, a bash script with `for`-loops for the relevant parameters is used for all simulation scans. The impedance input files inside the loops are also created in a separate python [99] script. Based on [96], an example of a current scan script is:

Bash script: CurrentScan.sh

```bash
#!/bin/bash
config="config_f1234.cfg"
alphaC="1000e-6"
accVolt="1000e3"
Z0="1000"   # impedance parameter: shunt impedance
Q="3"       # impedance parameter: quality factor
fres="100"  # impedance parameter: resonance frequency
fs=‘python3 "./syncFreq".py --alpha0 $alphaC --accVolt $accVolt‘
impedanceFile=‘python3 "./impedance".py --ShuntImpedance $Z0 --QualityFactor $Q ResonanceFrequency $fres‘
lasti="500"
./inovesa -I ${lasti}e-6 -c $config -T 150 -o $lasti.h5 # settling simulation
for curri in {500..100..5}
do
./inovesa -I ${curri}e-6 -i $lasti.h5 --alpha0 $alphaC -V $accVolt -f $fs -c $config -T 500 -o $curri.h5 --Impedance $impedanceFile
lasti=$curri
done
```

in which the synchrotron frequency is calculated from α_c and U in the script *syncFreq.py* and the impedance input file is created in *impedance.py*. The three impedance parameters shunt impedance Z_0, quality factor Q, and resonance frequency f_{res} are introduced and discussed in detail in Chapter 6.

5. Advancement of Methods and Techniques

For this thesis, the characterization of the impedance of a corrugated structure, depending on the corrugation parameters, and its impact on the longitudinal beam dynamics and the micro-bunching instability are key parts. This chapter presents the methods and techniques used and (further) developed for the analysis and characterization of the impedance and beam dynamics simulation. The first part focuses on the impedance parameters of the corrugated structure and their finding with a suitable fitting of the impedance. The second part introduces the so-called spectrograms, with the help of which the changes in the beam dynamics depending on the bunch current can be visualized. Furthermore, this part discusses the characteristic properties of the micro-bunching instability and how they can be determined from the Inovesa simulation data. Since the additional impedances can change the beam dynamics significantly, the established routines (see e.g. [61]) are partially not robust enough to determine the instability properties correctly. Therefore, the routines need to be adapted or new routines must be implemented.

5.1. Impedance

For the analysis of the corrugated structure impedances, the CST simulation results (described in Section 4.1.1) with the real and imaginary parts are used. Figure 5.1 shows an example of an impedance across the entire simulated frequency range ($f_{\mathrm{max}} \approx 3.5\,\mathrm{THz}$) as well as an enlargement of the peak at the resonance frequency. The limited mesh cell resolution and the finite plate length cause the periodic ringing visible at higher frequencies. The simulation results can be compared to the theoretical description (Equation (2.50)). The latter, however, describes the resonance with an infitly narrow δ-distribution. This function, in the real part, defines the resonance wave number k_{res} and therefore the resonance frequency $f_{\mathrm{res}} = \frac{c}{2\pi} k_{\mathrm{res}}$. However, the finite width of the peak around f_{res} cannot be described properly by this equation. This parameter, however, is crucial for the impedance description since the width of the peak also affects its amplitude. Consequently, both parameters, peak width and amplitude, are affected by the corrugation parameters, and the maximal impedance does not only depend on the plate distance $2b$. In combination with the δ-distribution, the principal value P.V. indicates that the imaginary part is basically the derivative of the real part.

Since the pair of parallel plates with periodic rectangular corrugations can be seen as a series of passive resonators, it is a good approximation to describe its impedance by a complex broadband resonator impedance [100]

$$Z^{\parallel}(f) = \frac{Z_0}{1 + iQ\left(\frac{f_{\mathrm{res}}}{f} - \frac{f}{f_{\mathrm{res}}}\right)} \tag{5.1}$$

with the resonance frequency f_{res}, the shunt impedance Z_0, and the quality factor Q. In this context, Z_0 is defined as the real part impedance at f_{res} and the last one is a measure

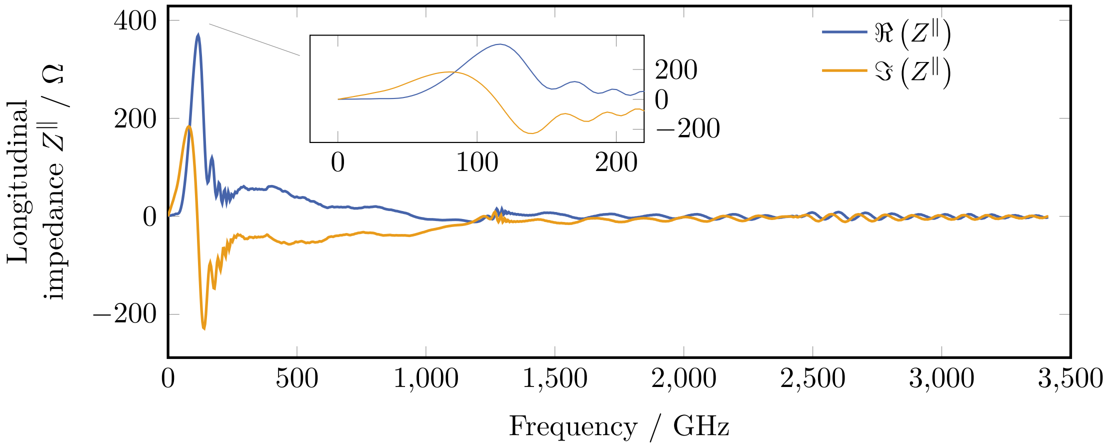

Figure 5.1. Longitudinal impedance. Example of a longitudinal impedance of a corrugated structure (real and imaginary parts in blue and orange, respectively). The ringing is based on the limited mesh cell resolution of the simulation and the finite structure length. The zoomed box shows the impedance around the resonance frequency. The dimensions of the corrugations are: half plate distance b =5 mm, corrugation depth h =125 µm, periodic length L=40 µm, duty cycle L/g =2, and structure length s =10 cm.

of the resonance width (full width at half maximum (FWHM)) Δf_{FWHM} via $Q \overset{def.}{=} \frac{f_{\mathrm{res}}}{f_{\mathrm{FWHM}}}$. These three parameters are sufficient to characterize the corrugated plate impedance fully. The Equation (5.1) can be rewritten as:

$$Z^{\parallel}(f) = \frac{Z_0}{1 + Q^2\left(\frac{f_{\mathrm{res}}}{f} - \frac{f}{f_{\mathrm{res}}}\right)^2}\left[1 - i \cdot Q\left(\frac{f_{\mathrm{res}}}{f} - \frac{f}{f_{\mathrm{res}}}\right)\right] \tag{5.2}$$

with its real part

$$\Re\left(Z^{\parallel}(f)\right) = \frac{Z_0}{1 + Q^2\left(\frac{f_{\mathrm{res}}}{f} - \frac{f}{f_{\mathrm{res}}}\right)^2} \tag{5.3}$$

and imaginary part

$$\Im\left(Z^{\parallel}(f)\right) = -\Re\left(Z^{\parallel}(f)\right)\left[Q\left(\frac{f_{\mathrm{res}}}{f} - \frac{f}{f_{\mathrm{res}}}\right)\right] = -\frac{\mathrm{d}}{\mathrm{d}f}\Re\left(Z^{\parallel}(f)\right) \quad . \tag{5.4}$$

Note that the resonator model has the same relation between the real and imaginary parts as the theoretical equation, where the different sign of the imaginary part is caused by the convention of the causality in the time domain.

For the determination of the impedance parameters from the CST simulation results, a fit with the resonator model for the real part of the impedance is used. Based on that, the imaginary part is calculated from the fit parameters. In Figure 5.2 the result of this fit shows a good agreement with the simulated impedance.

However, a significant second peak, independent of the periodic ringing, occurs for some corrugation parameter settings (see Figure 5.3) and is an artifact of the limited meshing in the simulation tool. This side peak must be addressed within the fit. Otherwise, the resonance frequency and peak width of the main peak cannot be determined precisely. In those cases, the impedance is fitted by the superposition of two individual resonators,

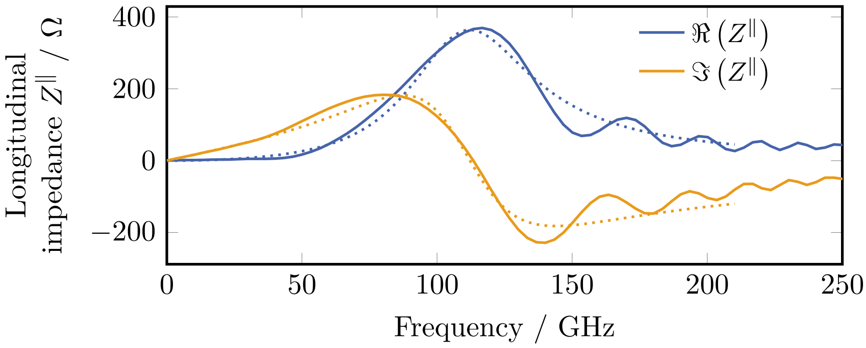

Figure 5.2. Impedance resonator fit. Fitting (dotted lines) of the simulated (dashed lines) corrugated plate impedance with a broadband complex resonator model.

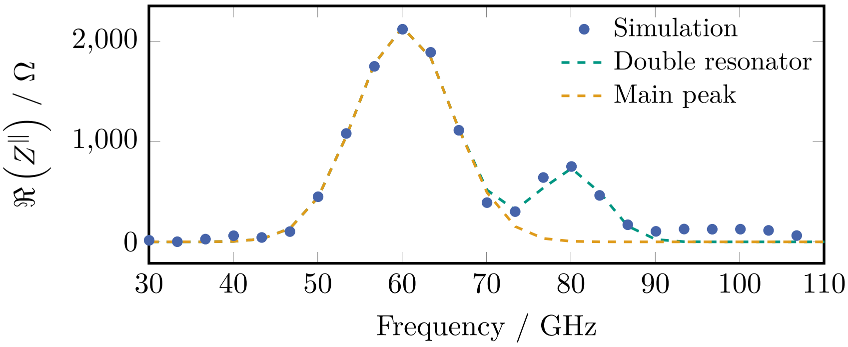

Figure 5.3. Double resonator model. A superposition of two resonator functions is used to determine the impedance parameters properly. For further studies, only the impedance parameters of the main peak are of interest. The dimensions of the corrugations are: half plate distance b =5 mm, corrugation depth h =300 µm, periodic length L=200 µm, duty cycle L/g =2, and structure length s =20 cm (Will also be presented in [Mai]).

described in detail in Appendix C. To decide whether a single resonator or a double resonator fits the corrugated plate impedance more accurately, the quality of the two fittings is quantified by the χ^2 parameter

$$\chi^2 = \frac{1}{N_{\mathrm{DoF}}} \sum_{i=1}^{N} \frac{\left(y[i] - f(x[i])\right)^2}{f(x[i])} \quad , \tag{5.5}$$

in which N_{DoF} is the Degree of Freedom (DoF). The DoF is defined as the number of data points of the simulated impedance minus the number of fit parameters. Thereby, the fit function with χ^2 closer to 1 is used. Furthermore, y are the simulated impedance values, and $f(x)$ is the fitting function evaluated at the corresponding frequency. If not mentioned otherwise, only the impedance parameters of the dominant peak are considered for the impedance studies as a function of the different corrugation parameters.

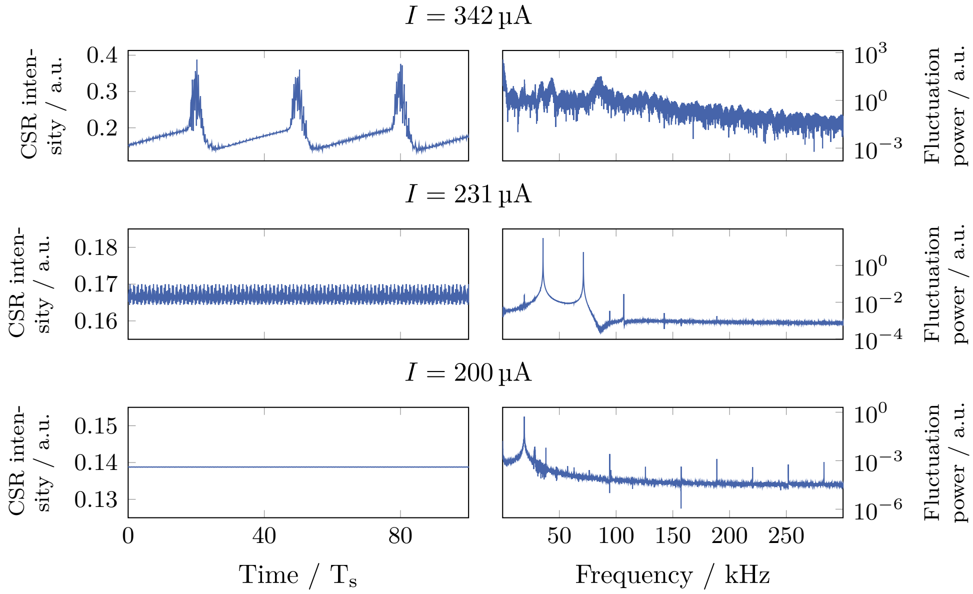

Figure 5.4. Simulated CSR intensity and fluctuation power. For different bunch currents and micro-bunching instability regimes, the temporal development of the CSR intensity over several synchrotron periods T_s (left side) and its Fourier transform (right side) is shown. This fluctuation power indicates the different dominant fluctuation frequencies of the instability that arise in the different regimes.

5.2. Beam Dynamics

For the beam dynamics studies throughout this thesis, the Inovesa simulations of the longitudinal phase space density Ψ and the temporal evolution of the derived parameters longitudinal bunch profile ϱ, CSR intensity, and CSR spectrum are investigated.
Depending on the bunch current, the temporal development of the CSR intensity differs due to the different regimes of the micro-bunching instability, which is shown on the left side of Figure 5.4. For the characterization of the micro-bunching instability, the temporal changes of the emitted CSR intensity and the dominant frequencies of the fluctuations are of interest. The so-called fluctuation power is the Fourier transform of the CSR intensity over time. The intensity is computed for 1000 timesteps per T_s over the simulation time range of 350 T_s. The fast Fourier transform (FFT), which is described in Appendix B, is optimized for the number of data points $N_{\mathrm{data}} = 2^x$. To reach the next integer value of 2^5, the so-called zero-padding is used to extend the number of data points (explained in Appendix B). The fluctuation power is shown in the right part of Figure 5.4 for different currents and micro-bunching regimes. The relevant regimes - from bottom to top in Figure 5.4 - are:

- In the **no bursting** regime, no temporal fluctuation of the CSR occurs
- In the **bursting regime**, fast sinusoidal fluctuation of the CSR occur
- In the **slow outburst regime**, sawtooth-like slow outbursts of intense CSR appear in addition to the sinusoidal fluctuation.

Depending on the different instability regimes, dominant fluctuation frequencies in different frequency ranges arise.
The changes in the power fluctuation and the transition between the different regimes can be visualized in a spectrogram. Figure 5.5 shows the fluctuation power as a function of the bunch current. In these spectrograms, the bunch currents, which mark a change in the

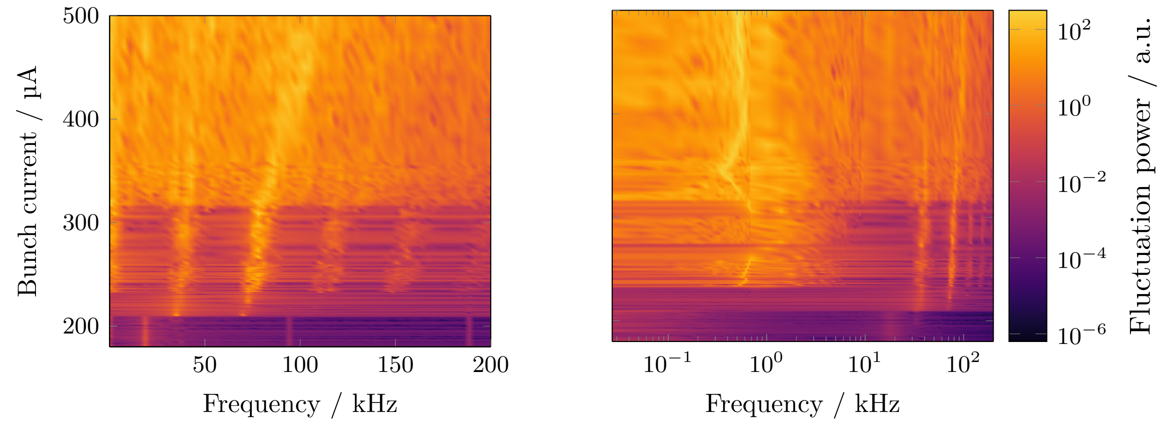

(a) **(b)**

Figure 5.5. **Spectrograms** show the color-coded Fourier transform of the emitted CSR intensity as a function of the bunch current. The changes in fluctuation power indicate changes in the underlying beam dynamics. (a) and (b) show the same fluctuation power for linear and logarithmic frequency axis scaling.

fluctuation and indicate a change in the underlying micro-bunching instability, can be seen easily. The linear frequency axis (Figure 5.5a) points out the current dependency of the fast intensity fluctuation. The development of the outbursts of intense CSR, taking place on a longer time scale, become more visible with a logarithmic frequency axis (Figure 5.5b).

5.2.1. Characteristic Properties of the Instability

To investigate the impact of different machine settings or additional impedances on the longitudinal beam dynamics and especially the micro-bunching instability, the characteristic properties of the instability have to be identified. The important instability parameters discussed in this thesis are the threshold current (so-called bursting threshold) and the dominant fluctuation frequency directly above the bursting threshold. For the regime of the intense sawtooth-like CSR outbursts, the additional slow bursting threshold and its corresponding repetition rate can be determined. All these parameters can be extracted from the fluctuation power over the beam current scans.

5.2.1.1. Threshold Currents

Above the bursting threshold I_{thr}, the first fluctuations of the CSR intensity occur. That is why it is an important parameter for characterizing the micro-bunching instability. Below this threshold, the emission of CSR is stable over time (see $I = 200\,\mu\text{A}$ in Figure 5.4). Therefore, it is simple to recognize the regime change by eye in the spectrogram in Figure 5.5a, but a systematic and quantitative determination is required for a quanitative analysis of the micro-bunching instability.

Going from low to higher charge one can see that every new regime is characterized by an additional significant fluctuation with a different fluctuation frequency. Because of that, the standard deviation (STD) of the CSR intensity over time is a good parameter to look at. In Figure 5.6 it is shown as an example next to the corresponding spectrogram. A significant kink in the STD of the CSR intensity is visible at the thresholds of the two regimes, which are indicated by the horizontal dashed lines in the spectrogram. Consequently, the currents of the two first kinks are defined as the bursting threshold current I_{thr} and the slow outburst threshold current $I_{\text{thr;slow}}$.

However, the examples in this chapter show the spectrogram and STD of the CSR intensity

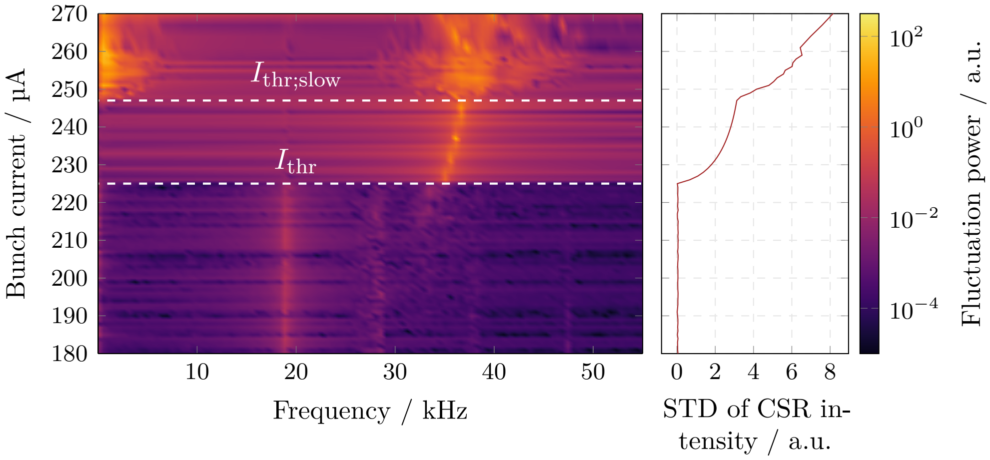

Figure 5.6. Threshold current determination. The left part shows a zoomed part of the spectrogram in Figure 5.5 around the bursting and slow outburst threshold currents (dashed lines). The right part shows the STD of the CSR intensity as a function of the current. The kinks indicate the threshold currents.

for a reference setting without an additional corrugated structure impedance. In Chapter 7, it is shown that the additional impedance affects the instability parameters and can lead to small changes in the shape of the spectrogram and the current dependency of the STD. Therefore, the STD is not suitable for determining the thresholds for all impedance scan settings, and a more robust method for the variation of the spectrogram needs to be found. The fluctuation power at the bursting frequency f_{burst} has been found as a variable derived from the CSR intensity that meets this requirements [Mai22b]. The determination of f_{burst} is explained in detail in the next section. Figure 5.7 shows that - for the same reason as the STD of the CSR intensity - the fluctuation power at f_{burst} has a clear kink at I_{thr}. Due to the broadening of the dominant frequency range around f_{burst} above the slow outburst threshold current, an abrupt drop of the maximal fluctuation power in this frequency range is notable, which is used for the automatic determination of $I_{\text{thr;slow}}$.

5.2.1.2. Bursting Frequency (“*Finger*” Frequency)

The bursting frequency f_{burst} means the frequency of the dominant fluctuation power directly above the bursting threshold current. Thus, this is the frequency of fast CSR intensity fluctuation due to the micro-bunching instability. Since it marks the tip of the finger-like structure in the spectrogram and is defined by the rotation of the finger-like substructures of the charge distribution in the longitudinal phase space, it is also referred to as “*finger*” frequency. Since the synchrotron frequency f_s corresponds to the rotation frequency of the whole phase space, the bursting frequency has to be larger than f_s. To avoid a false identification of the synchrotron frequency as f_{burst}, a frequency range between 30 kHz and 60 kHz is used for the determination. The lower frequency limit is chosen to be larger than f_s for all simulation parameter settings. The upper limit is set to avoid the false identification of higher orders of the bursting frequency. In Figure 5.8, it is obvious that the resolution of the FFT of the pure CSR intensity data is not good enough to identify the peak properly. A higher data point density in the frequency domain would require a CSR intensity for over a longer time range. In the simulation, the time range scales with the simulation time. Since, in the frequency domain, only the peak position should be determined precisely, this can be achieved with a zero-padding, so that the simulation does not need to be increased further. The additional zero-padding ($N_{\text{data}} = 2^{17}$) increases the data point density but increases the *sinc*-artefacts of the discrete Fourier transform (DFT).

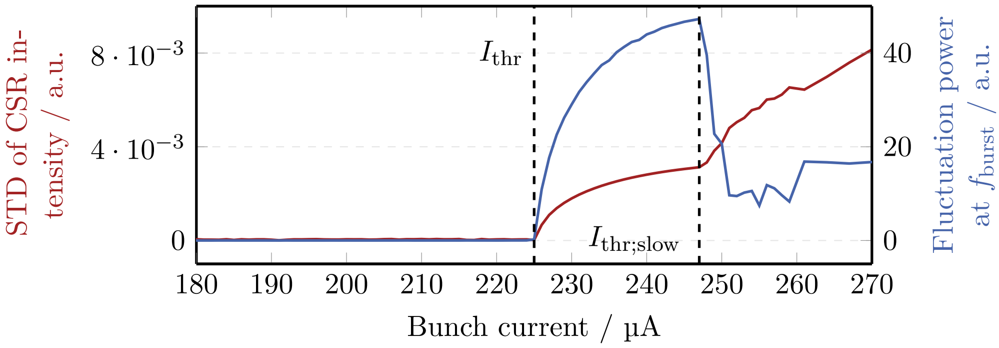

Figure 5.7. Threshold current determination. The kinks in the STD of the CSR intensity determine the bursting and slow outburst threshold current (dashed lines). However, this parameter is not robust enough to determine these thresholds for studies with additional corrugated structure impedances. Therefore the kink and drop in the fluctuation power at the bursting frequency is used.

This spectral leackage is based on the fact that the DFT only operates on the data point (and not from $-\infty$ to $+\infty$), so that it has a implicit rectangular function, causing the *sinc*-contribution. These ripples are also suppressed here by a moving average with a 20 Hz window width to avoid the misidentification of the ripples as side peaks. The optimized reconstruction is shown in Figure 5.8, too. A simple maximum finder is applied to identify f_{burst} as the frequency of the dominant fluctuation power. Instead of methods, that do not need the zero-padding to reach the required resolution, this method is used to have the same procedure as with experimental data like in [61].

The width σ_{burst} of the spectral peak in Figure 5.8 around f_{burst} corresponds to the frequencies contributing to the CSR time profile. Therefore, it is a measure of the temporal stability of the CSR power and the micro-bunching instability regime. Since a single narrow-band peak of the fluctuation power only exists in a current range directly above I_{thr}, it is not suitable to determine the spectral bursting width as the FWHM of the peak. Instead, the width is calculated via the second statistical moment

$$\text{Var} = \sigma^2 = \frac{\sum_{i=1}^{N} (x_\text{i} - \mu)^2 \cdot f(x_\text{i})}{\sum_{i=1}^{N} f(x_\text{i})} \quad .$$

Thereby, x_i is the frequency, $f(x_\text{i})$ is the fluctuation power and μ is the bursting frequency f_{burst}. For the calculation, a frequency window of $f_{\text{burst}} - 5\,\text{kHz} < f < f_{\text{burst}} + 5\,\text{kHz}$ is used, so only the frequency range of the bursting is taken into account. Since the frequency steps of the fluctuation power are equidistant, the number of data points (N) is independent of f_{burst} and the additional impedance.

5.2.1.3. Slow Outburst Frequency (Repetition Rate)

The repetition rate of the sawtooth-like outburst is referred to as the slow outburst frequency $f_{\text{burst;slow}}$, identified directly above the slow outburst threshold current. These periodic outbursts of the CSR intensity stretch across several synchrotron periods T_s. Consequently, its repetition frequency always has to be smaller than the synchrotron frequency and is in a non-overlapping frequency range with f_{burst} and is determined independently. Although the 50 Hz noise signal of the utility frequency does not occur in the simulation, the lower limit of the investigated frequency range is set at 75 Hz to have the same procedure as with experimental data like in [61]. In contrast to the case with the bursting frequency,

the synchrotron frequency f_s defines the upper limit here. It is set to $0.3\,\mathrm{f_s}$ to avoid misidentifications. For the determination of $f_\mathrm{burst;slow}$, the same method as for f_burst within the respective frequency range is used.
M. Brosi [61] has shown that the repetition rate is directly related to the time the energy spread takes to shrink from its maximal to minimal value. Depending on the exact machine settings, the slow outburst frequency is below or in the order of 1 kHz for the low-α_c mode at the KARA storage ring.

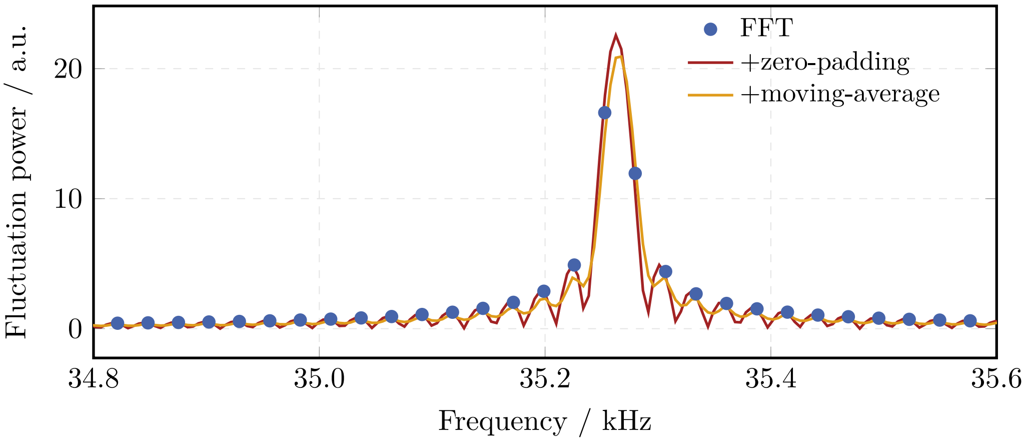

Figure 5.8. **Bursting frequency.** A section of the Fourier transform of the CSR intensity around the bursting frequency. The additional zero-padding of the CSR intensity (red) increases the data point density, and the moving average on the fluctuation power (orange) with a window width of 20 Hz reduces the *sinc*-artefacts of the DFT. A simple maximum finder determines the bursting frequency.

5.2.2. Number and Size of Substructures

The rotation of the substructures in the charge distribution of the longitudinal phase space and the resulting periodic change of the substructures in the bunch profile is the underlying mechanism of the sinusoidal fluctuation of the CSR intensity in the micro-bunching instability. Consequently, the number of the phase space substructures determine the bursting frequency f_burst and are an important parameter for the beam dynamics description. Since the substructures are only present above the bursting threshold, a current clearly above I_thr is chosen to count the substructures. For a comparison of different machine settings, a current 100 µA above the respective I_thr is used, which also is clearly above $I_\mathrm{thr;slow}$.
Theoretically, the number of substructures can be determined at any simulation step. However, the intensity of the substructures drastically varies over one outburst period. Therefore, three characteristic points during that cycle have been chosen: the simulation steps with the shortest bunch length, with the longest bunch length, and with the highest CSR intensity. A simple maximum or minimum finder finds all three time steps in the simulation data after a moving average has reduced the noise.
The number of substructures is extracted from the *relative* phase space density at these time steps, which is shown in Figure 5.9a and described in Section 4.2. For certain machine and beam settings, this number can differ for the inner and outer parts of the longitudinal phase space, which is why it is calculated for these two regions individually. For this purpose, two circles (dashed and solid line in Figure 5.9a) are defined such that they form the smallest and largest ring in the phase space along which the respective maximum relative phase space density is at least 30 % of the maximal relative density of the whole

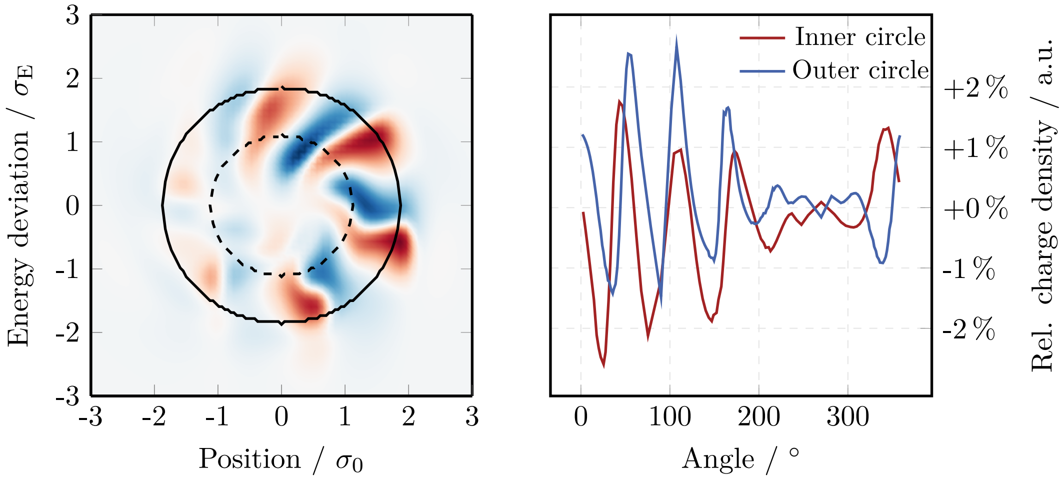

(a) **(b)**

Figure 5.9. Number of substructures. (a) The relative phase space from Figure 4.5b is shown here with dashed and solid circles indicating the inner and outer parts of the phase space. In (b), the relative phase space density along the two circles as a function of the angle is used to count the substructures by counting the sign changes.

phase space. The threshold has no physical meaning but has proven to be both accurate in separating the two rings and regions of the phase space and robust again variation between different machine and phase space settings. The phase space density along the two circles is shown in Figure 5.9b, where the angle rotates clockwise with the arbitrary starting angle at $\Psi(z = 0, E = \text{maximal energy deviation}, t)$ (top of the respective circle). Each substructure consists of a positive and negative part deviating from the temporal averaged phase space density. Therefore, the number of substructures is determined by counting the sign changes of relative phase space density. The number of substructures for the machine setting or simulation step is given by $\bar{N} = \frac{N_{\text{inner}}+N_{\text{outer}}}{2}$. Consequently, $\bar{N}$ can be either an integer or a half-integer value. The concept of a different number of substructures in the inner and outer part of the longitudinal phase space, has been mentioned and shortly discussed in the doctoral theses by P. Schönfeldt [59] and M. Brosi [61] with regard to the ratio between the synchrotron frequency and f_{burst}. The determination of number of substructures $\bar{N}$ by counting the sign changes has been cross-checked with the ratio $\frac{f_{\text{burst}}}{f_s}$. This is related to the numbers of fingers by $\bar{N}_{\text{finger}} = \frac{f_{\text{thr}}}{f_s} + 1$ [61], which has been verified for the investigated range of the machine and bunch settings at the KARA storage ring.

The size of the substructures is extracted from the longitudinal bunch profile. Analog to the longitudinal phase space, the temporal averaged bunch profile is subtracted to make the imprinted substructures ($\mathcal{O}(1\,\%)$) more visible (see Figure 5.10). This method is inspired by T. Boltz *et al.* [101], who used a similar approach to identify cluster centers in the bunch profile. The Fourier transform of this relative substructure bunch profile $\Delta\varrho$ shows the dominant frequency of its spectrum f_{sub} (bottom of Figure 5.10). This frequencies is a measure of the size of the substructures - consisting of a positive and negative deviation from the time-averaged profile - and describes the period size of the substructure. In opposite to the FWHM or 1σ bunch length, the size of the substructures describes its full longitudinal extend. Consequently, this dominant substructure frequency might correlate to the bunch length. For the systematic studies of bunch current, machine settings, or impedance scans, $\Delta\varrho$ and its spectrum is taken from that simulation time step at which the maximum amplitude of $\Delta\varrho$ is the largest.

For the choice of the impedance resonance frequency of the additional impedance, this

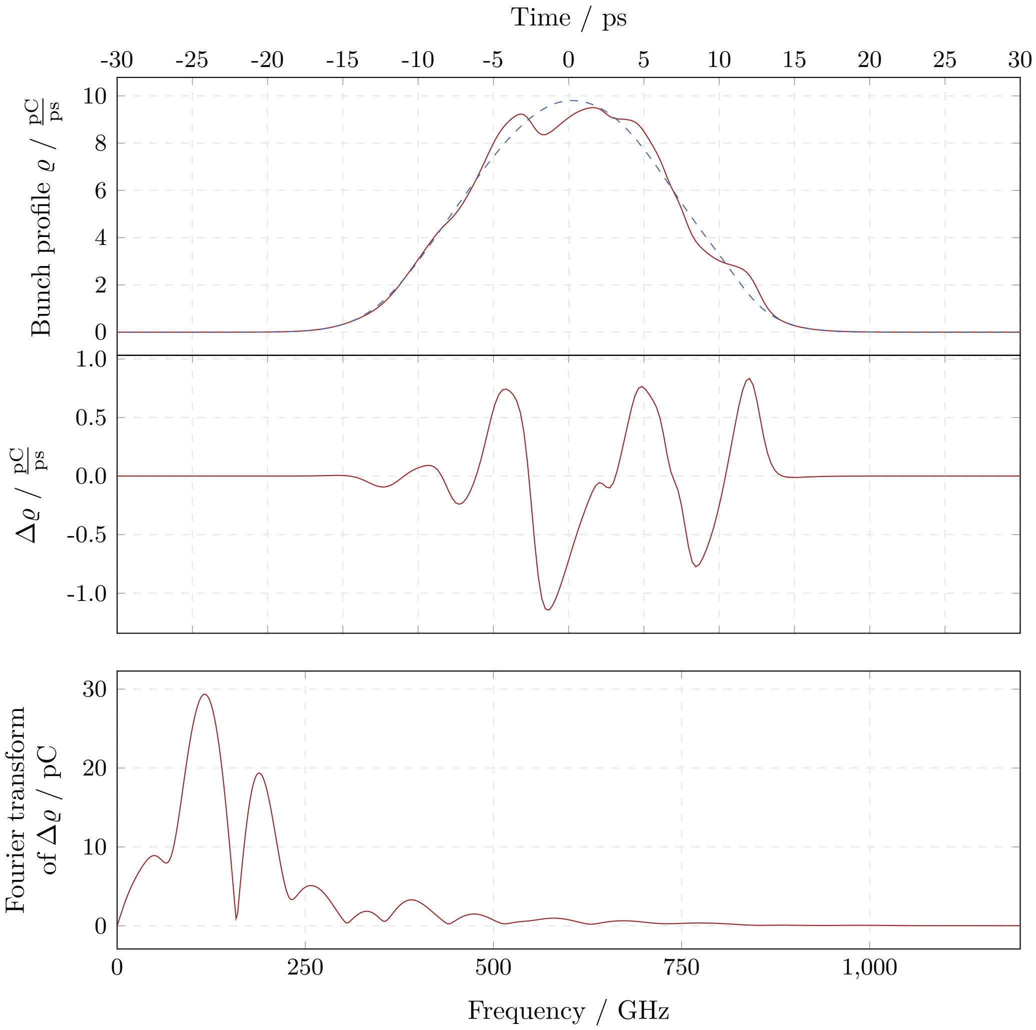

Figure 5.10. Substructure bunch profile and spectrum. The substructures in the longitudinal bunch profile for a bunch current in the bursting regime (top) become more visible and better investigable after subtracting the temporal average profile (blue dashed), shown in the center. The Fourier transform of the relative substructure bunch profile $\Delta\varrho$ (bottom) indicates the dominant frequencies of its spectrum (Adapted version will also be presented in [Mai]).

frequency range around f_{sub} is interesting, since the substructures and their size are fundamental parameters of the micro-bunching instability. That is one of the reasons why the frequency range from 50 GHz to 200 GHz is investigated for the impedance resonance frequency. The following Chapters will show that a structure with its resonance frequency in this range is manufacturable and has a significant contribution to the overall impedance in the KARA storage ring.

6. Impedance Studies

Before the impact of a corrugated structure impedance on the longitudinal beam dynamics can be studied, it is crucial to know how the impedance of the corrugated plate can be described as a function of the frequency. In the first section, the minimal plate distance between the two corrugated plates is estimated by a study of the beam lifetime while changing the gap of a vertical scraper in the KARA storage ring. Afterward, the impact of the different corrugation parameters on the impedance is investigated systematically in simulations. Based on this, the optimized corrugation parameters to create a certain impedance can be found by introducing a new corrugation impedance parameter, which is shown in the last section of this chapter.

6.1. Scraper Experiment

In this experiment at the KARA storage ring, the minimal plate distance b without a drastic particle loss is elaborated so that this value can be used for impedance simulations and studies. For this purpose, the beam lifetime for different gaps of a vertical scraper, which is placed upstream of the SUL wiggler (s=53.845 m), was measured. A significant drop in the lifetime indicates blocking the outer part of the electron beam and, therefore, determines the minimal possible distance of the corrugated plates. For this measurement, the well understood seetings of the KARA fill *f05135* (listed in Appendix D) with normal and low-α_c are used at the beam energy E=1.3 GeV. V. Judin [102] has shown that a reduction of the scraper gap affects the longitudinal beam dynamics and the CSR emission. Since, in comparison with the corrugated plate, the impedance of a scraper is only significant for lower frequencies (because of the larger dimensions), the impact on the longitudinal beam dynamics is significantly smaller, so that a study and measurement of the beam dynamics for different scraper impedances is not a part of this thesis.

In Figure 6.1, the vertical betatron-function β_y is shown for the two momentum compaction settings used. As the grey areas indicate, both the scraper and the planned chamber are located in straight sections with small and comparable values of β_y. However, the different beam size caused by the beta-function can be corrected afterwards. These experiments use one bunch train with a current of about 50 mA.

The multi-bunch mode has been used to reduce the jitter of the measured beam current and, therefore, to improve the determination of the beam lifetime. All the bunches in the train are equally filled so that a loss in the total current corresponds directly to the losses in the single bunch current. At KARA, the beam lifetime is determined from the beam current and is defined by:

$$\frac{1}{\tau} = -\frac{1}{N_\mathrm{e}}\frac{\mathrm{d}N_\mathrm{e}}{\mathrm{d}t} = -\frac{1}{I_\mathrm{beam}}\frac{\mathrm{d}I_\mathrm{beam}}{\mathrm{d}t} \quad . \tag{6.1}$$

In Figure 6.2, the measured lifetime is shown for the time range of the normal-α_c experiment. In the time range from approximately 10 min to 30 min, the scraper has been closed step-wise.

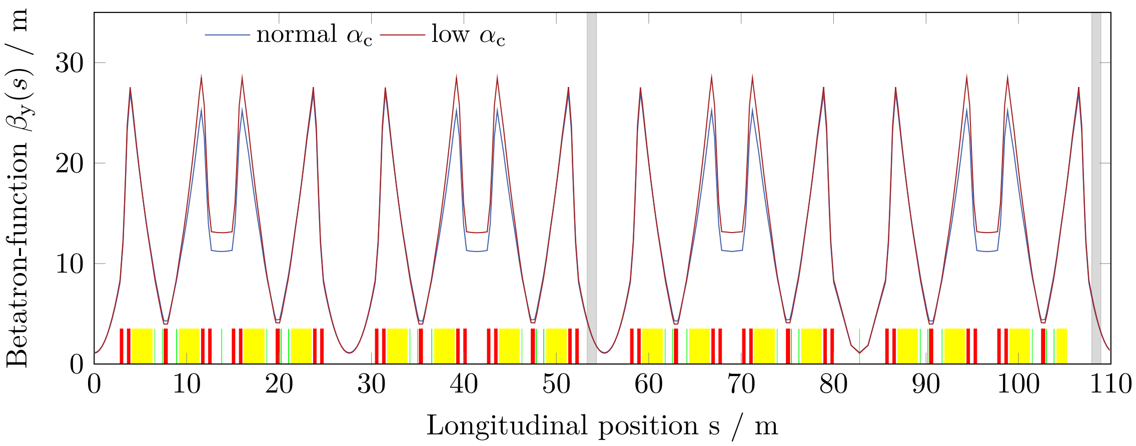

Figure 6.1. **Vertical betatron-function** β_y along the KARA ring circumference for two α_c settings. The grey areas indicate the position of the scraper and the planned location of the versatile impedance manipulation chamber. At the bottom, the location of the dipole (yellow), quadrupole (red), and sextupole (green) magnets are shown.

Table 6.1. **Scraper and corrugated plate gap.**

Parameter	**normal-α_c**	**low-α_c**
y_{top} / mm	6.5	7.0
y_{bottom}/ mm	-1.0	0.0
$\Delta y_{scraper}$ / mm	7.5	7.0
$\beta_{scraper}$ / m	3.409	3.473
$\beta_{corr.}$ / m	5.589	5.752
$\sqrt{\beta_{corr.}/\beta_{scraper}}$	1.280	1.287
$\boldsymbol{\Delta y_{corr.}}$ **/ mm**	**9.6**	**9.0**

There is a position asymmetry between the top and bottom scrapers, so the center of the electron beam does not match the zero position of the two vertical scrapers. Consequently, the two scrapers are moved and investigated individually.

All the time steps in which both scrapers are removed completely are used to determine the undisturbed lifetime $\tau(t)$ as a function of the time. The current changes are nearly linear at the KARA storage ring during the experiment. A fit with a polynomial of the second order is used to determine the lifetime over time. The second-order term considers deviations from the linear behavior, and higher orders do not improve the fit. This fit is also shown in Figure 6.2. It can be seen that the lifetime is reduced due to the closing of the gap, even though the lifetime would increase with a completely removed scraper during that time. Consequently, the overlap of these two opposite tendencies needs to be taken into account to identify the lifetime change depending on the scraper position. To separate these effects, the scraper was removed completely after each insertion, which generates additional time steps with removed scrapers so that the fitting of the undisturbed lifetime can be improved significantly. To remove the jitter of the measured current loss and improve the lifetime statistics, each scraper position has been holding for about 60 s.

In Figure F.2, the change in the lifetime $\Delta\tau$ due to the scattering with the scraper and the corresponding scraper position is shown. The value of $\Delta\tau$ is determined by subtracting the fitted undisturbed lifetime from the calculated lifetime to make the impact of the scraper position on the beam loss more visible. Since the lifetime is reduced for the low-α_c mode,

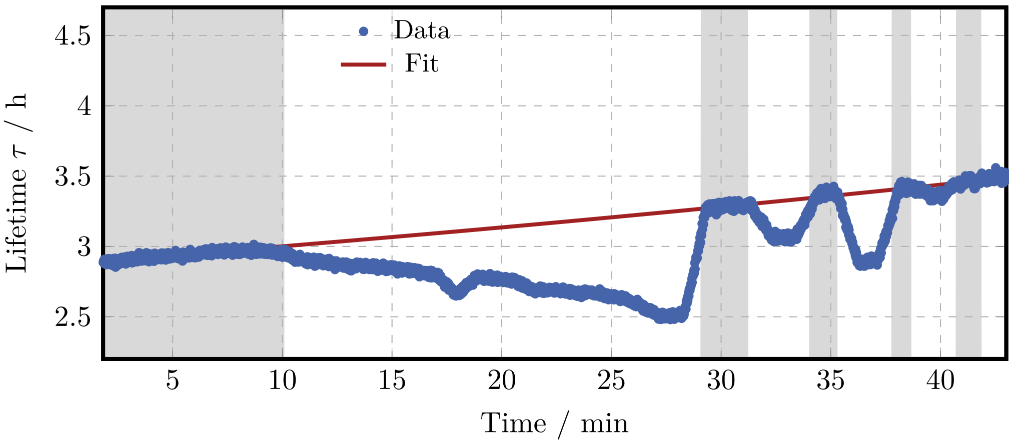

Figure 6.2. Beam lifetime at KARA while changing the scraper position for the normal-α_c experiment. The fit function only takes timesteps with a completely removed scraper (grey) into account.

not only the lifetime change is reduced, but the fluctuation of $\Delta\tau$ is increased drastically. However, for both α_c modes but especially for normal-α_c, a significant reduction of the beam lifetime can be recognized for a small scraper gap since the outer parts of the beam are stripped off.

The dependency on the scraper position is even more evident in Figure 6.3. The time-averaged lifetime change $\overline{\Delta\tau}$ for a constant scraper position is shown as a function of the scraper position. The $\overline{\Delta\tau}$ uncertainties result from the temporal jitter with a constant scraper position during the time span of the experiment. In the normal-α_c mode, the significant lifetime reduction can be noticed if the position of the top scraper is smaller than $y_{\text{top}} = 6.5\,\text{mm}$ or the position of the bottom scraper is smaller than $y_{\text{bottom}} = -1.0\,\text{mm}$, which results in a total gap height $\Delta y_{\text{scraper}} = 7.5\,\text{mm}$. However, the chamber of the corrugated plate will be placed in a different place than the vertical scraper. Therefore, the differences in the optical function and the resulting transverse beam size must be considered. Since the vertical dispersion D is negligible for both operation modes and under the assumption of a constant emittance ϵ (based on Equation (2.16)), the beam size only depends on the vertical β_y-function:

$$\frac{\sigma_y}{\sqrt{\beta_y}} = const. \quad \rightarrow \quad \sigma_{y,2} = \sigma_{y,1}\sqrt{\frac{\beta_{y,2}}{\beta_{y,1}}} \quad .$$

To estimate the maximal beam size at the corrugated structure, the maximal value of the vertical betatron-function β_y in the area of the chamber (grey area in Figure 6.1) is used. This Figure also shows that the vertical β_y does not differ drastically between the two operation modes at the planned location of the impedance chamber. Therefore, the change of bunch size and the bunch size itself is nearly independent of the α_c at the planned position of the versatile impedance manipulation chamber. All the parameters are summerized in Table 6.1. The difference of the β_y means that the beam size at the planned chamber position is 28 % larger than at the scraper position. Based on the experiment and by taking this change of the beam size along the storage ring into account, it can be seen that the gap size of 10 mm is reasonable to avoid significant beam losses due to the reduced aperture. For this reason, the minimal studied half plate width b is set as $b = 5\,\text{mm}$. If it is not mentioned otherwise, the simulation results in the following sections are based on this minimal plate distance. The impact of the plate distance on the impedance will be discussed later in Section 8.1.4.

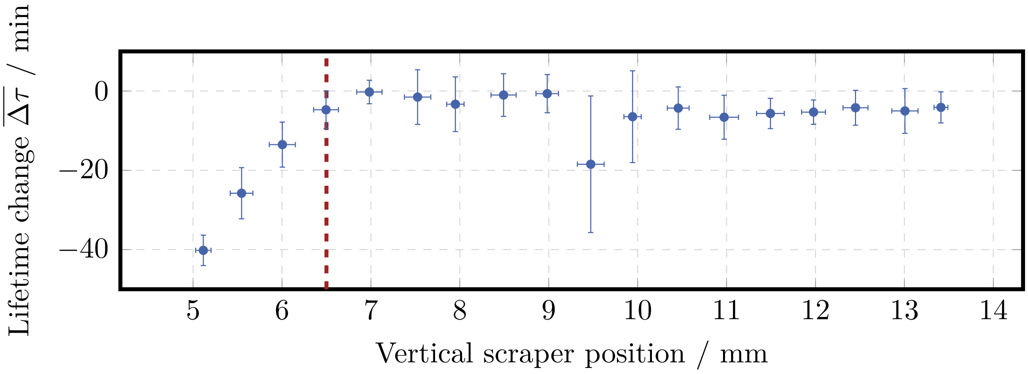

(a) Top scraper at normal-α_c

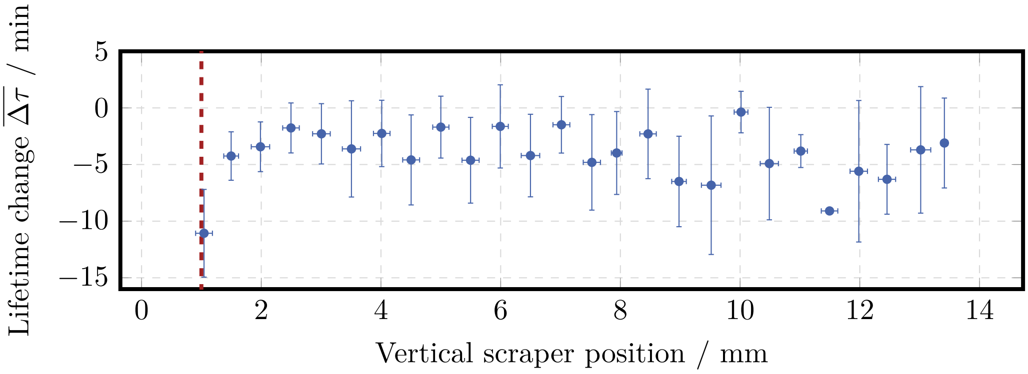

(b) Bottom scraper at normal-α_c

Figure 6.3. Lifetime reduction by vertical scraper position. For each vertical scraper position, the lifetime reduction is averaged over the entire time at this position. The vertical red dashed lines indicate the outermost scraper postion, which cause a significant lifetime reduction. The vertical uncertainties are based on the jitter of the calculated lifetime during a fixed scraper postion setup.

6.2. Corrugation Parameters Scan

For manufacturing the optimal corrugated structure for the manipulation of the microbunching instability, it is crucial to understand the impact of all corrugation parameters - namely the corrugation depth h, the periodic length L, the longitudinal gap g, and the duty cycle L/g derived from the last two - on the impedance of the structure. Therefore, the influence on the resonance frequency f_{res}, shunt impedance Z_0, and quality factor Q - in the following referred to as the impedance parameters - are studied, where the corrugation parameter dependencies on the first one can be compared with the theoretical prediction of Equation (2.50). The following sections show that a certain resonance frequency is not limited to one combination of corrugation parameters but can be realized by a variety of combinations, as indicated by Equation (2.50). Thus, L and L/g are used to find the optimal setting.

6.2.1. Impact on Impedance Resonance Frequency

As mentioned previously, Equation (2.50) by Ng *et al.* describes the impedance of a cylindrical corrugated structure. However, for the KARA storage ring, a geometry with two flat parallel corrugated plates is planned. Consequently, the theoretical prediction can only be used as a reference. However, the dependency of f_{res} on the corrugation parameters must be determined not only due to the different geometry but also for the parameter range which does not meet the validity criterion ($L \lesssim h$) of the theoretical formula.

In Figure 6.4 the real part of the simulated corrugated plate impedance is shown as a scan for the different corrugation parameters, whereby all the other corrugation parameters as well as the plate distance b=5 mm and the structure length s=10 cm are fixed. For the scan of the periodic length, this fixed s results in a variation of the number of corrugations N_{corr} that is inversely proportional to L. It can be seen clearly that L/g, which is equivalent to a change of the longitudinal gap g, and h do not only affect one but all three impedance parameters.

The dependency of f_{res} on the two affecting corrugation parameters h and L/g is presented in Figure 6.5. The red area in Figure 6.5b indicates the corrugation parameter range, where the criterion for the validity of Equation (2.50) ($L \lesssim h$) is not fulfilled. However, the validity range is only relevant for the comparison with the theoretical model rather than for studying the impedance. It has been found that the power law $f(x) = A \cdot x^{\rho}$, which seems to be an appropriate model to express the fitting results shown in Figure 6.5 not only matches the theoretical prediction but also shows the best agreement with the data points. In the following, for the discussion of the f_{res} dependence on a certain corrugation parameter, the index of A and ρ corresponds to this respective corrugation parameter. This means that these two power laws give empirical relations between the f_{res} and L/g and the f_{res} and h respectively. The theoretical dependency and the power law fit are shown in the Figure, too. For the corrugation parameters settings in Figures 6.5a and 6.5b the exponent of the power law is determined as $\rho_{\mathrm{Lg}} = (0.542 \pm 0.004)$ and $\rho_{\mathrm{h}} = (-0.684 \pm 0.002)$ respectively. The first one is in good agreement with the theoretical prediction ($\rho_{\mathrm{Lg,th.}} = 0.5$). In contrast to all the other corrugation parameters, the different duty cycles can be separated into two structure types that are independent of the plate geometry:

- $L/g \geq 2$: a plate with periodic deepenings and
- $L/g<2$: a plate with periodic elevations.

Despite the differences in the shape characteristics of the corrugated structure, the theoretical prediction of f_{res} is valid for the whole studied range of the duty cycle.

For the scan of the corrugation depth, the exponent ρ turns out to be significantly larger compared to the theoretical prediction ($\rho_{\mathrm{h,th.}} = -0.5$) by Ng *et al.*. The fitting parameters do not change noteworthly by only taking the settings with $L \lesssim h$ for the fit. Consequently, the slight deviation of ρ is caused by the different structure. Therefore, the formula can only estimate the resonance frequency of a pair of flat parallel corrugated plates. Moreover, due to the non-cylindrical shape, the theoretical model underestimates the amplitude A_h. Thus, the resonance frequency is overestimated for shallow corrugations and underestimated for deep corrugations by the theoretical prediction as can be seen in Figure 6.5b.

During the study of the agreement between the model and simulation results, it must also be borne in mind that the theoretical model takes only the first order of the azimuthal multipole development of the impedance into account. Regardless, a closer look at the higher-order azimuthal modes makes little sense due to parallel plate geometry. Nevertheless, the good agreement between the simulated f_res and the theoretical prediction not only shows certain robustness of the resonance frequency concerning the structure geometry but also verifies the CST simulations and, therefore, justifies the simplifications used here (described in Section 4.1). Based on this proved corrugation parameter dependency of f_res, the simulation-determined parameters Z_0 and Q, which cannot be predicted theoretically, can be trusted.

Since the resonance frequency is affected by both h and L/g, the power law exponent ρ depends on the respective other corrugation parameter, which is shown in Table 6.2. The uncertainties are based on the accuracy of the exponential fit. There, it can be seen that ρ_h does not have a clear tendency but fluctuates significantly over L/g - independent of the structure type. Still, the absolute value is permanently larger than the theoretical prediction in this parameter range. Starting from the shallow corrugations (red), ρ_{Lg} decreases slightly but clearly with the corrugations becoming deeper. So, by reaching and further penetrating the theoretical validity range, ρ_{Lg} converges towards the theoretically predicted value. This shows that the agreement with the theoretical prediction improves, and the theoretical model becomes more robust against geometrical differences for deeper corrugations. However, this is also partly based on the fact that for the shallow corrugations with the lower and broader resonance peak, the simplifications of the CST model result in more considerable inaccuracies on the simulated impedance and its resonance frequency.

Table 6.2. Resonance frequency as a function of the corrugation parameter: Power law exponent. The index of ρ indicates the scanned parameter. As in Figure 6.5, the red columns indicate the corrugation parameter range in which the validity criteria for theoretical model are not fulfilled.

(a)

h / mm	ρ_Lg	σ_ρ
75	0.540	±0.004
100	0.542	±0.004
125	0.539	±0.004
150	0.535	±0.003
175	0.530	±0.003
200	0.528	±0.003
225	0.523	±0.004
250	0.521	±0.003
275	0.516	±0.004
300	0.515	±0.003

(b)

Lg	ρ_h	σ_ρ
1.33	-0.686	±0.002
1.5	-0.641	±0.002
1.66	-0.637	±0.002
2.0	-0.643	±0.002
3.0	-0.665	±0.002
4.0	-0.684	±0.002

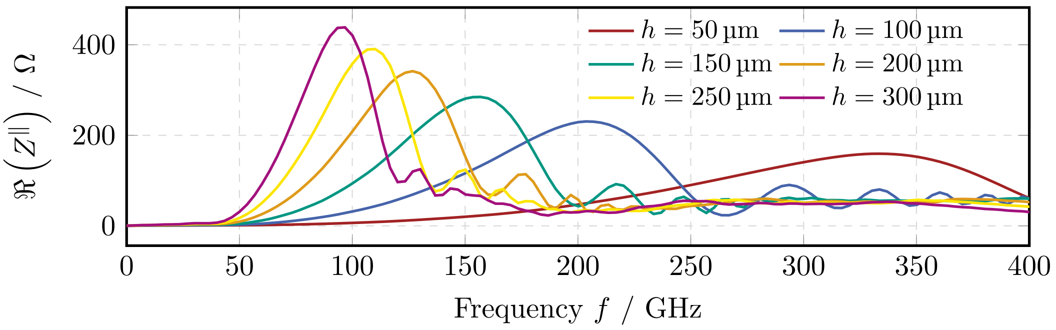

(a) Variation of h: The fixed parameters are plate distance b= 5 mm, periodic length L= 100 µm, and duty cycle L/g= 4 (Also presented in [Mai21; Mai]).

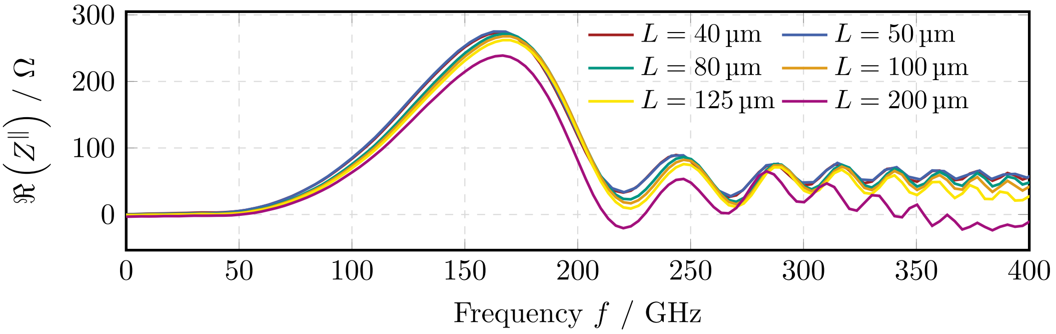

(b) Variation of L: The fixed parameters are plate distance b= 5 mm, corrugation depth h= 75 µm, and duty cycle L/g= 2. Note that the variation of L at a fixed structure length results in a variation of the number of corrugations N_{corr}. The longitudinal gap changes like the periodic length for a fixed duty cycle.

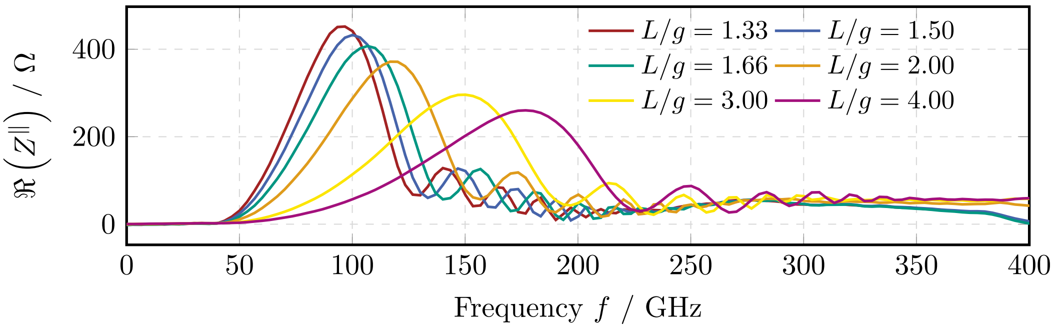

(c) Variation of L/g: The fixed parameters are plate distance b= 5 mm, periodic length L= 100 µm, and corrugation depth h= 100 µm.

Figure 6.4. Impedance scan: corrugation parameters. Real part of the longitudinal impedance $Z^{\parallel}$ for different corrugation parameters. The structure length is fixed at s=10 cm for all these scans.

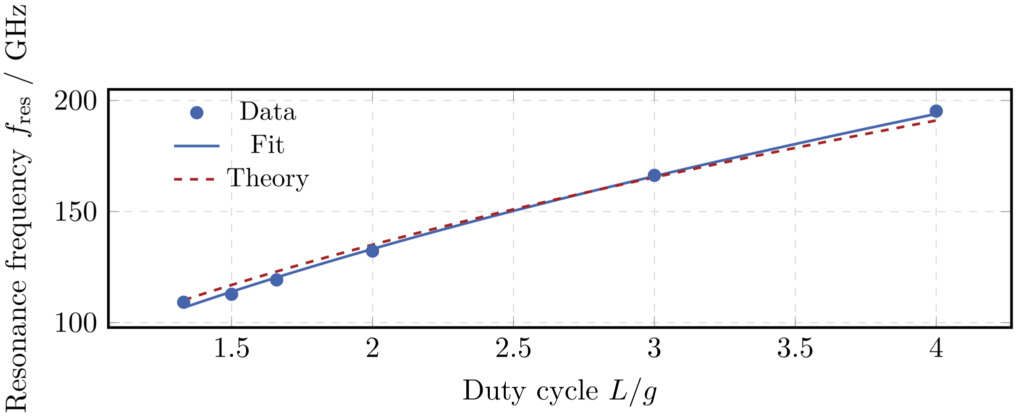

(a) Resonance frequency as a function of duty cycle

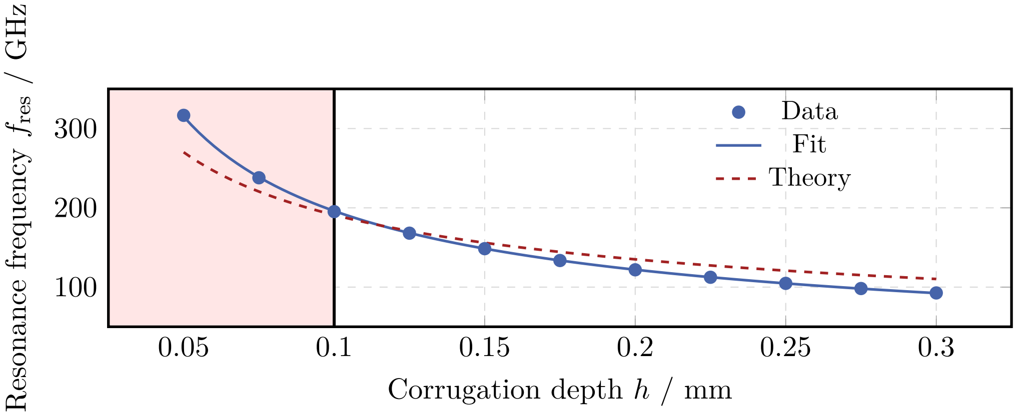

(b) Resonance frequency as a function of corrugation depth (Also presented in [Mai21; Mai]).

Figure 6.5. Resonance frequency as a function of corrugation parameters. The impedance resonance frequency for different corrugation depths h with the same fixed parameters as in Figures 6.4a and 6.4c. The theoretical prediction (red dashed) is based on Equation (2.50). The red area shows the parameter range in which the parameter assumptions for the theoretical case are not fulfilled. A power law with the function $A \cdot x^{\rho}$ is used for the fit. The deviation from the theoretical prediction is a result of the limited validity range of the equation.

6.2.2. Impact on Shunt Impedance and Quality Factor

In Figure 6.4, it can be seen that by adjusting the resonance frequency of the impedance by changing a single corrugation parameter, the height and width of the resonance peak are changed as well.

A deepening of the corrugations leads to a decrease in the resonance frequency and an increase of the shunt impedance Z_0. Furthermore, the deepening causes a narrowing of the resonance peak and consequently a higher quality factor Q. The same tendencies for all three impedance parameters are caused by a reduction of the duty cycle and the corresponding increase of the longitudinal gap g, too. In contrast to f_{res}, the shunt impedance and the quality factor are directly affected by the periodic length L of the corrugations, and this tendency can be used for the optimization of the corrugated structure in Section 6.3.

Z_0 and Q as functions of the different corrugation parameters are plotted in the subfigures of Figure 6.6. For the shunt impedance and resonance peak width, there is no theoretical prediction by Equation (2.50) with a limited validity range, so that in Figure 6.5, there are no red areas. However, according to the theory of the Smith-Purcell radiation (SPR), there is a power law to express the quality factor with the geometrical corrugation parameters (Equation (2.56)). Based on Equation (2.56), a power law ($Q(x) = C \cdot x^{\nu}$), analogous to f_{res}, is utilized to depict the dependency of Q on L/g and h. As the shunt impedance in Figure 6.4 indicates the same dependency on these parameters, the power law ($Z_0(x) = B \cdot x^{\mu}$) is also used for fitting the shunt impedance. In the following disucssions, the index of the power law parameters indicates the investigated corrugation parameter. Figures 6.6a and 6.6c show the impedance parameters Z_0 and Q in dependence on the corrugation parameters. The shown fit corresponds to the power law of Z_0. The scan of h and L/g shows, that Z_0 and Q are scaled in the same way, but inversely to f_{res}. However, the different scaling used for the two different y-axes must be considered.

For these two parameters, the exponents of the power law are:

- **h scan**: $\mu_{\text{h}} = 0.581 \pm 0.008$ and $\nu_{\text{h}} = 0.092 \pm 0.011$
- **L/g scan**: $\mu_{\text{Lg}} = -0.502 \pm 0.017$

For both scans, the simulation results for the shunt impedance are in good agreement with the power law. Thereby, it is evident that $|\mu|$ and $|\rho|$ are similar in magnitude, which entails the relationship $\mu \approx -\rho$. From the plot and the uncertainty on the fitting parameter, it is evident that the power law for the whole parameter range cannot accurately describe the quality factor. The power law relationship holds valid when L/g is smaller than 2, and therefore, for plates with periodic increases. The exponent of the power law, only taking this parameter range into account, is given by $\nu_{\text{Lg}} = -0.11 \pm 0.02$. For the plate exhibiting periodic elevations, the quality factor remains constant or insignificantly increases within its uncertainties. However, it should be noted that exponent of the quality factor power law ν does not match the dependency of the SPR quality factor Q_{THz} on the corrugation parameters. For both corrugation parameters, the absolute value of the exponent is reduced by a factor of 5 to 6 compared with the prediction of SPR. Additionally, it should be noted that ν_{Lg} has the same sign as the dependency of Z_0 on L/g, but it differs from the sign of the exponent of the SPR.

Consequently, regarding the quality factor, the shape of the SPR pulse does not relate to the causing impedance. Instead, f_{res} defines the Z_0 and Q dependency on the corrugation parameters by

$$\rho \approx -\mu \approx -5 \cdot \nu \quad .$$

The relation can only be approximated since the scaling parameters depend on the respective fixed corrugation parameters.

The dimensions of the resonance peak are affected by the periodic length L in a manner distinct from that of the longitudinal gap and corrugation depth. The main discrepancy observable in Figure 6.6b relates to the inverse scaling of the impedance parameters Z_0 and Q. This is due to the fact that reducing Z_0 also reduces the peak width. As f_{res} remains nearly constant, the quality factor increases accordingly.

Beyond this, the effect of L on the shunt impedance is considerably smaller than for the other corrugation parameters. This is shown as an example by the fact that deepening h by a factor of five results in an 152 % increase of Z_0, whereas shortening the periodic length L by the same factor leads to only a 15 % increase of the shunt impedance. This is made clear by the different range of Z_0 on the y-axes of Figure 6.6. However, the dependency of Z_0 and Q on L cannot be described by a power law but with a polynomial without providing any physical information.

The systematic simulations of the impedance of the corrugated structure as a function of its three unique parameters have yet to be done to understand these dependencies. Over and beyond this, scans create a structure with a certain and pre-defined impedance.

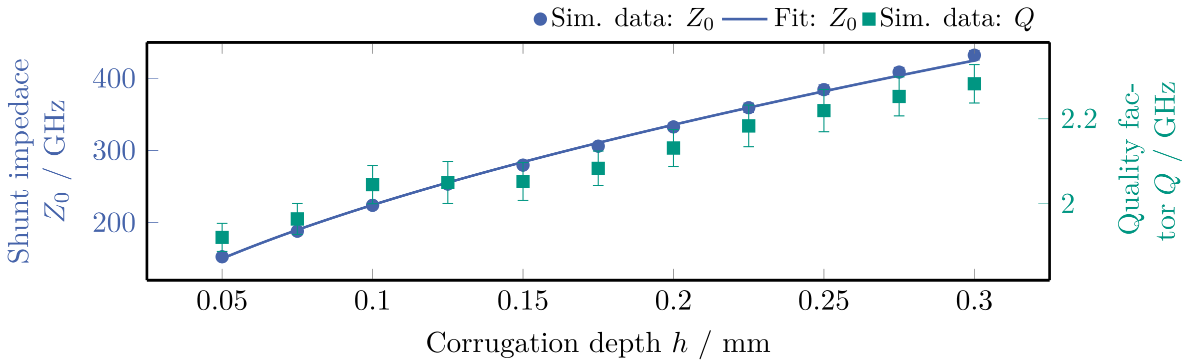

(a) Shunt impedance and quality factor as a function of the corrugation depth

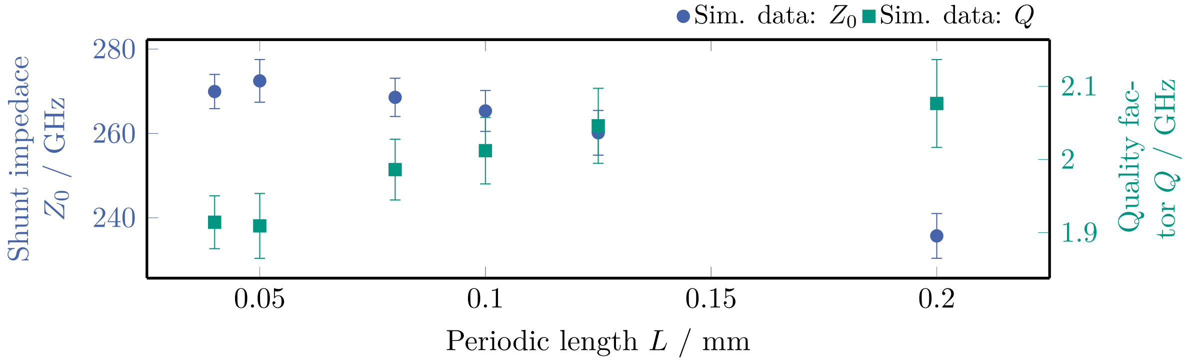

(b) Shunt impedance and quality factor as a function of the periodic length

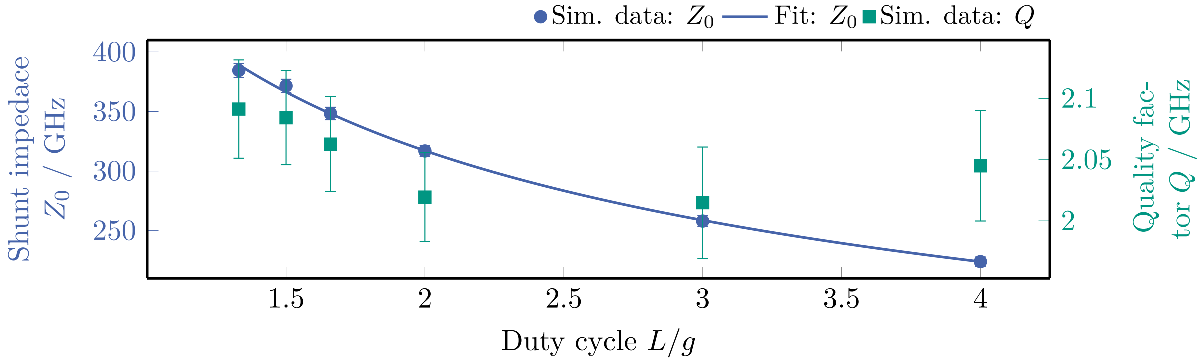

(c) Shunt impedance and quality factor as a function of the duty cycle

Figure 6.6. Shunt impedance Z_0 and quality factor Q as a function of the corrugation parameters. The fit in Figures 6.6a and 6.6c indicates the power law dependence of the shunt impedance by $Z_0(x) = B \cdot x^{\mu}$. Both impedance parameters do not correspond to a power law for a scan of the periodic length L. Therefore, no fit is shown for this scan. The fixed corrugation parameters are identical to Figure 6.4.

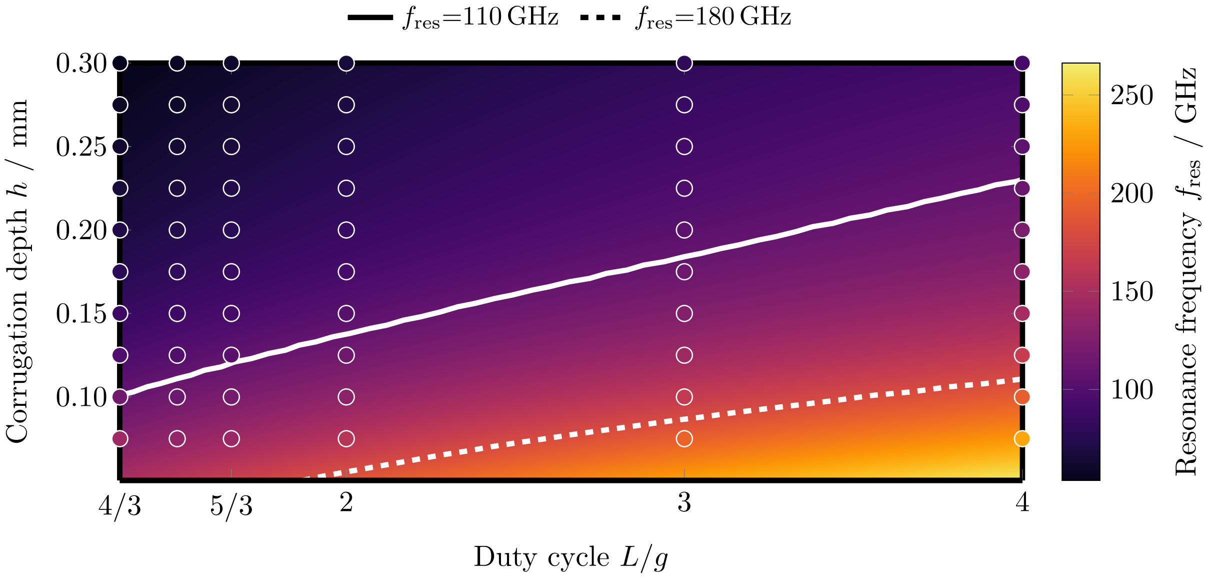

Figure 6.7. 2D resonance frequency scan. Resonance frequency in dependency of the corrugation depth h and the duty cycle L/g. The round dots indicate the settings of discrete simulations. Along the solid and dashed lines, the resonance frequencies are 110 GHz and 180 GHz respectively.

6.3. Optimization of Corrugation Parameter

As explained earlier, to find and design a specific impedance with characteristic impedance parameters such as resonance frequency f_{res}, shunt impedance Z_0, and quality factor Q, the three corrugation parameters - periodic length L, duty cycle L/g, and corrugation depth h - work together. The beam dynamics studies under the influence of the corrugated structure impedance (Chapter 7) will show that mainly the resonance frequency choice decides how the micro-bunching instability is affected. Furthermore, it is subordinate to determine the maximum achievable shunt impedance to enhance the impact of the structure. According to these criteria, a technique has been developed that can determine the optimal corrugation parameters globally and within the parameter restrictions specified by varying manufacturing methods in Section 8.3.

Resonance frequency

In Chapter 7 it will be shown, that f_{res} is the impedance parameter that determines how the beam dynamics is influenced by the corrugated structure. Consequently, f_{res} is the most important impedance parameter and the central parameter for the structure design. That is why, the different configurations to create an impedance with a certain f_{res} are determined in the first step.
Since the corrugation parameter L does not significantly affect the impedance resonance frequency, the corrugation parameter scan is reduced to a 2D scan (h and L/g) with a fixed periodic length. As demonstrated in Section 6.2.1, the power law exponent and amplitude of the 1D scans fluctuate slightly based on the respective other parameter. Consequently, their impact on f_{res} cannot be considered individually, and the 2D dependency must be used. As the resonance frequency scaling with h is almost inverse to the f_{res} scaling with L/g, the 2D dependency can be reduced to a one-dimensional scan for a fixed periodic

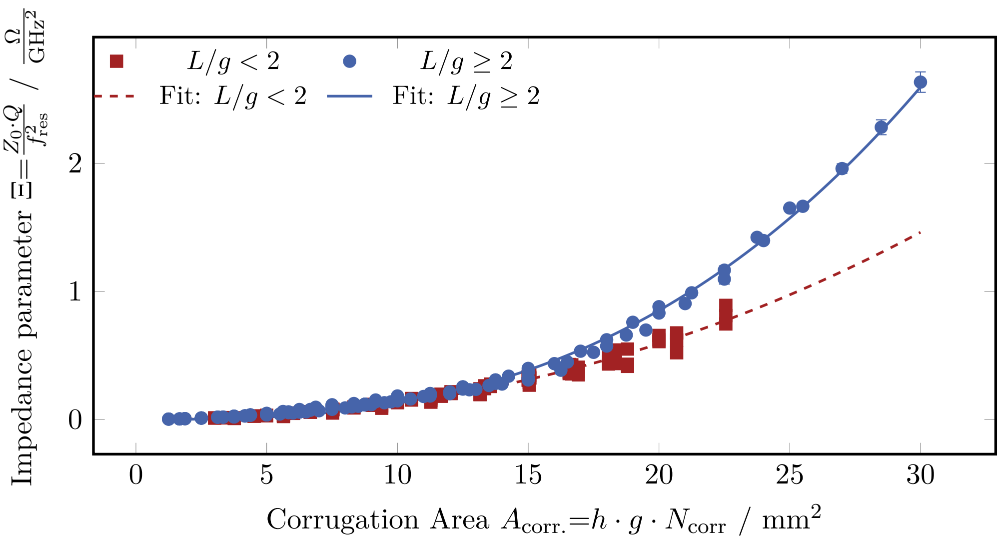

Figure 6.8. Corrugated Plate Impedance Parameter. The newly defined corrugated plate impedance parameter Ξ shows an exponential dependency on the area of the corrugations. The blue fit corresponds only to the blue settings, for which the structure is a plate with deepenings. For the red settings, the structure looks more like a plate with periodic elevations.

length and is described by

$$f_{\mathrm{res}}(h, L/g, L) = A_{h,Lg} \left(\frac{h}{L/g} \right)^{\rho_{h,Lg}} |_L \quad .$$

The fitting parameters $A_{h,Lg}$ and $\rho_{h,Lg}$ are determined by a 1D fit of the resonance as a function of the ratio $x = \frac{h}{L/g}$. Therefore all simulations in which all the other parameters of the structure were fixed are used. In Figure 6.7, the calculated resonance frequency obtained from the fitting parameters indicates a strong concordance with simulations (colored circles). This justifies the simplication $\rho_{h,Lg} = \rho_h = -\rho_{Lg}$, that has been used in here.
However, despite the determination of the periodic length - based on the equation and with the two fitting parameters $\rho_{h,Lg}$ and $A_{h,Lg}$ - only the ratio of h and L/g for a given resonance frequency can be clearly determined. For two specific resonance frequencies, the corrugation depth as a function of the duty cycle is plotted in Figure 6.7, too. The two exemplary chosen resonance frequencies $f_{\mathrm{res}} = 110\,\mathrm{GHz}$ and $f_{\mathrm{res}} = 180\,\mathrm{GHz}$ show a strong impact on the micro-bunching instability, which will be shown in Chapter 7 in detail.

Impedance parameter

To create a corrugated structure with a dedicated resonance frequency, until now, the corrugation depth or duty cycle can only be determined in dependency of the respective other parameter. However, this relation does not contain any information about which of these infinite combinations optimizes the shunt impedance and sets the quality factor to a certain value. Since it has been shown in the previous section that the power law is not suitable to describe the 2D dependence of these parameters on the corrugation dimensions, a different dependency parameter must be found. Moreover, finding a parameter to describe the corrugated plate impedance and a corrugation parameter whose relation allows a separation of the two design types (periodic deepenings or periodic elevations) has been required. To find and define these parameters, all simulated impedances with the half plate

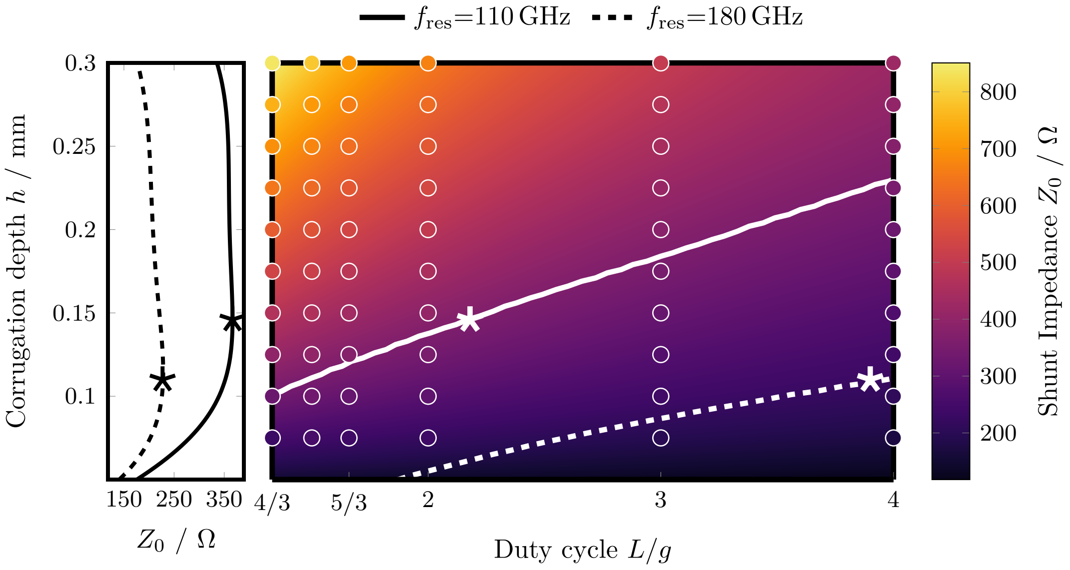

Figure 6.9. **2D shunt impedance scan.** Shunt impedance in dependency of the corrugation depth h and the duty cycle L/g. The round dots are simulation settings. The heatmap is calculated by a power law of the ratio $\frac{h}{L/g}$. Along the dashed and solid lines, the resonance frequencies are constant at 110 GHz and 180 GHz respectively. The left side plot shows the shunt impedance along the solid and dashed lines of fixed resonance frequencies. With this representation, the desired shunt impedance for a given f_{res} can be identified, the maximal values are marked with a star.

distance b=5 mm and with their according corrugation parameters are considered.
A parameter that takes all corrugation parameters into account is the volume of the corrugation. Since the corrugation width x_0 is unimportant, considering the longitudinal area contains all the relevant information of the corrugation. The area of all corrugations of one plate is given by

$$A_{\mathrm{corr.}} = N_{\mathrm{corr}} \cdot g \cdot h = \frac{h}{L/g} \cdot s \quad .$$

This quantity considers the dimensions of a single corrugation and the length of the whole plate.
The objective of defining the Corrugated Plate Impedance Parameter (CPIP) Ξ is to merge the three parameters (f_{res}, Z_0, and Q) that provide a complete description of the corrugated plate impedance. The symbol Ξ has not been chosen for a physical reason but because it looks like an abstracted beam between two parallel plates with the hint of a corrugation at the ends. Furthermore, the relationship should be as straightforward and robust as possible. Hence, Ξ is formulated as a product of the impedance parameters with different integer-value exponents. Since f_{res} scales inversely with $\frac{h}{L/g}$ in comparison to Z_0 and Q, it has been chosen, that its exponent should have the different sign. After testing various combinations, it has been demonstrated that the definition of CPIP

$$\Xi = \frac{Z_0 \cdot Q}{f_{\mathrm{res}}^2}$$

meets the required criteria for Ξ.
In Figure 6.8, the newly defined parameter Ξ is plotted as a function of the corrugation area $A_{\mathrm{corr.}}$, where the colors indicate the different plate types. It is evident that Ξ also conforms to a power law as a function of the corrugation area. Since the plot incorporates

Table 6.3. Optimized corrugated structures. Corrugation parameters and the corresponding impedance parameters, for a structure with the resonance frequency $f_{\text{res}} = 110\,\text{GHz}$ (Structure 1), $f_{\text{res}} = 110\,\text{GHz}$ (Structure 2), or $f_{\text{res}} = 140\,\text{GHz}$ (Structure 3) respectively. The shunt impedance is optimized and determined for the structure length $s = 20\,\text{cm}$.

Parameter	**Stucture 1**	**Structure 2**	**Structure 3**
Resonance frequency f_{res} / GHz	**110**	**180**	**140**
Periodic length L / µm	125	200	125
Longitudinal gap g / µm	49	100	67
Duty cycle L/g	2.56	2.00	1.86
Corrugation depth h / µm	159	55	78
Aspect ratio $\frac{h}{g}$	3.26	0.55	1.16
Quality factor Q	2.6	1.6	1.9
Shunt impedanceZ_0 / Ω	1000.1	436.2	718.7

simulation results for varying structure lengths, it is clear that this trend is not restricted to a particular structure length.

Shunt impedance

If we choose a certain value of f_{res} with a fixed periodic length L, the ratio $\frac{h}{L/g}$ is automatically defined with hardly any degrees of freedom. To determine the optimal or ideal values of h and L/g, the two free impedance parameters Z_0 and Q are used. Consequently, only the shunt impedance or quality factor can be optimized, whereas the other must be fixed at an appropriate value. Since the extent of the effect of the additional impedance on the beam dynamics mainly depends on the shunt impedance Z_0, it is the parameter that ought to be maximized. Whether a wide or narrow impedance resonance peak is suitable to manipulate the longitudinal beam dynamics effectively is discussed in Chapter 7. Figure 6.9 shows the 2D dependency of the shunt impedance on the corrugation parameters. Thus, a power law cannot properly describe the shunt impedance dependency on a single corrugation parameter. The color map is based on a 2D polynomial fit of the third order, showing good agreement with the simulation results (colored circles).

Along the lines of fixed f_{res}, the shunt impedance can be calculated from the relationship between $A_{\text{corr.}}$ and the impedance parameter Ξ since the shunt impedance is the only free parameter for a fixed quality factor. This Z_0 along the lines of the fixed resonance frequency, is illustrated in the left part of Figure 6.9. It can be seen that the shunt impedance - for a constant f_{res} - increases drastically with L/g or h in the regime of $L/g < 2$ and is almost constant in the other regime. From this, the optimal corrugation setting that maximizes Z_0 for a chosen f_{res} and Q can be found.

Repeating this procedure for all different L finds the overall optimized corrugation settings. This routine not only allows to find the general and overall optimized settings but can also be used to find the best setting in a certain parameter range. This limitation may be due to constraints in the aspect ratio $\frac{h}{L-g}$ or a minimal possible longitudinal gap g resulting from the chosen manufacturing process. Table 6.3 sums up the overall optimized corrugation parameters for structures with a length of s=20 cm and the corresponding impedance parameters. The structures are optimized for $f_{\text{res}} = 110\,\text{GHz}$ (Strucutre 1), $f_{\text{res}} = 180\,\text{GHz}$ (Structure 2), and $f_{\text{res}} = 140\,\text{GHz}$ (Structure 3). It is apparent that the resonance frequency can be increased mainly by reducing the corrugation depth. However, this entails a significant decrease in the shunt impedance, which must be considered for the design of the corrugated plates. In parallel to the impedance studies, the corresponding beam dynamics simulation has been performed to find the most relevant and interesting corrugation impedances and geometries for the installation into the KARA storage ring.

7. Beam Dynamics Studies

Based on the information and insights regarding the impedance of the corrugated plates, their impact on the longitudinal beam dynamics has been studied. By using systematic scans across the defined impedance parameter, the influence on the micro-bunching instability is investigated to understand the underlying mechanisms. It has to be noted that for this understanding, the added impedance is based on Equation (5.1) and is defined by the three impedance parameters, namely resonance frequency f_{res}, shunt impedance Z_0, and quality factor Q. If not mentioned explicitly otherwise, the shunt impedance and quality factor are fixed to the following values: $Z_0 = 1\,\mathrm{k\Omega}$ and $Q = 3$. Unlike using a simulated impedance with dedicated corrugation dimensions, the use of the resonator model allows the impedance parameters to be modified individually. Therefore, their effect on beam dynamics and micro-bunching instability can be determined independently.

In the first Section of this chapter, the KARA machine settings, for which the longitudinal beam dynamics have been well examined, both experimentally and by simulations [96], are used. For these settings, the resonance frequency of the additional impedance is scanned to identify the most effective f_{res} to enhance and suppress the emission of intense CSR. Furthermore, a scan of Q identifies the suitable values of the quality factor for later manufacturing. For promising impedances, a whole beam current scan is simulated. Following, the change of the thresholds and the current range of the different micro-bunching instability regimes are studied.

For a methodical understanding of the underlying and driving mechanisms of the micro-bunching instability, the second part of this chapter focuses on how the impedance that affects the bursting threshold most effectively depends on the machine parameters. These systematic machine scans on the acceleration voltage U_{acc} and momentum compaction factor α_{c} show that the most effective impedance to enhance the CSR intensity is directly dependent on the bunch profile.

7.1. Machine Settings of KARA Fill *f05135*

The micro-bunching imstability has been studied in detail for the machine settings, that correspond to the KARA fill *f05135*. For the beam dynamics simulations as well as for experiments at KARA with the settings of *f05135*, the relevant machine settings are fixed at U=1.048 MV and α_{c}=5.2×10^{-4}, which results in a zero-current bunch length σ_0=4.1 ps and the synchrotron frequency f_{s}=9.44 kHz. All the other parameters are listed in Appendix D. In the case without an additional corrugated plate impedance, which will be referred to as "*unperturbed*" throughout this thesis, the bursting threshold current is at I_{thr}=225 µA.

7.1.1. Impedance Resonance Frequency Scan

For the study of the impact of additional impedances with different f_{res} the focus is on the current range around the unperturbed bursting threshold I_{thr}. Therefore, a current

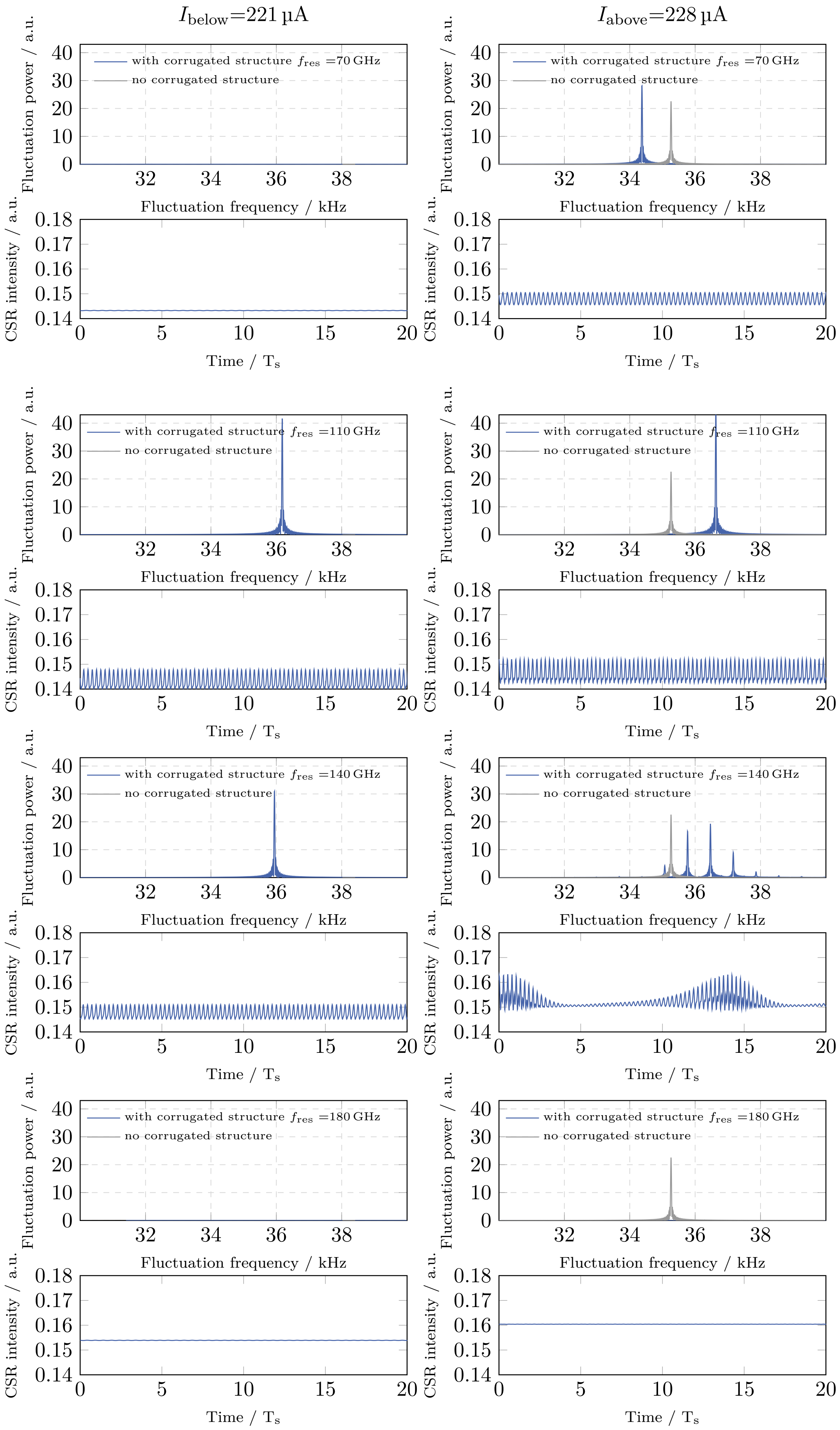

Figure 7.1. Fluctuation power for different additional impedances. Dedicated impedance steps out of Figure F.3.

slightly above $I_{\text{above}} = 228\,\mu\text{A}$ and a second current slightly below $I_{\text{below}} = 221\,\mu\text{A}$ the unperturbed bursting threshold are selected. For both currents, the CSR intensity and the corresponding fluctuation power have been simulated and are investigated in dependency of the additional impedances. Without an additional resonator impedance, no fluctuation of the emitted CSR occurs below I_{thr}, and the emitted intensity is relatively low. Above the threshold, the micro-bunching instability arises so that a fluctuation of the intensity at the bursting frequency f_{burst}=35.02 kHz is observable.

In Figure 7.1, the unperturbed case is shown in grey. The animation in Figure F.3 shows the fluctuation power around the unperturbed f_{burst} and the corresponding CSR intensity as a scan of the impedance resonance frequency f_{res} below and above the unperturbed threshold current.

The scan at the current I_{below} indicates the impedances that not only enhance the CSR intensity but also cause temporal fluctuations of the emitted radiation at lower beam currents than without a corrugated structure and therefore reduce the bursting threshold current. It can be seen that for a specific range of f_{res}, a narrow peak in the fluctuation power at about $f_{\text{burst}} = 36\,\text{kHz}$ arises, which strongly differs in its intensity, width, and peak frequency depending on the impedance resonance frequency. This goes along with a slight increase of the time-averaged CSR intensity. The peak frequency, which is related to f_{burst}, increases nearly as a linear function of the impedance resonance frequency up to $f_{\text{res}} \approx 120\,\text{GHz}$ and decreases in the same manner for larger f_{res}. The same tendency is notable for the maximal fluctuation power as well, although this peaks at about $f_{\text{res}} = 110\,\text{GHz}$.

Above the threshold current, the dominant fluctuation frequencies and the temporal profile of the CSR intensity depend on the additional impedance. Until $f_{\text{res}} \approx 110\,\text{GHz}$ the fluctuation power scales in the same way as below the unperturbed threshold as a function of f_{res}. The only difference is, of course, that even without an additional impedance, the emitted CSR fluctuates over time. In the frequency range from 135 GHz to 150 GHz, a clear enhancement of the time-averaged CSR intensity in combination with the arising of the slow outburst is visible. In this regime, additional side peaks in the range of f_{burst} occur as well. From the slow outbursts slightly above the unperturbed threshold current, it follows that not only the I_{thr} but also the slow outburst threshold $I_{\text{thr;slow}}$ can be manipulated by a corrugated plate impedance. However, it is impossible to determine how the threshold currents change and whether they change identically or individually from these impedance scans at a fixed current. For dedicated impedance settings, this will be discussed in Section 7.1.3. For even higher values of f_{res}, the outbursts and the amplitude of the maximal fluctuation power vanish. Consequently, above $f_{\text{res}} = 180\,\text{GHz}$, the fluctuations disappear completely so that an enhanced and temporally constant CSR intensity remains.

The different effects of additional impedances with varying resonance frequencies on beam dynamics and threshold currents are more clearly visualized in Figure 7.2. It shows the fluctuation power at f_{burst} as a function of f_{res} for the two current settings. The fluctuation power at f_{burst} (or maximal fluctuation power) is defined as the peak value at each step in Figure F.3. In both plots, a red dashed line indicates the maximal fluctuation power without an additional impedance.

Based on the definition of the unperturbed threshold I_{thr}, at the current I_{below}, either no effect or an increase in the maximum fluctuation power is possible. As described above, the latter effect is noticeable for the impedance resonance frequency in the range of $85\,\text{GHz} < f_{\text{res}} < 160\,\text{GHz}$ [Mai22b]. Here, the bursting threshold is reduced to such an extent that it is below I_{below} and therefore, the micro-bunching occurs at these low currents as well. Below the unperturbed bursting threshold current I_{thr}, the impedance resonance frequency which causes the strongest enhancement of the CSR fluctuation power (e.g. in Figure 7.2a), is referred to as the "*most effective resonance frequency*" $\hat{f}_{\text{res}}$ throughout this thesis. From Figure 7.2a, this most effective resonance frequency can be

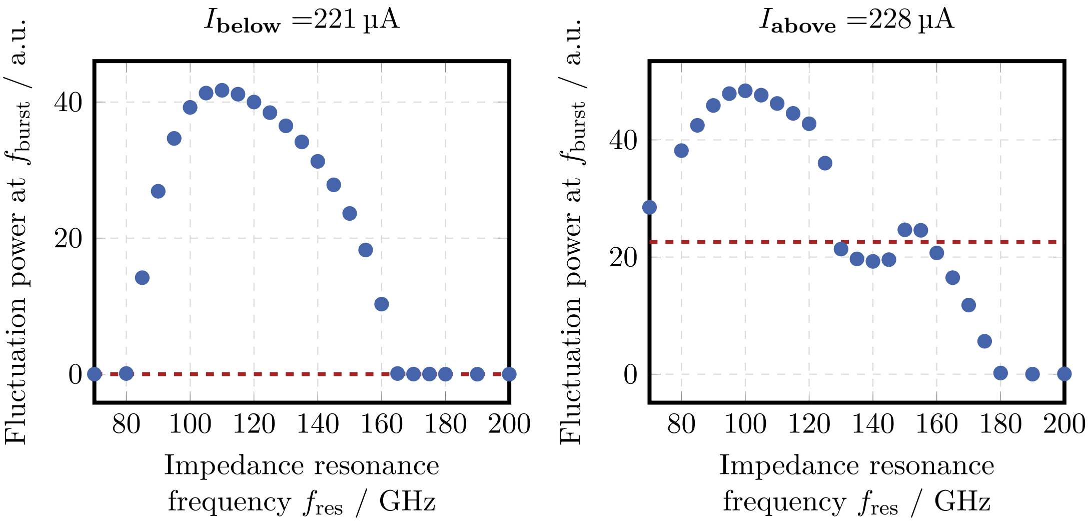

(a) (b)

Figure 7.2. Maximal fluctuation power as a function of the resonance frequency. The red dashed line marks the fluctuation power without an additional impedance. Certain impedances lead to an enhanced fluctuation power. Depending on the impedance, above the threshold, the fluctuation power can either be amplified or suppressed. Shunt impedance and quality factor are fixed at Z_0=1 kΩ and Q=3 (Also presented in [Mai22b]).

determined as $\hat{f}_{\mathrm{res}} = 110\,\mathrm{GHz}$. Furthermore, the fluctuation power at f_{burst} in the range $90\,\mathrm{GHz} < f_{\mathrm{res}} < 150\,\mathrm{GHz}$ is comparable or even - up to a factor of two - higher than slightly above I_{thr} without the additional impedance.

In Figure 7.2b, the different regimes can be identified clearly. In the case of $f_{\mathrm{res}} \leq 125\,\mathrm{GHz}$, where only a single dominant fluctuation frequency is notable, the maximal fluctuation power is significantly enhanced. This is caused by the reduction of the bursting threshold and, therefore, further advance into the fluctuation regime of the micro-bunching instability. In contrast, the fluctuation power at f_{burst} in the range of $125\,\mathrm{GHz} < f_{\mathrm{res}} < 160\,\mathrm{GHz}$ is almost constant and of the same magnitude as in the unperturbed case. This is because, in the outburst regime, the fluctuation power is distributed over a larger frequency range so that the maximal peak value does not increase further. The reduction of the CSR power, which happens until the complete disappearance of the fluctuation power above $f_{\mathrm{res}} = 180\,\mathrm{GHz}$, is also recognizable. Consequently, the different micro-bunching instability regimes at a certain bunch current caused by different additional impedances can be identified in a single plot.

Based on the results of these f_{res} scans, the resonance frequencies of the corrugated plates for more elaborated studies and to be built and installed in the KARA storage ring are selected. The first one (Structure 1: f_{res}=110 GHz) is the impedance with which the maximal fluctuation power below I_{thr} is most enhanced. The second impedance (Structure 2: f_{res}=180 GHz) has the smallest impedance resonance frequency, which causes a complete suppression of the fluctuation power at I_{above} and increases the I_{thr}. Structure 3 (f_{res}=140 GHz) creates the slow CSR outburst already at the unperturbed bursting threshold.

7.1.2. Quality Factor Scan

In Section 6.3, it has been discussed that the quality factor of the corrugated plate impedance must be set to a suitable value to optimize the impedance. Therefore, the impact of Q on the emitted fluctuation power is studied for the same two current settings around the

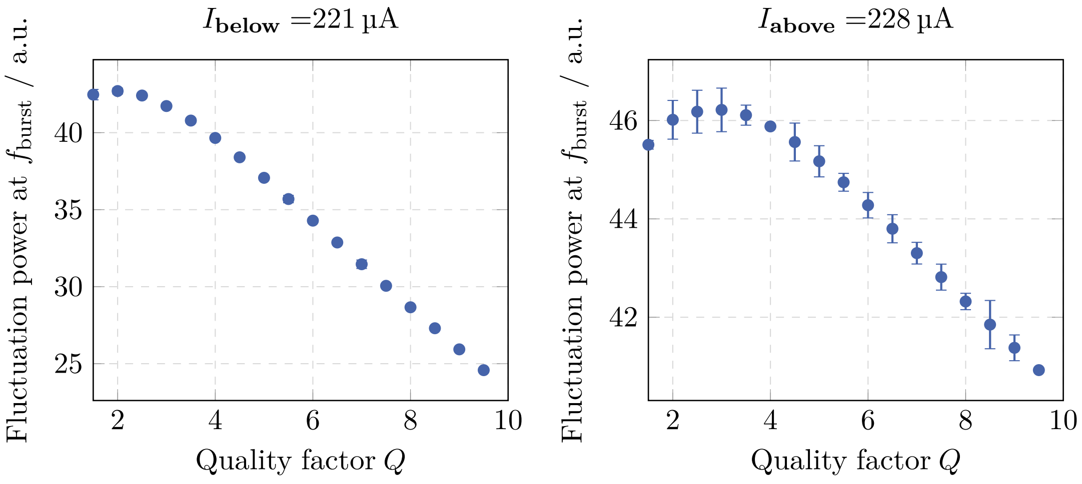

(a) **(b)**

Figure 7.3. Maximal fluctuation power as a function of the quality factor. An increase of the quality factor, which corresponds to a narrowing of the resonance peak, leads to a reduction of the fluctuation power at f_{burst} so that the impact of the additional impedance decreases. The shunt impedance and resonance frequency are fixed at Z_0=1 kΩ and f_{res}=110 GHz.

unperturbed bursting threshold as the previous f_{res} scan. For the most effective enhancement of the fluctuation power at f_{burst}, the impedance resonance frequency is utilized for the sake of a clear influence observation. Consequently, its value is $f_{\text{res}} = \hat{f}_{\text{res}} = 110\,\text{GHz}$.

Figure 7.3 presents the result of this impedance scan by showing the maximal fluctuation power as a scan of the quality factor of the additional impedance. Above I_{thr} (Figure 7.3b), the impedance causes a significant enhancement of the fluctuation power at f_{burst}, for the whole investigated Q range. However, a higher quality factor, corresponding to a narrower resonator impedance peak, reduces the fluctuation power and the emitted CSR power. The decrease is nearly linear from $Q = 4$ onwards. Below the unperturbed threshold, the same linear tendency is notable. However, at this current, the reduction starts already from $Q = 3$ on. The decrease is significantly steeper than for I_{above} so the fluctuation power at f_{burst} for $Q = 10$ is only almost half its maximal value. Independent of the bunch current, the maximal fluctuation power converges to its unperturbed value for an inceasing quality factor Q. The different slope is caused by the fact that in the unperturbed setting, the maximal fluctuation power is only negligible below I_{thr}.

The linear reduction tendency for both current settings can be attributed to two factors for a constant shunt impedance. For one thing, a broader resonance peak tolerates more a deviation of the resonance frequency from $\hat{f}_{\text{res}}$. If the resonance frequency does not exactly correspond with $\hat{f}_{\text{res}}$, the impedance contribution at the most influential frequency is drastically higher for a smaller quality factor. This is shown as an example using $f_{\text{res}} = 110\,\text{GHz}$ and $\Delta f = \pm 5\,\text{GHz}$. If the quality factor is Q=3, a positive deviation in frequency results in a reduction of impedance by 6.6 % whereas a negative deviation reduces it by 7.2 %. In contrast, for a Q=10, a positive deviation reduces the impedance by 44.1 % and a negative deviation reduces it by 46.4 %. Figure F.4 shows the impedance reduction as a function of the frequency deviation for different Q. On the other hand, for fixed Z_0 and f_{res}, the resonator impedance integrated via the frequency increases with the width of the resonance peak and scales with $1/Q$. Therefore, the impact and contribution to the overall impedance depends on the quality factor in the same way.

For the non-linear scaling part in the region of the low Q values with broad resonance peaks, the fluctuation power at f_{burst} is nearly constant, as seen in Figures 7.3a and 7.3b.

Consequently, the maximal impact of the corrugated plate impedance with a fixed Z_0 on the CSR emission of these certain bunch currents is reached since the impedance contribution of the relevant frequency is large enough. So, at least for the simulation results, a further reduction of the quality factor does not cause a more significant impact on the CSR, but information and accuracy about $\hat{f}_{\mathrm{res}}$ might get lost.

Based on this, the quality factor for both the simulations and the optimized corrugated structure parameters can be set. In Chapter 6, it is discussed that broadening the impedance resonance peak reduces the shunt impedance, independent of the scanned corrugation parameter. Therefore, for the simulations, the quality factor is fixed at Q=3, which creates the narrowest resonator peak without reducing its impact on the longitudinal beam dynamics. As mentioned previously, the value is also used as a starting point for the determination of the optimal corrugation parameters. However, if the corrugated parameters have some restrictions because of the real corrugated structure, the configuration of the corrugated parameters should be chosen for a broader peak, namely the quality factor should be smaller than 3. This results in a less reduced impact on the longitudinal beam dynamics compared to a reduced shunt impedance setting.

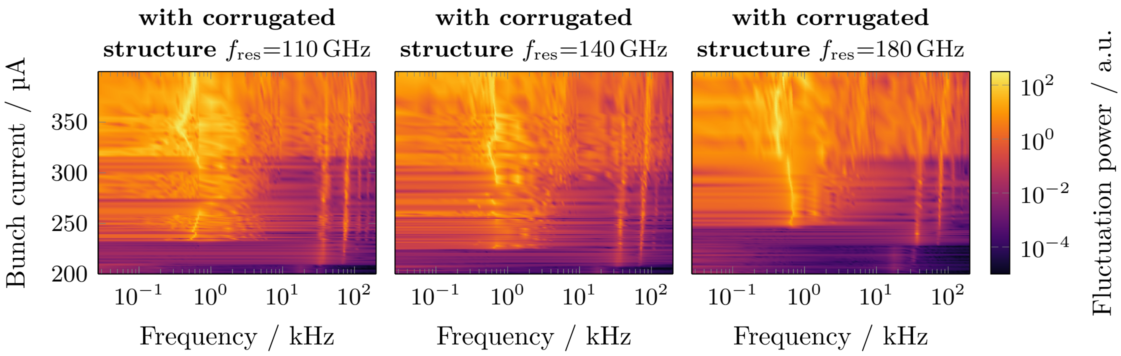

Figure 7.4. Spectrogram with corrugated plate impedances. The Fourier transform of the emitted CSR power is shown as a function of the beam current in the spectrograms for the different additional impedances with different resonance frequencies f_{res}. The logarithmic frequency axis makes the slow outbursts ($f \lesssim 2\,\mathrm{kHz}$) just as visible as the bursting regime ($f \gtrsim 20\,\mathrm{kHz}$). The multiple finger-like structures are caused by the different orders of the bursting frequency f_{burst}.

7.1.3. Beam Current Decay

In this Section, the impact of the three impedance structures, whose resonance frequencies are 110 GHz, 180 GHz, and 140 GHz (Structures 1-3 in Table 6.3) is investigated in more detail to study the influence on the micro-bunching instability properties. In the first part, the shunt impedance is fixed at Z_0=1 kΩ. Since in the range from 110 GHz to 180 GHz, the CSR impedance has nearly a plateau (see Figure 2.8), the maximal spectral contribution to the total impedance is comparable for all three structures: 9.31 % ($f_{\mathrm{res}} = 110\,\mathrm{GHz}$), 8.92 % ($f_{\mathrm{res}} = 140\,\mathrm{GHz}$), and 9.20 % ($f_{\mathrm{res}} = 180\,\mathrm{GHz}$). The differences in their effects on the beam dynamics are only based on the different f_{res}.

The beam dynamics related to the micro-bunching instability and its properties cannot only be visualized but also determined in a beam current scan (going from high to low beam currents, "*decay*"). In Figure 7.4 the spectrograms with the different additional impedances with f_{res}=110 GHz, f_{res}=140 GHz, and f_{res}=180 GHz are shown. In contrast, the reference without an additional impedance has already been shown in Section 5.2 (Figure 5.5). The logarithmic scaling of the frequency axis makes the dynamics of the slow bursting regime more visible. On the other side, the linear scaling and the reduced current range in Figure 7.5 focus on the finger-like structure around the bursting frequency f_{burst}. This frequency indicates the dynamics of the micro-bunching instability directly above the threshold current I_{thr} [47]. Since the further finger-like structures at higher frequencies (see Figure 5.5a) correspond to the higher orders of the bursting frequency, they are neglected in the following discussions. For the studied additional impedances, it can be seen that they do not cause a substantial change of the beam dynamics, and the finger-like structure is still visible. Consequently, the micro-bunching instability cannot be completely suppressed, and the bursting and outburst regimes still occur. However, the characteristic parameters of the instability change notably but in different ways for the impedances with different f_{res}, which will be discussed in the following.

As a reference, the parameters for a simulated decay without an additional corrugated plate ("*unperturbed case*") impedance are listed here:

- Slow outburst threshold current $I_{\mathrm{thr;slow}}$=(247 ± 1) µA
- Bursting threshold current I_{thr}=(226 ± 1) µA
- Slow outburst frequency $f_{\mathrm{burst;slow}}$=(746 ± 18) Hz

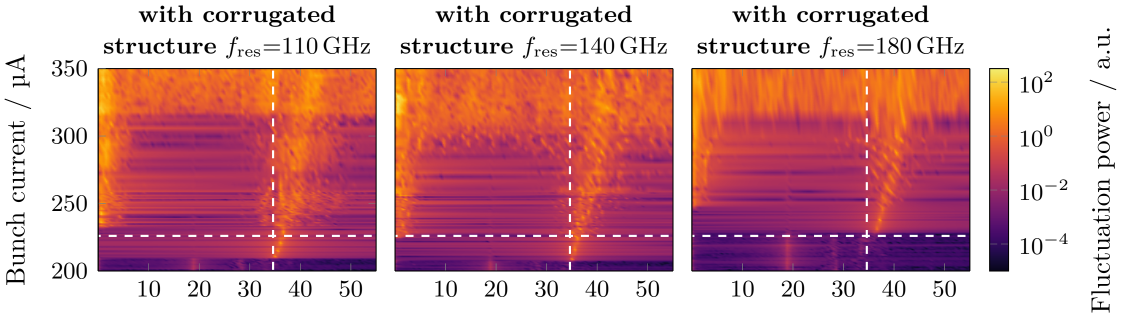

Figure 7.5. Spectrogram with corrugated plate impedances at bursting. This shows the same spectrograms as Figure 7.4 but with a linear frequency axis. Furthermore, the current and frequency range is reduced so that the finger-like structure around f_{burst} is more focussed on. The dashed lines indicate the bursting threshold current (horizontal line) and bursting frequency (vertical line) of the unperturbed simulations. The slow outbursts at the left side of the spectrograms arise significantly above the bursting threshold and the horizontal line (Partially also presented in [Mai22b; Mai]).

- Bursting frequency f_{burst}=(35.02 ± 0.10) kHz

Furthermore, the change of the finger-like structure at a certain current relative to the threshold ($\Delta I = I - I_{\mathrm{thr}}$) is studied. The absolute value of the width σ_{burst} is a measure of spectral bandwidth of the CSR fluctuation. In this Section, the absolute value is not of interest, so only the relative value $\sigma_{\mathrm{burst}}/\sigma_{\mathrm{burst,wo}}(\Delta I)$ is used. Thereby, σ_{burst} and $\sigma_{\mathrm{burst,wo}}$ are calculated for their respective current ΔI. The index *wo* means the unperturbed case without an additional impedance. The width for the unperturbed case at some current steps are $\sigma_{\mathrm{burst,wo}}(\Delta I = 30\,\mu\mathrm{A}) = 1.14\,\mathrm{kHz}$ and $\sigma_{\mathrm{burst,wo}}(\Delta I = 50\,\mu\mathrm{A}) = 2.37\,\mathrm{kHz}$.
The effects of the three additional impedances on the longitudinal beam dynamics are described individually for a detailed analysis.

110 GHz

The left spectrogram in Figure 7.5 shows a substantial reduction of I_{thr} in comparison with the unperturbed setting (horizontal dashed line) of (16.0 ± 1.4) µA (7.1 %), which causes enhanced CSR power at lower beam currents. The uncertainty results from the simulated current steps of 1 µA and the resulting uncertainty on the two determined threshold currents. In contrast to I_{thr}, the bursting frequency f_{burst} does not undergo any significant change due to the additional impedance. It should be noted, however, that the dominant bursting frequency increases slightly with the beam current, which can also be referred to as the skewness of the finger. Consequently, the positive skewness increases the f_{burst} at the unperturbed threshold (compared to the crossing of the two dashed lines).
Figure 7.6 and Table 7.1 show the relative width of the finger-like structure $\sigma_{\mathrm{burst}}/\sigma_{\mathrm{burst,wo}}$ in the spectrogram as a function of ΔI. In the region above I_{thr} without the slow outbursts ($\Delta I \lesssim 30\,\mu\mathrm{A}$) the width varies around the $\sigma_{\mathrm{burst,wo}}$. Since the fluctuation of the CSR power is sinusoidal and the fingers in the longitudinal phase space only rotate and do not change amplitude over time, this regime of the micro-bunching instability is referred to as the "*stable regime*"[11]. This relatively large variation and deviation from the unperturbed width has its origin in the narrow peak in this current regime - the absolute width σ_{burst} versus the beam current is shown in Figure F.5. Therefore, a small absolute change of the width of σ_{burst} or $\sigma_{\mathrm{burst,wo}}$ results in a large change of $\sigma_{\mathrm{burst}}/\sigma_{\mathrm{burst,wo}}$. As soon as the outburst regime ($\Delta I \gtrsim 30\,\mu\mathrm{A}$) is reached, the width increases significantly. Thereby,

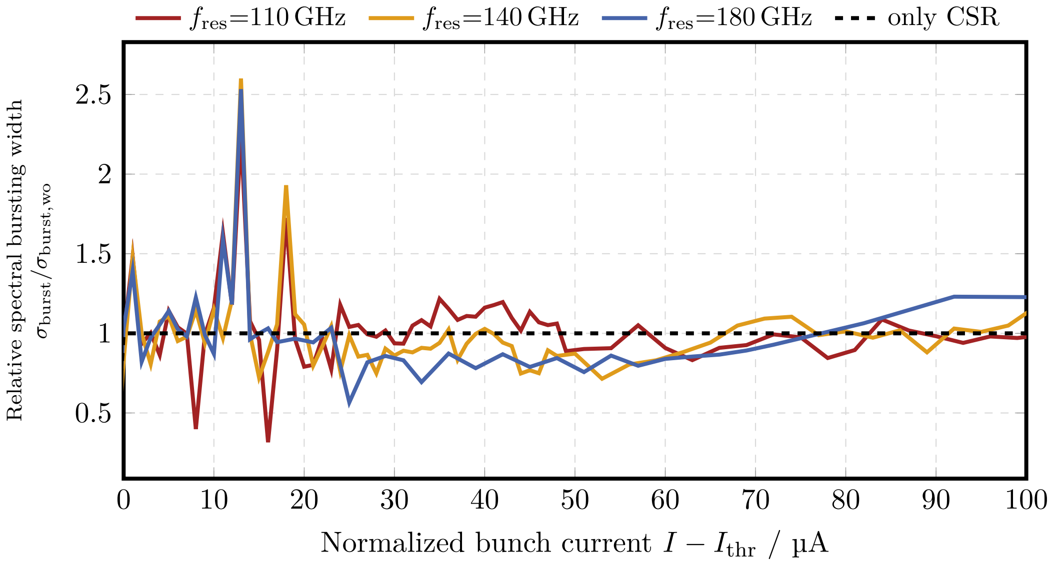

Figure 7.6. Relative spectral bursting width. The spectral bursting width σ_{burst} is divided by the unperturbed width $\sigma_{\mathrm{burst,wo}}$. Both widths are calculated for the same current relative to the threshold. Below the outburst regime ($\Delta I \lesssim 30\,\mu\mathrm{A}$), the relative value fluctuates strongly due to the narrow finger. In the outburst regime, it stabilizes depending on the additional impedance.

not only the amplitude of the fluctuation is reduced, but the ratio of the widths converts to $\sigma_{\mathrm{burst}}/\sigma_{\mathrm{burst,wo}} = (1.00 \pm 0.05)$. So, a structure with f_{res}=110 GHz shifts the bursting regime of the longitudinal beam dynamics and the resulting fast fluctuating CSR emission to lower beam currents. Indirectly, this also changes the beam dynamics at a fixed beam current in comparison to the unperturbed setting.

In the middle current range of the outburst regime ($270\,\mu\mathrm{A} \lesssim I \lesssim 300\,\mu\mathrm{A}$), however, a systematic impact on the temporal outbursts is visible. In Figure 7.4, the frequency range around $f_{\mathrm{burst;slow}}$ shows a smearing out and no clear dominant frequency of the fluctuation power. In the time domain, this corresponds to the creation of "*sub-bursts*" at twice the slow outburst frequency ($2 \cdot f_{\mathrm{burst;slow}}$) (see Figure 7.7). This appearance of higher orders of the slow outburst frequency causes a reduction of the amplitude of the "*regular*" outbursts compared to the unperturbed setting.

Nevertheless, this brings out an increase in the time-averaged CSR power. Not just because of the last point but also because of the fact that the impedance with f_{res}=110 GHz triggers the underlying mechanisms of the micro-bunching instability and produces enhanced CSR below the unperturbed I_{thr} makes this impedance interesting for further studies.

180 GHz

Even though it has the identical absolute and nearly the same relative contribution to the KARA impedance, a corrugated plate with f_{res}=180 GHz has a distinct impact on the longitudinal beam dynamics compare to f_{res}=110 GHz, not only quantitatively but qualitatively as well. As already indicated by the scan in Figure 7.2b, where the micro-bunching instability is suppressed directly above the unperturbed bursting threshold, I_{thr} is slightly increased by (1.3 %), as seen in the right figure in Figure 7.5. Furthermore, the spectrogram shows that f_{burst} is also altered, in addition to the threshold current. This additional impedance causes a shift of the finger-like structure by 1.9 kHz (5.4 %).

The impedance with f_{res}=180 GHz not only shifts the bursting frequency and thereby changes the temporal CSR fluctuation pattern but also yields a change of the width of the finger-like structure in the spectrogram. As seen in Figure 7.6, in the stable regime

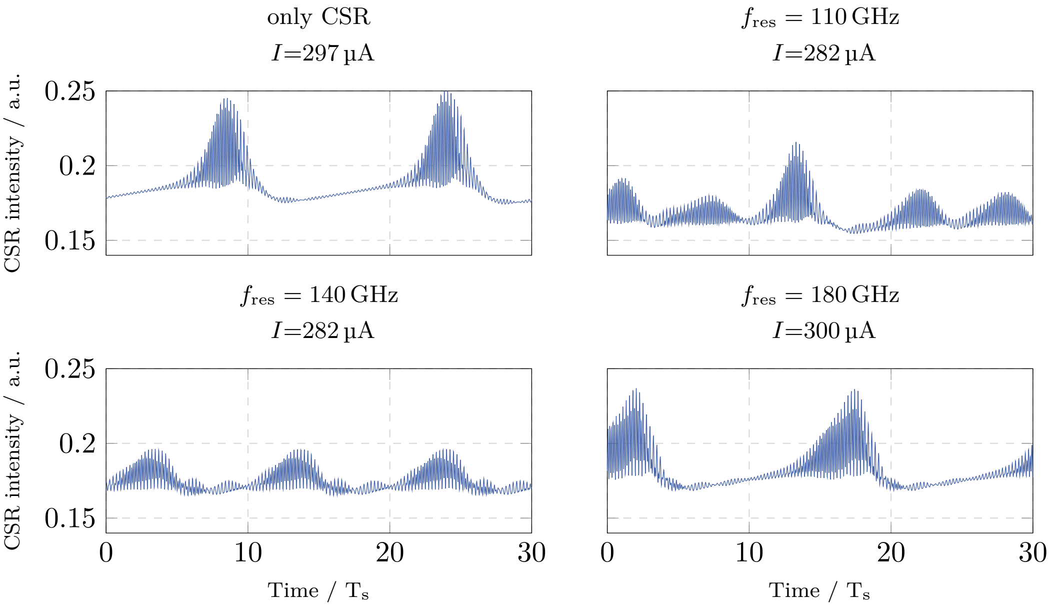

Figure 7.7. CSR intensity. It is shown as a function of time in units of the synchrotron period. The displayed current settings are 50 µA above the respective bursting threshold I_{thr}.For f_{res} = 180 GHz and the setting with only the CSR impedance the slow outbursts are visible. In contrast, the other two additional impedances show the creation of sub-bursts at higher harmonics. This leads to a reduction of the bursting amplitude but an increasing time-averaged CSR intensity.

($\Delta I \lesssim 30\,\mu\mathrm{A}$), this additional impedance causes strong variations of $\sigma_{\mathrm{burst}}/\sigma_{\mathrm{burst,wo}}$ in the region between 50 % and 250 %. However, directly above the threshold current of the outburst regime, the finger width is systematically reduced in comparison to the unperturbed finger, and the relative width remains in the range of 75 % to 85 %.
This narrowing of the dominant fluctuation power frequency range leads to a more stable CSR fluctuation and, therefore, a higher quality of the emitted CSR pulses. In combination with the increased bursting threshold current, this impedance is of interest to suppress the micro-bunching instability and improve the beam and radiation quality.

140 GHz

The additional impedance with f_{res}=140 GHz, which has been chosen for the decay study because it affects the slow outburst threshold most effectively, structurally shows a combination of the effects of the two previously discussed impedances.
Analog to the impedance with f_{res} = 110 GHz, the bursting frequency is not changed significantly, but I_{thr} is reduced substantially. With a structure with f_{res} = 140 GHz, the threshold is reduced by $(18.0 \pm 1.4)\,\mu\mathrm{A}$ (8.0 %), which is comparable to the reduction with f_{res} = 110 GHz. Additionally, the slow bursting shows the same vanishing of the dominant frequency in the spectrogram, based on the higher harmonic orders of $f_{\mathrm{burst;slow}}$. Also, it shows the identical non-significant change of f_{burst} at the bursting threshold current.
However, the width of the finger scales between the other two studied impedance resonance frequencies. After the substantial fluctuation range, which is the same for all the f_{res}, the width is systematically smaller than for the unperturbed case in the range of 85 % to 95 % and converges to it as soon as the finger in the spectrogram turn into a broadband fluctuation power ($\Delta I \gtrsim 65\,\mu\mathrm{A}$).

Table 7.1. Relative spectral bursting width. The spectral width of the bursting finger is shown for dedicated current above the threshold current. They are normed by the width without an additional impedance at the current with the same distance ΔI to the bursting threshold current.

$\sigma_{\text{burst}}/\sigma_{\text{burst,wo}}$	110 GHz	140 GHz	180 GHz
@ΔI =10µA	1.16	1.15	0.87
@ΔI =20µA	0.79	1.06	0.97
@ΔI =30µA	0.94	0.86	0.86
@ΔI =40µA	1.16	1.03	0.78
@ΔI =50µA	0.89	0.87	0.76

7.1.4. Shunt Impedance Scan

As discussed in Section 3.3, there is limited space in the KARA storage ring for the chamber with additional corrugated plate impedance. Since Z_0 scales with the structure length s, this means that Z_0 cannot be completely freely chosen and adjusted. The study investigates how the properties of the micro-bunching instability depend on Z_0. The results with spectrograms for scanning with different shunt impedances and resonant frequencies (Z_0 and f_{res}), are shown in Figure F.6 to Figure F.11.

In Figure 7.8 the threshold currents of the two micro-bunching regimes ("*bursting*" and "*slow outburst*") are shown as a function of the shunt impedance of the additional corrugated plate impedance for the different f_{res} ($f_{\text{res}} = 110\,\text{GHz}$, $f_{\text{res}} = 140\,\text{GHz}$, and $f_{\text{res}} = 180\,\text{GHz}$). It can be seen that the qualitative impact on the thresholds is independent of Z_0 but is only affected by the resonance frequency of the impedance. Independent of Z_0, the impedance with f_{res}=180 GHz does not change I_{thr} significantly. However, the threshold I_{thr} can be decreased by the additional impedances with f_{res}=110 GHz and f_{res}=140 GHz. For both impedances, I_{thr} scales linearly with Z_0, as seen in Figure 7.8. The bursting threshold is identical and nearly unperturbed for both impedances.

As already discussed for $Z_0 = 1\,\text{k}\Omega$, the slow outburst threshold is not affected similarly for the two impedances (f_{res}=110 GHz and f_{res}=140 GHz). Even though, the two lower f_{res} both reduce $I_{\text{thr;slow}}$ linearly with increasing shunt impedance. The slopes differ so that the outburst regime occurs even below the unperturbed bursting threshold for $f_{\text{res}} = 140\,\text{GHz}$ with $Z_0 = 2\,\text{k}\Omega$. For this impedance setting, not only the slow outburst parameters are changed, but also the whole dynamics of this regime are disturbed in the spectrogram (Figure F.8). Therefore, $I_{\text{thr;slow}}$ cannot be determined by the automated routine but has been determined "*by eye*", causing increased uncertainty. At the largest investigated shunt impedance (Z_0=2 kΩ), an additional corrugated plate impedance with $f_{\text{res}} = 180\,\text{GHz}$ causes a small but significant reduction of the slow outburst threshold.

Due to different scaling degrees of the slow outburst threshold across the three f_{res} options, the current range between the two thresholds differs among them. This is shown in the bottom of Figure 7.8, where the current range of the stable bursting regime ($I_{\text{thr;slow}}$-I_{thr}) is shown. The higher two f_{res} lead to a reduction of current range for the bursting micro-bunching instability regime. On the other hand, $f_{\text{res}} = 110\,\text{GHz}$ causes the stronger reduction of the tresholds for the investigated Z_0 range, which however does not change with Z_0. Consequently, with this impedance, the two thresholds change in parallel. On the other hand, the plot reveals that the $f_{\text{res}} = 110\,\text{GHz}$ increases the current range of the stable regime. So this impedance can cause an enhanced CSR in the THz range without the temporal outbursts. Consequently, this corrugated plate can be used to increase the current range, in which intense and stable CSR is created in the low-α_c operation mode at KARA.

The bursting frequency f_{burst} is only affected significantly by the impedances with f_{res} =

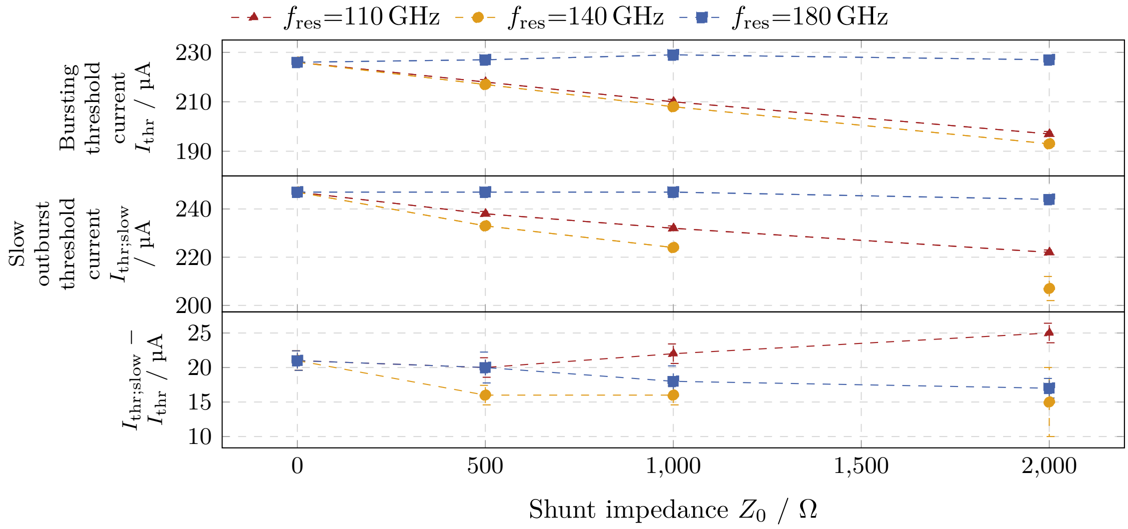

Figure 7.8. Bursting thresholds: Z_0 scan. The thresholds of the bursting (top) and slow outburst (middle) regime are shown as a function of the shunt impedance Z_0 of the additional impedance. Due to the different changes in the two thresholds, the current range of the stable regime between these thresholds can be varied depending on the resonance frequency of the impedance.

180 GHz, which is shown in Figure 7.9. For this resonance frequency, f_{burst} increases nearly linearly, whereas the other impedances do not change the bursting frequency f_{burst}. This linear dependence on Z_0 cannot be seen for the slow outburst frequency $f_{burst;slow}$ since the linearity breaks down for $Z_0 = 2\,\mathrm{k\Omega}$ - independent of the resonance frequency of the impedance, as seen in Figure 7.9 (bottom). For the two most extreme of those examined resonance frequencies (f_{res}=110 GHz and f_{res}=180 GHz), this results in an enhanced shift of the CSR outburst frequency. As discussed in the previous Section, the higher order modes of $f_{burst;slow}$ become relevant for the $f_{res} = 140\,\mathrm{GHz}$ corrugated plate, and their contribution increases with Z_0. Thereby, the beam dynamics and the CSR emission over time is changed in such a way for $Z_0 = 2\,\mathrm{k\Omega}$, that $f_{burst;slow}$ cannot be determined properly by the automatic routine. Nonetheless, this is no longer the dominant frequency to describe the temporal outbursts.
To sum it up, it can be said that at least a shunt impedance of about $Z_0 = 1\,\mathrm{k\Omega}$ is required to see a significant impact on the dynamics of the micro-bunching instability. Furthermore, the way of manipulating the properties of the instability is decisively defined by the choice of the impedance resonance frequency.

7.2. Machine Setting Scan

Until here, this chapter mainly describes the impact on the longitudinal beam dynamics by adding the corrugated plate impedance for the machine settings of the KARA fill *f05135*. Through this, the underlying and driving mechanisms of the micro-bunching instability and the resulting impedance to control the instability could not be found. Nevertheless, the dependence of the most effective impedance to reduce the bursting threshold $\hat{f}_{res}$ on the machine settings is of great interest for the design of the corrugated plates and the understanding of the micro-bunching instability. For the identification of these mechanisms, the impact of an additional corrugated plate impedance on the longitudinal beam dynamics around the bursting threshold I_{thr} has been studied in dependence on the machine settings. In Inovesa simulations, systematic scans with different values of the momentum compaction

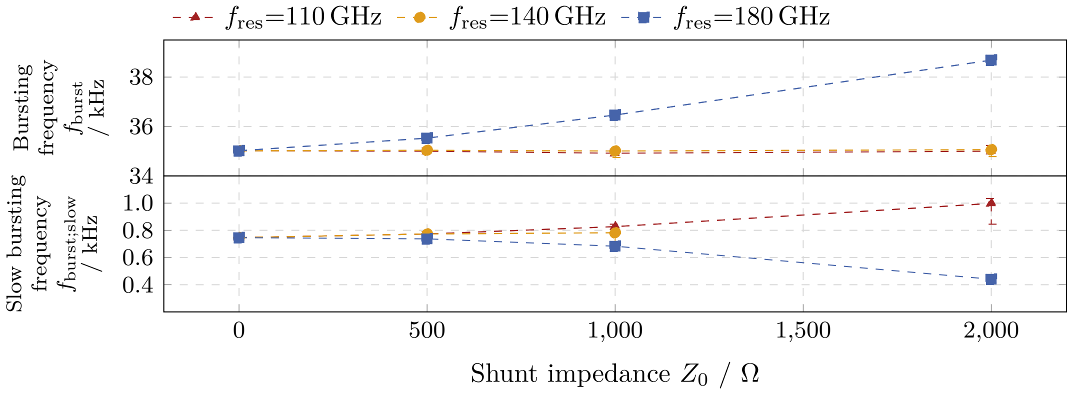

Figure 7.9. Bursting frequencies: Z_0 scan. The dominant frequency of the bursting (top) and slow outburst (bottom) regime are shown as a function of the shunt impedance Z_0 of the additional impedance. For the impedance with $f_{\mathrm{res}} = 140\,\mathrm{GHz}$ and $Z_0 = 2\,\mathrm{k}\Omega$ the dynamics of the outbursts change in such a way that slow outburst frequency $f_{\mathrm{burst;slow}}$ cannot be determined properly.

factor α_c (8×10^{-4} to 1.4×10^{-3}) and acceleration voltage amplitude U_{acc} (0.8 MV to 1.1 MV) have been performed. These two accelerator parameters have been chosen for two main reasons. On the one hand, at the KARA storage ring, these two parameters are relatively easy to adjust and set through the different states of the low-α_c squeeze. Furthermore, α_c and U_{acc} have a direct impact on the bunch length σ_0, via Equation (2.27). This allows to set and scan machine parameters and an important beam parameter to get a deeper insight into the longitudinal beam dynamics.

The first part of the Section focuses on the scans of the fluctuation power as a function of f_{res} of the additional impedance for the different machine settings. Afterward, the dependency of the most effective impedance to reduce the bursting threshold on U_{acc}, α_c, and σ_0 is presented. The last Section shows how the most effective impedance to enhance CSR intensity depends on the longitudinal bunch profile and bunch spectrum.

7.2.1. Impedance Resonance Frequency Scan

As mentioned previously, the most effective resonance frequency $\hat{f}_{\mathrm{res}}$ describes the impedance which causes the strongest enhancement of the CSR fluctuation power below the unperturbed threshold current. The $\hat{f}_{\mathrm{res}}$ identifies the impedance frequency whose contribution triggers the creation of the substructures in the longitudinal phase space and bunch profile. This consequently causes the radiation of CSR below I_{thr}. However, it must be noted that a corrugated structure with $\hat{f}_{\mathrm{res}}$ is effective in increasing the CSR emission and not in manipulating the bursting frequency or suppressing the micro-bunching instability. Besides this most effective impedance, the minimal and maximal impedance resonance frequencies ($f_{\mathrm{res;max}}$ and $f_{\mathrm{res;min}}$) that enhance the fluctuation power at I_{thr}, compared to the unperturbed case, are of interest. These frequencies are calculated from the fitting of the fluctuation power scan. They are defined as the smallest and largest f_{res}, which cause a significant enhancement of the negligible but not exactly zero unperturbed fluctuation power.

The scan over the different machine parameters entails that the bursting threshold and I_{below} change accordingly. The theoretical prediction of I_{thr} and its dependence on the machine settings is given by Equation (2.70). In case of short bunch length or small shielding parameter, Figure 2.13 shows an overestimation of the threshold by the semi-empirical formula because of the Short-bunch-length bursting (SBB). In her doctoral thesis, M. Brosi [61] has studied and confirmed this deviation for KARA in the range of $\Pi \lesssim 1$.

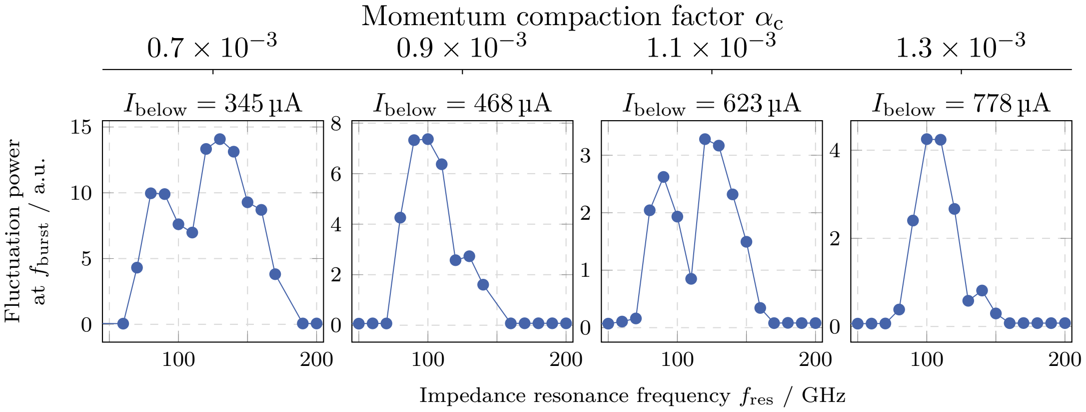

Figure 7.10. Maximal fluctuation power as a function of the resonance frequency: α_c scan. Analog to Figure 7.2a, the maximal fluctuation power as function of the impedance resonance frequency is shown for different values of the momentum compaction factor. The simulations are performed at 98.5 % of the bursting threshold current (I_below). Depending on α_c, either a single or double peak is visible. The acceleration voltage is fixed at U_acc=1.0 MV (Will also be presented in [Mai]).

Due to the chosen ranges of the machine parameter settings α_c and U_acc, the minimal value of the shielding parameter throughout this simulation study is Π=1.51. Thus, the SBB regime is not reached but close to the investigated bunch length range. Consequently, the predicted value of I_thr cannot be trusted completely and can only be used as a rough estimation and a starting point for a precise determination. To do this, a current decay without an additional impedance is simulated with Inovesa around the predicted threshold. From this, the used I_thr is determined by the routine that is described in Section 5.2. For the parameter range of U_acc and α_c, the assosiated I_thr extend over the range from 266 µA to 951 µA, which increases with α_c and decreases with U_acc. These dependencies are not only based on their direct impact due to Equation (2.70) but also because of their intrinsic impact on the synchrotron frequency. This I_thr is then also used for the finding of I_below for all the machine settings. For a comparability of the systematic scans, I_below is defined as 98.5 % of I_thr. This relative and arbitrary current deviation has been chosen since it is nearly identical to the deviation for the *f05135* scan. For the different machine settings, a simulation scan of the beam dynamics with different f_res has been performed at the respective I_below.

A scan of the momentum compaction factor is described in detail for a first one-dimensional discussion. In Figure 7.10, the maximal fluctuation power as a function of f_res is shown for different values of α_c but with fixed acceleration voltage U_acc=1.0 MV. What can be seen directly is that this f_res-scan below the unperturbed bursting threshold does not necessarily have a single peak like for the *f05135*-setting in Figure 7.2a. For some machine settings, two zones of f_res cause significantly enhanced CSR power so that the scan of the fluctuation power has a double-peak shape. To account for these different shapes of the f_res-scans, a double-peak Gaussian is used as the fitting function for all machine settings.

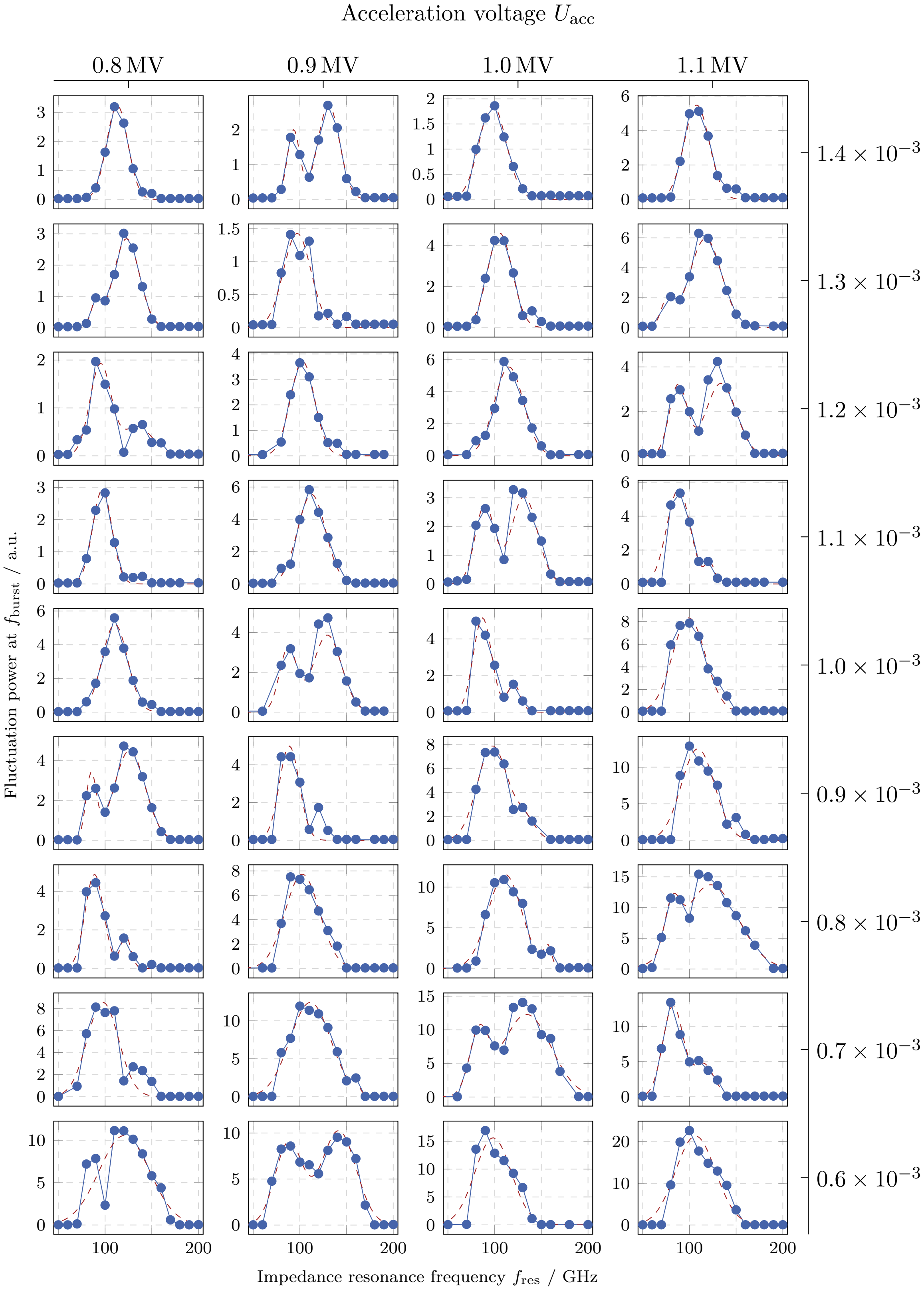

Figure 7.11. Maximal fluctuation power as a function of the resonance frequency: U_{acc} and α_c scan. (Modified version will also be presented in [Mai]).

The red dashed curve in the figure shows the fitting results with the double Gaussian

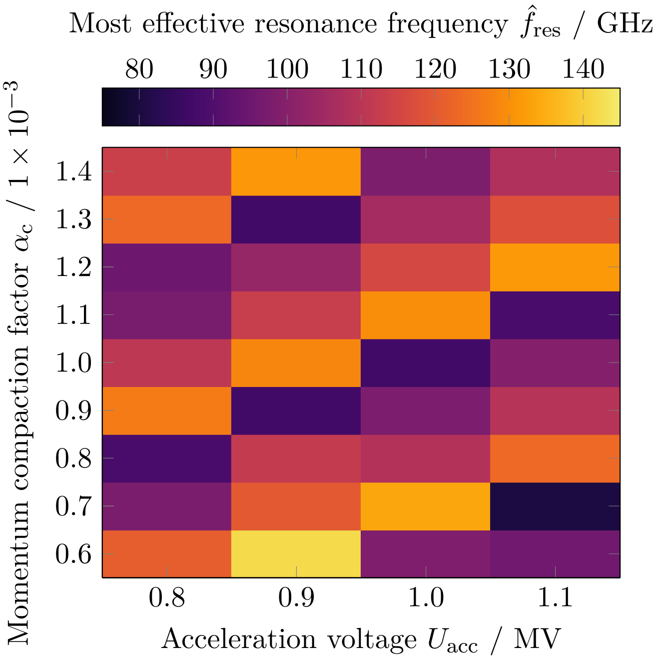

Figure 7.12. Most effective resonance frequency: machine setting scan. The simulated $\hat{f}_{\mathrm{res}}$ is shown as a function of the machine setting parameters; namely acceleration voltage U_{acc} and momentum compaction factor α_{c}. The bunch length decreases along the falling diagonal. Orthogonal to that, corresponding to comparable bunch length settings, $\hat{f}_{\mathrm{res}}$ is almost constant but changes periodically along the axis of increasing or decreasing bunch length (Modified version also presented in [Mai23]).

function. These fits are not only used to describe the f_{res}-dependency of the fluctuation power but also for the determination of $\hat{f}_{\mathrm{res}}$, which is given as the maximum of the fitting function. Besides the f_{res}-dependence and $\hat{f}_{\mathrm{res}}$ for the different machine settings, the fluctuation power at $\hat{f}_{\mathrm{res}}$ varies, too. However, a comparison or systematic study of the fluctuation power at $\hat{f}_{\mathrm{res}}$ is not meaningful due to the different beam currents for different machine settings.

In Figure 7.10 it is shown that $\hat{f}_{\mathrm{res}}$ and therefore the single peak or both peaks shift to smaller f_{res} with increasing momentum compaction factor. Above $\hat{f}_{\mathrm{res}} \approx 100\,\mathrm{GHz}$ only a single impedance frequency range with a width of about $\Delta f_{\mathrm{res}} \approx 40\,\mathrm{GHz}$ causes an amplification of the emitted CSR at I_{below}. As soon as the most effective resonance frequency reaches this border value, a side peak at about $f_{\mathrm{res}} = 170\,\mathrm{GHz}$ arises. By further increment of α_{c}, the two peaks shift simultaneously. Furthermore, the ratio of the maximal fluctuation power of the two peaks changes. This leads to an increase of the fluctuation power in the higher frequency range and reduction in the lower freqeuncy range. This "*redistribution*" continues until the left peak becomes insignificant below 70 GHz. Consequently, the peak at higher f_{res} becomes dominant at around 135 GHz. This also means that the most effective resonance frequency stays in the range of $80\,\mathrm{GHz} \leq \hat{f}_{\mathrm{res}} \leq 135\,\mathrm{GHz}$ and varies periodically with the momentum compaction factor.

The full machine setting scan of the fluctuation power as a function of f_{res} is shown in Figure 7.11 in a matrix form for α_{c} and U_{acc}. It is obvious that the identical dependencies on α_{c} occur independently of the acceleration voltage. Furthermore, it shows that in the complete investigated parameter range of the low-α_{c} mode, the f_{res}-scan of fluctuation power systematically looks similar. Independent of the machine parameters, an additional corrugated plate impedance with f_{res}<60 GHz or f_{res}>180 GHz does not cause enhanced CSR below the unperturbed threshold. In the f_{res} range in between, the fluctuation power

can always be described by a double-peak Gaussian. For the settings in which the two peaks have nearly the same magnitude in fluctuation power, almost the complete range $60\,\mathrm{GHz} \leq f_{\mathrm{res}} \leq 180\,\mathrm{GHz}$ shows a significant enhancement of the CSR. The range between $f_{\mathrm{res;min}}$ and $f_{\mathrm{res;max}}$ decreases with the reduced relative magnitude of the side peak. This narrowing goes until for the single peak, a range of about $\pm 40\,\mathrm{GHz}$ around $\hat{f}_{\mathrm{res}}$ is significantly excited.
However, since the f_{res}-scans are not identical within one row, U_{acc} also affects the most effective resonance frequency. Due to the limited number of simulated U_{acc} steps, such clear tendencies as for α_{c} cannot be identified easily. For example, for $\alpha_{\mathrm{c}} = 1.4 \times 10^{-3}$, a behavior similar to the discussed α_{c}-scans occurs when U_{acc} changes. With increasing U_{acc}, first a peak at higher f_{res} becomes dominant, and then a further increase leads to a reduction of $\hat{f}_{\mathrm{res}}$. Depending on the value of α_{c}, the arising of the second peak and the resulting jump of $\hat{f}_{\mathrm{res}}$ is more or less pronounced. In general, the periodic change of the most effective resonance frequency is also visible in dependence of U_{acc}.
The combined matrix form shows that increasing the acceleration voltage shifts the fluctuation power scans to larger α_{c}.The shape of the fluctuation power curve is constant along the rising diagonal in Figure 7.11. Since the zero-current bunch length σ_0 decreases with the falling diagonal (according to Equation (2.27)), the machine parameter settings along the rising diagonal correspond to settings with approximately the same or at least comparable bunch lengths.
Besides the shape of the fluctuation power scan, the most effective resonance frequency $\hat{f}_{\mathrm{res}}$ depends in a similar way on both machine parameters, which is shown in Figure 7.12. The constant value along the rising diagonal is even more visible in this depiction. In addition, it can be seen that $\hat{f}_{\mathrm{res}}$ repeats periodically in the direction of the change in bunch length. This indicates strongly that $\hat{f}_{\mathrm{res}}$ not only depends but is defined by the longitudinal dimension of the electron bunch. In the whole scanning ranges of U_{acc} and α_{c}, $\hat{f}_{\mathrm{res}}$ stays in the limited frequency range between 80 GHz and 135 GHz in the low-α_{c} operation mode at KARA. This allows the effective usage of a single corrugated structure to manipulate the CSR emission efficiently for different machine and beam settings. This will be discussed in more detail in the upcoming Sections.

7.2.2. Bunch Length Dependency

The knowledge of the impact of the machine parameters on the longitudinal beam dynamics, the creation of substructures, and the micro-bunching instability is important for the operation of the KARA storage ring. These parameters can be set to control the beam dynamics and the temporal profile of the emitted radiation in the THz frequency range. For the understanding of the underlying mechanisms, it is important to know the dependency on beam parameters. As the studies in the previous Section suggest, the zero-current bunch length σ_0 seems to be a crucial longitudinal beam parameter to determine the optimized additional corrugated structure impedance. The most effective resonance frequency $\hat{f}_{\mathrm{res}}$ is also being investigated for this purpose.
For the different machine parameter settings, the natural zero-current bunch length is determined by Equation (2.27). For a better comparison between different facilities, this study uses the dimensionless and accelerator-independent shielding parameter Π instead of σ_0. Equation (2.66) shows that it is propotional to σ_0 and scales with the unchangeable machine dimensions bending radius ρ and chamber height h_{c}.
The most effective impedance resonance frequency in dependence of Π is shown in Figure 7.13, in which a periodic reverse sawtooth like behavior with a sharp rise and a slower downramp can be recognized. The following fitting function can describe this sawtooth

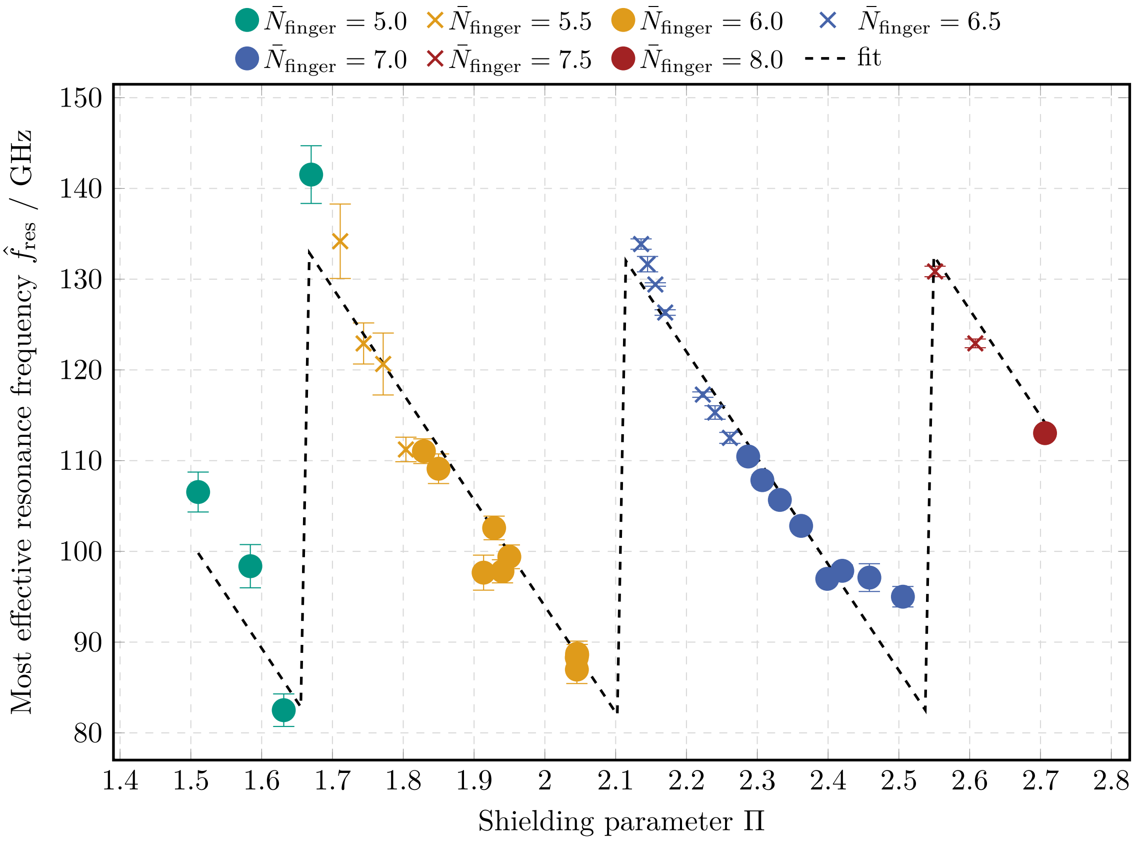

Figure 7.13. Most effective resonance frequency: bunch length scan. Impedance resonance frequency f_{res} of the maximal fluctuation power enhancement in dependence of the shielding parameter $\Pi \propto \sigma_0$. The color and shape coding corresponds to the number of fingers in the longitudinal phase space. The half-integers result from an unequal number of fingers in the inner and outer parts of the phase space. As soon as an additional substructure can be formed in the outer area of the phase-space, the most effective resonance frequency makes an unsteady change (Also presented in [Mai23],[Mai]).

dependence:

$$f(x) = -a \cdot \operatorname{mod}(x - b, c) + d^{11} \quad . \tag{7.1}$$

In this equation, the minus sign in front takes care of the negative slope, c is the periodicity and d is the maximal value of the function and, therefore, describes the maximal value of $\hat{f}_{\text{res}}$. The amplitude of the sawtooth is given by $c \cdot a$ so that the minimal value of $\hat{f}_{\text{res}}$ is defined as $d - c \cdot a$. The offset $\Pi_0 = 0.3381$ can be determined by $\operatorname{mod}(c, b)$.
The color and shape code in Figure 7.13 indicate the number of substructures in the longitudinal phase space for the respective simulated machine settings. As discussed in Section 5.2.2, the half-integer values are based on an unequal number of substructures in the inner and outer part of the phase space. In all cases, the higher number is determined in the outer part, which means that the creation of the substructures starts in this outer part. Because, therefore, the color corresponds to the substructure number in the outer part, it can be seen clearly that $N_{\text{finger,outer}}$ is a driving beam parameter that defines $\hat{f}_{\text{res}}$. As long as $N_{\text{finger,outer}}$ is constant, the most effective resonance frequency reduces linearly with Π and the bunch length, respectively. Thereby $\hat{f}_{\text{res}}$ is fixed in the range between

---

[11] Euclidean division: $\operatorname{mod}(x, y) = x \bmod y$

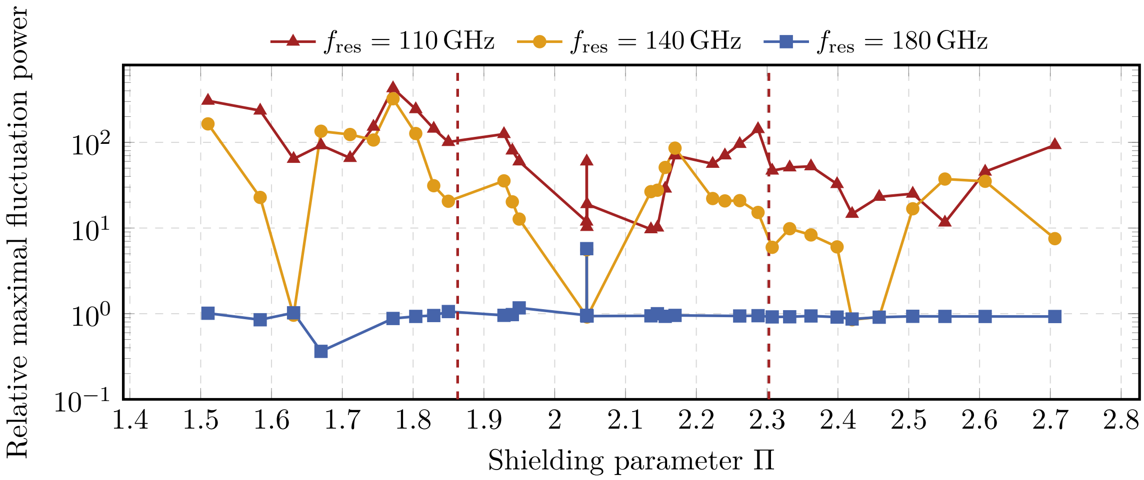

Figure 7.14. Fluctuation power for different f_{res}. The fluctuation power below the bursting threshold with a dedicated additional impedance, divided by the unperturbed fluctuation power for the respective machine setting. Additional impedances, whose resonance frequency is in the possible range of $\hat{f}_{\mathrm{res}}$, cause an enhanced CSR power.

$\hat{f}_{\mathrm{res,min}} = (82.9 \pm 3.2)\,\mathrm{GHz}$ and $\hat{f}_{\mathrm{res,max}} = (132.8 \pm 1.4)\,\mathrm{GHz}$, which has been examined as the limits in the previous Section. As soon as the bunch length is large enough so that another substructure fits in, it forms in the phase space distribution and bunch profile. Since Π does not change at this transition, the size of substructures changes instantly to its minimal possible value. This is synchronized with the sharp rises of $\hat{f}_{\mathrm{res}}$. The reduction of the substructure size to its minimal value corresponds to a sharp increase in the dominant substructure frequency in the bunch spectrum. This indicates that $\hat{f}_{\mathrm{res}}$ is directly related to the dominant substructure frequency. This relation will be discussed in detail in the following Section. The last green and blue data points deviate strongly from the fit. Both are close to the transition in which an additional substructure arises and the two peaks in the f_{res}-scan (Figure 7.11) have almost the same magnitude. Due to the limited frequency resolution, it is possible that the wrong peak is identified for determining the most effective resonance frequency $\hat{f}_{\mathrm{res}}$.

The jumps of $\hat{f}_{\mathrm{res}}$ match with the switch of the dominant peak in the f_{res}-scans of the fluctuation power. Aside from that, the double peaks in the fluctuation power only occur close to this transition range of the bunch length, where another substructure can be created. From the fit, the periodicity of the sawtooth is calculated as $\Delta\Pi = (0.443 \pm 0.011)$ and $\Delta\sigma_0 = (1.260 \pm 0.031)\,\mathrm{ps}$ for the KARA storage ring. The periodicity indicates the required change of machine settings to effectively manipulate the bursting threshold with the same impedance. It is a measure of the required longitudinal space to form another substructure. It must be noted that the latter relates to the zero-current bunch length σ_0. Therefore, it is not applicable to get real information about the actual size of the substructure at any non-zero bunch current, where the bunch length is increased in comparison to σ_0. This is especially the case as the bunch current and, therefore, the actual bunch length directly below I_{thr} is not comparable for the different machine and beam settings.

Due to the periodic change of $\hat{f}_{\mathrm{res}}$ over Π or σ_0, a corrugated structure with a dedicated resonance frequency can be used to enhance the emitted CSR power effectively for different machine settings. Figure 7.14 shows the fluctuation power, divided by the respective unperturbed value, as a function of Π for the three previously discussed impedances. For a structure with $f_{\mathrm{res}} = 110\,\mathrm{GHz}$ a clear enhancement by at least a factor of 10 can be recognized for the complete parameter range investigated. This can be explained by the fact that this impedance resonance frequency is relatively close to the middle of the range of $\hat{f}_{\mathrm{res}}$. Therefore, the resonance frequency of such an impedance is close to $\hat{f}_{\mathrm{res}}$ for all settings, so this impedance still causes a strong CSR enhancement. On top of that, it shows a roughly periodic oscillation, whereby the maximal enhancement is not reached for $\hat{f}_{\mathrm{res}} = 110\,\mathrm{GHz}$ (vertical red dashed lines), but for slightly larger $\hat{f}_{\mathrm{res}}$.

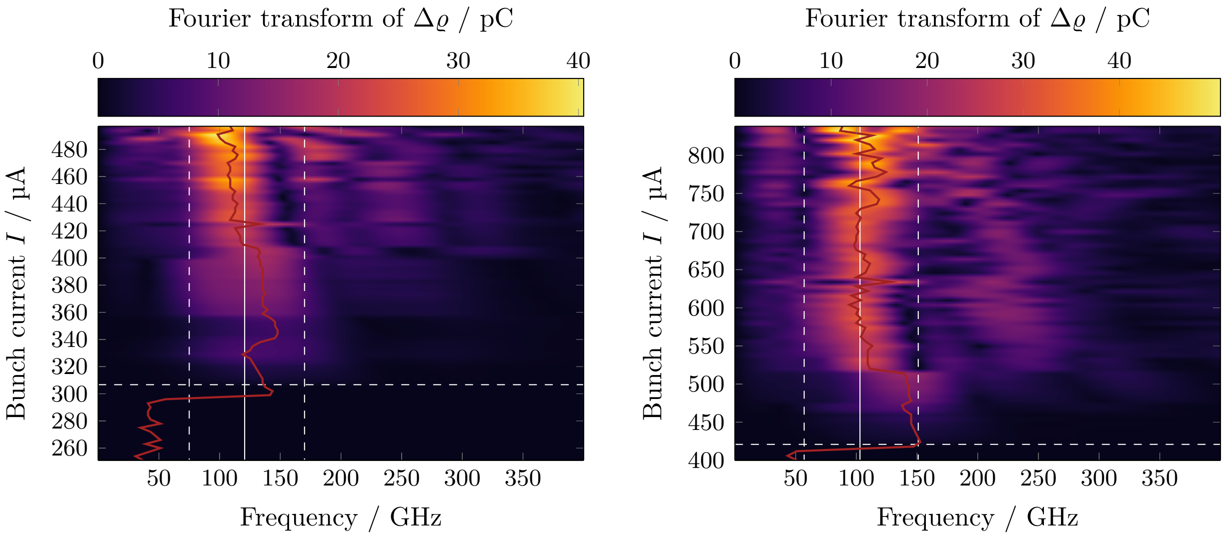

(a) $\alpha_c = 0.6 \times 10^{-3}$, $V_{acc} = 0.8\,\mathrm{MV}$ **(b)** $\alpha_c = 0.8 \times 10^{-3}$, $V_{acc} = 0.9\,\mathrm{MV}$

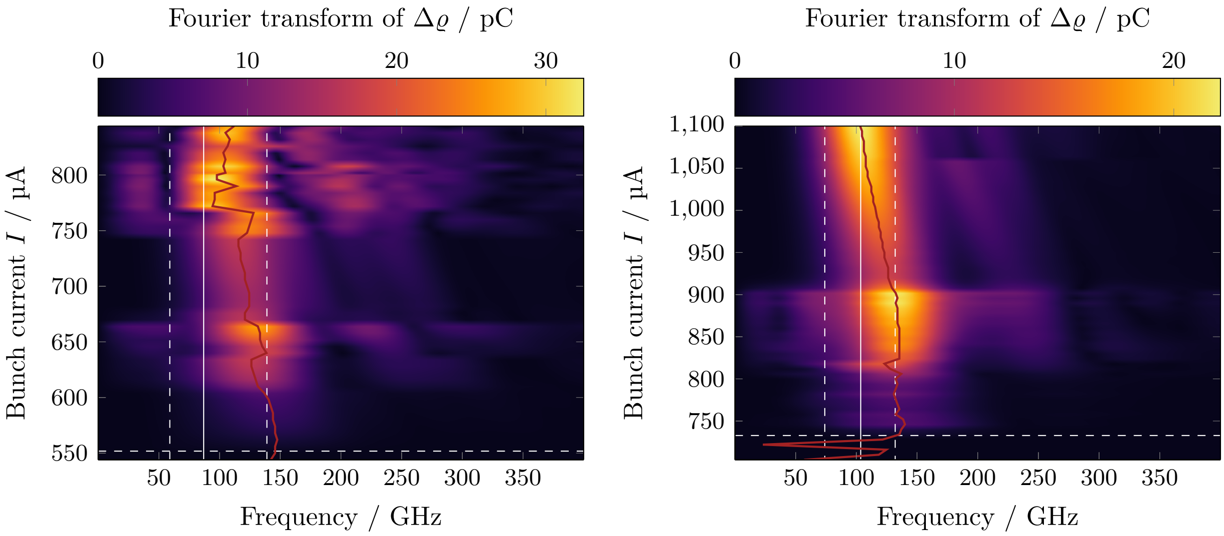

(c) $\alpha_c = 1.0 \times 10^{-3}$, $V_{acc} = 1.0\,\mathrm{MV}$ **(d)** $\alpha_c = 1.2 \times 10^{-3}$, $V_{acc} = 0.9\,\mathrm{MV}$

Figure 7.15. Substructure bunch spectrum. This spectrum, based on the relative substructure bunch profile $\Delta\varrho$ (see Figure 5.10), is shown as a function of the beam current for different machine settings ((a)-(d)). The horizontal dashed line indicates the bursting threshold. The vertical lines represent $\hat{f}_{res}$ (solid) and $f_{res;min}$ and $f_{res;max}$ (dashed). The red line shows the dominant frequency of the spectrum versus the current and converges towards $\hat{f}_{res}$ with increasing beam current.

This means that for these settings the enhancement of the fluctuation power is strong for a broader f_{res} range of the additional impedance. The scan for $f_{\mathrm{res}} = 140\,\mathrm{GHz}$ reveals a very similar behaviour. However, this resonance frequency lies outside of the $\hat{f}_{\mathrm{res}}$-range. Consequently, for the settings with the minimal $\hat{f}_{\mathrm{res}}$, this structure does not cause any additional CSR below I_{thr}, which can be seen by the drops in Figure 7.14. Since a impedance with $f_{\mathrm{res}} = 180\,\mathrm{GHz}$ does not cause any CSR radiation below the unperturbed threshold, the maximal fluctuation power is not affected by the additional impedance.
In his investigations of the rotation of the substructures in the longitudinal phase, T. Boltz [12] found a similar sawtooth behavior of the rotation frequency ($\mathcal{O}\,(\mathrm{kHz})$) as a function of the shielding parameter (see Figure 5.11 in [12]). However, in that work, the chamber heights have been scanned so that the oscillation frequency shows a normal sawtooth instead of a reverse sawtooth in dependency of Π. Nevertheless, it shows that the number of substructures and their size is a crucial parameter for different phenomena of the micro-bunching instability in different frequency ranges over several orders of magnitude (kHz to GHz).

Bunch Spectrum

The results of the previous Sections have shown that an additional impedance with the correct resonance frequency causes CSR emission in current ranges that - until now - have been unattainable for intense THz radiation. A strong indication has been provided that this $\hat{f}_{\mathrm{res}}$ directly depends on the size of the substructures in the longitudinal bunch profile. For a better comparison with the frequencies of the impedance, not the relative substructure bunch profile $\Delta\varrho$ but its spectrum with the dominant substructure frequency f_{sub} is investigated (see Figure 5.10 in Section 5.2.2).
In Figure 7.15, these spectra are shown as a function of the beam current for four machine settings as an example. To see the structures and dominant frequencies of the micro-bunching that can be triggered to enhance or suppress the creation of the substructures, the presented current scans show the simulation results without an additional impedance but only with the already existing impedance. The white lines indicate the respective bursting threshold current I_{thr} (horizontal), the most effective resonance frequency $\hat{f}_{\mathrm{res}}$ (vertical solid), and the two outermost frequencies $f_{\mathrm{res;min}}$ and $f_{\mathrm{res;max}}$ (vertical dashed). The red curve corresponds to the most dominant frequency in the substructure bunch spectrum f_{sub} in dependence on the beam current.
Since there are no substructures developed below I_{thr}, it is obvious and can be seen, especially in Figure 7.15a, that the bunch profile does not vary over time and no substructures are imprinted on the bunch profile. Consequently, no dominant substructure frequency f_{sub} arises. Above the threshold, the creation of the substructures is shown by the fact that in the Fourier transform of $\Delta\varrho$, a dominant frequency becomes visible. Its contribution increases with the beam current so that its color changes from red to yellow in the figures. First and foremost, it can be seen that this dominant frequency range of the substructure bunch spectrum remains mainly - except the lower current part in Figure 7.15d - in the range between $f_{\mathrm{res;min}}$ and $f_{\mathrm{res;max}}$. The exception is the machine setting with the longest bunch and highest threshold current out of the four. However, for this setting, the dominant substructure frequency also converges towards the area between the two dashed lines. The most dominant substructure frequency f_{sub} (red) stays for all the machine settings and is independent of the current and bursting regime between $f_{\mathrm{res;min}}$ and $f_{\mathrm{res;max}}$. With increasing current and deeper advance into the bursting regime and even the transition to the slow outburst regime, f_{sub} reduces slightly and converges towards $\hat{f}_{\mathrm{res}}$. The enlargement of the bunch can explain the reduction. With a stable number of substructures, the substructures themselves are enlarged so that the dominant substructure frequency f_{sub} decreases.
Previously, it has been shown that the creation of the substructures of the micro-bunching instability can be triggered by an external interaction with the environment by an additional

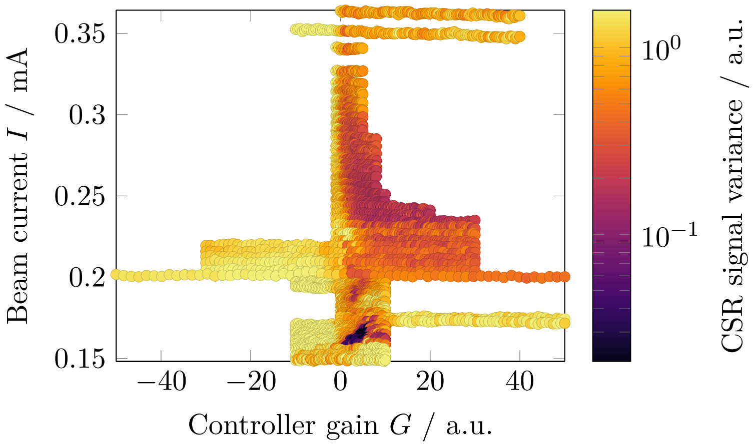

Figure 7.16. Feedback control at KARA: gain scan. A small value of the ratio of the variance of the CSR signal with and without the feedback control (blue) indicates a significant reduction of the amplitude of the sawtooth outbursts.

impedance. The study of the Fourier transform of $\Delta\varrho$ indicates that the additional impedance is most effective when its resonance frequency f_{res} corresponds to the size of the substructures that can be developed in the respective machine and bunch settings. In future simulation studies, it can be checked whether and how a reduction of the impedance at $\hat{f}_{\text{res}}$ can help to reduce or avoid the creation of the substructures at even higher bunch currents. In such a case, it must be considered that this might suppress the outbursting and the stable bursting regime, which is an essential source of temporal stability and enhanced CSR in the THz range.

7.3. Feedback Control

With the same goal of observing, understanding, and controlling the micro-bunching instability, the feedback control, which has been developed by C. Evain *et al.* [11] for the Synchrotron Optimized Light Source of Intermediate Energy to LURE (fr. Source optimisée de lumière d'énergie intermédiaire du LURE) (SOLEIL), has been adapted by Clément Evain for current decay mode at KARA. Luca Scomparin has implemented this feedback control on the Field Programmable Gate Array (FPGA) platform and integrated it into KARA. The setup has been tested at the KARA storage ring, leading by Luca Scomparin, Andrea Santamaria Garcia and the colleagues from Laboratory of Physics of Laser, Atoms, and Molecules (PhLAM) around Clément Evain. The controller for KARA is fundamentally different from the SOLEIL one. As described in [11], the SOLEIL controller determines the applied signal $\Delta U_{\text{acc}}(t) = G \cdot$ [CSR(t)-CSR(t-delay)] with controller gain G. For the setup at KARA only the signal $\Delta U_{\text{acc}}(t) = G \cdot \text{CSR(t)}$ is used, to avoid any issues due to the current decay. Consequently, a scan of the gain can only be executed as a function of the beam current.

The emitted CSR intensity is converted into an electrical signal by a Schottky diode detector, and is then digitized with KAPTURE[12] [103] at the *IR1* beamline (see Section 3.6 in [73]) of KARA, which is connected to an FPGA. This FPGA is connected to a second FPGA inside the storage ring via a fiber. This second FPGA is connected to the low-level RF (LLRF) system of one of the two RF sections, so that the $\Delta U(t)$ can be applied. The cavities in the RF section, used for the feedback control, are operated at the zero-crossing phase of the accleration voltage so that only the other section is used for the regain of the radiated power.

---

[12] Karlsruhe Pulse Taking Ultra-fast Readout Electronics

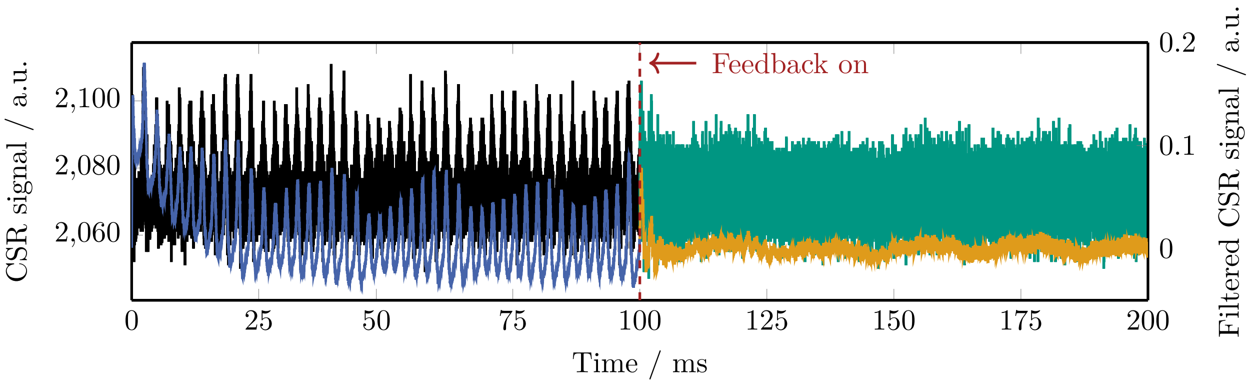

Figure 7.17. Feedback control at KARA: Effective outburst suppression. At $t = 100\,\mathrm{ms}$, the feedback control is turned on. The black and green curves represent the orignal electrical signal of the Schottky diode. The blue and orange curves correspond to the filtered data, which suppress the fast sinusoidal fluctuation of the CSR signal in the bursting regime. Through this filtering, the sawtooth outbursts and their effectivly suppression becomes more visible.

The results presented here, which will be part of a forthcoming publication [Sco], refer to a scan with the settings of momentum compaction factor α_c=3.1×10^{-4}, acceleration voltage amplitude U_acc=767 kV, and the bursting threshold I_thr=115 µA. To determine the efficiency of the gain to control the sawtooth behavior of the micro-bunching instability, the ratio of the variance of the CSR signal with and without the feedback control is shown in Figure 7.16. The blue area indicates that the amplitude of the outbursts can be reduced effectively only in small current range in the slow outburst regime. The applied modulation of the acceleration voltage amplitude $\Delta U(t)$ can cause an elongation of the bunch. For the right gain, the equilibrium between the formation and disappearance of the substructures can be reached. Therefore, even at higher beam currents, the stable bursting regime without the periodic sawtooth outbursts of intense CSR can be achieved. In the stable bursting regime below the slow outburst threshold $I_\mathrm{thr;slow}$, the variance of the CSR signal is already relatively small. Therefore, the feedback control cannot reduce the variance by orders of magnitude, so that for smaler currents than the effective blue island the impact of the feedback control is decreasing again.

Figure 7.17 shows as an example the most effective current and gain setting ($I = 159\,\mu\mathrm{A}$ and $G = 3.55$). The filtering of the electrical signal of the Schottky diode removes the fast sinusoidal fluctuation of the CSR signal (low-pass filter) and corrects dynamically the offset (high-pass filter). It can be seen that after turning on the feedback control, the temporal profile of the CSR signal changes instantly. In comparison to the blue curve (feedback off), the amplitude of the sawtooth outbursts in the orange curve (feedback on) is significantly reduced and almost completely suppressed. It should be stressed that the fast CSR fluctuations are still present, so that the enhanced THz radiation is usable in the stable bursting regime. In this most effective configuration, the variance of the CSR signal is reduced by a factor of 28, which makes this operation mode much more attractive to the users of the synchrotron light. However, that does not just mean that the emission of the CSR can be manipulated. Rather, this shows that at a fixed beam current it is possible to control the longitudinal beam dynamics by an external influence - like the feedback control - in such a way, that the regime of the micro-bunching instability can be changed.

7.4. Summary

In this chapter, it was shown that corrugated structures with a shunt impedance $Z_0 = 1\,\mathrm{k}\Omega$ and a resonance frequency f_res in the range from 60 GHz to 180 GHz can affect the longitudinal beam dynamics and the properties of the micro-bunching instability significantly. For $80\,\mathrm{GHz} \leq f_\mathrm{res} \leq 135\,\mathrm{GHz}$, the threshold of the bursting regime I_thr can be reduced most effectively. Since the threshold of the outburst regime with the slow periodic outbursts is less strongly affected, such an impedance can be used to better understand the underlying mechanisms of the instability. Additionally and more importantly, the current range between the two thresholds with enhanced but temporal stable CSR power can be increased and used as a source of intense THz radiation.

The dependency of the most effective impedance resonance frequency $\hat{f}_\mathrm{res}$ to cause CSR below I_thr on the machine and beam setting shows a sawtooth behavior as a function of the bunch length. Combined with a study of the size of the substructures on the longitudinal bunch profile, this reveals that the creation of the substructures is caused and triggered if the frequency of an external impedance matches the dominant frequency in the bunch spectrum, which corresponds to the size of the substructures.

In the planned impedance manipulation chamber at the KARA storage ring, only two different corrugated structures with their respective impedances can be installed. Since, not only in this chapter but also in several experiments, the micro-bunching instability is studied in detail for the machine settings of the KARA fill *f05135*, the resonance frequency of one structure should be equal to $\hat{f}_\mathrm{res} = 110\,\mathrm{GHz}$ of this settings. Furthermore, the resonance frequency lies in the middle of the effective range, so it can be used to manipulate the properties of the micro-bunching instability over an extensive range of machine and beam settings. The second impedance should have the resonance frequency $f_\mathrm{res} = 180\,\mathrm{GHz}$. With this structure, it will be possible to increase the bursting threshold and to study the impact of the additional impedance on the fluctuation frequency of the CSR power. The dimensions of these corrugated structures are given in Table 6.3, and the production of prototypes is discussed in the upcoming chapter.

8. Manufacturing of the Structures

In the previous chapter, it has been shown that corrugated structure impedances with f_{res}=110 GHz and f_{res}=180 GHz are the most interesting for the installation in the KARA storage ring. Based on the studies in Chapter 6, the optimized corrugation parameters for these two structures can be determined (see Table 6.3). However, discussions with different institutes and companies concerning the production of corrugated structures have revealed that the acceptable tolerances of the corrugation parameters must be defined and that the idealized perfectly rectangular shape cannot be guaranteed.

This chapter describes the way to produce prototypes for the corrugated plates. The first section focuses on the design of the plates and discusses the need for side walls and additional cooling due to the heat loading. Afterward, the tolerances of the corrugation parameters are defined so that the deviations of the impedance parameters are still acceptqable. In the same section, impedance simulations are presented to determine the impact of different kinds of deviation from the perfectly rectangular corrugation shape. In Section 8.3, different manufacturing methods and prototypes are presented.

8.1. Corrugated Structure Design

Before the structures can be installed, the dimensions of the corrugations and the design and dimensions of the plates must be determined. Although the width and length of the structure do not affect the impedance resonance frequency, they are crucial to getting the maximal impact by the additional impedance and avoiding boundary effects.

8.1.1. Plate Width

The width x_0 of the corrugate plates should not affect its longitudinal impedance. However, this is only the case above a certain threshold width, from which the side edges do not affect the traveling bunch. Below this threshold, the bunch "sees" the side edges of the plate, which causes boundary effects and therefore can change the longitudinal impedance as well.

For the determination of the required minimal width, to avoid these effects of the lateral edges, the impedance as a function of the plate width x_0 has been simulated. For a corrugated structure with $h = 200\,\mu\mathrm{m}$, $L = 100\,\mu\mathrm{m}$, and $L/g = 2$, the shunt impedance and resonance frequency as a function of x_0 are shown in Figure 8.1. It can be seen that a narrower plate causes a suppression of the shunt impedance Z_0 and a simultaneous shift of the resonance frequency f_{res}. In the case of $x_0 \leq 12\,\mathrm{mm}$, the shunt impedance decreases nearly linearly. The resonance frequency decreases exponentially for the same range of x_0. For broader plates, these two impedance parameters approach a saturation level. Their asymptotic limit is reached for $x_0 \geq 16\,\mathrm{mm}$ for Z_0 and f_{res}. Consequently, $x_0 = 16\,\mathrm{mm}$ can be defined as the minimal plate width to avoid boundary effects and significant Z_0 reductions [Mai22a].

For the determination of the value of x_0, used for the horizontal beam size ($\sigma_{\mathrm{x}} \approx 0.5\,\mathrm{mm}$)

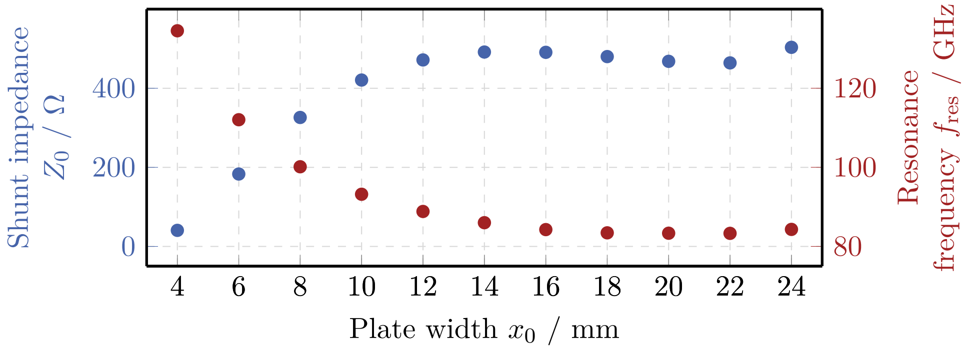

Figure 8.1. Impedance parameters in dependence of plate width. Shunt impedance Z_0 (blue) and resonance frequency f_{res} (red) in dependence of the width x_0 of the corrugated plate for a fixed corrugation depth $h = 200\,\mu\mathrm{m}$, periodic length $L = 100\,\mu\mathrm{m}$, and plate distance $b = 5\,\mathrm{mm}$. A saturation for both parameters is reached at $x_0 = 16\,\mathrm{mm}$ (Also presented in [Mai22a]).

must be taken into account. For the CST impedance simulation, the bunch is represented by a line-current without a transverse spread. From the conclusion of Figure 8.1, the corrugated plates should have a width larger than 20 mm so that the outer particles in the beam only see the desired corrugated structure.

This parameter is essential for different reasons. As discussed in Section 4.1, the number of mesh cells and, therefore, the simulation time depends on the dimensions of the investigated structure - including x_0. Furthermore, the production time and costs for most of the possible manufacturing methods scale with the area, so as little unnecessary area as possible should be structured. In comparison with the horizontal width of the normal beam pipe of the KARA storage ring ($x_{\mathrm{KARA}} = 70\,\mathrm{mm}$), the corrugated plate is relatively narrow. This makes it possible to install three strips with different and independent corrugation parameters (and therefore different additional impedances) horizontally next to each other. With this configuration, it is possible to exchange the additional impedance without the elaborating and time-consuming breaking of the vacuum in the chamber. However, this requires additional motors so the chosen strip can be centered over (and under) the bunch by moving the plates horizontally. One of these three - and ideally the middle one - strips is required to be a reference strip without any corrugations to distinguish the impact of the corrugations and the change of the aperture. Consequently, only two strips with different corrugations can be installed, tested, and studied at the same time. As discussed in the previous chapter, the first installed additional impedances should be created by the corrugated Structure 1 ($f_{\mathrm{res}} = 110\,\mathrm{GHz}$) and Structure 2 (180 GHz).

8.1.2. Plate Material

Since the plates will be installed in an accelerator complex, there are several requirements for the material so that the corrugated structures only manipulate the longitudinal impedance and do not affect the machine in any other ways. Therefore, it must be compatible with the UHV and non-magnetic to avoid the uncontrolled creation of magnetic fields and the resulting forces on the particles. The material must be electrically conductive to realize appropriate wakefields and impedance.

The impact of the material choice on the longitudinal impedance is presented in Figure 8.2 for two values of plate distance b (red and blue). The parameters of the three materials used in the study (copper, steel, and stainless steel) are listed in Table 4.1. For both b settings, the impact of the material on the resonance frequency is negligible. For the larger plate distance, the material has no visible influence on the impedance. In the case of the

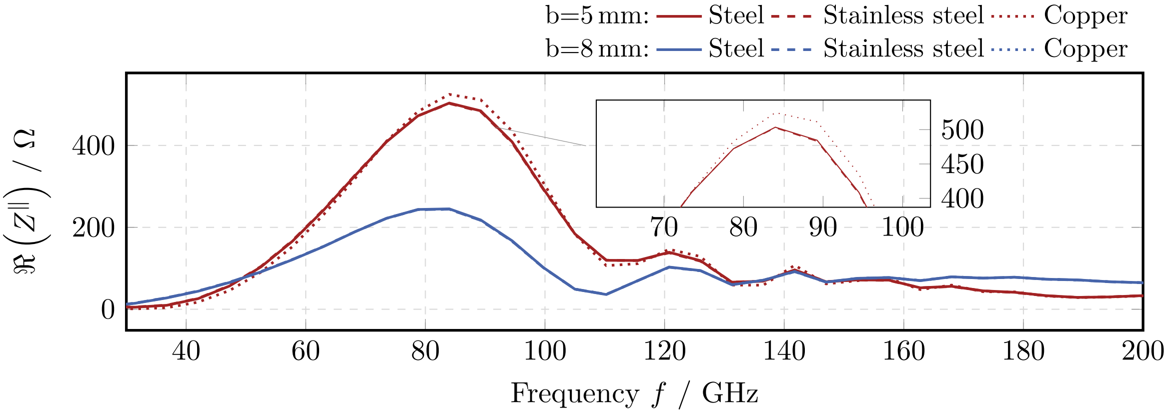

Figure 8.2. Shunt impedance for different plate materials. The real part of the impedance shows no significant change in dependency of the plate material (different line style) for both values of the plate distance b. There is only a minimal dependence of the shut impedance on the electrical conductivity visible. The fixed parameters are corrugation depth $h = 200\,\mu\text{m}$, periodic length $L = 50\,\mu\text{m}$, and duty cycle $L/g = 2$.

smaller b (red), there is at least a small impact on the shunt impedance recognizable. It can be seen that Z_0 scales with electric conductivity σ_{el} ($\sigma_{\text{stainless}} < \sigma_{\text{steel}} < \sigma_{\text{copper}}$). However, this material impact on the shunt impedance is still significantly smaller than for all other corrugation and plate parameters. This mainly negligible material dependency is consistent with the expectation, based on Equation (2.50), that the impedance is only determined by the geometry of the corrugations.

Due to this small impact of the material, which can also be compensated by a minor adjustment of the corrugation parameters, all three materials are acceptable for the corrugated plates. The final material choice is mainly determined by the requirements, preferences, and experiences of the manufacturing methods, as well as by the availability and material costs.

8.1.3. Structure Length

The beam dynamics studies in Chapter 7 have shown that at least Z_0=1 kΩ is required to create a significant impact on the micro-bunching instability. The structure length must be maximized to create an impactful impedance, and the plate distance must be minimized. However, the structure length s is limited by the available space, and the minimal value of the plate distance b is defined by the significant particle losses due to the small geometric aperture. To avoid unplanned impedance contributions due to a discontinuous change in the cross-section (see Collimator impedance in Section 2.4), taper sections are necessary up- and downstream of the structure. Based on the experience of the insertion devices at the KARA storage ring, like X-SPEC [79], the maximum slope of the taper should be 1 mm per 1 cm (10 %) between the half chamber height $\frac{h_c}{2}$ and b. Since the length of the taper section increases with a smaller opening gap, a trade-off between b and s must be found. Therefore, their quantitative impact on $Z^{\parallel}$ needs to be checked.

In Figure 8.3a the impedance for structure lengths 10 cm$\leq s \leq$20 cm is shown. Since the dimensions of a single corrugation are kept constant, their number N_{corr} is proportional to s. It can be seen that Z_0 can be changed significantly, whereas the resonance frequency and the absolute peak width stay nearly constant. Furthermore, for the chosen corrugation settings, $Z_0 > 2\,\text{k}\Omega$ can be reached for $s = 20$ cm.

For different corrugation depths, the shunt impedance as a function of s is shown in Figure 8.3b. For a better comparison of the different corrugation settings, Z_0 is normalized

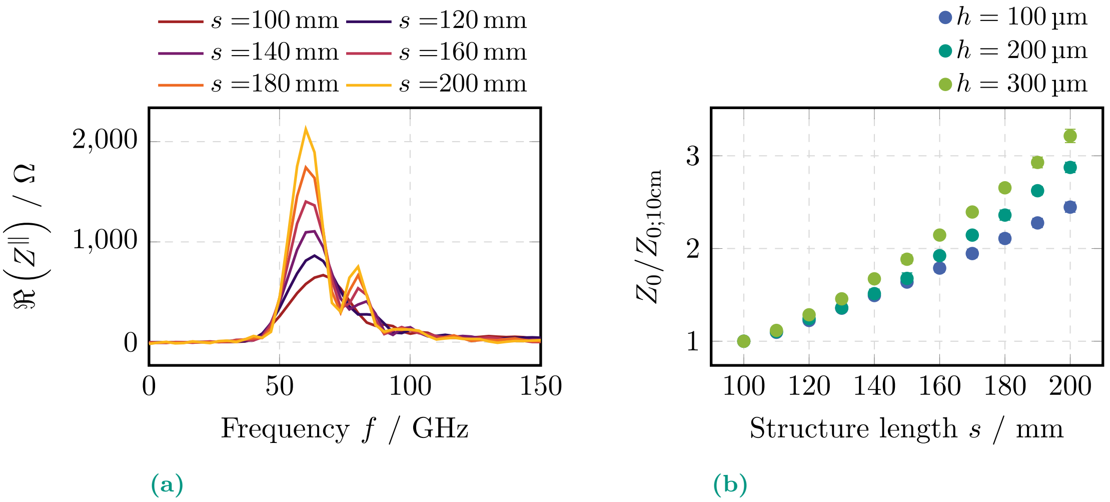

Figure 8.3. **Shunt impedance for different plate lengths.** (a) The real part of the longitudinal impedance $Z^{\|}$ for different structure lengths s show that only the shunt impedance increases with s and the resonance frequency remains unchanged. (b) The shunt impedance increases nearly linearly with the structure length; however, the slope increases with the deepening of the corrugations. For better comparison, Z_0 is normalized by its value for $s = 10\,\mathrm{cm}$ ($Z_{0;10\mathrm{cm}}$). The fixed parameters are corrugation depth $h = 300\,\mu\mathrm{m}$, periodic length $L = 200\,\mu\mathrm{m}$, and duty cycle $L/g = 2$.

by its value for $s = 10\,\mathrm{cm}$. The s-dependence, shown as the slope of the data points in Figure 8.3b, clearly scales with the corrugation dimensions. In the examples shown here, the slope of the data points increases with the corrugation depth h. Independently of the corrugation parameter, Z_0 grows nearly linearly to a first approximation. It can be seen that a doubling of the structure length (from 10 cm to 20 cm) causes more than a doubling of the shunt impedance.

8.1.4. Plate Distance

A direct impact of the half plate distance b on the shunt impedance is expected since the amplitude of electromagnetic fields, such as the wakefields, decreases with the increasing distance. This dependence is of great interest for two main reasons. Firstly, the plate distance is the only tuning knob that will be changeable during the experiments since the structure of the corrugation and the size of the corrugated plate are fixed. Secondly, the impedance manipulation studies will only take place in dedicated "*machine physics*" time slots. The additional impedance by the corrugated structures must be deactivated or removed during the normal UO and the other experiments.

Figure 8.4a shows the variation of the simulated impedance as a function of the half plate distance b of the corrugated plates with fixed values of $h = 200\,\mu\mathrm{m}$, $L = 50\,\mu\mathrm{m}$, and $L/g = 2$. With increasing b, a distinct reduction of the impedance magnitude can be seen, which matches the prediction from Equation (2.50). As expected, the plate distance does not significantly affect f_{res} because the corrugation geometry does not change by changing the plate distance b. The shunt impedance as a function of the plate distance is shown in Figure 8.4b for a quantitative discussion of this reduction. From Equation (2.50), combined with the pre-factors and the δ-function, a $1/b^{5/2}$ dependency of Z_0 can be expected for a cylindrical pipe. The real exponent of the power-law $1/b^{\gamma}$ for the simulation results has been determined as $\gamma = (2.23 \pm 0.02)$ by the fit. So, the scaling with a power-law is in very good agreement with the prediction. However, the exponent is significantly smaller than

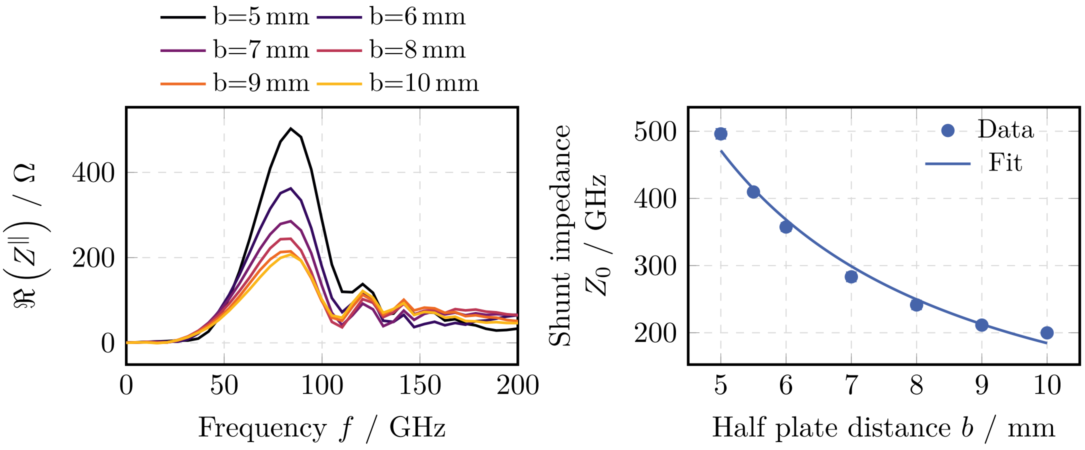

(a) (b)

Figure 8.4. Shunt impedance for different plate distances. (a) The real part of the longitudinal impedance $Z^{\parallel}$ for different half plate distances b shows, that the shunt impedance decreases with b, whereas the resonance frequency remains unchanged. (b) The dependency of the shunt impedance Z_0 on b can be described by $1/b^{\gamma}$ with $\gamma = (2.23 \pm 0.02)$. The fixed parameters are corrugation depth $h = 200\,\mu\text{m}$, periodic length $L = 50\,\mu\text{m}$, and duty cycle $L/g = 2$ (Also presented in [Mai22a]).

the description of a theoretical model for a cylindrical corrugated pipe. Analogous to the discussions in Chapter 6 for the corrugation parameters, the deviation might be explained by the different geometric shapes of the structure. As described previously, the parallel plate geometry used and studied here can cause boundary effects that do not occur for symmetrical and closed cylindrical geometry. For a fixed plate width x_0, this effect can be scaled width b since the effective width of the structure increases with the plate distance for a constant opening angle. Therefore, the boundary effects occur for larger values of b and influence the scaling of Z_0 [Mai21].

Analogous to the permanent magnet in-vacuum IDs, like X-SPEC [79], only the strength of the corrugated structure can be modified by opening or closing the gap. Furthermore, it can be seen that the impact of the additional impedance is in the order of 5 % if the structures are removed to the normal beam pipe radius ($b = h_c/2$). With the plane reference strip as the middle strip, no additional cover to suppress the additional impedance is necessary.

Compared to the s scan, it reveals that the plate distance has a stronger influence on the shunt impedance. Due to the exponential reduction of Z_0, the minimal possible gap size $b = 5\,\text{mm}$ should be used for the experiments. This, however, requires longitudinal tapers up- and downstream of the structure of at least 11 cm, each. Therefore, $s = 20\,\text{cm}$ gives the maximal possible structure length.

The design of the moveable plates in two dimensions with the matching taper section can be adapted from the X-SPEC permanent magnet undulator [79] and the corrugated plate dechirper at SwissFEL [14].

8.1.5. Side Walls

The corrugated structure will be installed in a dedicated chamber that is significantly broader than the KARA beam pipe. The width is needed not only but especially because of the required extra space for the horizontal movement and exchange of the different corrugated strips. This design might require vertical side walls to reduce the transverse discontinuity of the beam pipe, in particular for the case with the "*deactivated*" structure in the normal UO. Therefore, it is studied whether and how side walls made of the same

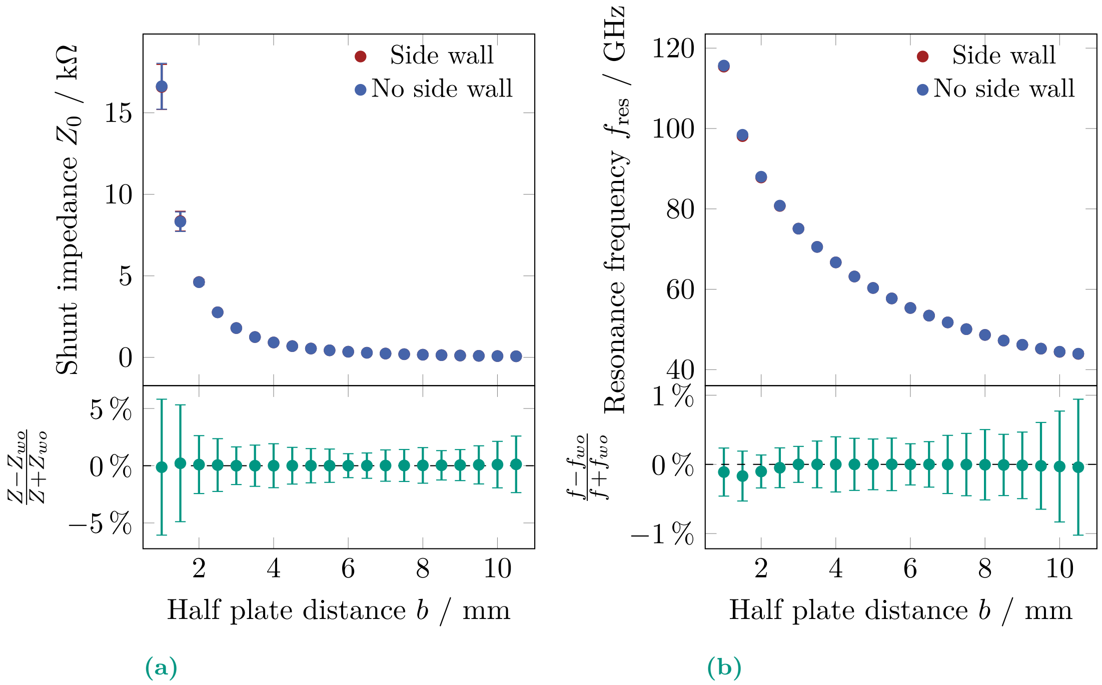

Figure 8.5. Side wall impact on longitudinal impedance. For different values of the plate distance, the impedance parameters shunt impedance (a) and resonance frequency (b) are shown with and without additional side walls. To make the small deviation more visible, the bottom shows the relative deviation of the respective parameter between the simulation with and without the side walls. For both parameters and, therefore, the longitudinal impedance, the impact of side walls is negligible. The fixed parameters are corrugation depth $h = 300\,\mu\mathrm{m}$, periodic length $L = 200\,\mu\mathrm{m}$, and duty cycle $L/g = 2$.

material as the corrugated plates influence or disturb the longitudinal impedance of the corrugated structures.

Since the impact of side walls should not change for different corrugation geometries but can be affected by the plate distance, an impedance scan with and without side walls has been simulated for different values of b. To estimate the strongest possible impact, the side walls are added at both sides of a single strip with the width $x_0 = 20\,\mathrm{mm}$. This determines (for only one side wall) the situation if one of the outer strips is selected.

Figure 8.5 shows Z_0 and f_{res} as a function of the plate distance with (red) and without (blue) the additional side walls. Since no difference is visible in the upper parts, the bottom of the plots shows the relative deviation between the settings with and without the side walls. For these two impedance parameters, the deviation is for all plate distances on a level below 2 ‰ and, therefore, negligible. In comparison, relatively large uncertainties in the order of 1 % are based on uncertainties of the fit parameters.

In order to maintain the possibility of keeping the plate distance b flexible, the side walls cannot be fixed at both corrugated plates. Consequently, both side walls should only be mounted on one plate. Figure 8.6 illustrates the case if the two side walls are mounted at the different plates. With this configuration, choosing a single strip and a combination of different impedances at the top and bottom plates would be possible.

8.1.6. Heat Load Estimation

Due to the interaction with the environment via the wakefield, the particles emit radiation (e.g., SPR, see Section 2.5), which leads to power loss. This radiation can hit the corrugated

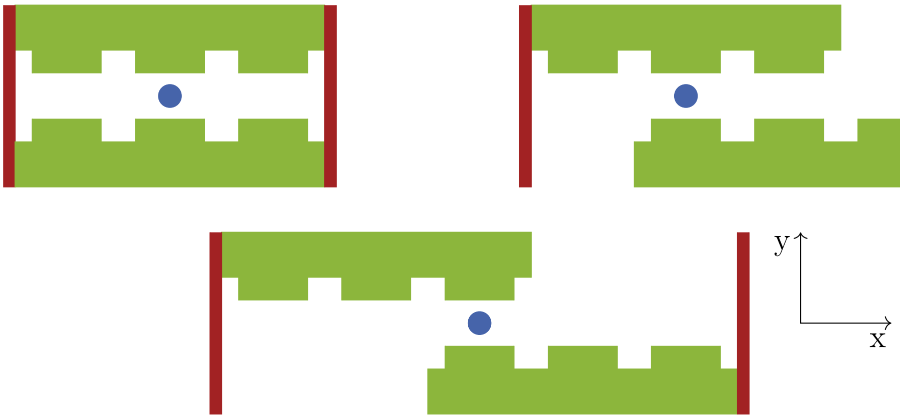

Figure 8.6. **Side-wall design.** All three subfigures show the three corrugated strips (green). If one side wall (red) is fixed at the top plate and the other one at the bottom plate, it is not only possible to choose a single strip, but also a combination of different corrugations at the top and bottom are possible. Here, only a selection of the possible combinations is shown.

plate and can be deposited there in the form of heat. An estimation of this influence is necessary for the material choice regarding thermal conductivity and the necessity of active cooling.

In order to determine the total power loss of the bunch during its passing of the structure, the wake loss factor has been calculated for different bunch lengths with Equation (2.43). This has been done assuming a Gaussian charge distribution and the RMS bunch length σ. The bunch charge is fixed on $q = 100\,\text{pC}$, which corresponds to 271 µA in single bunch operation. Furthermore, a corrugation setting with a relatively high Z_0 has been used [Mai21]. Since the wake loss factor is determined by the overlap of the wake potential and the bunch profile, the area included in the calculation is limited to $\pm 5\sigma$, as the charge distribution only has a relevant contribution in this.

Figure 8.7a shows that the amplitude of the wake potential V increases with a shortening of the bunch. The wake loss factor k_l calculated from this is shown as a function of σ in Figure 8.7b. The corresponding power loss is proportional to k_l and determined by Equation (2.44) for a single bunch. Obviously, k_l decreases with lengthening the bunch. However, the dependency differs from the impedance of a beam scraper, which has a $1/\sigma$ behaviour [51]. For the corrugated structure, the wake loss as a function of the bunch length can be described in good agreement with $k_\text{l}(\sigma) = A \cdot \exp\left(B \ln\left(\sigma\right)^C\right)$. From this, it can be calculated that for a bunch length of $\sigma = 2\,\text{ps}$, a power of 0.74 W gets lost. For the zero-current bunch length of the KARA fill *f05135* (σ_0=4.1 ps) the loss is already reduced to 0.18 W. Therefore, it must be considered that the real bunch length for this machine setting is even longer, so the actual power loss is smaller.

To estimate how large this power loss is compared to the synchrotron radiation power that occurs during UO, the fraction of the SR that goes towards the impedance chamber needs to be assessed. In Figure 8.8, the impedance chamber and the upstream bending magnet with its emitted radiation are shown schematically. Thereby, it is assumed that all 16 bending magnets emit the same amount of SR homogeneous over their bending angle of 22.5 °. The left corner of the impedance chamber, marked as green color in Figure 8.8, is located 1.875 m downstream of the bending magnet with a horizontal offset of 20 cm from the reference beam path . From this, it can be geometrically calculated that the SR component in the range from 22.197 ° to 22.500 ° can hit the area of the chamber. For

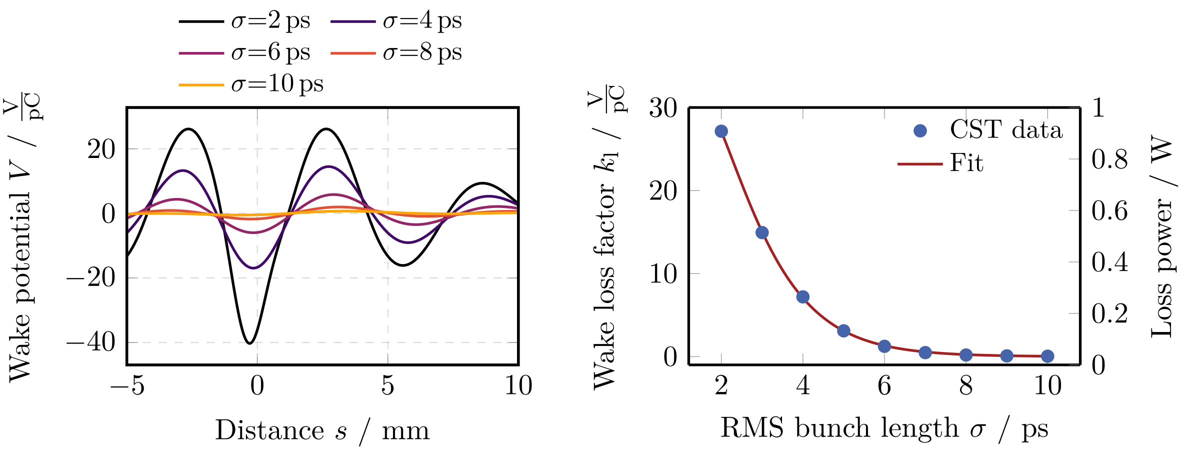

(a) **(b)**

Figure 8.7. Wake potential and wake loss factor. (a) The wake potential V of the corrugated structure decreases with the bunch length. The head of the bunch is at the left side for negative values of s.(b) Under the assumption of a Gaussian charge distribution with the charge q=100 pC, the wake loss factor k_l can be calculated as a function of the RMS bunch length. The fit can describe the dependence of k_l and the corresponding loss power. The fixed corrugation parameters are corrugation depth $h = 300\,\mu\mathrm{m}$, periodic length $L = 100\,\mu\mathrm{m}$, and duty cycle $L/g = 1.33$ (Also presented in [Mai21]).

the UO at 2.5 GeV and 200 mA, this corresponds to a SR power of 90 mW. This power is irradiated towards the planned position of the impedance chamber, and there is no cooling of the current and normal beam pipe necessary.

It must be mentioned that both SR and wake powers are not wholly converted into heat in the corrugated plates, so the heating power is overestimated. Even if both the loss power of the wakefield and the SR power are only estimated, they are in the same order of magnitude. Consequently, at least for the single bunch mode, no additional cooling is required. Nevertheless, mounting the corrugated plate on a holder with a large thermal conductivity should be considered to dissipate the energy in the structure deposited.

8.2. Manufacturing Tolerances

Every single manufacturing process can produce the corrugations only inside its tolerances. At the beginning of this section, the acceptable tolerances of the corrugation parameters are discussed so that the impedance remains within a suitable range. Afterward, the impact of a phase shift due to the production from several parts, a deviation from perpendicular corrugation side walls, and a nonconstant corrugation depth/height are described.

8.2.1. Corrugation Parameters

In Chapter 6, it has been described in detail and how the parameters corrugation depth h, periodic length L, and the duty cycle L/g or longitudinal gap g respectively, influence and define the impedance of the corrugated structure.

For the determination of the tolerances, the relation found between the corrugation and impedance parameters via the Corrugated Plate Impedance Parameter (CPIP) Ξ (see Section 6.3) is used so that only h and g are studied. Furthermore, the tolerances of the corrugation parameters have been investigated individually. This means that only one parameter is varied, whereas the other two corrugation dimensions are fixed at the

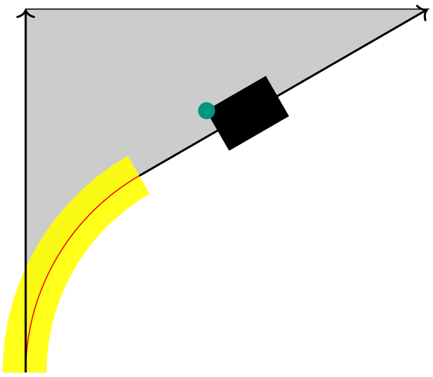

Figure 8.8. CSR power hitting the impedance chamber. The bending magnet (yellow) emits CSR radiation over an angle of 22.5 ° (gray area). A part of this radiation hits the impedance chamber (black), which is placed downstream of the bending magnet. The left front corner (green mark) marks the point of the chamber that is hit by the radiation under the smallest deflection angle of the previous bending magnet.

optimized and desired value. Since no absolute but relative tolerances are determined, the tolerances are independent of the corrugation and impedance parameters.

To find the maximal acceptable deviation of the corrugation parameters from the optimized settings, the tolerances for Z_0 and f_{res} need to be set. As the tolerance for the shunt impedance, only a lower limit for the value of Z_0 has been settled as $-10\,\%$ and no upper limit has been set because a higher Z_0 value is more farasable. In contrast, a positive and negative deviation of f_{res} is equally undesirable. Consequently, the acceptance range around f_{res} is symmetric. The studies in Chapter 7 have shown, that the impedance resonance frequency defines, how the beam dynamics are affected. Therefore, it has be decided that f_{res} should be in a range of $\pm 5\,\%$ around the optimized value.

In Figure 8.9, the deviation of Z_0 (red) and f_{res} (blue) is shown as a function of the relative change of the two investigated corrugation parameters. The horizontal dashed lines indicate the acceptable relative deviations of the impedance parameters. The marks and the corresponding vertical line present the maximal acceptable production tolerances to remain in the chosen impedance parameter ranges. Table 8.1 summarizes the acceptable corrugation tolerances and the resulting deviations of the impedance parameters. It can be seen that the acceptable resonance frequency mainly determines the tolerances of the corrugation parameters.

Furthermore, it can be noticed that the tolerances are asymmetric due to the non-linear scalings. The tolerances in the order of 5 % to 10 % are accessible for different manufacturing methods, which will be explained in the upcoming section. They have been used not only for discussions about the feasibility of a method but also for the quality check of the

Table 8.1. Corrugation production tolerances. The bold impedance parameter deviation defines the maximal production tolerance of the respective corrugation parameter.

Parameter	Δ Parameter / %	ΔZ_0 / %	Δf_{res} / %
h	-9.30	-3.74	**5.00**
	+10.80	4.09	**-5.00**
g	-6.34	**-10.00**	3.33
	+10.80	17.95	**-5.00**

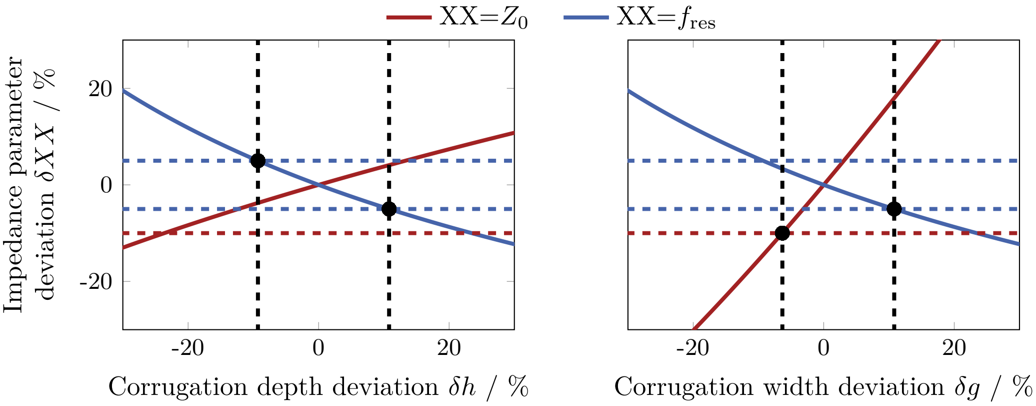

Figure 8.9. Corrugation production tolerances. The relative shunt impedance (red) and resonance frequency (blue) deviation caused by a deviation from the desired value of a corrugation parameter is shown. The horizontal dashed lines indicate the maximal acceptable deviation of the impedance parameter. Because a higher Z_0 is ideal, there is only a lower limit for this parameter. The intersections of the curves with the impedance parameter tolerances (black marks) define the tolerances for the corrugation parameters.

prototypes.

8.2.2. Phase Shift

Multiple manufacturing methods considered in this thesis are limited in the plate size that can be microstructured in one run. Therefore, assembling the corrugated plate from at least two pieces longitudinally to the total length s might be necessary. Due to undesirable edges and misalignments, the periodicity of the corrugations can be disrupted at the transition between the different parts (see Figure 8.10) by a longer corrugation or gap. This leads to a reduction of Z_0 due to the reduced corrugated lengths and can cause a phase shift of the corrugated plate impedance.

The phase shift can be described by

$$\begin{aligned} Z^{\|}(\omega) &= Z_1^{\|}(\omega) + Z_2^{\|}(\omega) \\ &= \frac{1}{2} Z_0^{\|}(\omega) + \frac{1}{2} Z_0^{\|}(\omega) \mathrm{e}^{-i\omega \frac{\Delta s}{c}} \end{aligned} \tag{8.1}$$

with the impedance of two substructures $Z_{1,2}^{\|}$, the impedance of the total length without the disruption $Z_0^{\|}$, and the phase shift distance Δs. The latter causes the time delay $\Delta t = \frac{\Delta s}{c}$. Mathematically speaking, the phase shift causes a mixing of the real and imaginary parts of the impedance. For the resonator model, the real part of the impedance with the phase shift can be written as:

$$\Re(Z^{\|})(\omega) = \frac{Z_0}{2} \left[1 + \cos\left(\omega \frac{\Delta s}{c}\right) - Q \left(\frac{\omega_{\mathrm{res}}}{\omega} - \frac{\omega}{\omega_{\mathrm{res}}} \right) \sin\left(\omega \frac{\Delta s}{c}\right) \right] \quad . \tag{8.2}$$

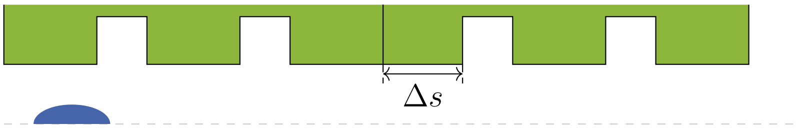

Figure 8.10. Schematic corrugated structure with phase shift.

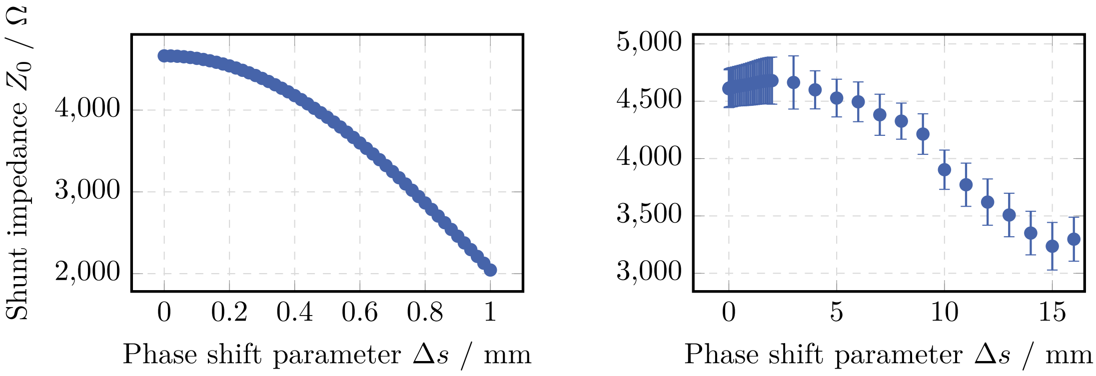

(a) Theory **(b)** Simulation

Figure 8.11. Shunt impedance as a function of phase shift. Decreasing shunt impedance Z_0 for the theoretical prediction (a) similar to the two scenarios of the simulations (b) with the offset Δs. The simulations show that larger values of Δs are required to reach the same impact as in theory. The fixed corrugation parameters are corrugation depth $h = 300\,\mu\text{m}$, periodic length $L = 200\,\mu\text{m}$, duty cycle $L/g = 2$, and plate distance $b = 2\,\text{mm}$.

For this, no analytical determination of the "*new*" shunt impedance and resonance frequency is known from the literature, so they need to be determined numerically (see Appendix E). The impact of the phase shift distance Δs is studied for the corrugation parameters $h = 300\,\mu\text{m}$, $L = 200\,\mu\text{m}$, $L/g = 2$, and $b = 2\,\text{mm}$ and the impedances are shown in Figure F.12. The theoretical change of the impedance is compared with simulation results in Figures 8.11 and 8.12. Without a phase shift, this corrugation settings create an impedance with Z_0=4.66 kΩ and f_{res}=89.4 GHz.
For both impedance resonance parameters (Z_0 in Figure 8.11 and f_{res} in Figure 8.12), it can be seen that the dependency on Δs is comparable to the prediction. However, the simulated impact is significantly smaller for comparable values of Δs, or rather, the simulations only achieve the same influence at substantially larger offsets. For the theory model, the frequency-dependence of the the impedance changes drastially for $\Delta s > 1\,\mu\text{m}$, so that it is not possible to define a resonance frequency. Consequently, the regime of the f_{res}-saturation in the simulation results can not be reached. The phase shift distance, which would be in the tolerances defined in Section 8.2.1, is $\Delta s_{\text{theo}} = 400\,\mu\text{m}$ and $\Delta s_{\text{sim}} = 14\,\text{mm}$ respectively. Both limits are determined by the reduction of Z_0. The tolerable shift due to the splitting in the manufacturing process in the order of cm can only be exceeded if the plate cannot be completely microstructured since a misalignment can only lead to a phase shift distance up to $\frac{L}{2}$, which is significantly below the tolerance. Consequently, a significant phase shift effect can be prevented by cutting away the edges of the plate that are not sub-structured to the very edges, so that Δs is typically in the order of $\mathcal{O}\,(10\,\mu\text{m})$.

8.2.3. Corrugation V-shape

In discussions with potential manufacturers, it has been pointed out that perfectly vertical corrugation side walls are a challenge that can only be achieved with some methods. For the other methods, the side walls can only be manufactured with a finite angle α (also referred to as "*V-shape angle*"), which is schematically illustrated in Figure 8.13a. In this study, it is defined in that way that the longitudinal gap g is fixed at the top of the corrugation, and the side wall angle causes a change of the gap at the ground of the corrugations by $2\Delta g$. Thereby, the angle is defined by $\tan\alpha = \frac{\Delta g}{h}$.

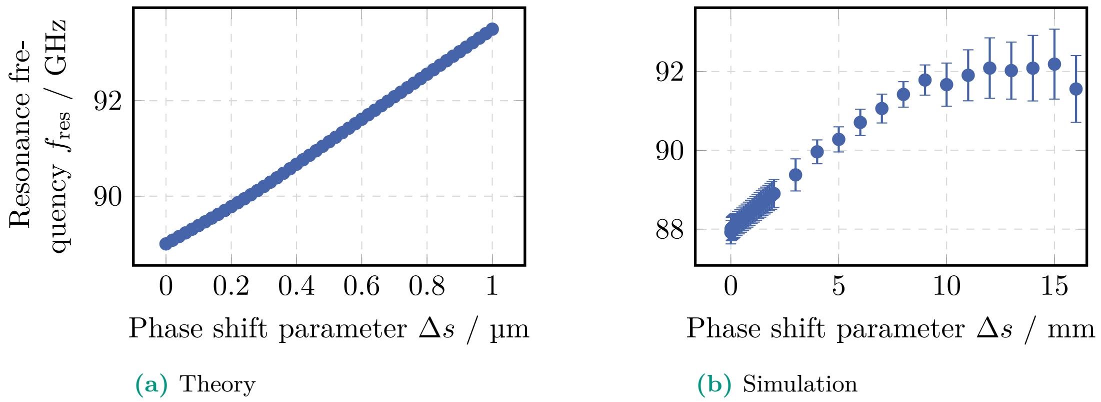

(a) Theory

(b) Simulation

Figure 8.12. **Resonance frequency as a function of phase shift.** The resonance frequency f_{res} increases for the theoretical prediction (a) and the simulations (b) nearly linearly with the offset Δs. Analog to the shunt impedance, the simulations show that larger values of Δs are required to reach the same impact as in theory. The fixed corrugation parameters are identical to Figure 8.11.

Figure 8.14a shows the longitudinal impedance for the optimized corrugation settings of Structure 1 for different V-shape angles. At the value $\Delta g = 0.5 \cdot g$, an exact V-shape is reached so that the corrugations do not have any horizontal ground anymore. A further increase of Δg would not change the shape but reduces the corrugation depth h. Therefore, only the region below this threshold is studied here. It can be seen that the shunt impedance decreases and the resonance frequency increases with α. It must be considered that the simulations have been performed for equidistant steps of Δg so that the angle steps are not perfectly equidistant. Due to hexahedral mesh-cells in the CST simulations, the V-shape causes mesh-cells which are partly corrugation and partly vacuum. As long as there are at least 3 celles between 2 such "*mixed cells*" in each direction, the impedance can be accurately simulated.

Negative values of Δg and α are not manufacturable in this micrometer scale, however, they have been studied and are included in the impedance parameter scan in Figure 8.14b. Both impedance parameters (Z_0 and f_{res}) scale nearly linear with the V-shape factor $\frac{\Delta g}{g}$, which is slightly interrupted by a small plateau in the area $\alpha \approx 0\,°$, where the shape

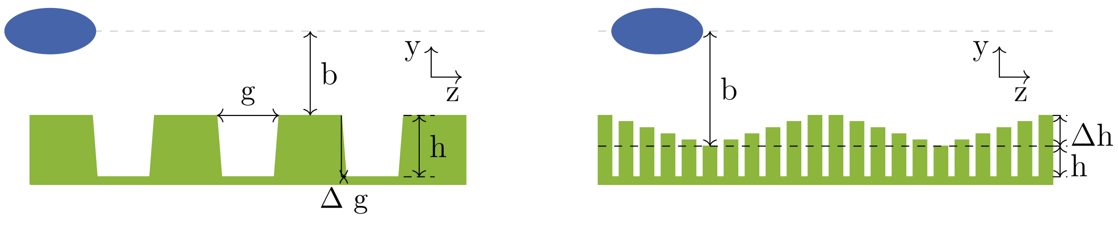

(a)

(b)

Figure 8.13. **Schematic W-&V-shape.** (a) In the case of non-vertical corrugation side walls, the shape of a single corrugation converges towards a V-shape. (b) The W-shape is based on different corrugation depths in the longitudinal direction. For the manufaction out of two parts, a bathtub shape of each part results in this W-shape.

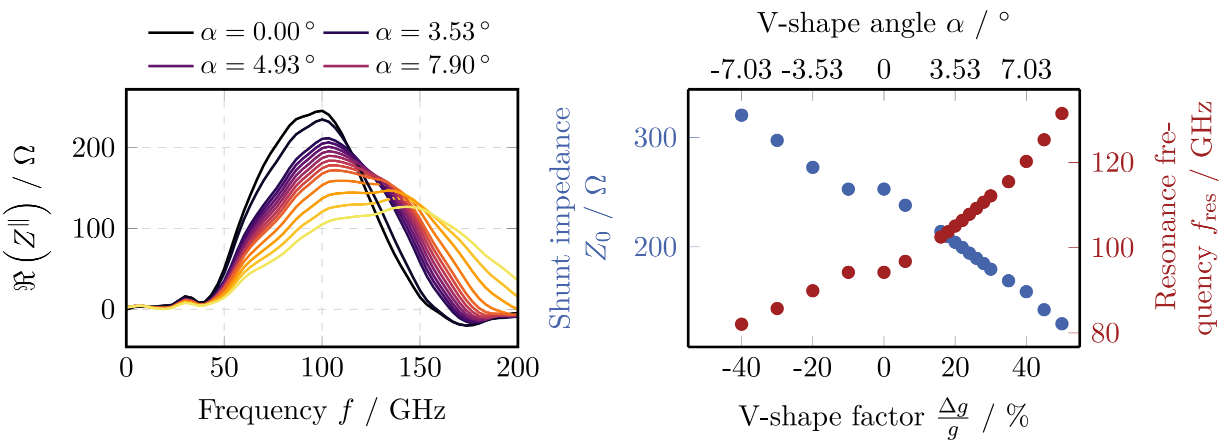

(a) (b)

Figure 8.14. V-shape. The real part of the longitudinal impedance $Z^{\parallel}$ (a), as well as the impedance parameters shunt impedance and resonance frequency (b), show that an increase of the side wall angle α, corresponding to a reduction of the surface and volume of the corrugations, results in a near-linear scaling reduction of the shunt impedance and a linear shift of the impedance resonance frequency. The fixed corrugation parameters are corrugation depth $h = 159\,\mu\mathrm{m}$, periodic length $L = 125\,\mu\mathrm{m}$, duty cycle $L/g = 2.55$, which are the optimized settings for Structure 1.

changes systematically. Another important point is this: Figure 8.14a strongly suggests the resonator-like impedance with a well-defined resonance frequency and shunt impedance is not limited to perpendicular, rectangular corrugations but holds for different corrugation shapes. The scaling of Z_0 indicates that the shunt impedance is directly proportional to the volume (or area for a fixed width x_0). On the other hand, f_{res} scales with the path through the plate material along the corrugation surface. This path is defined for a single corrugation as $2 \cdot h + g + 2 \cdot \Delta g$.

Nevertheless, this impact of the V-shape angle has not only been investigated to understand the impedance of the corrugated structure better but also to determine the tolerance for the manufacture in terms of α. The changes of Z_0 and f_{res} cause by the V-shape both set the limits for the maximal acceptable offset at $\Delta g = 7.8\,\mu\mathrm{m}$. Due to the large aspect ratio $\frac{h}{g} = 3.2$, this results in a small tolerable V-shape angle of $\alpha = 2.9\,°$.

8.2.4. Bathtub/W-shape

In Section 8.2.1, the impact of systematic deviation due to production uncertainties on the corrugation h has been discussed. Evidently, this systematic deviation should have a stronger impact on the longitudinal impedance of the corrugated structure than a statistical variation of h. However, fabrication methods that are mostly based on growing the structure due to material applied on a substrate might manufacture structures whose material height depends on the position of the substrate plate or wafer.

More material is applied at the edges (most relevant in the longitudinal direction) than in the center. Due to the resulting shape, this is referred to as "*bathtub-effect*". A schematic drawing of this effect is illustrated in Figure 8.13b. The amplitude of this effect is more enhanced if the plate is manufactured out of two parts, which then creates the W-shape. In this study, the W-shape is investigated, whereby the corrugation in the middle of each half-block has the depth (or height) h. Towards the edges, the depth increases linearly so that the outermost corrugation has the depth $h + \Delta h$. For this study, the exact corrugation dimensions are used for the investigation of the V-shape angle - corresponding to the

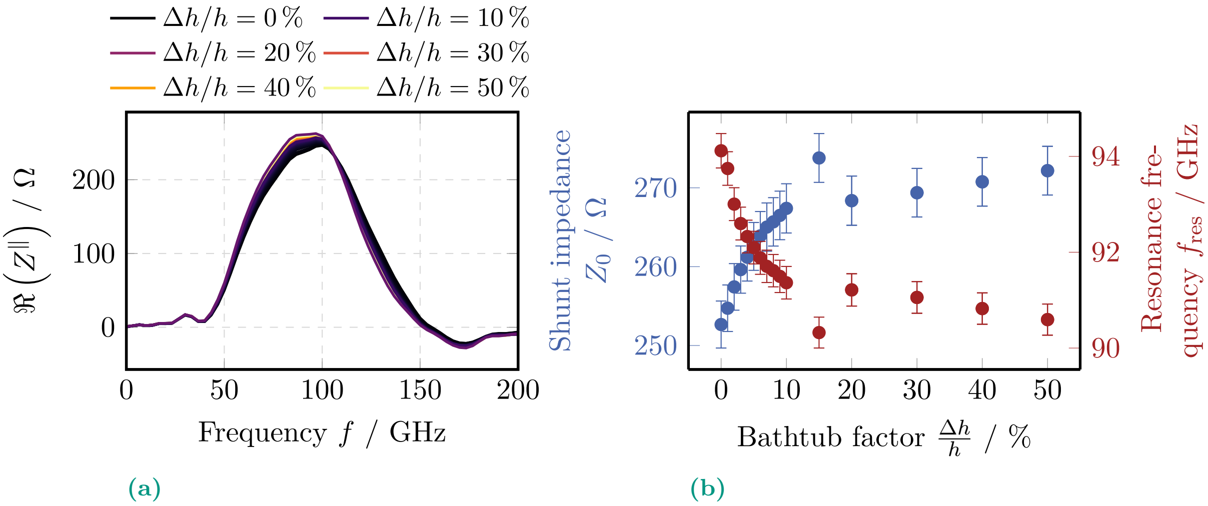

Figure 8.15. **W-shape** (a) The real part of the longitudinal impedance $Z^{\|}$ for different longitudinal W-shape factors shows - in comparison with the other deviations from the idealized structure - no significant impact. However, the shunt impedance increases and the resonance frequency decreases slightly with an increasing $\frac{\Delta h}{h}$ (b). The fixed corrugation parameters are identical to Figure 8.14

optimized settings of Structure 1.

In the impedance scan for different values of the height of the bathtub Δh in Figure 8.15a, it can be seen that f_{res} decreases and Z_0 increases very slightly with the bathtub parameter. In the range of $\frac{\Delta h}{h} \leq 50\,\%$, the tolerance thresholds for both impedance parameters are not reached. Compared with the previously presented possible differences from the designed geometry, the bathtub effect is significantly smaller and, therefore, negligible for the choice of the manufacturing method.

8.3. Production Methods

As described in the previous section, the different parameters of the corrugated structure must be manufactured with certain precision and within given tolerances to ensure the desired impedance quantities. One of the main difficulties in finding the optimal manufacturing methods is that the precision on the single-digit micrometer (µm) scale must be sustained over an area of $20 \times 200\,\mathrm{mm}^2$, which then is needed at least two times. Furthermore, the financial, temporal, and material budget has to be taken into account. Smaller pieces are produced with different methods and partners to validate and save all three budgets. Before the final decision about the production of the complete corrugated structure can be made, these prototypes will be checked regarding the accuracy of the corrugation parameters and their electrical properties. As a starting point, the optimized settings for Structure 1 (f_{res}=110 GHz) and Structure 2 (f_{res}=180 GHz) are used (see Table 6.3). However, due to the limitations of the different methods and some flexibility of the corrugation parameters, a manufacturable compromise for the dimensions of the corrugations has been developed with colleagues from the manufacturing institute or company. The relevant frequency range in the order of 100 GHz means a penetration depth is below 1 µm (discussed in Chapter 4). Therefore, methods that produce the structure out of any material and metalize it afterward with a layer of a few µm can be considered as well.
Before the most promising methods and prototypes are presented, a list of methods that have turned out to be unsuitable should be given. It must be clearly mentioned that the decision against this method has nothing to do with the quality of the method but with the high and very specific requirements for the corrugated structures.

Wire Erosion

The wire erosion method has no further material requirements, so copper, aluminum, or steel for the complete required area can be structured in one piece. A considerable advantage of this method is that - based on experiences - a production time of only about 12 h has been estimated for a complete corrugated structure. An important point is that the periodicity L and the depth h can be chosen freely and adjusted very precisely. However, the periodicity has to be larger than about 200 µm, and the corrugation depth can be in the range up to several hundred µm. The longitudinal gap g is defined by the thickness of the wire. The smallest wire thickness available is 100 µm, and only defined thicknesses exist. Therefore, it must be considered that the ditch is larger than the wire thickness and depends on the material removal. It means that the required dimensions of Structure 1, in the longitudinal dimension, are too small for this method. Due to the erosion with a circular wire, the bottom of the corrugations would not be flat but semicircular.

Light Lithography & Screen Printing

The setup for this screen printing method is used at the Institute for Data Processing and Electronics (dt. Institut für Prozessdatenverarbeitung und Elektronik) (IPE) of the KIT. For this method, a rectangular ceramic surface ($100 \times 100\,\mathrm{mm}^2$) is used. Consequently, the complete plate needs to be split into two parts longitudinally. However, the large width allows the manufacturing of multiple strips next to each other so that either both parts of the same structure or the three strips can be made from one block. For the manufacturing process, masks with a defined height 25 µm are produced by the light-lithography so that the material of the masks only remains in the parts in which the gaps should be. In each turn, the gaps of the mask are filled with a silver-palladium paste. Due to the small dimensions of the corrugations, the finest paste, with the size of the silver-palladium balls of 5 µm to 10 µm, is used. The structure is then heated so that the paste material is baked out. Repeating this process can achieve the final height/depth by stacking multiple layers.

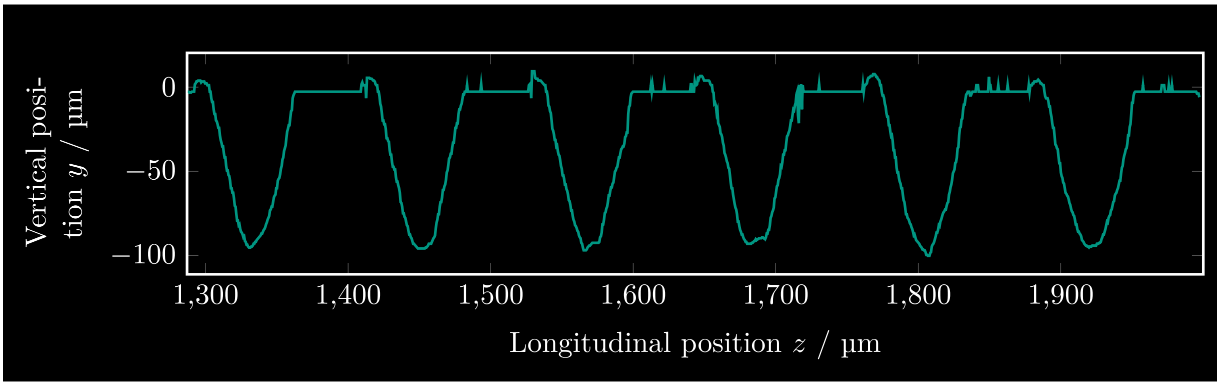

Figure 8.16. Laser processing prototype aluminum: corrugation height profile. The height profile, perpendicular to the corrugations, is extracted from the scanning electron microscope (SEM) topography image (Courtesy M. Schäfer (Photonic Centre Kaiserslautern (dt. Photonik-Zentrum Kaiserslautern e.V.) (PZKL))).

Therefore, all produced strips can vary in their longitudinal dimensions but must have the same corrugation depth. Unfortunately, the first tests revealed that the paste and, therefore, the method is not suitable for the needed dimensions of the corrugations. The paste melts away so separated and clearly defined corrugations cannot be screen-printed.

X-ray Lithography & Electroplating

The X-ray lithography and electroplating as possible manufacturing methods have been discussed with microworks GmbH[13], which has been founded as a spin-off from the KIT. For this method, a resist with the desired thickness is applied to a 6" silicon wafer. The dimensions of the wafer make a longitudinal splitting of the structure necessary. This method can manufacture the corrugations with a periodicity down to 20 µm and a depth up to 300 µm. Therefore, it would be possible to build the structures with the optimized parameters without any compromises concerning the dimensions of the corrugations. The wafer is irradiated at the LIGA beamline of the KARA storage ring. Based on the pattern, the resist is structured by the X-ray lithography. These structures have nearly vertical and smooth side walls. The corrugated structure is then produced from this mask by electroplating the gaps with gold. Supporting structures are required to stabilize the narrow and high resist bridges over the length of $x_0 = 20\,\text{mm}$. These structures will be removed after electroplating but will leave gaps in the transverse direction of the structure. As discussed in Section 8.1.1, the width of the corrugated structure is crucial, so this method has not been taken into account any further.

8.3.1. Laser Processing

A feasibility study of the laser processing to manufacture the corrugated structure has been performed at the Photonic Centre Kaiserslautern (dt. Photonik-Zentrum Kaiserslautern e.V.) (PZKL)[14]. This manufacturing process requires an aspect ratio $\frac{h}{g} < 3$. Since this is not fulfilled for Structure 1, the corrugation parameters need to be adjusted so that still an impedance with $f_\text{res} = 110\,\text{GHz}$ is created:

- **h**: 125 µm
- **L**: 117 µm and

---

[13] `www.microworks.de`

[14] `https://www.photonik-zentrum.de/`

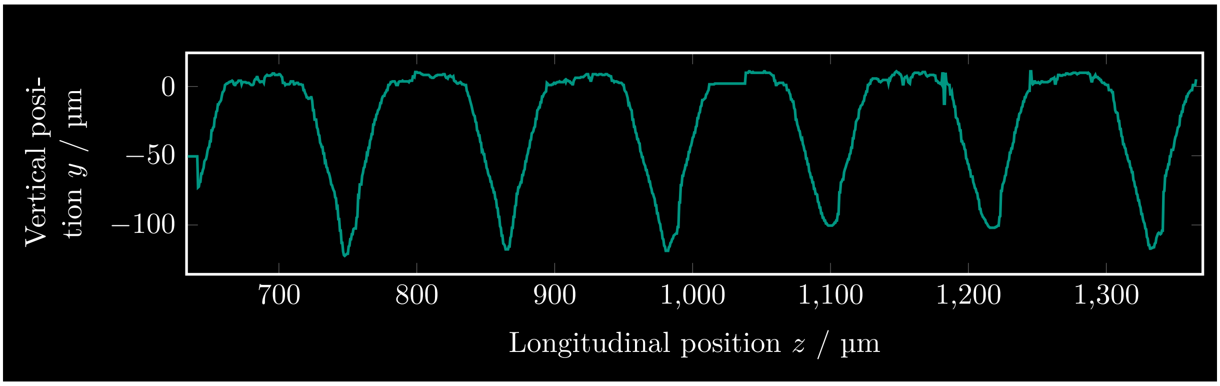

Figure 8.17. Laser processing prototype copper: corrugation height profile. The height profile, perpendicular to the corrugations, is extracted from the SEM topography image (Courtesy M. Schäfer (PZKL)).

- **g**: 58.4 µm .

With their control and deflection system, scanning with the laser pulse over the area that should be microstructured is possible. The ultra-short laser pulses ($\mathcal{O}$ (10 ps)) deposit high energy peaks on this short time scale so that the chemical bonds can be broken without heating the material. Thereby, the material is removed layer by layer. The limitation of the aspect ratio is due to the fact that the laser pulse, guided by the optics, must hit the ground of the corrugation to deposit the energy so that the material is removed. For the same reason, the side walls cannot be vertical, and a non-zero V-shape angle occurs.
For the prototypes, a laser with 500 kHz repetition rate and power of 0.7 W has been applied. For the processing of an aluminum sample, an ultraviolet (UV) and a visible (VIS) laser has been used for the copper sample.
In Figures 8.16 and 8.17 the measured height profiles, provided by the colleagues at PZKL, for the two material samples are shown. The roughness and bumps on the top of the corrugations are caused by the attaching of the removed material during the laser processing. This can be polished afterward. In both cases, the V-shape angle is pronounced, and it can be seen that this angle is so large that no flat bottom part is reached. The target depth is clearly not achieved for the aluminum sample and the UV laser processing, so this has not been further investigated and studied. In Figure 8.18, some microscope images of the copper sample are shown. Hereby, it must be noted that the surface of the material has not been polished for this first test. For this reason, the same macroscopic scratches can be detected, which have nothing to do with the laser processing quality. The microscope image is also used to measure the longitudinal dimensions for a larger number of corrugations. This allows the determination of the periodic length and longitudinal gap with better accuracy and allows statements about the quality of the variation between the corrugations.

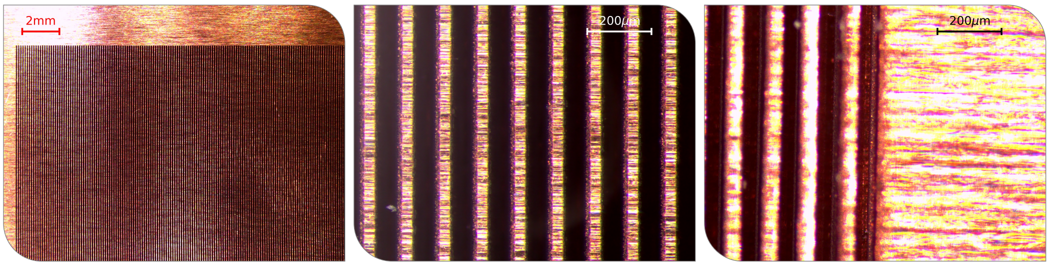

(a) **(b)** **(c)**

Figure 8.18. Laser processing prototype copper: optical microscope images.

Table 8.2. Laser processing prototypes: Corrugation dimensions. The uncertainties result from the variation of the dimensions of the corrugations.

		Aluminum		**Copper**	
Parameter	**Target**	**Value**	**Uncertainties**	**Value**	**Uncertainties**
L / µm	117.0	117.8	1.2	116.5	1.2
h / µm	125.0	96.1	2.2	113.0	8.5
g / µm	58.4	59.8	1.6	56.8	1.6
α_1 / °	0.0	16.6	1.4	14.5	1.1
α_2 / °	0.0	17.4	1.6	13.56	0.4

From this, only the periodic longitudinal dimensions can be determined from the edges since the brightness does not scale with the corrugation depth. The depth and the side wall angles are determined from the height profiles. All these parameters are collected in Table 8.2 for both material samples. For both samples, the longitudinal dimensions (L and g) are in good agreement with the required values within the acceptable tolerances and are constant on a 1 % to 2 % level. It has already been discussed that laser processing in aluminum cannot provide the required aspect ratio and corrugation depths. In contrast, it is possible to reach this depth h in copper. However, Figure 8.17 reveals that this is not the case for all corrugations and that, therefore, h is manufactured with a relatively large uncertainty. Thereby, either the required depth is reached (h=122.30 µm) or it is comparable to the aluminum sample. This issue might be solved by increasing the processing time and optimizing the laser and optics settings. However, the side wall angles α are by a factor of 4.6 to 6.0 too large. Nonetheless, even this parameter is better for the copper sample in comparison with aluminum.

Using a quartz glass sample and magnetic field-supported processing, the laser processing method can improve the V-shape angles α. However, using the magnetic field does not help reach the required V-shape angle. Due to the necessary subsequent electroplating, the processing of the quartz glass has been neglected for the first tests. Since it promises significantly better side wall angles, a quartz glass sample has been structured with magnetic field-supported laser processing for the second test. Additionally, the aspect ratio has been further decreased by accepting a reduced shunt impedance (Z_0=965 Ω) with the corrugation dimensions L=85 µm, g=58.4 µm, and h=90 µm. For the final structure design, the thickness of the additional metal layer must be considered. Since it should be applied with a homogenous thickness on the tops and bottoms of the corrugations, it must only be considered for the side walls and, therefore, the longitudinal gap s. Therefore, this parameter should be increased by two times the thickness of the metal coating. This would help to decrease the aspect ratio for the laser processing even further. Analogous to the copper sample, the VIS laser but with increased power (1.6 W) is used. In Figure 8.19, the height profile of the corrugation is shown. Thereby - from left to right - the number of processing cycles and, consequently, the material deposit is increased step-wise. Especially for the first three steps, the side walls are nearly perpendicular, and the corrugations are nearly rectangular for the first two steps. From a depth of $h \approx 25$ µm, the right side wall and the corrugation bottom begin to tilt. This causes not only an increasing side wall angle but a complete deformation of the corrugation shape. Furthermore, the maximal reachable depth is about 60 µm and thus way below the even reduced required target value.

Consequently, with the current setup and lasers at the PZKL, the requirements for the small V-shape angle in combination with the aspect ratio > 1.5 can neither be fulfilled for metal nor for quartz glass plates.

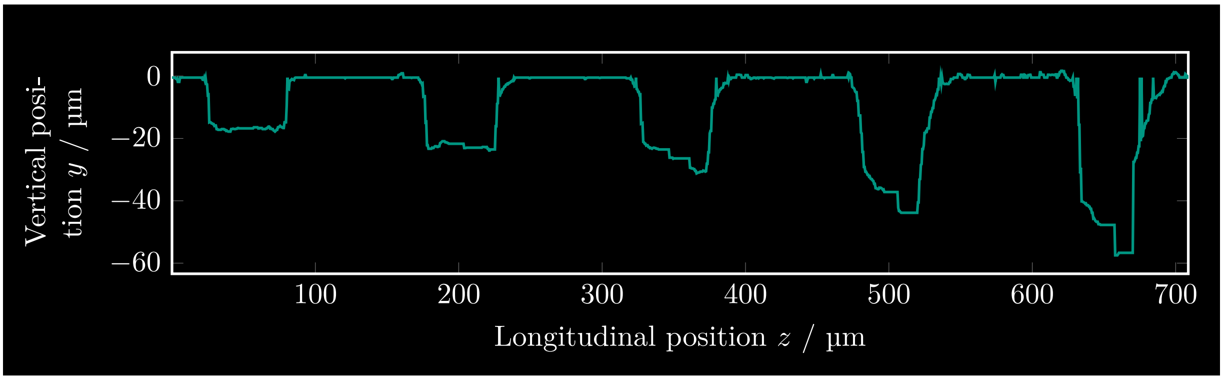

Figure 8.19. Laser processing prototype: corrugation height profile quartz glass. With increasing corrugation depth, the flat corrugation bottom cannot be reached, and the V-shape angle increases. The height profile, perpendicular to the corrugations, is extracted from the SEM topography image (Courtesy M. Schäfer (PZKL)).

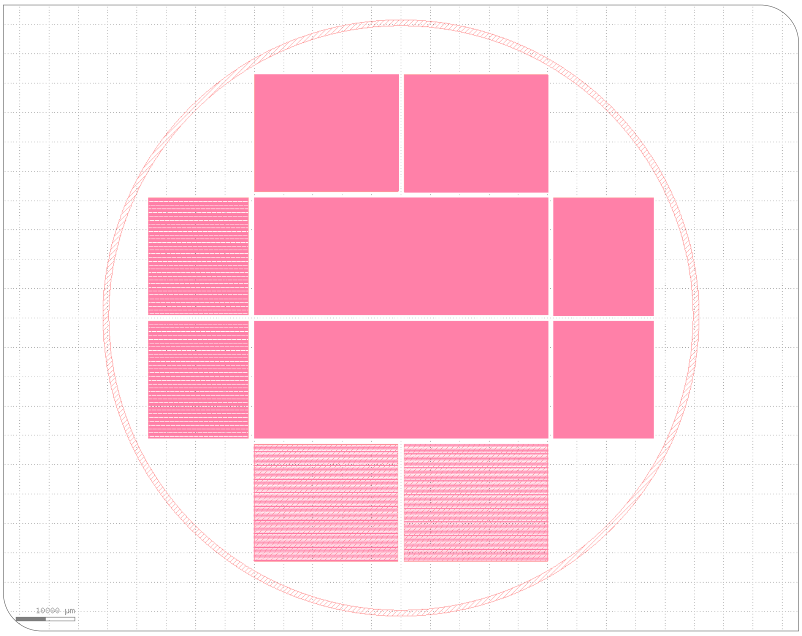

Figure 8.20. Wafer mask: Bosch process. The different areas consist of corrugated structures with different longitudinal corrugation parameters to optimize the use of the mask area.

8.3.2. Deep Reactive Ion Etching

The Center for High-resolving Superconducting Sensors (HSS) is operated as a collaboration of the two KIT institutes IPE and Institute of Micro- and Nanoelectronic Systems (IMS) together with the Kirchoff Institute for Physics of Heidelberg University. In this center, deep reactive ion etching (DRIE) system (also known as "*Bosch process*") has been set up as a relatively new machine. In this method, the corrugated structure can be manufactured from a 4" silicon wafer, so a subsequent metallization is necessary. The production of a prototype wafer sample with corrugated structures has been commissioned by the colleagues at IMS. However, supporting and participating in preparing the wafer in the HSS clean room has also been possible. This preparation involves applying a photoresist at the parts of the wafer where no material should be removed by the etching process.

After a heating of the wafer, 3 ml of a positive resist (AZ®4562 [105]) is applied on a spin coater. A positive resist, will be developed and removed where it has been exposed. This resist is soluble in an alkaline solution, so it can be removed completely without residue and be reapplied if the developed mask does not fulfill the quality criteria. After resting and additional heating, the photoresist is exposed to the predefined mask. The mask in Figure 8.20 is used for the prototype. The different areas on the wafer consist of corrugations with different longitudinal parameters (L,g, and L/g) to validate the possible dimensions and limits of the method. The corrugation depth is defined later during the etching process. After an exposure time of about 40 min, the resist is developed in a developer bath. In the last step of the preparation, the surplus and developed resist are removed by shaking the wafer in highly purified water. In the first tests, the resists did not adhere properly so that the relatively long (x_0=20 mm) and narrow corrugations did not stand but stuck together. With the usage of an adhesion enhancer, this problem is solved so that the fine lines of the resist adhere to the wafer surface properly.

This prepared wafer is then used for the DRIE process, whose working principle is illustrated in Figure 8.21. In the areas without the resist, the material is removed by the etching in a semi-elliptical shape. To avoid the chemical interaction by removing more material under the resist and to protect the side walls, the etching is stopped, and the surface of the silicon and resist is passivated (orange line). Due to the directed plasma ion etching, the passivation layer at the bottom is removed way faster than at the side walls to ensure anisotropic etching. This combination of etching and passivation is repeated until the desired depth is achieved. The comb-like side walls have a typical roughness of $\mathcal{O}\,(10\,\mathrm{nm})$. In Figure 8.22, images taken with a SEM are shown (additional images can be found in Figure G.13). The set longitudinal corrugation dimensions of the mask are: g=50 µm and L=120 µm. ItIt can be seen that for the measured area, the corrugation parameters achieved $L = (122.27 \pm 0.45)$ µm and $g = (49.31 \pm 0.26)$ µm are clearly inside the acceptable tolerances and with relatively small variations. Furthermore, the silicon has a substantially better surface quality and flatness than the laser-processed samples in Section 8.3.1. The large rectangle in the right image has nothing to do with the corrugated structures. It must be added for endpoint detection with a laser. This is required to detect the end of the area which should be structured. However, this rectangle allows a better look at the corners, edges, and side walls of the corrugations. Thereby, sharp edges and no V-shape angle are recognizable.

Overall, this first prototype looks very promising, which makes it worth going on with this method. However, the post-processing with the metalization is very challenging - especially for the side walls. Therefore, another manufacturing method, which processes metal directly, has been tested in parallel.

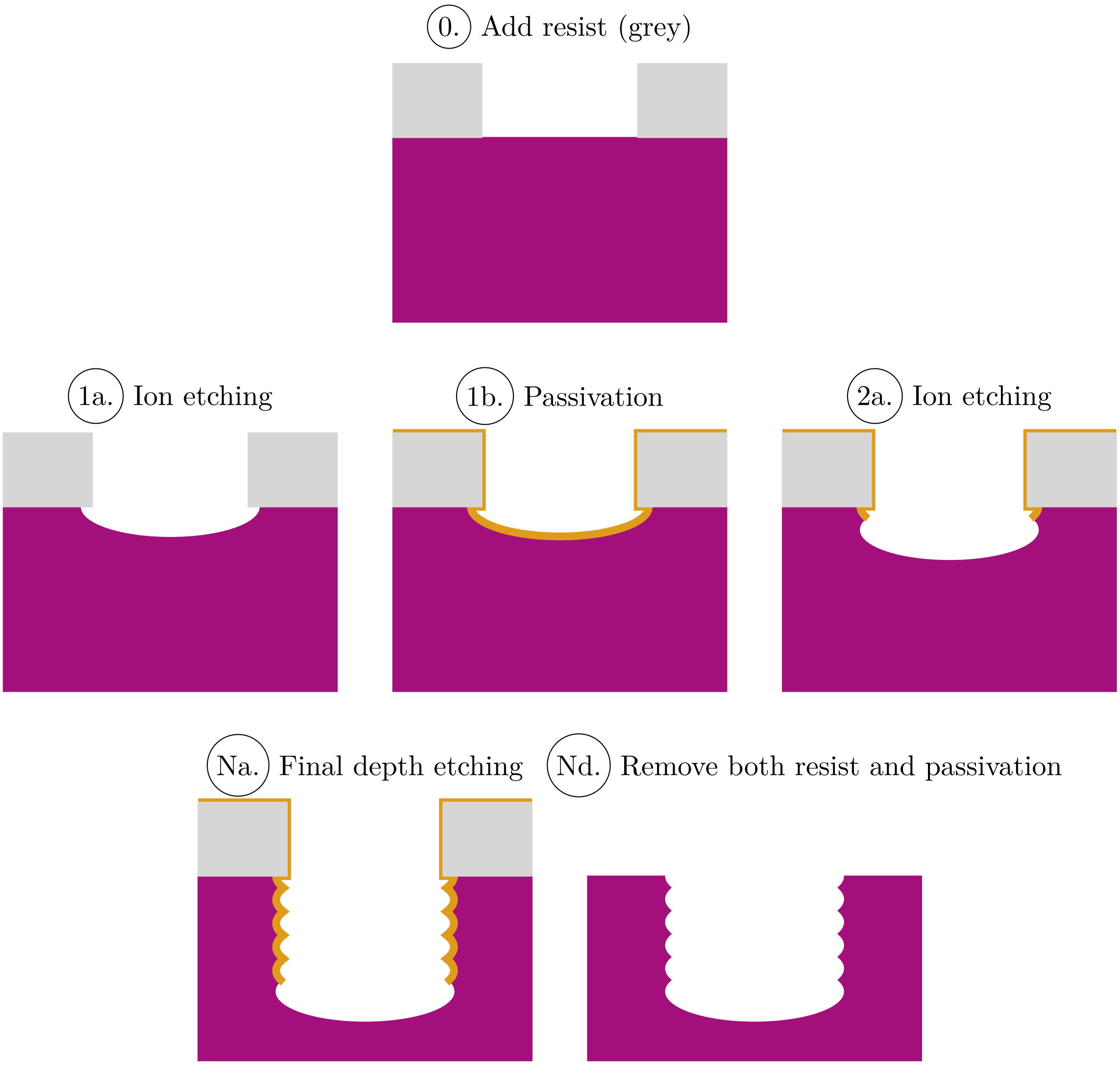

Figure 8.21. Procedural steps of DRIE. Before the first etching step, a mask is applied with a photoresist. After each ion etching step, the surface is passivated to prevent the side walls from further material removal. Since the plasma ions are directed towards the bottom, the passivation is removed way faster than at the side walls so that the anisotropic etching can be ensured (adapted from [104]).

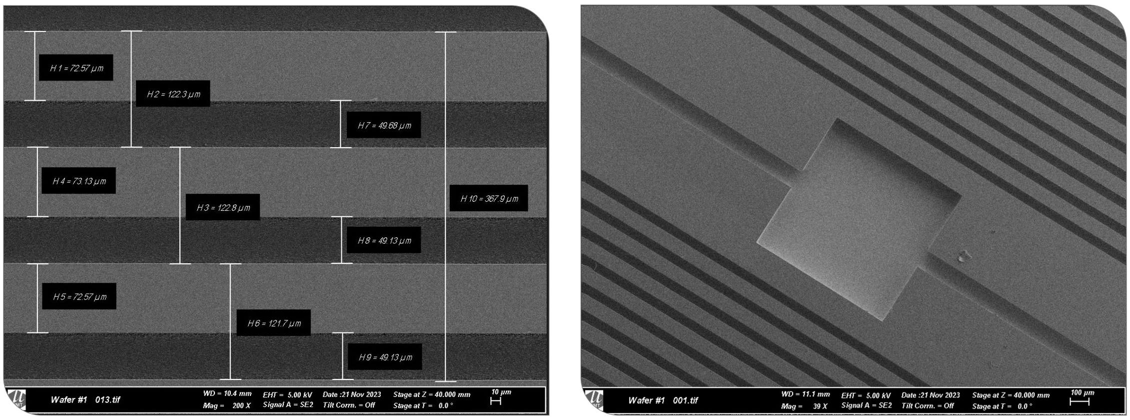

Figure 8.22. DRIE prototype silicon: SEM images. Courtesy A. Muslija (IMT)

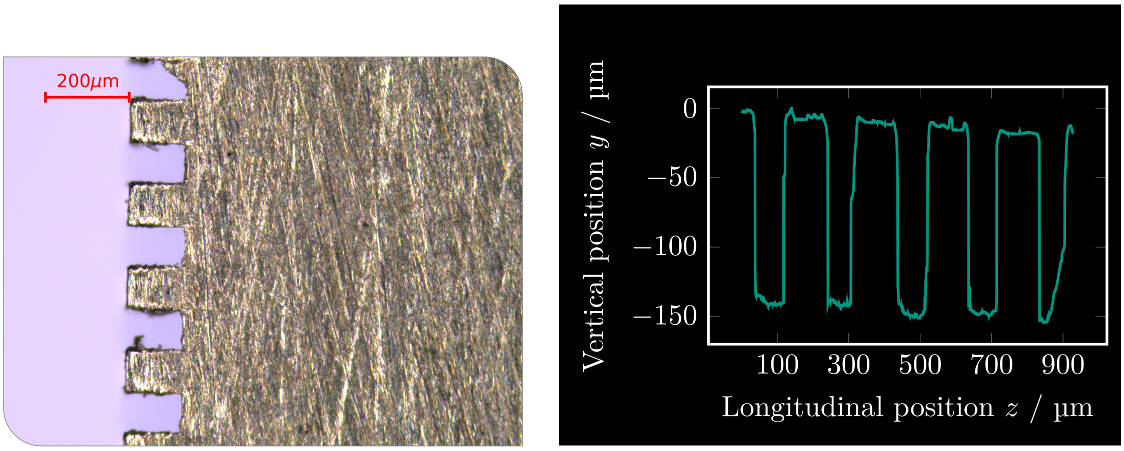

(a) (b)

Figure 8.23. Milling prototype aluminum: optical microscope image and height profile. The height profile, perpendicular to the corrugations, is extracted from the brightness of the optical microscope image.

8.3.3. Milling

An important advantage of milling is that the material choice is not further restricted. Depending on the schedule of the machine, the colleagues at the workshop of the Institute for Micro Process Engineering (dt. Institut für Mikro-Verfahrens-Technik) (IMVT), who produce the prototype, can manufacture the two identical plates with the total length $s = 20\,\mathrm{cm}$ not only in one piece but in about 1-2 weeks. This is significantly faster than the other presented methods, which have production and delivery times of several months. For the setup of the eigenmode measurements (see Section 8.4), a width of $x_0 = 5\,\mathrm{cm}$ is necessary to get a signal (described in the next section). To be able to use the milled prototype for these measurements, two aluminum plates are structured on an area of $5 \times 5\,\mathrm{cm}^2$. For the positioning of spacers, the plates have a length of 6 cm, so there is a strip without corrugations before and after the structured area - in longitudinal direction. For the required corrugation parameter range, the limiting factor of the fly cutting [106] is the size of the diamond milling cutter, which defines the minimal possible longitudinal gap $g = 100\,\mu\mathrm{m}$. Therefore, the dimensions of a corrugated structure with $f_{\mathrm{res}} = 110\,\mathrm{GHz}$ need to be chosen differently from the overall optimized settings. With the restriction for the longitudinal gap, the best corrugation parameters are $g = 100\,\mu\mathrm{m}$, $L = 200\,\mu\mathrm{m}$, and $h = 125\,\mu\mathrm{m}$. However, this leads to a just acceptable shunt impedance reduction of 10 %. Figure 8.23a shows a side view image of one of the fabricated plates of an optical microscope with a 200 µm scale. This is used to determine the corrugation dimensions. Already here, it can be recognized that the corrugations are almost rectangular with no visible V-shape angle. Based on this image, Figure 8.23b displays the surface profile along the five corrugations to determine the corrugation parameters properly. In the longitudinal direction it shows that both parameters ($L = (197 \pm 3)\,\mu\mathrm{m}$ and $g = (96 \pm 4)\,\mu\mathrm{m}$) are within the acceptable tolerances. However, the variations of the dimensions between the different corrugations are an order of magnitude larger than for the DRIE prototype. The corrugation depth of this prototype is determined as $h = (137 \pm 1)\,\mu\mathrm{m}$. Therefore, it is at the very edge of the tolerances. Since the milled depth is systematically too large, this can be corrected for producing the final structures by reducing the milling time for all corrugation accordingly. In comparison with the laser processing, the side wall angles are significantly smaller, so that for the aspect ratio $\frac{h}{g} = 1.25$, a large part of the corrugation bottom is horizontal and flat. The quantitative determination reveals for the both V-shape angles: $\alpha_1 = (4.0 \pm 1.7)\,^\circ$ and $\alpha_2 = (5.2 \pm 1.7)\,^\circ$, which is not perfectly rectangular but still acceptable.

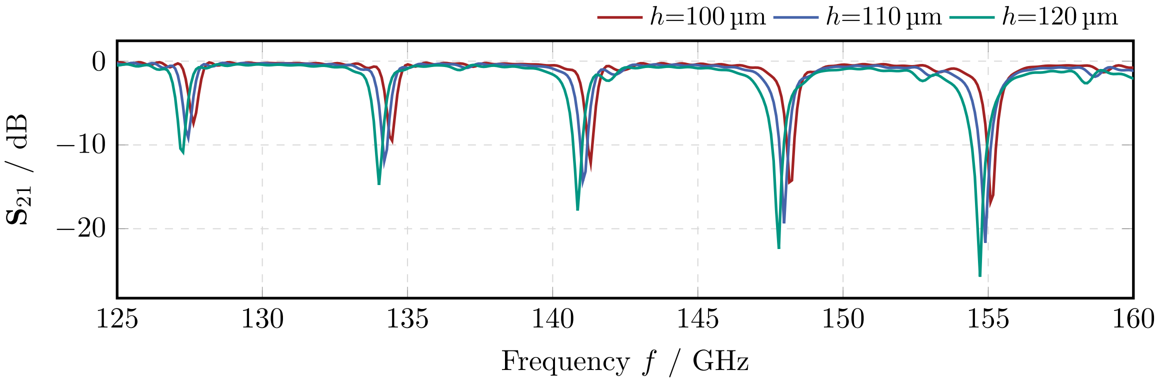

Figure 8.24. Simulated corrugated plate S-parameter $\mathbf{S}_{2,1}$ for different corrugation depth. The different dips correspond to the eigenfrequencies of the resonating eigenmodes. A deepening of the corrugations causes a reduction of the eigenfrequencies.

In Appendix G.2, a selection of images with an optical microscope and a SEM are shown. Analogous to the other methods, the samples have not been polished before or after the structuring, so macroscopic scratches and depositions are visible. Besides that, especially the SEM images reveal only microscopic but negligible surface roughnesses. Furthermore, the clean side walls have sharp edges, and only a small periodic pattern due to the milling can be seen.

Preferred Manufacturing Method

Before a decision about the manufacturing method for the final corrugated plates can be made, the measurements of the eigenmode need to be awaited. Nevertheless, the milling of an aluminum block is the most promising. Although the milling could perform better regarding the precision of the corrugation production, the total package is the best. With consideration of manufacturing time and that there is no need for time-consuming and difficult metalization, the acceptance of larger variations of the corrugation parameters in comparison with DRIE is reasonable. However, it must be mentioned that despite the lower corrugation parameter accuracy, these are still within the previously determined tolerances, so the impedance parameters are also within the acceptable range. Furthermore, the production from a single piece is a clear advantage for mounting and aligning the corrugated structures on the backing plate.

8.4. Eigenmodes

Before the corrugated structures will be installed into the KARA storage ring, the geometric accuracy and electrical properties need to be verified. Therefore, the transmission power $\mathbf{S}_{2,1}$ (see Section 2.8.2) is measured at an in-air test stand at the IHM. Since the DUT, which consists of the two parallel corrugated plates and four spacers at the corners, is entirely point and axis symmetrical, there is no preferred direction, and thus $\mathbf{S}_{1,2} = \mathbf{S}_{2,1}$ should apply.

At the test setup at the IHM, the power waves are focused on the position of the DUT. At this position, the pulse has a width of 50 mm. All parts of the pulse that do not travel through but around the DUT cannot form a standing wave in the structure. Consequently, these signal parts cannot contribute to damping the $\mathbf{S}_{i,j}|_{i\neq j}$ at the eigenmode frequencies. To get the best possible signal-noise-ratio, the width of the corrugated plate should be

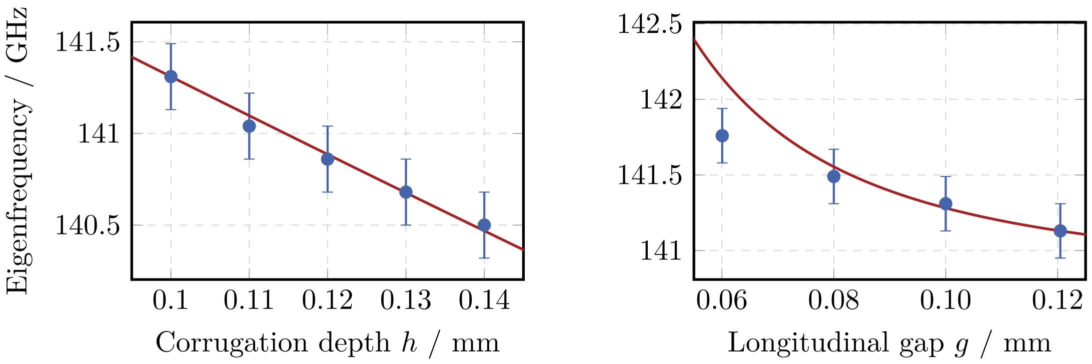

(a) **(b)**

Figure 8.25. Eigenfrequency in dependence of corrugation parameters. (a) The simulated eigenfrequency for corrugated structures with different corrugation depths shows the same dependency on h as the eigenfrequencies of rectangular cavities (red line). (b) Due to the small dimensions of the corrugations, the impact of the longitudinal gap g on the 140 GHz eigenfrequency is based on longitudinal sub-modes.

at least $x_0 = 50\,\mathrm{mm}$. At the test stand, a measurement device is in use that can cover a frequency range from 140 GHz to 220 GHz. In discussions with colleagues at IHM, it has been decided that the plate distance should be minimized. This is because the corrugations have a stronger relative contribution, and lower eigenmodes can be measured or studied in this frequency range. Therefore, the plate distance is set to $2b = 6\,\mathrm{mm}$. As mentioned in the previous section, the milled prototypes have the optimized width for the eigenmode measurements and the not-microstructured areas to place the spacers. Unfortunately, the test stand has not been available for the measurements of the corrugated plates within the time frame of this thesis, so only the simulated dependencies are discussed here as preparation for the measurements.

Figure 8.24 shows $\mathbf{S}_{2,1}$ for different corrugation depths h in the frequency range of 125 GHz to 160 GHz to investigate the lower part of the frequency range that the setup at IHM can cover. The multiple dips correspond to the different eigenmodes of the respective corrugated structure. It can be seen that the dimension of the corrugations affects all the eigenmodes in such a way that a deepening of the corrugations results in a slight reduction of the eigenfrequencies. This tendency matches the expectation that the construct of two parallel corrugated plates is similar to a series of rectangular cavities. Based on Equation (2.78), the eigenfrequencies of the resonating eigenmodes are predicted. Due to the open sides, the width a_x can be set to infinity so that the horizontal modes do not contribute to the eigenmodes.

The longitudinal dimension of the resonator is defined by the longitudinal gap g and the vertical dimension is defined by the plate distance $2b$ and the corrugation depth h so that the dependence of the eigenfrequency on g and h is studied. For this study, the lowest eigenfrequency above 140 GHz (at about 141 GHz) is used. Figure 8.25a shows this eigenfrequency for different values of h but with the fixed longitudinal corrugation parameters $L = 200\,\mathrm{\mu m}$ and $g = 100\,\mathrm{\mu m}$. The uncertainties are based on the limited frequency resolution in the CST simulations. For the comparison with the eigenfrequencies of the rectangular cavities, the fit as a function of h is described by:

$$f(h) = \frac{c}{2}\sqrt{\left(\frac{m_\mathrm{y}}{2b+2h}\right)^2 + \mathcal{O}\left(m_\mathrm{x}, m_\mathrm{z}\right)} \quad , \tag{8.3}$$

where $\mathcal{O}\left(m_{\mathrm{x}}, m_{\mathrm{z}}\right)$ contains all contributions of the non-vertical modes. This function (red) in Figure 8.25a shows the same dependence on the corrugation depth as the simulation results. In addition, the fit reveals that the vertical mode of this eigenfrequencies is $m_{\mathrm{y}} = 4$. Without the contributions of the non-vertical mode, this eigenfrequency is in the order of 100 GHz. The difference of about 40 GHz is based on the non-vertical eigenmodes.
In the longitudinal direction, the contribution to the eigenfrequencies is determined by the longitudinal gap g. However, due to the dimensions of the corrugations, the first mode ($m_{\mathrm{z}} = 1$) is of the order of THz, and therefore an order of magnitude larger than the investigated frequency range. Consequently, longitudinal sub-modes can only affect the eigenfrequency at 140 GHz. In Figure 8.25b, this eigenfrequency as a function of the longitudinal gap is shown with the fixed parameters $L = 200\,\mu\mathrm{m}$ and $h = 100\,\mu\mathrm{m}$. The function of the 140 GHz eigenfrequency

$$f(g) = \frac{c}{2}\sqrt{\left(\frac{m_{\mathrm{z}}}{g}\right)^2 + \left(\frac{4}{2b+2h}\right)^2 + \mathcal{O}\left(m_{\mathrm{x}}\right)} \quad ,$$

is also used for the determination of the relevant longitudinal mode. In this process, it is considered that the vertical is already determined and, therefore, defines an upper limit for the longitudinal contribution of the eigenfrequency. For $g \geq 80\,\mu\mathrm{m}$, the simulation results are in good agreement with the sub-mode $m_{\mathrm{z}} = 2^{-7} = \frac{1}{128}$ (red line), which overestimates the impact of g on this eigenfrequency for a shorter longitudinal corrugation gap.

In the experiment, this dependency of the eigenfrequencies on g can be checked by investigating different corrugated plates with the same geometry but different longitudinal gaps. In contrast, the vertical modes can be used to determine the corrugation depth of a single structure. Based on Equation (8.3) and by measuring the eigenfrequencies with different spacers and, therefore, different plate distances b, the corrugation depth h can be determined.

9. Summary and Outlook

In electron storage rings the longitudinal micro-bunching instability occurs due to the interaction of short electron bunches with their self-emitted coherent synchrotron radiation (CSR). The synchrotron radiation is emitted coherently for wavelengths that are larger than the emitting structure - leading to an amplification by several orders of magnitude. Since the substructures in the longitudinal bunch profile appear as emitting dimensions, the CSR can be extended to the hundred GHz to THz frequency range. However, above the slow outburst threshold current, the substructures arise and vanish quasi-periodically, which leads to a sawtooth-like change of the intense CSR power. These outbursts are a roadblock to higher brilliance via an increased and temporal stable photon flux. Consequently, controlling the micro-bunching instability and the CSR outbursts are important to meet the increasing demands of the applications of synchrotron radiation. Thereby, the substructures need to be stabilized over time to suppress the outbursts but at the same time extend the intense radiation to the THz frequency range.

It is a new approach to manipulate the longitudinal impedance to control the instability. For this purpose, an additional impedance, which is created by a pair of parallel metallic plates with periodic rectangular corrugations in the longitudinal direction, will be installed in the Karlsruhe Research Accelerator (KARA) storage ring. Installing this corrugated structure will be the first of its kind in an electron storage ring. This thesis presents systematic simulation studies of the impact of the corrugation dimensions on the structure impedance and of the longitudinal beam dynamics in the bursting regimes of the micro-bunching instability under the influence of an additional corrugated structure impedance for the KARA storage ring. Based on these simulation results, two influential impedances and the corresponding corrugation parameters are defined. For these structures, prototypes are manufactured, facing the challenges of a rectangular corrugation shape and micrometer (µm) accuracy for about 2000 corrugations.

The CST Studio Suite® 2020 (CST) simulations of the longitudinal impedance for the corrugated plates reveal that this impedance can be described as a complex broadband resonator, which can be characterized by the shunt impedance Z_0, the quality factor Q, and the resonance frequency f_{res}. It is shown that the theoretical model to describe f_{res} for a cylindrical corrugated structure is in good agreement with the simulation results within the validity range of the prediction. The systematic corrugation parameter scans reveal that the dependence of the impedance parameters on the different corrugation dimensions can be described by a power law, where the exponents vary between the different parameters. These multi-dimensional parameter scans allow the determination of the optimized corrugation dimensions to create a certain impedance. A semi-automatic procedure is set up based on the systematic corruation parameter scans to find these optimal corrugation parameters. Thereby, the dimensions of the corrugations are chosen in a way that Z_0 is maximized for a given resonance frequency. In the course of this, the new Corrugated Plate Impedance Parameter (CPIP) Ξ is introduced and defined, which consists of all three impedance parameters. In dependence on the longitudinal corrugation area, Ξ distinguishes the two different types of plates with corrugations: a plate with periodic deepenings or a plate with periodic elevations. The simulation study of the plate dimension shows that the corrugated plates need to have a width of x_0=20 mm so that three strips next to each other fit in the planned impedance manipulation chamber. Furthermore, it can be seen that the plate distance only affects the shunt impedance and, thereby, the contribution of the additional corrugated structure. Consequently, the possibility of changing the distance between the plates and the electron beam offers a tuning knob to change the impact of the structure.

For the decision of the corrugated structures and the respective impedance that should be installed into the KARA storage ring, the impact of different impedances on the longitudinal beam dynamics is studied in this thesis. These beam dynamics studies with the Karlsruhe Institute of Technology (KIT) in-house developed Vlasov-Fokker-Planck solver (VFPS) Inovesa indicate that f_{res} is the crucial parameter of the additional impedance, which decides in which way the characteristic frequencies and threshold currents of micro-bunching instability are affected. The shunt impedance, on the other hand, determines the magnitude of the impedance impact on the beam dynamics. By choosing the corresponding impedance resonance frequency, it is possible to either reduce the bursting thresholds or to manipulate the dominant bursting frequency f_{burst} of the micro-bunching . For large resonance frequencies ($f_{\mathrm{res}} \geq 180\,\mathrm{GHz}$), the bursting frequency and the bursting threshold can be increased. In case of $70\,\mathrm{GHz} < f_{\mathrm{res}} < 160\,\mathrm{GHz}$, the additional impedance causes a reduction of the bursting threshold I_{thr}, so that the intense THz radiation is emitted in a beam current range that has been unaccessible for the THz radiation without an additional corrugated plate impedance. The most effective impedance resonance frequency $\hat{f}_{\mathrm{res}}$ is introduced in this thesis. It is defined as the f_{res} that causes the strongest additional CSR emission in the current range, in which no CSR is irradiated without an additional impedance. The study of this new parameter is interesting for two main reasons. The simulated beam current scans reveal that the threshold currents of the two micro-bunching regimes are affected to varied degrees. The bursting threshold, above which the intense CSR is emitted periodically with a constant fluctuation amplitude, is strongly affected by the additional impedance than the slow outburst threshold $I_{\mathrm{thr;slow}}$. Above $I_{\mathrm{thr;slow}}$, the temporally unstable outbursts occur, so the radiation is not necessarily usable for the applications. Due to the different reduction of the two thresholds, the current range of intense THz radiation can be increased significantly. Furthermore, $\hat{f}_{\mathrm{res}}$ gives insight into the underlying and causing mechanisms of the creation of the substructures and the micro-bunching instability.

In a scan of KARA machine settings, namely acceleration voltage U_{acc} and momentum compaction factor α_{c}, $\hat{f}_{\mathrm{res}}$ varies in the range of 83 GHz to 133 GHz. Thereby, a periodic sawtooth-like dependence of the zero-current bunch length is observed. The limited area and periodicity of $\hat{f}_{\mathrm{res}}$ also make it possible to effectively influence the beam dynamics with a single impedance structure for several machine settings effectively. The occurring instant jumps of $\hat{f}_{\mathrm{res}}$ correspond with the change of the number of substructures that arise in the longitudinal phase space and are imprinted on the longitudinal bunch profile. It is shown that the most effective impedance resonance frequency matches with the dominant substructure frequency f_{sub}, which determines the size of the substructures in the longitudinal bunch profile. Consequently, the creation of the substructures can directly be triggered if the periodicity of the wake function, caused by an additional source like the corrugated structure, corresponds to the size of the substructures that can be created for certain machines and beam settings.

For the first experiments, it is planned to mount three strips next to each other on a plate so that the different structures can be tested without breaking the vacuum. Since the middle strip will act as a reference without any corrugations to separate the impact of the corrugated structure from the change of the geometric aperture, only two different corrugated structures can be installed. Because, not only in this thesis but also in several simulation and experiment studies at KARA, the micro-bunching instability is studied in detail for the machine settings of the KARA fill *f05135*, the decision is made that the resonance frequency of one structure is equal to $\hat{f}_{\text{res}} = 110\,\text{GHz}$ of this settings. Furthermore, the resonance frequency lies in the middle of the range of $\hat{f}_{\text{res}}$, so it can be used to manipulate the properties of the micro-bunching instability over an extensive range of machine and beam settings. The second impedance has the resonance frequency $f_{\text{res}} = 180\,\text{GHz}$. With this structure, it is possible to increase the bursting threshold and to study the impact of the additional impedance on the fluctuation frequency of the CSR power.

The discussions with potential manufacturers of the corrugated plates have revealed limitations in the side wall angles of the corrugations, the reachable aspect ratio, and the achievable accuracy. The performed impedance simulations of the different production limitations show that the reduction of the corrugation side wall angle is significantly more important than variations in the corrugation depth for the creation of an additional impedance within the acceptable tolerances. For the so-called V-shape angle, defining the deviation from perfectly perpendicular sidewalls of the corrugations, the tolerable angle is limited to α=2.9 °. Furthermore, the impact of a phase shift in the impedance by splitting the structure longitudinally into multiple parts does not significantly influence the impedance. This expands the range of possible fabrication methods to include those that cannot microstructure a plate with the lengths of 20 cm. The production of several prototypes with different manufacturing methods shows that producing corrugated plates with corrugation dimensions in the order of 100 µm with the required aspect ratio is challenging. Even though it does not reach the highest precision for the dimensions of the corrugations, it is still within the tolerances; the milled prototype is the currently favored manufacturing method. Significant advantages are the relatively short manufacturing time and that it can be manufactured in one piece, which improves the mounting and alignment. The most important advantage compared to other methods is that the structure can be made directly from metal. Therefore, no time-consuming and difficult metallization is required.

In the next step at KARA, the electrical properties of the corrugated plate prototypes will be characterized by measuring the eigenmodes on a test stand at the Institute for Pulsed Power and Microwave Technology (dt. Institut für Hochleistungsimpuls- und Mikrowellentechnik) (IHM). Based on these results and in combination with the already performed investigations of the prototypes, the final decision of the manufacturing method will be made so that the final structures with a length of 20 cm can be produced. In parallel, the chamber that will contain the corrugated plates needs to be designed and fabricated.This has not been part of the scope of this thesis. This chamber will include vertical and horizontal motors to exchange the different corrugated plates and to change the plate distance for the setting of the shunt impedance. Furthermore, it is required to include tapers before and after the plate to avoid discontinuous changes in the geometric aperture. The new chamber must also have vacuum pumps, scrapers, and valves as supplemental devices.

After the installation and commissioning, the impact of the two different corrugated plate impedances on the beam dynamics will be measured systematically for different current, machine, and beam settings. It will be compared with the simulation results of this thesis. For the control of the micro-bunching instability, it can also be an option to include the additional impedance source as a parameter in the feedback control. Thereby, the plate distance and the respective shunt impedance can be used as a (slowly) adjustable parameter during the beam current decay to remain constantly in the stable bursting regime with enhanced CSR emission in the THz range.

Since the inclusion of an additional impedance enhances the creation of the substructures, the installation of a corrugated plate cannot suppress the instability entirely. To reduce or avoid the creation of the substructures, the impact of the reduction of the impedance in the frequency range from 70 GHz to 160 GHz should be investigated.

The detailed simulation studies show that a corrugated plate and the resulting additional impedance are useful for manipulating and controlling the micro-bunches and micro-bunching instability in the KARA storage ring. Even though Inovesa is optimized for the beam dynamics at and the machine setting of KARA, the underlying solution of the Vlasov-Fokker-Planck equation (VFPE), which describes the collective effects by the wake potential or impedance, is generally valid for all storage rings. M. Brosi *et al.* [107; 108] have shown that the Inovesa can describe the beam dynamics and instabilities of different electron storage rings, like MAX IV and SOLEIL, adequately. Consequently, an additional impedance source can similarly manipulate the beam dynamics for these machines and future electron storage rings and synchrotron light sources to provide higher photon flux and brilliance for the different applications.

List of Abbreviations

CPIP	Corrugated Plate Impedance Parameter
CLIC	Compact Linear Collider
CSR	coherent synchrotron radiation
CST	CST Studio Suite® 2020
DBA	Double-Bend-Achromat
DFT	discrete Fourier transform
DoF	Degree of Freedom
DRIE	deep reactive ion etching
DUT	device under test
E-Gun	electron gun
FEM	finite element method
FFT	fast Fourier transform
FPGA	Field Programmable Gate Array
FWHM	full width at half maximum
HSS	Center for High-resolving Superconducting Sensors
IBPT	Institute for Beam Physics and Technology
ID	insertion device
iDFT	inverse discrete Fourier transform
iFFT	inverse fast Fourier transform
IHM	Institute for Pulsed Power and Microwave Technology (dt. Institut für Hochleistungsimpuls- und Mikrowellentechnik)
IMS	Institute of Micro- and Nanoelectronic Systems
IMT	Institute of Microstructure Technology
IMVT	Institute for Micro Process Engineering (dt. Institut für Mikro-Verfahrens-Technik)
Inovesa	Inovesa Numerical Optimized Vlasov Equation Solver Application
IPE	Institute for Data Processing and Electronics (dt. Institut für Prozessdatenverarbeitung und Elektronik)
ISR	incoherent synchrotron radiation
KARA	Karlsruhe Research Accelerator
KIT	Karlsruhe Institute of Technology
Linac	linear accerator
LLRF	low-level RF
MA	RF acceptance
NIST	National Institute of Standards and Technology
PhLAM	Laboratory of Physics of Laser, Atoms, and Molecules
PZKL	Photonic Centre Kaiserslautern (dt. Photonik-Zentrum Kaiserslautern e.V.)
RF	radio frequency
RMS	root mean square
SBB	Short-bunch-length bursting
SCU20	Superconducting Undulator with 20 mm periodic length
SEM	scanning electron microscope

SOLEIL	Optimized Light Source of Intermediate Energy to LURE (fr. Source optimisée de lumière d'énergie intermédiaire du LURE)
SSMB	Steady-state micro-bunching
SPR	Smith-Purcell radiation
SR	synchrotron radiation
STD	standard deviation
UHV	ultra-high vacuum
UltraSync	ULTRAfast exploration and control of electron bunch dynamics in SYNChrotron light sources
UO	user operation
VFPE	Vlasov-Fokker-Planck equation
VFPS	Vlasov-Fokker-Planck solver

Symbols: Latin

Symbol	Description	Value	Unit
U	Acceleration voltage		V
U_{acc}	Acceleration voltage amplitude		V
I_{A}	Alfvén current	17 045	A
h_{c}	Beam chamber height	KARA: 32	mm
I_{b}	Bunch current		µA
f_{burst}	Bursting frequency		kHz
I_{thr}	Bursting threshold current		µA
q	Charge		C
C	Accelerator circumference	KARA: 110.4	m
$f_{\mathrm{cut.}}$	Cutoff frequency		Hz
$f_{\mathrm{c,SPR}}$	Characteristic frequency of Smith-Purcell radiation		GHz
D	Dispersion		m
f_{sub}	Dominant substructure spectrum frequency		GHz
e	Elementaty charge	1.602×10^{-19}	C
$\vec{E}_{\mathrm{el}}$	Electric field		$\frac{\mathrm{V}}{\mathrm{m}}$
m_0	Electron mass	9.11×10^{-31}	kg
E	Energy		eV
W_0	Energy loss per revolution		eV
h	Harmonic number	KARA: 184	
Z	Impedance		Ω
$Z^{\parallel}$	Longitudinal impedance		Ω
$\vec{B}$	Magnetic flux density		T
f_{max}	Maximal simulation frequency		GHz
$f_{\mathrm{res;max}}$	Maximal effective impedance resonance frequency		GHz
$f_{\mathrm{res;min}}$	Minimal effective impedance resonance frequency frequency		GHz
p_{s}	Momentum of synchronous particle		GeV/c
$\hat{f}_{\mathrm{res}}$	Most effective impedance resonance frequency		Hz
L_0	Orbit length		m
Q	Quality factor		
f_{RF}	RF frequency	KARA: 499.7	MHz
f_{res}	Resonance frequency of the impedance		Hz
f_{rev}	Revolution frequency	KARA: 2.7	MHz
T_{rev}	Revolution period	KARA: 368	ns
C_{γ}	Sands' radiation constant	8.8575×10^{-5}	$\frac{\mathrm{m}}{\mathrm{GeV}^3}$
$\mathbf{S}$	Scattering matrix		

Symbol	**Description**	**Value**	**Unit**
Z_0	Shunt impedance		
$f_{\mathrm{burst;slow}}$	Slow outburst frequency (repetition rate)		Hz
$I_{\mathrm{thr;slow}}$	Slow outburst threshold current		µA
c	Speed of light	2.998×10^8	$\frac{\mathrm{m}}{\mathrm{s}}$
f_{s}	Synchrotron frequency		Hz
T_{s}	Synchrotron period		s
P_{s}	Synchrotron radiation power		W
Z_{vac}	Vacuum impedance	$120\,\pi$	Ω
$\vec{v}$	Velocity		$\frac{\mathrm{m}}{\mathrm{s}}$
U	Voltage		V
k	Wave number		$\frac{1}{\mathrm{m}}$
E	Wake field		
W	Wake function		
k_{l}	Wake loss factor		$\frac{\mathrm{V}}{\mathrm{pC}}$
V	Wake potential		V

Symbols: Greek

Symbol	Description	Value	Unit
ρ	Bending radius	KARA: 5.559	m
β	betatron-function		
σ_{c}	Conductivity		$\frac{\mathrm{S}}{\mathrm{m}}$
ω_{c}	Critical frequency		1/s
τ_{D}	Damping time		s
ϵ_0	Dielectric constant in vacuum	8.85×10^{-12}	$\frac{\mathrm{A\,s}}{\mathrm{V\,m}}$
σ_{el}	Electrical conductivity		$\frac{\mathrm{S}}{\mathrm{m}}$
ρ_{el}	Electrical resistivity		$\Omega\,\mathrm{m}$
σ_{E}	Energy spread		eV
Ξ	Corrugated Plate Impedance Parameter		$\frac{\Omega}{\mathrm{Hz}^2}$
τ	Lifetime		h
ϱ	Longitudinal bunch profil		$\frac{\mathrm{C}}{\mathrm{m}}$
α_{c}	Momentum compaction factor		
Ψ	Phase space charge density		$\frac{\mathrm{C}}{\mathrm{ps\,GeV}}$
μ_{r}	Relative permeability		
β	Relativistic beta		
γ	Relativistic gamma		
Π	Shielding parameter		
η_{c}	Slippage factor		
δ	Skin depth		µm
Ψ_{s}	Synchronous phase		
$\omega_{\mathrm{typ.}}$	Typical frequency		1/s
μ_0	Vacuum permeability	$4\pi \times 10^{-7}$	$\frac{\mathrm{H}}{\mathrm{m}}$
σ_0	Zero current bunch length		mm

Symbols: Corrugation Parameters

Symbol	Description	Value	Unit
$A_{\text{corr.}}$	Corrugation Area		mm^2
b	Plate distance		mm
h	Corrugation depth		µm
L/g	Corrugation duty cycle		
s	Corrugation plate length		µm
L	Periodic length		µm
g	Longitudinal gap		µm
t	Plate thickness		mm
x_0	Plate width		mm
N_{corr}	Number of corrugations		
α	Sidewall angle		$^\circ$
Δs	Phase shift distance		µm

Appendix

A. Frequencies

In this thesis several different important frequencies occur, which strech across a wide range from kHz to THz. Following, a list and explaination of these frequencies is given:

- **Impedance resonance frequency f_{res}:** The resonance frequency of both the corrugated structure impedance and the broadband resonator model, which is used to describe the additinal impedance in the Inovesa beam dynamics simulations. Throughout this thesis, f_{res} is the range from 50 GHz to 200 GHz.
- **Characterisitc frequency of Smith-Purcell radiation $f_{\mathrm{c,SPR}}$:** The charactersitic frequency, that describes the temporal intensity fluctuation of the Smith-Purcell radiation (SPR) pulse. It is identical with the f_{res} of the causing corrugated structre impedance. Consequently, it is also in the range from 50 GHz to 200 GHz.
- **Synchroton frequency f_{s}:** Frequency of the longitudinal oscillation around the synchronous particle of the bunch. For the KARA low-α_{c} machine settings of this thesis, f_{s} is between 8.89 kHz and 15.90 kHz.
- **Bursting frequency f_{burst}:** Domiant fluctuation frequency of the CSR emission power due to the rotation of the substructures in the longitudinal phase space. Therefore it is always larger than f_{s} and is the range of a few tens of kHz.
- **Slow outburst frequency $f_{\mathrm{burst;slow}}$:** Dominant frequency of the temporal outbursts of the CSR emission power due to the creation and vanishing of the substructures on the longitudinal bunch profile. The $f_{\mathrm{burst;slow}}$ for the KARA low-α_{c} is typically in the range of a few hundreds Hz to a few kHz. It should be noted that the bursting and slow outburst frequency characterize the temporal changes in the power emssion and give no direct information about the wavelength and frequency spectrum of the emitted photons.
- **RF frequency f_{RF} and revolution frequency f_{rev}:** The frequency of the RF accerleration voltage at KARA is $f_{\mathrm{RF}} = 500\,\mathrm{MHz}$ and defines the spacing bewtween the bunches in the storage ring. The revoluion frequency is determined by the circumference of the accelerator and the velocity of the particles. For the KARA settings it is given by $f_{\mathrm{rev}} = 2.7\,\mathrm{MHz}$.
- **Cutoff frequency $f_{\mathrm{cut.}}$:** The cutoff frequency defines the minimal frequency of radiation that can propagade inside the beam pipe. For the height of the KARA beam pipe it is given by $f_{\mathrm{cut.}} = 61\,\mathrm{GHz}$.
- **Maximal simulation frequency f_{max}:** The maximal simulation frequency defines the frequency range, for which the impedance simulations in CST. It is defined by the required frequency range of Inovesa Numerical Optimized Vlasov Equation Solver Application (Inovesa) and is in the range from 0.1 THz to 5 THz.

B. Fourier Transform

For the calculation of the (inverse) Fourier transform, the predefined functions from the python scipy package [109] are used. In case of the inverse Fourier transform, the time axis and its required resolution have been defined by some other simulation results. Therefore, for the inverse fast Fourier transform (iFFT), the required time axis is an additional input parameter. For an improvement of the data point density, the length of the signal array can be increased by zero-padding, i.e. by adding a list of zeros to the signal array before the Fourier transform is performed before. In case of the CSR intensity, which does not vanish for long times, the average over time is used as the offset, which is subtracted from the array. The implementation of the (inverse) Fourier transform and the zero-padding is shown here:

```python
import numpy as np
from scipy as sc

def FFT(t,signal):
    Nrfft=len(signal)
    SAMPLE_RATE=Nrfft/(t[-1]-t[0])
    fourierTransform=sc.fft.rfft(signal)
    Freq=sc.fft.rfftfreq(Nrfft, 1/SAMPLE_RATE)
    return Freq,np.array(np.abs(fourierTransform))


def iFFT(freq,signal,time):
    Nrfft=len(signal)
    fourierTransform=sc.fft.irfft(signal,2*len(time))
    time=sc.fft.rfftfreq(Nrfft)
    return time,np.array(np.abs(fourierTransform))

def zero_padding(x,y,newLength,offset):
    DeltaX=x[1]-x[0]
    while len(x)<newLength:
        x=np.append(x,x[-1]+DeltaX)
        y=np.append(y,offset)
    return x,y
```

C. Fit Function: Resonator

For the fitting with the resonator function, the data must be pre-selected. Since the double-peak can not be determined by a single fit properly, the two peaks are fitted individually. Therefore, the two peak impedances and the corresponding resonance frequencies are determined. For the fit of each peak, only the ydata points that drop manotonically - for increasing and decreasing frequency - from the corresponding maximum impedance, are taken into account. It turns out that a preliminary guess $p0$ of the resonator parameters Z_0, f_{res}, and Q is also necessary. The first one ist estimated by the maximal value of the ydata points and the second one as the xdata value of this ydata value. For the quality factor, an arbitrary estimated width $\sigma = 0$ of an Gaussian peak is used, which is connected to the quality factor via $Q = \frac{\bar{y}}{2\pi \log(2)} \cdot \sigma$. The python script looks like:

```python
import numpy as np
from scipy.optimize import curve_fit

def Resonator(x,Z0,Q,omega0): # fitting function
    return Z0/(1+Q**2*(omega0/x-x/omega0)**2)

def fitResonator(xList,yList):
    meanCalc=xList[yList.index(max(yList))] # position of maximal value
    sigmaCalc=20 # approximated peak width
```

```
    X=[]
    Y=[]
    weight=[]
    for i in range(len(xList)):
    if yList[i]>0:  # only taking positive values into account for the fit
    X.append((2*np.pi*xList[i]))
    Y.append(yList[i])
    weight.append(max(yList[i],1e-6))    # fit weighted by y-value
    z,cov=curve_fit(Resonator,X,Y,p0=[max(yList),meanCalc/(2*np.sqrt(2*np.log
        (2))*sigmaCalc),meanCalc],sigma=[1/i**2 for i in X])
    R=z[0]
    Q=z[1]
    omegaC=z[2]
    Rerr=np.sqrt(cov[0][0])
    Qerr=np.sqrt(cov[1][1])
    omegaCerr=np.sqrt(cov[2][2])
    Yfit=[R/(1+Q**2*(omegaC/(2*np.pi*i)-(2*np.pi*i)/omegaC)**2) for i in
        xList]
    return R,Q,omegaC,Rerr,Qerr,omegaCerr
```

D. KARA Fill *f05135*

In the KARA fill *f05135* the storage ring has been performed in a well established und understood low-α_c setting. Therefore, the machine settings of this run has been used several times for experiments and comparable simulations. A list with the most important and relevant machine and simulations settings, corresponding to *f05135*, is given in this table:

Table D.4. **KARA machine parameters for *f05135*.**

Parameter	Value	Unit
Electron beam energy E	1.3	GeV
Energy spread σ_E	0.047	%
Damping time τ_D	1.04	ms
RF frequency f_{RF}	499.705	MHz
Revolution frequency f_{rev}	2.7157	MHz
Synchrotron frequency f_s	9.44	kHz
Accelerating voltage U_{acc}	1.048	MV
Momentum compaction factor α_c	5.2×10^{-4}	
Zero-current bunch length σ_0	4.1	ps

E. Phase Shift

As discussed in Section 8.2.2, the whole structure length of s=20 cm cannot be manufactured in one piece for all the tried methods. Consequently, this can cause a phase shift of the impedance at the transition between the different pieces, depending on the offset length Δs (see Figure 8.10).

Figure E.1 shows that a fit with the resonator model (blue) cannot describe the real part of the impedance properly, due to negative contribution of the phase shift. However, the Equation (8.2) is too complicated for a fit. To get a comparable but easier function, the cos and sin terms have been written as a Taylor series, where the contributions up to $\mathcal{O}(\omega^2)$ are taken into account. This approximation is in good agreement with the actual exact theoretical impedance (see Figure E.1) and delivers the impedance parameters Z_0 and f_{res} from a fit.

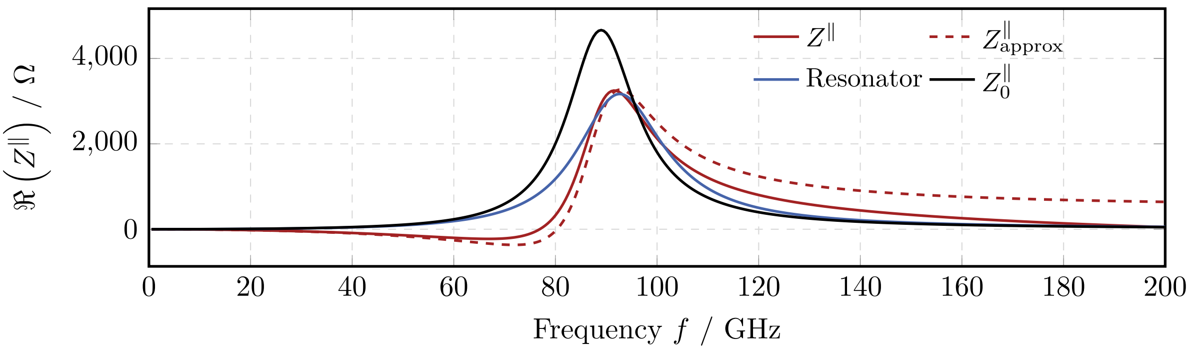

Figure E.1. Theoretical impedance with phase shift. The longitudinal impedance of a structure with a phase shift distance Δs, cannot be described properly with the resonator model. A fit with a Taylor expand version of Equation (8.2) can describe the impedance.

F. Supplementary Figures

F.1. Scraper Experiment

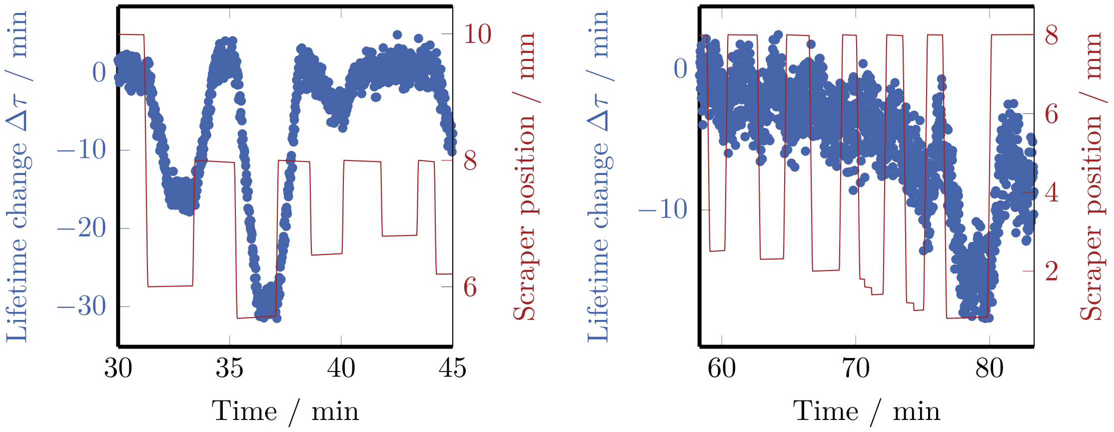

(a) Top scraper at normal-α_c **(b)** Bottom scraper at normal-α_c

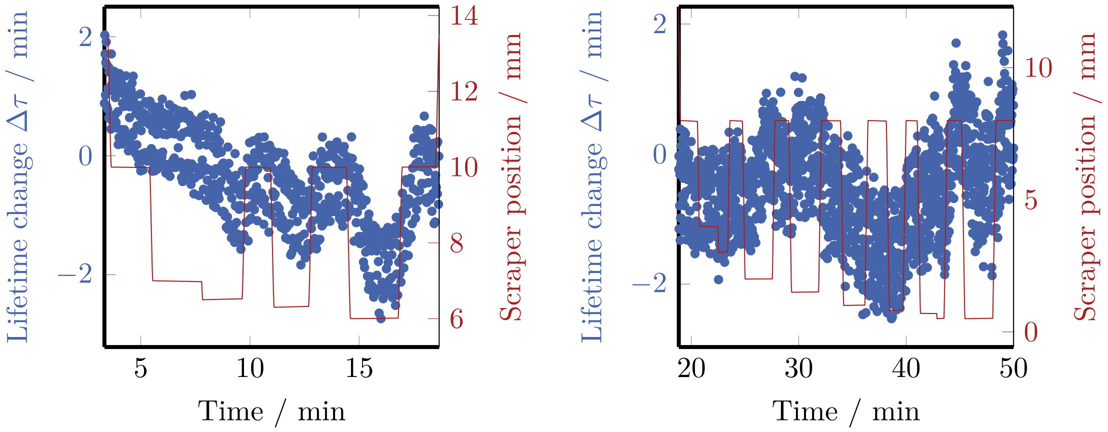

(c) Top scraper at low-α_c **(d)** Bottom scraper at low-α_c

Figure F.2. Lifetime change by vertical scrapers. The red curves describe the position of the respective scraper. The other sceaper is completely removed. Due to the closing of the gap, the beam lifetime (blue) is reduced.

F.2. Beam Dynamics

F.2.1. Fluctuation Power For Different Additional Impedances

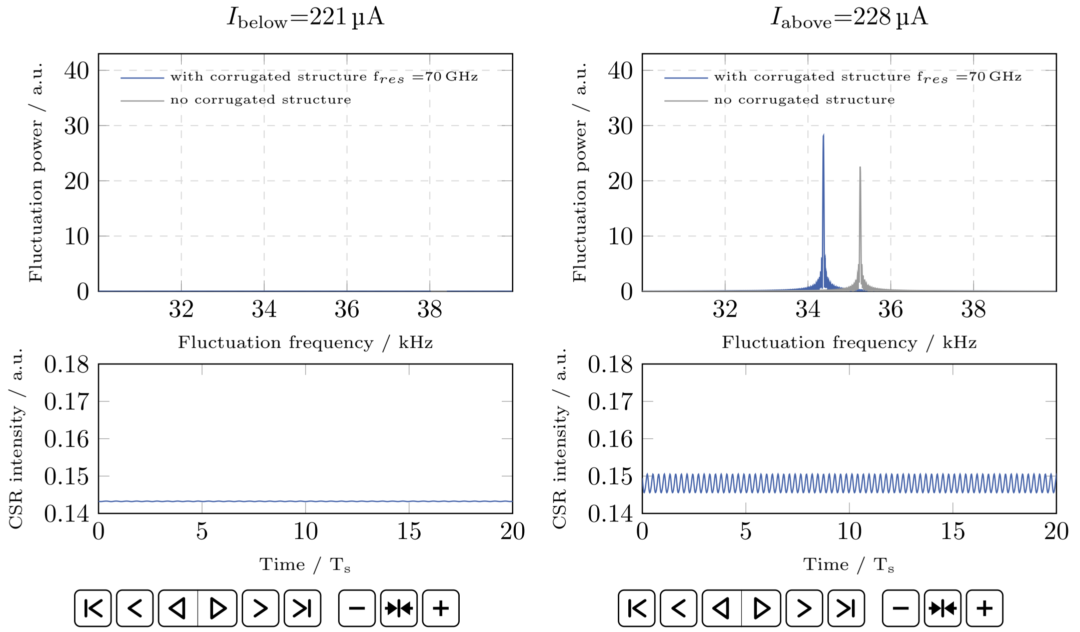

Figure F.3. Fluctuation power for different additional impedances around the bursting frequency. The shunt impedance and quality factor are fixed at Z_0=1 kΩ and Q=3. The bottom plot shows the emitted CSR intensity over time for the same simulation.

F.2.2. Quality Factor Scan

The contribution at a frequency that deviates from f_{res} to the resonator impedance only depends on the quality factor for a fixed shunt impedance.

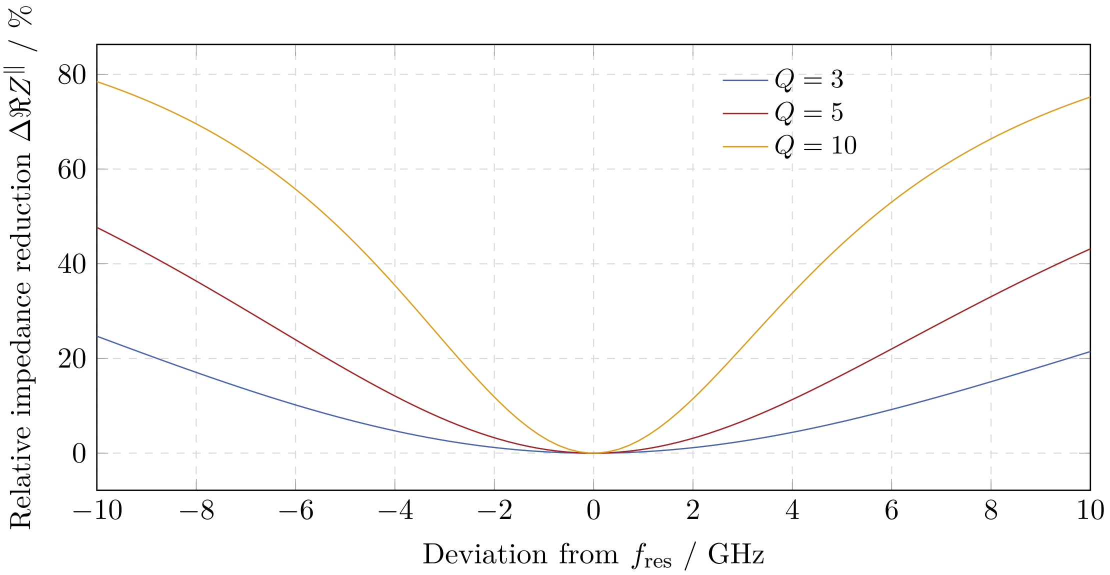

Figure F.4. Impedance reduction for different quality factors. A deviation from f_{res} leads to a reduction of the impedance contribution depending on the quality factor. A higher quality factor, corresponding to a narrower peak, has a smaller impedance contribution for the same frequency deviation. The resonance frequency is fixed at $f_{\mathrm{res}} = 110\,\mathrm{GHz}$.

F.2.3. Current Decay

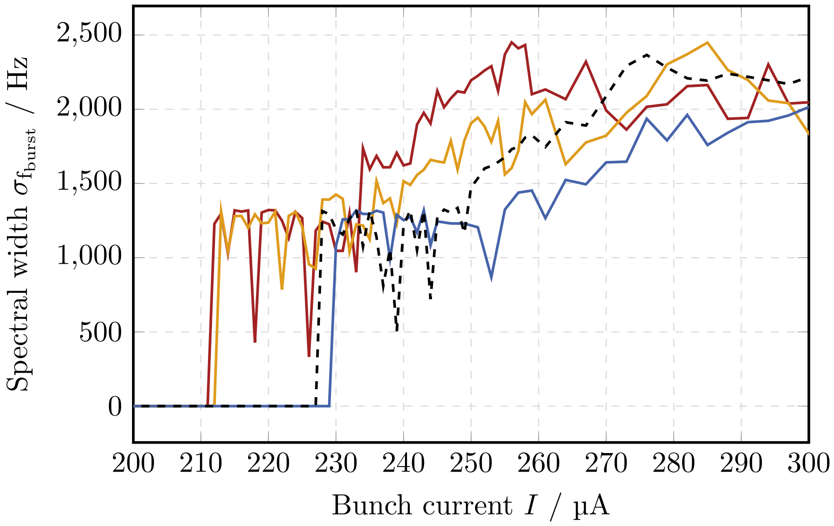

Figure F.5. **Spectral bursting width σ_{burst}** is shown as a function of the beam current I. With increasing current the width increases as well, whereby the jumps indicate the changes between the different micro-bunching instability regimes.

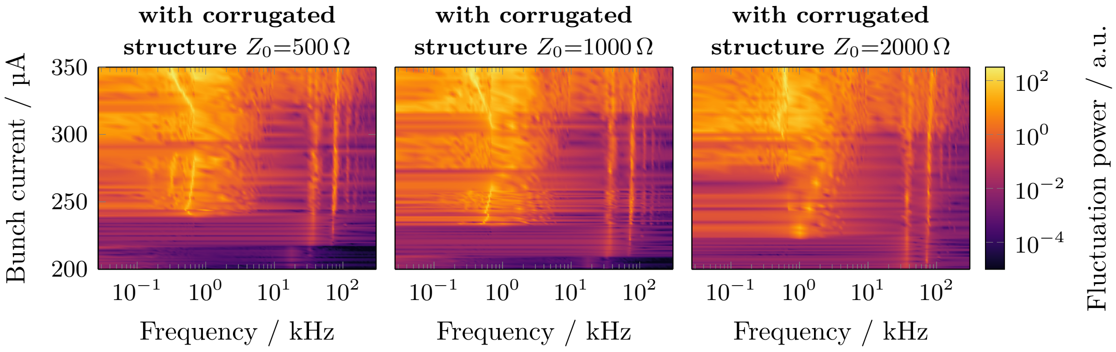

Figure F.6. **Z_0 scan: spectrograms with $f_{\mathrm{res}} = 110\,\mathrm{GHz}$.**

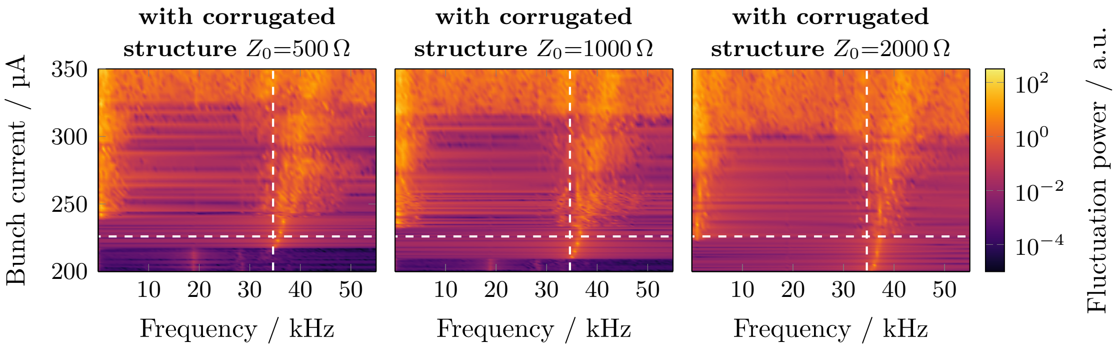

Figure F.7. **Z_0 scan: spectrograms with $f_{\mathrm{res}} = 110\,\mathrm{GHz}$ at bursting.**

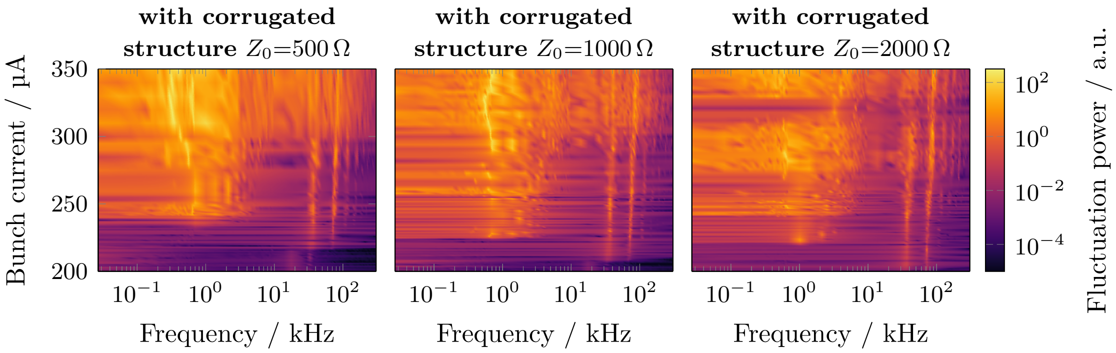

Figure F.8. Z_0 **scan: spectrograms with** $f_{\text{res}} = 140\,\text{GHz}$.

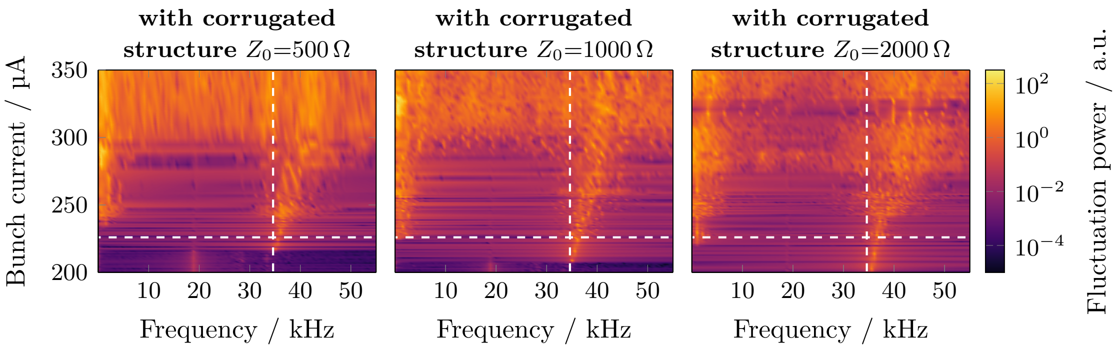

Figure F.9. Z_0 **scan: spectrograms with** $f_{\text{res}} = 140\,\text{GHz}$ **at bursting.**

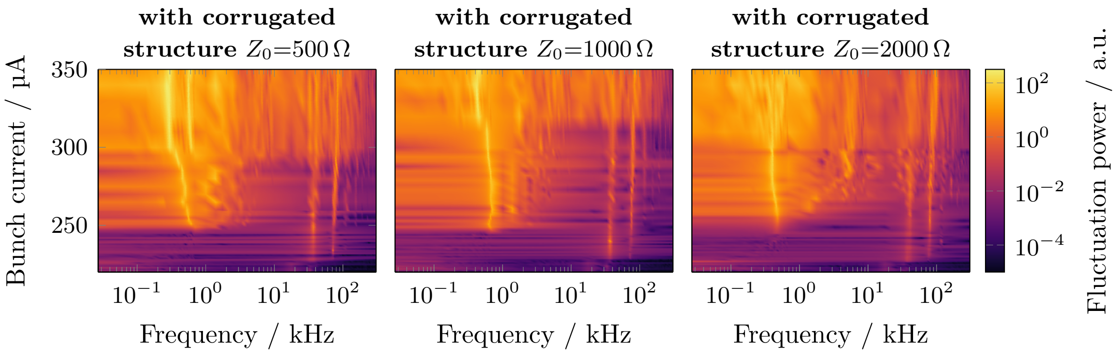

Figure F.10. Z_0 **scan: spectrograms with** $f_{\text{res}} = 180\,\text{GHz}$.

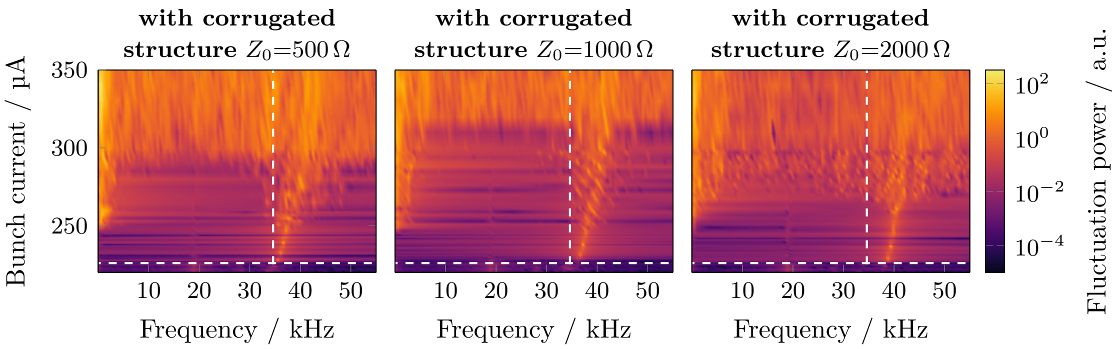

Figure F.11. **Z_0 scan: spectrograms with $f_{\text{res}} = 180\,\text{GHz}$ at bursting.**

F.3. Manufacturing

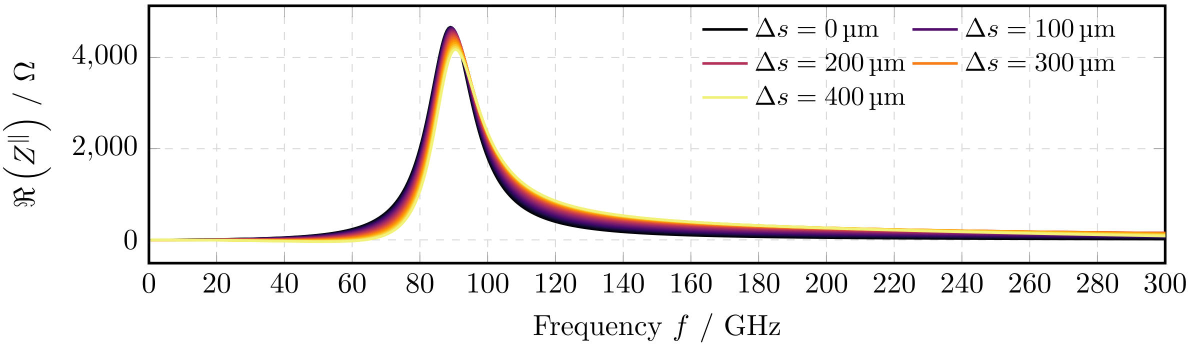

(a)

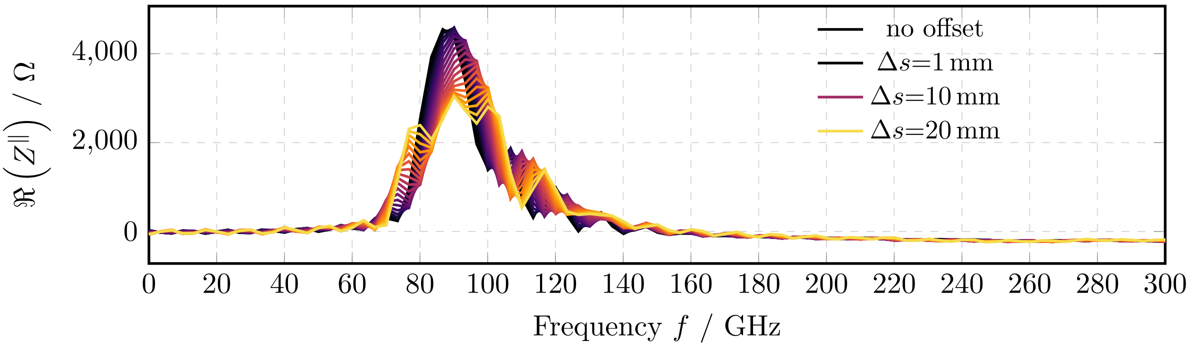

(b)

Figure F.12. Impedance for different phase shift distances. The theoretical (a) and simulated (b) longitudinal impedance of a corrugated structure for different values of the phase shift distance Δs. The fixed corrugation parameters are corrugation depth $h = 300\,\mu m$, periodic length $L = 200\,\mu m$, duty cycle $L/g = 2$, and plate distance $b = 2\,mm$. The parameters of the impedance $\Delta s = 0\,mm$ are Z_0=4.66 kΩ and f_{res}=89.4 GHz

G. Supplementary Microscope Images

For studying the accurarcy of the corrugation parameters, the surface roughness, or the side wall angles, the prototyps of the corrugated structures are investigated with optical microscopes and a scanning electron microscope (SEM).

G.1. Deep Reactive Ion Etching

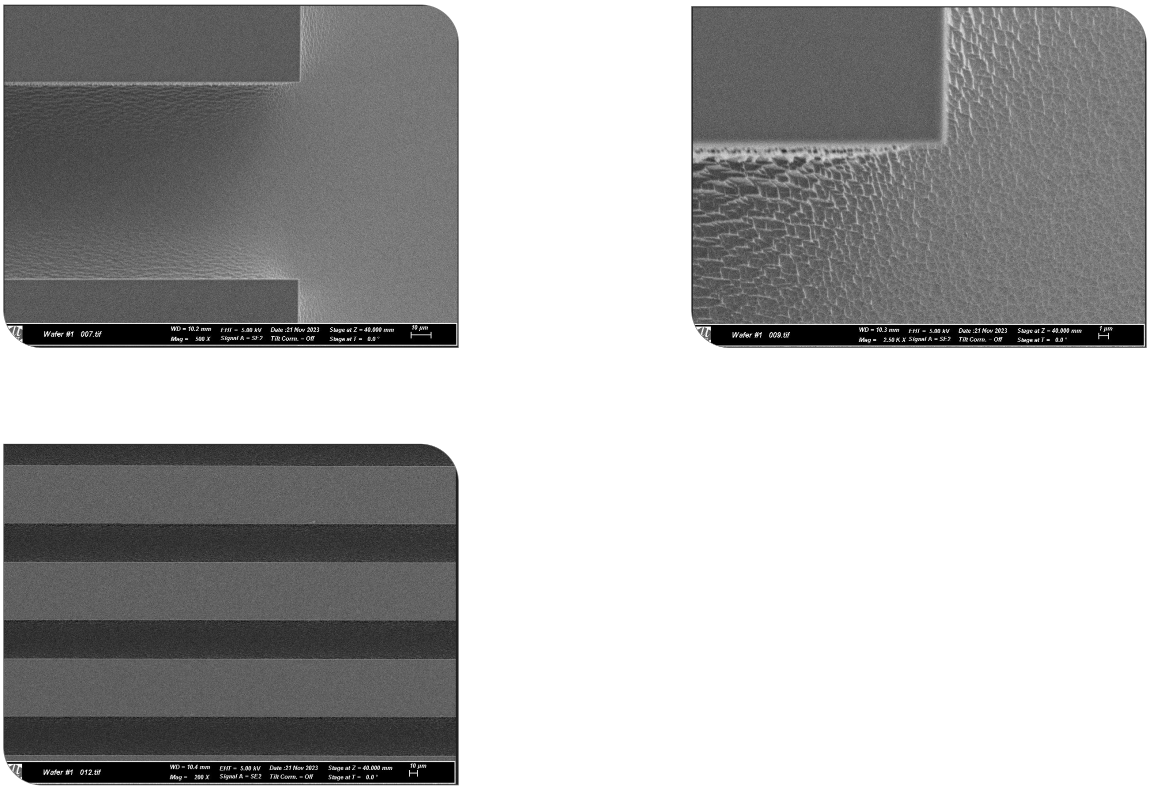

Figure G.13. SEM images: deep reactive ion etching (DRIE) in silicon. Courtesy A. Muslija (IMT)

G.2. Miling

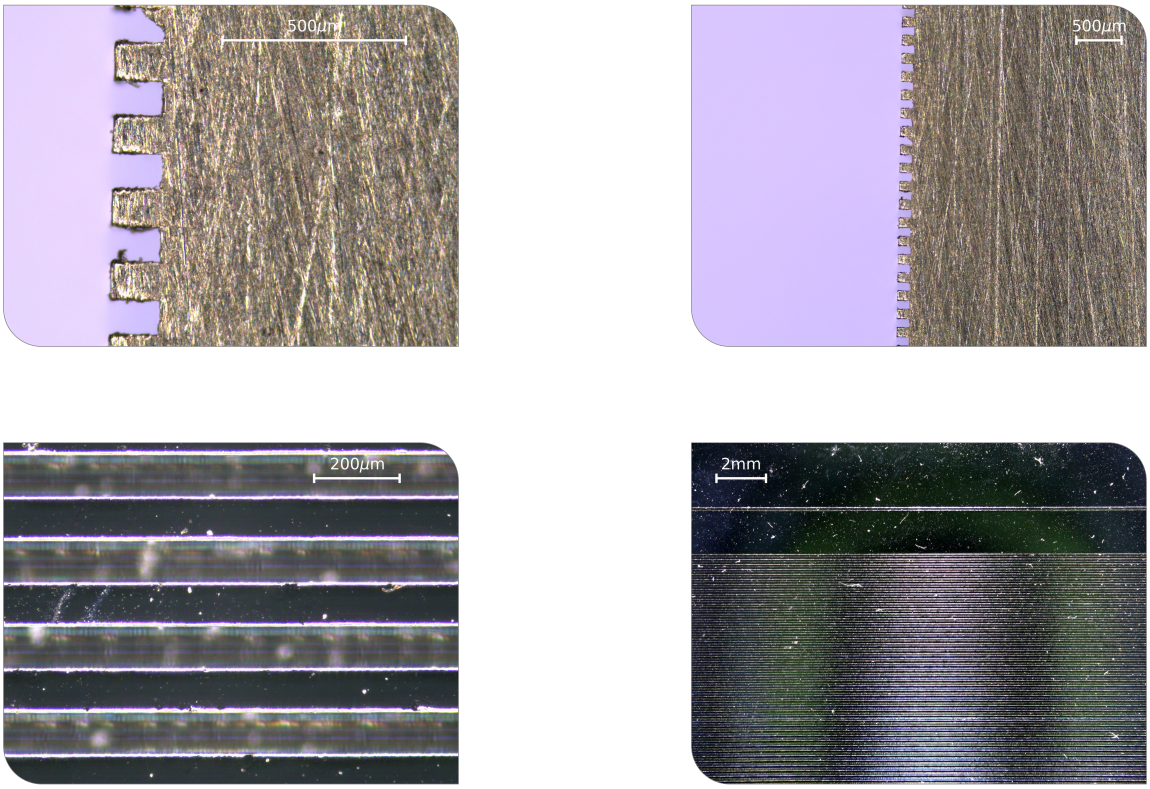

Figure G.14. **Optical microscope images: Milling in aluminum**

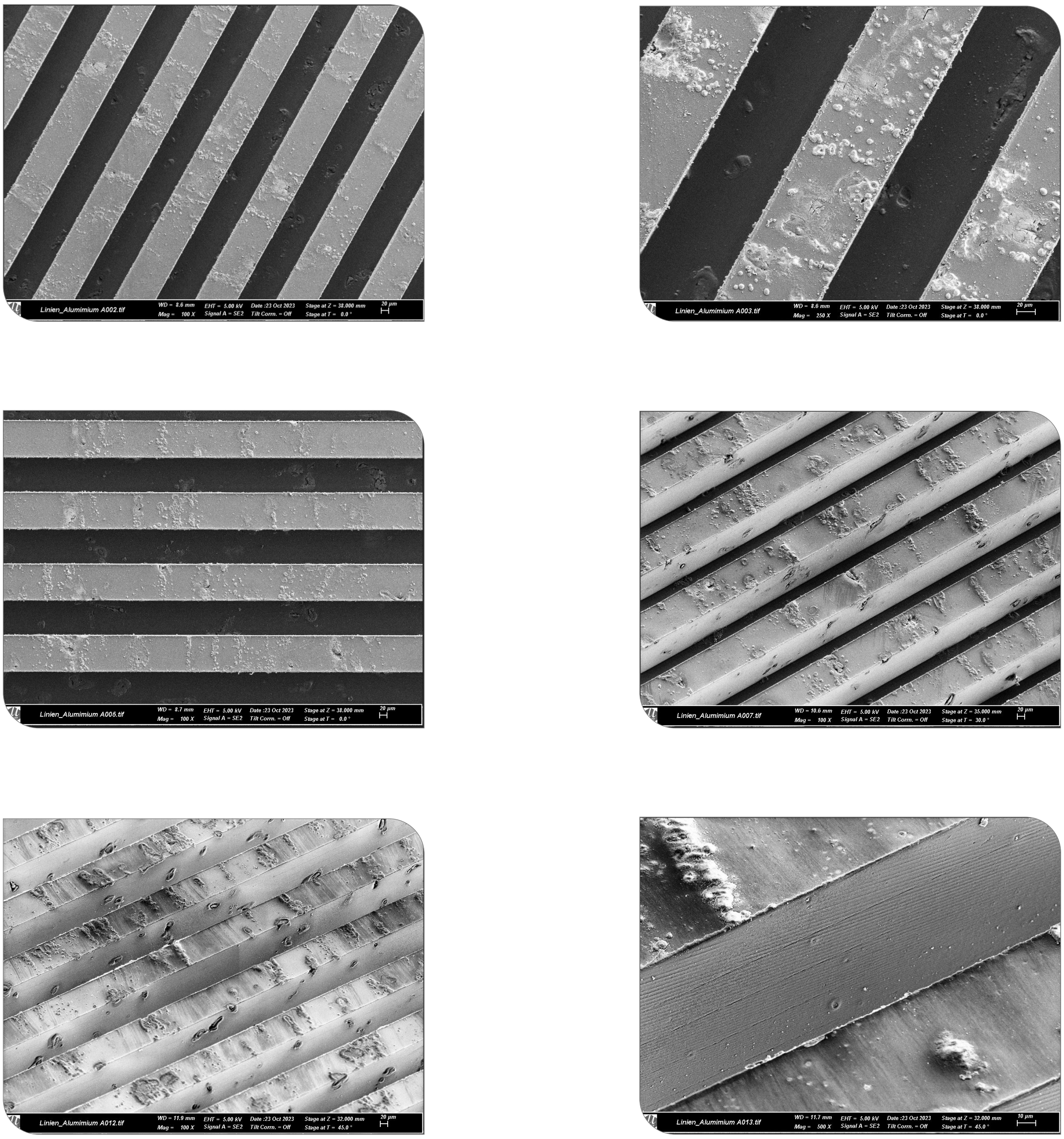

Figure G.15. **SEM images: Milling in aluminum**

Publications

[Mai] S. Maier, M. Brosi, A. Mochihashi, M. Nasse, M. Schwarz, and A.-S. Müller „Influencing the bursting dynamics by an additional corrugated structure impedance at KARA“ to be published (see pp. 49, 56, 63, 64, 80, 86, 87, 90).

[Mai17] S. Maier „Untersuchung von stickstoffangereichertem Silizium als strahlenhartes Sensormaterial“ BA thesis Karlsruhe Institut für Technologie (KIT), 2017
`https://publish.etp.kit.edu/record/21458`.

[Mai20] S. Maier „Systematic studies of RF phase modulation at KARA“ MA thesis Karlsruher Institut für Technologie (KIT), 2020
DOI: `10.5445/IR/1000123900`.

[Mai21] S. Maier, M. Brosi, A. Mochihashi, A.-S. Müller, M. Nasse, and M. Schwarz „Impedance Studies of a Corrugated Pipe for KARA“ in: *Proc. IPAC'21* (Campinas, SP, Brazil) International Particle Accelerator Conference JACoW Publishing, Geneva, Switzerland, 2021, TUPAB251, pp. 2039–2042 ISBN: 978-3-95450-214-1
DOI: `10.18429/JACoW-IPAC2021-TUPAB251` (see pp. 63, 64, 103, 105, 106).

[Mai22a] S. Maier, M. Brosi, H. Cha, A. Mochihashi, A.-S. Müller, M. Nasse, P. Schreiber, and M. Schwarz „Design Considerations of the Corrugated Structures in a Vacuum Chamber for Impedance Studies at KARA“ in: *Proc. 11th Int. Beam Instrum. Conf. (IBIC'22)* (Kraków, Poland) International Beam Instrumentation Conference 11 JACoW Publishing, Geneva, Switzerland, 2022, MOP27, pp. 100–104 ISBN: 978-3-95450-241-7
DOI: `10.18429/JACoW-IBIC2022-MOP27` (see pp. 99, 100, 103).

[Mai22b] S. Maier, M. Brosi, A. Mochihashi, A.-S. Müller, M. Nasse, P. Schreiber, and M. Schwarz „Simulation of the Effect of Corrugated Structures on the Longitudinal Beam Dynamics at KARA“ in: *Proc. IPAC'22* (Bangkok, Thailand) International Particle Accelerator Conference JACoW Publishing, Geneva, Switzerland, 2022, pp. 2241–2244 ISBN: 978-3-95-450227-1
DOI: `10.18429/JACoW-IPAC2022-WEPOMS006` (see pp. 52, 75, 76, 80).

[Mai23] S. Maier, M. Brosi, H. Y. Cha, A. Mochihashi, A.-S. Müller, M. Nasse, P. Schreiber, and M. Schwarz „Simulation studies on longitudinal beam dynamics manipulated by corrugated structures under different bunch length conditions at KARA“ in: *Proc. IPAC'23* (Venice, Italy) IPAC'23 - 14th International Particle Accelerator Conference 14 JACoW Publishing, Geneva, Switzerland, 2023, pp. 3570–3573
DOI: `10.18429/JACoW-IPAC2023-WEPL189` (see pp. 88, 90).

[Mai24] S. Maier, A. Mochihashi, A.-S. Müller, M. Nasse, and M. Schwarz „Microbunching Threshold Manipulation by a Corrugated Structure Impedance at KARA“ in: *Proc. IPAC'24* (Nashville, TN, USA) IPAC'24 - 15th International Particle Accelerator Conference 15 JACoW Publishing, Geneva, Switzerland, 2024
DOI: `10.18429/JACoW-IPAC2024-MOPS40`.

[Moc21] A. Mochihashi, S. Maier, E. Blomley, M. Schuh, E. Huttel, T. Boltz, B. Kehrer, A.-S. Müller, and D. Teytelman „Detuning Properties of RF Phase Modulation in the Electron Storage Ring KARA“ in: *arXiv* (2021) to be submitted to Phys. Rev. Accel. Beams arXiv: `2111.15555`.

[Nol23] M. Noll, S. Maier, E. Bründermann, D. El Khechen, J. Steinmann, C. Widmann, and A.-S. Müller „Towards fiber optics-guided synchrotron radiation-based longitudinal beam diagnostics at the KARA booster synchrotron“ English in: *Proc. IPAC'23* (Venice, Italy) IPAC'23 - 14th International Particle Accelerator Conference 14 JACoW Publishing, Geneva, Switzerland, 2023, pp. 4768–4771 ISBN: 978-3-95450-231-8
DOI: `10.18429/JACoW-IPAC2023-THPL126`.

[Sch23] P. Schreiber, S. Maier, A. Papash, R. Ruprecht, M. Schuh, and A.-S. Müller „Amplitude dependent tune shift measurements at KARA“ English in: *Proc. IPAC'23* (Venice, Italy) IPAC'23 - 14th International Particle Accelerator Conference 14 JACoW Publishing, Geneva, Switzerland, 2023, pp. 3371–3374
ISBN: 978-3-95450-231-8
DOI: `10.18429/JACoW-IPAC2023-WEPL111`.

[Sco] L. Scomparin, A. Santamaria Garcia, C. Evain, S. Bielawski, C. Szwaj, S. Maier, M. Nasse, and A.-S. Müller „Classical control of the microbunching instability at KARA“ in preparation (see p. 96).

Bibliography

[1] E. Bründermann, H.-W. Hübers, and M. F. Kimmitt *Terahertz techniques* vol. 151 Springer, 2012
DOI: `10.1007/978-3-642-02592-1` (see p. 1).

[2] D. F. Swearer, S. Gottheim, J. G. Simmons, D. J. Phillips, M. J. Kale, M. J. McClain, P. Christopher, N. J. Halas, and H. O. Everitt „Monitoring Chemical Reactions with Terahertz Rotational Spectroscopy“ in: *ACS Photonics* 5.8 (2018), pp. 3097–3106
DOI: `10.1021/acsphotonics.8b00342` (see p. 1).

[3] A. I. Papash et al. „Non-Linear Optics and Low Alpha Operation at the Storage Ring KARA at KIT“ in: *Proc. IPAC'18* (Vancouver, Canada, Apr.-May 2018) JACoW Publishing, Geneva, Switzerland, pp. 4235–4238
DOI: `10.18429/JACoW-IPAC2018-THPMF070` (see p. 1).

[4] A.-S. Müller et al. „Far Infrared Coherent Synchrotron Edge Radiation at ANKA“ in: *Proc. PAC'05* (Knoxville, TN, USA, May 2005) Particle Accelerator Conference 21 JACoW Publishing, Geneva, Switzerland, pp. 2518–2520
`https://jacow.org/p05/papers/RPAE038.pdf` (see p. 1).

[5] J. Byrd, W. Leemans, A. Loftsdottir, B. Marcelis, M. C. Martin, W. McKinney, F. Sannibale, T. Scarvie, and C. Steier „Observation of broadband self-amplified spontaneous coherent terahertz synchrotron radiation in a storage ring“ in: *Physical review letters* 89.22 (2002), p. 224801
DOI: `https://doi.org/10.1103/PhysRevLett.89.224801` (see p. 1).

[6] W. Shields, R. Bartolini, G. Boorman, P. Karataev, A. Lyapin, J. Puntree, and G. Rehm „Microbunch Instability Observations from a THz Detector at Diamond Light Source“ in: *Journal of Physics: Conference Series* 357.1 (2012), p. 012037
DOI: `10.1088/1742-6596/357/1/012037` (see p. 1).

[7] M. Brosi „Overview of the Micro-Bunching Instability in Electron Storage Rings and Evolving Diagnostics“ in: *Proc. IPAC'21* (Campinas, Brazil, May 2021) JACoW Publishing, Geneva, Switzerland, pp. 3686–3691
DOI: `10.18429/JACoW-IPAC2021-THXA02` (see p. 1).

[8] M. Venturini and R. Warnock „Bursts of coherent synchrotron radiation in electron storage rings: a dynamical model“ in: *Physical review letters* 89.22 (2002), p. 224802
DOI: `10.1103/PhysRevLett.89.224802` (see p. 1).

[9] E. Roussel, C. Evain, C. Szwaj, S. Bielawski, J. Raasch, P. Thoma, A. Scheuring, M. Hofherr, K. Ilin, S. Wünsch, M. Siegel, M. Hosaka, N. Yamamoto, Y. Takashima, H. Zen, T. Konomi, M. Adachi, S. Kimura, and M. Katoh „Microbunching Instability in Relativistic Electron Bunches: Direct Observations of the Microstructures Using Ultrafast YBCO Detectors“ in: *Phys. Rev. Lett.* 113 (2014), p. 094801
DOI: `10.1103/PhysRevLett.113.094801` (see p. 1).

[10] X. Deng, A. Chao, J. Feikes, A. Hoehl, W. Huang, R. Klein, A. Kruschinski, J. Li, A. Matveenko, Y. Petenev, M. Ries, C. Tang, and L. Yan „Experimental demonstration of the mechanism of steady-state microbunching“ in: *Nature* 590.7847 (2021), pp. 576–579 ISSN: 1476-4687
DOI: `10.1038/s41586-021-03203-0` (see p. 2).

[11] C. Evain, C. Szwaj, E. Roussel, J. Rodriguez, M. Le Parquier, M.-A. Tordeux, F. Ribeiro, M. Labat, N. Hubert, J.-B. Brubach, P. Roy, and S. Bielawski „Stable coherent terahertz synchrotron radiation from controlled relativistic electron bunches“ in: *Nature Physics* 15.7 (2019), pp. 635–639 ISSN: 1745-2481
DOI: `10.1038/s41567-019-0488-6` (see pp. 2, 80, 95).

[12] T. Boltz „Micro-Bunching Control at Electron Storage Rings with Reinforcement Learning“ 54.11.11; LK 01 PhD thesis Karlsruher Institut für Technologie (KIT), 2021 152 pp.
DOI: `10.5445/IR/1000140271` (see pp. 2, 94).

[13] L. Scomparin et al. „KINGFISHER: A Framework for Fast Machine Learning Inference for Autonomous Accelerator Systems“ in: *Proc. IBIC'22* (Kraków, Poland) International Beam Instrumentation Conference 11 JACoW Publishing, Geneva, Switzerland, 2022, pp. 151–155 ISBN: 978-3-95-450241-7
DOI: `10.18429/JACoW-IBIC2022-MOP42` (see p. 2).

[14] P. Dijkstal et al. „Corrugated wakefield structures at SwissFEL“ English in: *Proc. IPAC'23* (Venice, Italy) IPAC'23 - 14th International Particle Accelerator Conference 14 JACoW Publishing, Geneva, Switzerland, 2023, pp. 4828–4831 ISBN: 978-3-95450-231-8
DOI: `10.18429/JACoW-IPAC2023-THPL153` (see pp. 2, 103).

[15] P. Emma, M. Venturini, K. Bane, G. Stupakov, H.-S. Kang, M. Chae, J. Hong, C.-K. Min, H. Yang, T. Ha, et al. „Experimental demonstration of energy-chirp control in relativistic electron bunches using a corrugated pipe“ in: *Physical review letters* 112.3 (2014), p. 034801
DOI: `10.1103/PhysRevLett.112.034801` (see p. 2).

[16] K. Bane, G. Stupakov, S. Antipov, M. Fedurin, K. Kusche, C. Swinson, and D. Xiang „Measurements of terahertz radiation generated using a metallic, corrugated pipe“ in: *Nuclear Instruments and Methods in Physics Research Section A: Accelerators, Spectrometers, Detectors and Associated Equipment* 844 (2017), pp. 121–128 ISSN: 0168-9002
DOI: `https://doi.org/10.1016/j.nima.2016.11.041` (see pp. 2, 20).

[17] K. Bane and G. Stupakov „Terahertz radiation from a pipe with small corrugations“ in: *Nuclear Instruments and Methods in Physics Research Section A: Accelerators, Spectrometers, Detectors and Associated Equipment* 677 (2012), pp. 67–73 ISSN: 0168-9002
DOI: `https://doi.org/10.1016/j.nima.2012.02.028` (see p. 2).

[18] S. J. Smith and E. M. Purcell „Visible Light from Localized Surface Charges Moving across a Grating“ in: *Phys. Rev.* 92 (1953), pp. 1069–1069
DOI: `10.1103/PhysRev.92.1069` (see pp. 2, 20).

[19] S. Antipov, I. Agapov, I. Zagorodnov, and F. Lemery „Adiabatic bunch compression in storage rings from self wakes generated in Cherenkov waveguides“ in: *Journal of Instrumentation* 18.07 (2023), P07024
DOI: `10.1088/1748-0221/18/07/P07024` (see p. 2).

[20] K. Wille *Physik der Teilchenbeschleuniger und Synchrotronstrahlungsquellen : eine Einführung* 2., überarb. und erw. Aufl. Teubner-Studienbücher : Physik Stuttgart: Teubner, 1996 ISBN: 978-3-663-11039-2
DOI: `10.1007/978-3-663-11039-2` (see pp. 5, 8–10, 13, 38).

[21] H. Wiedemann *Particle Accelerator Physics* 4th ed. 2015 Springer, 2015 ISBN: 978-331-91831-7-6
DOI: `10.1007/978-3-319-18317-6` (see pp. 5, 7, 10–12, 14–16, 30).

[22] E. M. McMillan „The Synchrotron—A Proposed High Energy Particle Accelerator“ in: *Phys. Rev.* 68 (1945), pp. 143–144
DOI: `10.1103/PhysRev.68.143` (see p. 6).

[23] E. O. Lawrence and M. S. Livingston „The production of high speed light ions without the use of high voltages“ in: *Physical Review* 40.1 (1932), p. 19 (see p. 6).

[24] V. I. Veksler „New method for the acceleration of relativistic particles“ in: *Doklady Akademii Nauk USSR* 43.8 (1944), pp. 346–348
`https://cir.nii.ac.jp/crid/1571698600730706688` (see p. 6).

[25] G. W. Hill „On the part of the motion of the lunar perigee which is a function of the mean motions of the sun and moon“ in: *Acta mathematica* 8.1 (1886), pp. 1–36 (see p. 8).

[26] A.-S. Müller *Accelerator Physics I: Particle Accelerators* Lectures at KIT 2017 (see pp. 9, 11–13).

[27] J. Liouville „Note sur la Théorie de la Variation des constantes arbitraires.“ in: *Journal de mathématiques pures et appliquées* (1838), pp. 342–349 (see p. 9).

[28] A. Wolski *Beam Dynamics in High Energy Particle Accelerators* IMPERIAL COLLEGE PRESS, 2014
DOI: `10.1142/p899` (see pp. 12, 16, 25, 26).

[29] J. D. Jackson *Classical electrodynamics* 3. ed. New York [u.a.]: Wiley, 1998 ISBN: 978-0-471-30932-1 (see pp. 12, 25).

[30] J. Larmor „LXIII. On the theory of the magnetic influence on spectra; and on the radiation from moving ions“ in: *The London, Edinburgh, and Dublin Philosophical Magazine and Journal of Science* 44.271 (1897), pp. 503–512
DOI: `10.1080/14786449708621095` (see p. 12).

[31] F. Elder, A. Gurewitsch, R. Langmuir, and H. Pollock „Radiation from electrons in a synchrotron“ in: *Physical Review* 71.11 (1947), p. 829 (see p. 12).

[32] A.-M. Lienard „L’Eclairage elect. 16, 5, 53, 106 (1898); E. Wiechert“ in: *Arch. Neerl* 5 (1900), p. 549 (see p. 12).

[33] A.-S. Müller et al. „Experimental Aspects of CSR in the ANKA Storage Ring“ in: *In ICFA Beam Dynamics Newsletter No. 57* (2012), pp. 154–165
`http://icfa-usa.jlab.org/archive/newsletter/icfa_bd_nl_57.pdf` (see pp. 14, 33).

[34] G. Franchetti *CAS - CERN Accelerator School: Introduction to Accelerator Physics 2016: Collective Effects II* Lecture at CAS 2016
`https://cds.cern.ch/record/2252489` (see p. 14).

[35] R. L. Warnock and J. A. Ellison „A General Method for Propagation of the Phase SpaceDistribution, with Application to the Sawtooth Instability“ in: *The physics of high brightness beams. Proceedings, 2nd ICFA Advanced Accelerator Workshop, Los Angeles, USA,* (2000), pp. 322–348
DOI: `10.2172/753322` (see pp. 15, 21, 24, 42).

[36] E. W. Weisstein „Heaviside step function“ in: *https://mathworld.wolfram.com/* (2002) (see p. 15).

[37] K. Y. Ng *Physics of Intensity Dependent Beam Instabilities* WORLD SCIENTIFIC, 2005
DOI: `10.1142/5835` (see pp. 15–17, 21, 22).

[38] B. W. Zotter and S. Kheifets *Impedances and Wakes in High Energy Particle Accelerators* WORLD SCIENTIFIC, 1998
DOI: `10.1142/3068` (see p. 15).

[39] A. W. Chao *Physics of collective beam instabilities in high-energy accelerators* Wiley, 1993 ISBN: 9780471551843 (see p. 15).

[40] Y. Yoon „Arbitrary bunch shaping via wake potential tailoring“ in: *Proc. IPAC'23* (Venezia) IPAC'23 - 14th International Particle Accelerator Conference 14 JACoW Publishing, Geneva, Switzerland, 2023, pp. 855–858 ISBN: 978-3-95450-231-8
DOI: `https://doi.org/10.18429/JACoW-14thInternationalParticleAcceleratorConference-TUXD1` (see p. 15).

[41] S. Casalbuoni, M. Migliorati, A. Mostacci, L. Palumbo, and B. Spataro „Beam heat load due to geometrical and resistive wall impedance in COLDDIAG“ in: *Journal of Instrumentation* 7.11 (2012), P11008
DOI: `10.1088/1748-0221/7/11/P11008` (see p. 16).

[42] G. Stupakov, K. Bane, and I. Zagorodnov „Optical approximation in the theory of geometric impedance“ in: *Physical Review Special Topics-Accelerators and Beams* 10.5 (2007), p. 054401
`http.//www.slac.stanford.edu/pubs/slacpubs/12250/slac-pub-12369.pdf` (see p. 17).

[43] K. Ng, K. Bane, et al. *Explicit expressions of impedances and wake functions* tech. rep. Fermi National Accelerator Lab.(FNAL), Batavia, IL (United States), 2010 (see pp. 17, 19).

[44] J. B. Murphy, S. Krinsky, and R. L. Gluckstern „Longitudinal Wake Field for An Electron Moving on A Circular orbit“ in: *Part. Accel.* 57 (1997), pp. 9–64
`http://cds.cern.ch/record/1120287/files/p9.pdf` (see p. 17).

[45] T. Agoh „Steady fields of coherent synchrotron radiation in a rectangular pipe“ in: *Phys. Rev. ST Accel. Beams* 12 (2009), p. 094402
DOI: `10.1103/PhysRevSTAB.12.094402` (see p. 18).

[46] Y. Cai „Theory of Microwave Instability and Coherent Synchrotron Radiation in Electron Storage Rings“ in: *Proc. IPAC'11* (San Sebastian, Spain, Sep. 2011) JACoW Publishing, Geneva, Switzerland, 2011, pp. 3774–3778
`https://accelconf.web.cern.ch/ipac2011/papers/frxaa01.pdf` (see p. 18).

[47] M. Brosi, J. L. Steinmann, E. Blomley, E. Bründermann, M. Caselle, N. Hiller, B. Kehrer, Y.-L. Mathis, M. J. Nasse, L. Rota, M. Schedler, P. Schönfeldt, M. Schuh, M. Schwarz, M. Weber, and A.-S. Müller „Fast mapping of terahertz bursting thresholds and characteristics at synchrotron light sources“ in: *Phys. Rev. Accel. Beams* 19 (2016), p. 110701
DOI: `10.1103/PhysRevAccelBeams.19.110701` (see pp. 19, 22, 24, 79).

[48] A. Novokhatski and A. Mosnier „Wakefields of Short Bunches in the Canal Covered with Thin Dielectric Layer“ in: *Proc. PAC'97* (Vancouver, Canada, May 1997) JACoW Publishing, Geneva, Switzerland, 1997, pp. 1661–1663
`https://accelconf.web.cern.ch/pac97/papers/pdf/5V028.PDF` (see p. 19).

[49] K. Bane and A. Novokhatski „The resonator impedance model of surface roughness applied to the LCLS parameters“ in: *SLAC Report Nos. SLAC-AP-117, LCLS-TN-99-1* (1999)
`https://www-ssrl.slac.stanford.edu/lcls/papers/slac-ap-117.pdf` (see p. 19).

[50] V. S. Vladimirov *Equations of Mathematical Physics* M. Dekker, 1971 ISBN: 0824717139, 9780824717131 (see p. 19).

[51] S. A. Heifets and S. A. Kheifets „High-frequency limit of the longitudinal impedance of an array of cavities“ in: *Phys. Rev. D* 39 (1989), pp. 960–970
DOI: `10.1103/PhysRevD.39.960` (see pp. 19, 105).

[52] R. L. Gluckstern „Longitudinal impedance of a periodic structure at high frequency“ in: *Phys. Rev. D* 39 (1989), pp. 2780–2783
DOI: `10.1103/PhysRevD.39.2780` (see p. 19).

[53] K. Bane, M. Timm, and T. Weiland „The short range wakefields in the SBLC linac“ in: *Proceedings of the 1997 Particle Accelerator Conference (Cat. No.97CH36167)* vol. 1 1997, 515–517 vol.1
DOI: `10.1109/PAC.1997.749718` (see p. 19).

[54] A.-S. Müller and M. Schwarz „Accelerator-based thz radiation sources“ in: *Synchrotron Light Sources and Free-Electron Lasers: Accelerator Physics, Instrumentation and Science Applications* (2020), pp. 83–117 (see p. 20).

[55] I. M. Frank „Doppler effect in a refractive medium“ in: *Bulletin of the Russian Academy of Sciences: Physics* 6.1-2 (1942), pp. 2–2 (see p. 20).

[56] Y. Shibata, S. Hasebe, K. Ishi, S. Ono, M. Ikezawa, T. Nakazato, M. Oyamada, S. Urasawa, T. Takahashi, T. Matsuyama, K. Kobayashi, and Y. Fujita „Coherent Smith-Purcell radiation in the millimeter-wave region from a short-bunch beam of relativistic electrons“ in: *Phys. Rev. E* 57 (1998), pp. 1061–1074
DOI: `10.1103/PhysRevE.57.1061` (see p. 20).

[57] W. R. Hamilton „On a general method of expressing the paths of light, and of the planets, by the coefficients of a characteristic function“ in: *Dublin University Review and Quarterly Magazine* 1 (1833), pp. 795–826
`https://www.emis.de/classics/Hamilton/CharFun.pdf` (see p. 21).

[58] A. A. Vlasov „THE VIBRATIONAL PROPERTIES OF AN ELECTRON GAS“ in: *Soviet Physics Uspekhi* 10.6 (1968), p. 721
DOI: `10.1070/PU1968v010n06ABEH003709` (see p. 21).

[59] P. Schönfeldt „Simulation and measurement of the dynamics of ultra-short electron bunch profiles for the generation of coherent THz radiation“ 54.01.01; LK 01 PhD thesis Karlsruher Institut für Technologie (KIT), 2018 142 pp.
DOI: `10.5445/IR/1000084466` (see pp. 21, 43, 55).

[60] J. Haïssinski „Exact longitudinal equilibrium distribution of stored electrons in the presence of self-fields“ in: *Il Nuovo Cimento B (1971-1996)* 18.1 (1973), pp. 72–82
ISSN: 1826-9877
DOI: `10.1007/BF02832640` (see p. 22).

[61] M. Brosi „In-Depth Analysis of the Micro-Bunching Characteristics in Single and Multi-Bunch Operation at KARA“ PhD thesis Karlsruher Institut für Technologie (KIT), 2020 198 pp.
DOI: `10.5445/IR/1000120018` (see pp. 22, 24, 33, 47, 53–55, 85).

[62] T. Boltz et al. „Perturbation of Synchrotron Motion in the Micro-Bunching Instability“ in: *Proc. IPAC'19* (Melbourne, Australia, May 2019) JACoW Publishing, Geneva, Switzerland, 2019, pp. 108–111
DOI: `10.18429/JACoW-IPAC2019-MOPGW018` (see p. 22).

[63] P. Krejcik, K. Bane, P. Corredoura, F. Decker, J. Judkins, T. Limberg, M. Minty, R. Siemann, and F. Pedersen „High intensity bunch length instabilities in the SLC damping rings“ in: *Proceedings of International Conference on Particle Accelerators* 1993, 3240–3242 vol.5
DOI: `10.1109/PAC.1993.309612` (see p. 23).

[64] U. Arp, G. T. Fraser, A. R. Hight Walker, T. B. Lucatorto, K. K. Lehmann, K. Harkay, N. Sereno, and K.-J. Kim „Spontaneous coherent microwave emission and the sawtooth instability in a compact storage ring“ in: *Phys. Rev. ST Accel. Beams* 4 (2001), p. 054401
DOI: `10.1103/PhysRevSTAB.4.054401` (see p. 23).

[65] K. L. F. Bane, Y. Cai, and G. Stupakov „Threshold studies of the microwave instability in electron storage rings“ in: *Phys. Rev. ST Accel. Beams* 13 (2010), p. 104402
DOI: `10.1103/PhysRevSTAB.13.104402` (see pp. 24, 25).

[66] P. Kuske „CSR-driven Longitudinal Single Bunch Instability Thresholds“ in: *Proc. IPAC'13* (Shanghai, China, May 2013) JACoW Publishing, Geneva, Switzerland, 2013, pp. 2041–2043
`jacow.org/IPAC2013/papers/WEOAB102.pdf` (see p. 24).

[67] D. P. Hampshire „A derivation of Maxwell's equations using the Heaviside notation“ in: *Philosophical Transactions of the Royal Society A: Mathematical, Physical and Engineering Sciences* 376.2134 (2018), p. 20170447
DOI: `10.1098/rsta.2017.0447` (see p. 25).

[68] D. M. Pozar *Microwave engineering* Fourth edition John wiley & sons, 2011 ISBN: 978-0-470-63155-3 (see pp. 26, 27).

[69] K. Kurokawa „Power Waves and the Scattering Matrix“ in: *IEEE Transactions on Microwave Theory and Techniques* 13.2 (1965), pp. 194–202
DOI: `10.1109/TMTT.1965.1125964` (see p. 27).

[70] R. Voutta „Beam heat load investigations with a cold vacuum chamber for diagnostics in a synchrotron light source“ PhD thesis Karlsruher Institut für Technologie (KIT), 2016 116 pp.
DOI: `10.5445/IR/1000054479` (see p. 27).

[71] J. Neilson, P. Latham, M. Caplan, and W. Lawson „Determination of the resonant frequencies in a complex cavity using the scattering matrix formulation“ in: *IEEE Transactions on Microwave Theory and Techniques* 37.8 (1989), pp. 1165–1170
DOI: `10.1109/22.31074` (see p. 27).

[72] KIT-IBPT *construction department* (see pp. 29–31, 34).

[73] J. L. Steinmann *Diagnostics of short electron bunches with THz detectors in particle accelerators* Karlsruhe: KIT Scientific Publishing, 2019 ISBN: 9783731508892
DOI: `10.5445/KSP/1000090017` (see pp. 31, 32, 95).

[74] B. Kehrer „Time-resolved studies of the micro-bunching instability at KARA“ PhD thesis Karlsruher Institut für Technologie (KIT), 2019 143 pp.
DOI: `10.5445/IR/1000098584` (see p. 29).

[75] Synchrotron-Radiation-facility *ANKA instrumentation book 2012* http://www.anka.kit.edu/downloads_anka/instrumentation_books//Instrumentationbook-2012.pdf (see p. 29).

[76] A. Bernhard, J. Gethmann, S. Casalbuoni, S. Gerstl, et al. „A CLIC Damping Wiggler Prototype at ANKA: Commissioning and Preparations for a Beam Dynamics Experimental Program“ in: *Proc. IPAC'16* (Busan, Korea, May 2016) JACoW Publishing, Geneva, Switzerland, 2016, pp. 2412–2415
DOI: `10.18429/JACoW-IPAC2016-WEPMW002` (see pp. 30, 34).

[77] A. Zimina, K. Dardenne, M. A. Denecke, J. D. Grunwaldt, E. Huttel, H. Lichtenberg, S. Mangold, T. Pruessmann, J. Rothe, R. Steininger, and T. Vitova „The CAT-ACT Beamline at ANKA: A new high energy X-ray spectroscopy facility for CATalysis and ACTinide research“ in: *Journal of Physics: Conference Series* 712.1 (2016), p. 012019
DOI: `10.1088/1742-6596/712/1/012019` (see p. 30).

[78] S. Mangold, R. Steininger, T. dos Santos Rolo, and J. Göttlicher „Full field spectroscopic imaging at the ANKA-XAS- and -SUL-X-Beamlines“ in: *Journal of Physics: Conference Series* 430.1 (2013), p. 012130
DOI: `10.1088/1742-6596/430/1/012130` (see p. 30).

[79] L. Weinhardt, R. Steininger, D. Kreikemeyer-Lorenzo, S. Mangold, D. Hauschild, D. Batchelor, T. Spangenberg, and C. Heske „X-SPEC: a 70eV to 15keV undulator beamline for X-ray and electron spectroscopies“ in: *Journal of Synchrotron Radiation* 28.2 (2021), pp. 609–617
DOI: `10.1107/S1600577520016318` (see pp. 30, 101, 103).

[80] S. Casalbuoni, E. Blomley, N. Glamann, A. Grau, T. Holubek, E. Huttel, D. S. de Jauregui, S. Bauer, C. Boffo, T. Gerhard, M. Turenne, and W. Walter „Commissioning of a full scale superconducting undulator with 20mm period length at the storage ring KARA“ in: *AIP Conference Proceedings* 2054.1 (2019) 030025
ISSN: 0094-243X
DOI: `10.1063/1.5084588` (see pp. 30, 34).

[81] M. A. Denecke, J. Rothe, K. Dardenne, H. Blank, and J. Hormes „The INE-beamline for actinide research at ANKA“ in: *Physica Scripta* 2005.T115 (2005), p. 1001
DOI: `10.1238/Physica.Topical.115a01001` (see p. 31).

[82] S. L. Kramer „Direct observation of beam impedance above cutoff“ in: *Phys. Rev. ST Accel. Beams* 5 (2002), p. 112001
DOI: `10.1103/PhysRevSTAB.5.112001` (see p. 31).

[83] P. F. Tavares, S. C. Leemann, M. Sjöström, and Å. Andersson „The MAXIV storage ring project“ in: *Journal of Synchrotron Radiation* 21.5 (2014), pp. 862–877
DOI: `10.1107/S1600577514011503` (see p. 31).

[84] P. Schreiber „Negative Momentum Compaction Operation and its Effect on the Beam Dynamics at the Accelerator Test Facility KARA“ 54.11.11; LK 01 PhD thesis Karlsruher Institut für Technologie (KIT), 2022 131 pp.
DOI: `10.5445/IR/1000148354` (see p. 33).

[85] S. Dhillon, M. Vitiello, E. Linfield, et al. „The 2017 terahertz science and technology roadmap“ in: *Journal of Physics D: Applied Physics* 50.4 (2017), p. 043001
DOI: `10.1088/1361-6463/50/4/043001` (see p. 32).

[86] G. Wustefeld, J. Feikes, K. Holldack, and P. Kuske „Compressed Electron Bunches for THz-Generation - Operating BESSY II in a Dedicated Low Alpha Mode“ in: *Proc. EPAC'04* (Lucerne, Switzerland, Jul. 2004) JACoW Publishing, Geneva, Switzerland, 2004
`http://accelconf.web.cern.ch/e04/papers/THPKF015.pdf` (see p. 32).

[87] M. Klein, N. Hiller, A. Hofmann, E. Huttel, V. Judin, B. Kehrer, S. Marsching, and A.-S. Mueller „Modeling the Low-Alpha-Mode at ANKA with the Accelerator Toolbox“ in: *Proc. PAC'11* (New York, NY, USA, Mar.-Apr. 2011) JACoW Publishing, Geneva, Switzerland, 2011, pp. 1510–1512 `https://jacow.org/PAC2011/papers/WEP005.pdf` (see p. 32).

[88] A. I. Papash, E. Blomley, T. Boltz, M. Brosi, E. Bründermann, S. Casalbuoni, J. Gethmann, E. Huttel, B. Kehrer, A. Mochihashi, A.-S. Müller, R. Ruprecht, M. Schuh, and J. Steinmann „New Operation Regimes at the Storage Ring KARA at KIT“ in: *Proc. IPAC'19* (Melbourne, Australia, May 2019) JACoW Publishing, Geneva, Switzerland, 2019, pp. 1422–1425 DOI: `10.18429/JACoW-IPAC2019-TUPGW016` (see p. 33).

[89] A. Papash, A. Bernhard, E. Blomley, H. Hoteit, A. Mochihashi, R. Ruprecht, M. Schuh, J. Steinmann, and A.-S. Mueller „Application of three families of sextupoles at the KARA ring of Karlsruhe Institute of Technology“ in: *Proc. IPAC'23* (Venezia) IPAC'23 - 14th International Particle Accelerator Conference 14 JACoW Publishing, Geneva, Switzerland, 2023, pp. 630–634 ISBN: 978-3-95450-231-8 DOI: `10.18429/JACoW-14thInternationalParticleAcceleratorConference-MOPM007` (see p. 33).

[90] CERN *CERN Yellow Reports: Monographs, Vol 4 (2018): The Compact Linear Collider (CLIC) – Project Implementation Plan* en 2019 DOI: `10.23731/CYRM-2018-004` (see p. 34).

[91] *CST Studio Suite, Dassault Systèmes* `https:/www.cst.com` (see p. 37).

[92] *Metalcor GmbH, Datasheet: 1.4429 (AISI 316 LN)* Metalcor `https://www.metalcor.de/en/datenblatt/15/` (see p. 38).

[93] *CST Studio Suite Help* `https://space.mit.edu/RADIO/CST_online/cst_studio_suite_help.html` (see p. 40).

[94] K. L. F. Bane, Y. Cai, and G. Stupakov „Threshold studies of the microwave instability in electron storage rings“ in: *Phys. Rev. ST Accel. Beams* 13 (2010), p. 104402 DOI: `10.1103/PhysRevSTAB.13.104402` (see p. 42).

[95] P. Schönfeldt *Inovesa* DOI: `10.5821/zenodo.597356` (see p. 43).

[96] P. Schönfeldt, M. Brosi, M. Schwarz, J. L. Steinmann, and A.-S. Müller „Parallelized Vlasov-Fokker-Planck solver for desktop personal computers“ in: *Phys. Rev. Accel. Beams* 20 (2017), p. 030704 DOI: `10.1103/PhysRevAccelBeams.20.030704` (see pp. 43–45, 73).

[97] *The HDF Group, Hierarchical Data Format, version 5* `https://www.hdfgroup.org/HDF5/` 1997-2019 (see p. 44).

[98] P. Schreiber „Systematic Studies of the Influence of Impedances on Longitudinal Beam Dynamics“ MA thesis Karlsruher Institut für Technologie (KIT), 2018 (see p. 44).

[99] *Phyton Software Foundation. Phython Language Reference, version 3.8* `http://www.python.org` (see p. 45).

[100] K. Y. Ng *Impedance of bellows corrugations* tech. rep. FERMILAB-FN-449. FN-449 Batavia, IL: FERMILAB, 1987 `https://cds.cern.ch/record/177237` (see p. 47).

[101] T. Boltz et al. „Studies of Longitudinal Dynamics in the Micro-Bunching Instability Using Machine Learning“ in: *Proc. IPAC'18* (Vancouver, Canada, Apr.-May 2018) JACoW Publishing, Geneva, Switzerland, pp. 3277–3279 DOI: `10.18429/JACoW-IPAC2018-THPAK030` (see p. 55).

[102] V. Judin „Untersuchung von Bunch-Bunch-Wechselwirkungen und des Einflusses der geometrischen Impedanz bei der Erzeugung kohärenter THz-Strahlung“ PhD thesis 2013 DOI: `10.5445/IR/1000039528` (see p. 57).

[103] M. Caselle, L. A. Perez, M. Balzer, A. Kopmann, L. Rota, M. Weber, M. Brosi, J. Steinmann, E. Bründermann, and A.-S. Müller „KAPTURE-2. A picosecond sampling system for individual THz pulses with high repetition rate“ in: *Journal of Instrumentation* 12.01 (2017), p. C01040 DOI: `10.1088/1748-0221/12/01/C01040` (see p. 95).

[104] *schematische Darstellung der Prozessschritte des DRIE-Verfahrens, Wikimedia* `https://upload.wikimedia.org/wikipedia/de/1/17/Verfahrensschritte-DRIE.png` (see p. 120).

[105] *AZ4562 data sheet* `https://www.microchemicals.com/micro/tds_az_4500_series.pdf` (see p. 118).

[106] S. Zhang, S. To, Z. Zhu, and G. Zhang „A review of fly cutting applied to surface generation in ultra-precision machining“ in: *International Journal of Machine Tools and Manufacture* 103 (2016), pp. 13–27 ISSN: 0890-6955 DOI: `https://doi.org/10.1016/j.ijmachtools.2016.01.001` (see p. 121).

[107] M. Brosi, S. Bielawski, C. Evain, A.-S. Müller, E. Roussel, P. Schreiber, et al. „Simulations of the Micro-Bunching Instability for SOLEIL and KARA Using Two Different VFP Solver Codes“ in: *Proc. IPAC'22* (Bangkok, Thailand) International Particle Accelerator Conference 13 JACoW Publishing, Geneva, Switzerland, 2022, WEPOMS005, pp. 2237–2240 ISBN: 978-3-95450-227-1 DOI: `10.18429/JACoW-IPAC2022-WEPOMS005` (see p. 128).

[108] M. Brosi, A. Andersson, J. Breunlin, F. Cullian, and P. Tavares „Time-resolved measurement and simulation of a longitudinal single-bunch instability at the MAX IV 3 GeV ring“ English in: *Proc. IPAC'23* (Venice, Italy) IPAC'23 - 14th International Particle Accelerator Conference 14 JACoW Publishing, Geneva, Switzerland, 2023, pp. 2685–2688 ISBN: 978-3-95450-231-8 DOI: `10.18429/JACoW-IPAC2023-WEPA020` (see p. 128).

[109] P. Virtanen, R. Gommers, T. E. Oliphant, M. Haberland, T. Reddy, D. Cournapeau, E. Burovski, P. Peterson, W. Weckesser, J. Bright, S. J. van der Walt, M. Brett, J. Wilson, K. J. Millman, N. Mayorov, A. R. J. Nelson, E. Jones, R. Kern, E. Larson, C. J. Carey, İ. Polat, Y. Feng, E. W. Moore, J. VanderPlas, D. Laxalde, J. Perktold, R. Cimrman, I. Henriksen, E. A. Quintero, C. R. Harris, A. M. Archibald, A. H. Ribeiro, F. Pedregosa, P. van Mulbregt, and SciPy 1.0 Contributors „SciPy 1.0: Fundamental Algorithms for Scientific Computing in Python“ in: *Nature Methods* 17 (2020), pp. 261–272 DOI: `10.1038/s41592-019-0686-2` (see p. 138).

Acknowledgements

Such a thesis over four years is only possible with the help, support, and impact of many people in different ways. I am very grateful for all this support, which made working on the project and its everyday tasks much easier and more enjoyable.

Many thanks to Prof. Anke-Susanne Müller for providing me with the opportunity to do my Ph.D. thesis at the IBPT and the KARA storage ring.

I want to thank Prof. Ulrich Husemann for kindly taking on the role of the co-referent.

Thank Robert Ruprecht, for taking care of the administrative topics so I could concentrate on my research. Furthermore, his input, knowledge, and contacts were very helpful in finding possible manufacturing methods and institutes.

I acknowledge the support by the Doctoral School "Karlsruhe School of Elementary and Astroparticle Physics: Science and Technology" (KSETA), which gave me the opportunity to attend several courses on different scientific topics.

In addition, I would like to thank all the colleagues at PhLAM and Synchrotron SOLEIL, who are part of the UltraSync project, for the exchange and the discussions at the annual project meetings.

In the process of making the prototypes, I relied on the assistance and support of many different working groups, institutes, and especially colleagues, whom I would like to thank: Prof. Sebastian Kempf and his group for the production of a prototype using the Bosch process. Special thanks to Matthias Wegner for his interest in the topic, his efforts to optimize the process, and for giving me the opportunity to participate in the production in the HSS clean room. Heinz Lambach, Matthias Schöffler, and their colleagues at IMVT for the discussions about the possible manufacturing methods in their institute and the etching of two large test structures, which occupied the machine for about one week. Alban Muslija for taking the SEM images of different prototypes. I thank Tobias Ruess and Alexander Marek for multiple discussions and preparations of the eigenmode measurements at the test stand at the IHM.

A big thank you goes to all the current and former colleagues in the THz group at IBPT for the daily discussions and exchanges in a friendly working environment. I want to thank all of you who contributed to this thesis in one way or another, especially all of the proofreaders who helped to improve the understandability and readability of this thesis through their feedback. However, there is a group of people who deserve special and individual thanks: My special thanks go to Akira Mochihashi for his supervision during this thesis and during my master's thesis. His support and guidance were crucial to focus on the essentials. Without him, this thesis would not be the same. I want to thank Michael Nasse, whose project management allowed me to focus on physics. Despite all his obligations, he was (almost) always available for discussions and attended all the meetings with potential manufacturers.

A big thank you goes to Miriam Brosi, whose enthusiasm as a tutor of the accelerator lecture initially attracted me to the IBPT in the first place. Furthermore, her deep knowledge of the micro-bunching instability and Inovesa led to many meaningful discussions and suggestions for the project over the years. I want to thank Patrick Schreiber, who helped a lot with his knowledge of Inovesa and his support in correctly adding impedance into Inovesa. He also kindly provided me with his HDF5-viewer, which has greatly simplified the beam dynamics simulation results analysis. I thank Markus Schwarz for his frequent input during the regular project meetings. His more theoretical background caused many fruitful discussions and opened new perspectives. I thank Hyuk Jin Cha for his helpful comments and support with the CST impedance simulation.

I want to thank my fellow doctoral researchers Micha, Matthias, Jens, Chenran, and Marvin for the countless discussions and brainstorming during coffee breaks or informal meetings. Special thanks go to Chenran for sharing the office with me for about four years (except for the Covid lockdowns). I also want to thank Matthias for joining me on the bizarre "*Kangoo Roadtrip*" to Hamburg.

Last but not least, I have to thank my parents and the best little sister anybody could ever ask for. This work and my entire academic career would not have been possible without your unrestricted support and motivation during the last 10½ years of studies and my whole life.

THANK YOU ALL!